DOTTORATO DI RICERCA IN

CHIMICA

Ciclo XXXVI

Settore Concorsuale: 03/A2 - MODELLI E METODOLOGIE PER LE SCIENZE CHIMICHE

Settore Scientifico Disciplinare: CHIM/02 – Chimica Fisica

ELECTROCHEMISTRY OF POLYCYCLIC AROMATIC MOLECULES FOR ADVANCED CARBON NANOSTRUCTURES: LUMINESCENCE AND TRANSISTOR APPLICATIONS

Presentata da: *Lorenzo Ripani*

Coordinatore Dottorato   **Supervisore**

Prof. Luca Prodi   Prof. Massimo Marcaccio

Esame finale anno 2024

Alla mia famiglia

Abstract

Polycyclic aromatic hydrocarbons (PAHs) are a large class of π-conjugated organic molecules with fused aromatic rings, which can be considered as fragments of 2D-graphene and have been extensively studied for their unique optical and electronic properties. The aim of this study is to understand the complex electrochemical behaviour of planar, curved, and heteroatom doped polycyclic aromatic molecules, particularly focusing on the oxidative coupling of their radical cations and the electrochemically induced cyclodehydrogenation reactions.

In the first part of this thesis, the class of PAHs and aromatic nanostructures are introduced, and the reactivity of electrogenerated species is discussed, focusing on the electrochemical approach for the synthesis of extended π-conjugated structures. Subsequently, the electrochemical properties and reactivity of electrogenerated radical ions of planar and curved polyaromatics are correlated to their structures. In the third chapter, electrochemical cyclodehydrogenation of hexaphenylbenzene is used to prepare self-assembled hexabenzocoronene, directly deposited on an interdigitated electrode, which was characterised as organic electrochemical transistor. In the fourth chapter, the electrochemical behaviour of a family of azapyrene derivatives has been carefully investigated together with the electrogenerated chemiluminescence (ECL), both by ion-annihilation and co-reactant methods. Two structural azapyrene isomers with different nitrogen positions are thoroughly discussed in terms of redox and ECL properties. Interestingly, the ECL of only one of them showed a double emission with excimer formation. A detailed mechanism is discussed for the ECL by co-reactant benzoyl peroxide, to rationalise the different ECL behaviours of the two isomers on the basis of their topologically modulated electronic properties.

In conclusion, the different electrochemical behaviours of PAHs were shown, focussing on the chemical reactivity of the electrogenerated species and taking advantage of it for important processes spanning from unconventional synthesis methods for carbon nanostructures to the exploitation of self-assembled nanostructured systems in organic electronics, to novel organic emitters in ECL.

Preface

Carbon is the first atom of the 14th group of the period table, the etymology of its name was coined by the French scientist Lavoisier in 1787 as "*charbone*" from the Latin word "*carbonem*". Carbon is one of the most abundant elements on Earth and is even more abundant in the observed universe. Moreover, all the life on Earth is based on carbon in many different forms. In nature, carbon can assume many allotropic forms, notably the most known are graphite and diamond. Carbon is highly versatile, mostly due to its different chemical bonds that can form between itself and other atoms such as hydrogen, nitrogen, and oxygen, leading to different geometries and properties. One of the most important is the bond between carbons, whose orbitals are hybridized with sp^2 atomic orbitals, where there is a σ-bonding network that creates the structure of the molecule and the orthogonal p-orbitals that forms π-bonds. When many C–C bonds are together in a similar way, the π-bonds may extend through many carbon atoms, leading to a higher stabilisation of the molecule, a special case is that of aromatic molecules.

Polycyclic aromatic hydrocarbons (PAHs) are large π-systems composed of fused aromatic rings that have been the subject of investigation in many fields of natural sciences owing to their unique optical and electronic properties. Since the discovery of graphene, interest in PAHs has been further increased as versatile material in the field of optoelectronics and organic electronic.[1–4] Other research topics related to PAHs include bioimaging, sensing, and toxicology.

In this thesis, the focus is on the electrochemical studies of both planar and curved polycyclic aromatic molecules, including the reactivity of the electrogenerated species. Besides, it was explored the electrochemiluminescence of a family of nitrogen-doped polycyclic aromatic systems, namely derivatives of azapyrene, also to understand how the chemical structure and heteroatom position can influence its molecular properties. As a further aspect, the investigation involved the electrochemically induced graphitisation of a non-planar polyphenyl precursor and the self-assembly of the obtained hexabenzocoronene as material for electrochemical transistor applications.

Table of Contents

Chapter 1

Introduction

1.1 Polycyclic aromatic compounds

Polycyclic aromatic compounds (PACs) are a large class of organic molecules which can be found in nature, mainly as pigments or in organic sediments as fossil carbon like coal and petroleum. Depending on their chemical composition, we can define PAC subclasses: such as polycyclic aromatic hydrocarbons (PAHs) and polycyclic heteroaromatic molecules (PHMs). PAHs have usually planar chemical structures, composed exclusively of sp^2 carbon and hydrogen atoms such as pyrene, triphenylene, and hexabenzocoronene. PHMs have a similar structure to PAHs but include heteroatoms such as nitrogen or sulphur atoms in their structure, such as azapyrene.[2,5] PACs also include non-planar aromatic species, such as bowl-shaped corannulene and sumanene, or non-completely aromatic species with sp^3 carbons, such as fluorene.

In recent years, extensive research has been conducted on polycyclic aromatic molecules, covering many areas of natural science, ranging from environmental and health sciences to chemistry and material sciences.

Generally, PAHs can be produced by the incomplete combustion of many organic materials, such as fossil fuels, wood, and even (excessively) grilled food. PAH are widespread and can be found in different media, depending on their molecular weight. When released into the air from exhaustive gases, PAHs are dispersed as particulates (for larger PAHs) or in the gas phase, but as they are deposited, they can be found in water and soil. Unfortunately, all PAHs are environmental pollutants,[6] and some of them pose a risk to human health because they are lipid-soluble and metabolised by the organism into toxic, mutagenic, and/or carcinogenic species that can interact with DNA or cell membranes.[7] Interestingly, PAHs have also been extensively studied in astrochemistry because they are known to be abundant in interstellar media, and there is also a speculative hypothesis that some polycyclic aromatic hydrocarbons even contributed to the origin of life on Earth.[8]

Historically, benzene was first isolated from oily residues in the early 19th century, despite not being a polycyclic molecule, it can be considered as the simplest aromatic unit that composes the PAHs. For the entire century, benzene structure puzzled chemists of that era, until in 1865, when Friedrich Kekulè proposed the structure which nowadays names one of the resonance structures of benzene, i.e. the Kekulè structure. Shortly after the discovery of the benzene structure, other aromatic structures with condensed rings were discovered, i.e. the class of polycyclic aromatic hydrocarbons was unveiled. The PAHs family is characterised by condensed aromatic rings, and as a result of extended π-conjugation, PAHs show a narrow energy gap between the highest occupied molecular orbital (HOMO) and the lowest unoccupied molecular orbital (LUMO), high molar extinction coefficient, high emission quantum yield and redox potential which decreases for extended PAHs.[9] PAH properties are strongly dependent on their size but also on their topological arrangement (chemical structure), for example, an isomer with a higher number of Clar's sextets, i.e. six π-electrons localised in a single benzenoid ring, shows a higher stability with higher ionisation potential which reflects on its electrochemical oxidation potential and larger HOMO-LUMO gap compared to its structural isomers with less Clar's sextet.[10] An example of this behaviour is observed for triphenylene which is the most stable of the $C_{18}H_{12}$ isomers (benzo[c]phenanthrene and tetraphene).[11] The Clar's aromatic sextet rule can also explain the synthesis of hexabenzocoronene from hexaphenylbenzene since the cyclodehydrogenation reaction is driven by an increase of Clar's sextets which results in a particularly stable molecule (Figure 1.1).[10,12,13]
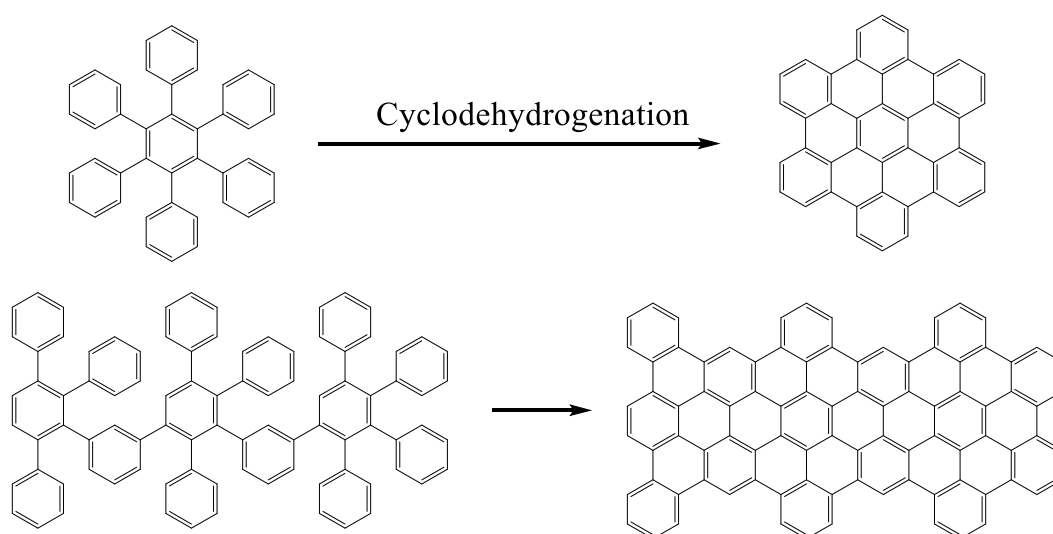

Figure 1.1 Cyclodehydrogenation of oligophenylenes to extended π-conjugated PAHs (nanographenes and graphene nanoribbons)

1.2 Advanced carbon nanostructures

The discovery and isolation of pure graphene in 2004 by A. Geim and K. Novoselov, which resulted in the Nobel prize in physics in 2010, have fostered impressive developments in the chemistry community, particularly in the PAHs research. These developments have resulted in new methods for the synthesis and characterisation of atomically thin 2D materials with new fundamental studies of their outstanding optical and charge-transfer properties which have rapidly translated into new technological advancements. New 2D materials and similar nanostructures have widely expanded the field of nanoscience and material science with a completely new class of materials (Figure 1.2).[14] The zero bandgap of graphene, owing to its unique electronic structure, restricts its applicability in many organic electronic devices, such as field-effect transistors. Nonetheless, by confining the dimensions of carbon nanostructures to quasi-0D (graphene quantum dots, GQDs, or nanographenes) or quasi-1D (graphene nanoribbons, GNRs), a nonzero band gap was achieved preserving the high charge-carrier mobility of graphene.[1,14] In the bottom-up synthesis of GNRs, based on the work of Clar and Scholl on cyclodehydrogenation and pioneered by Müllen et al.,[1,15–17] PAHs are used as molecular precursors for the preparation of well-defined oligophenylene species which are then oxidatively cyclodehydrogenated in solution or on a metal surface to produce fully π-conjugated PAH.
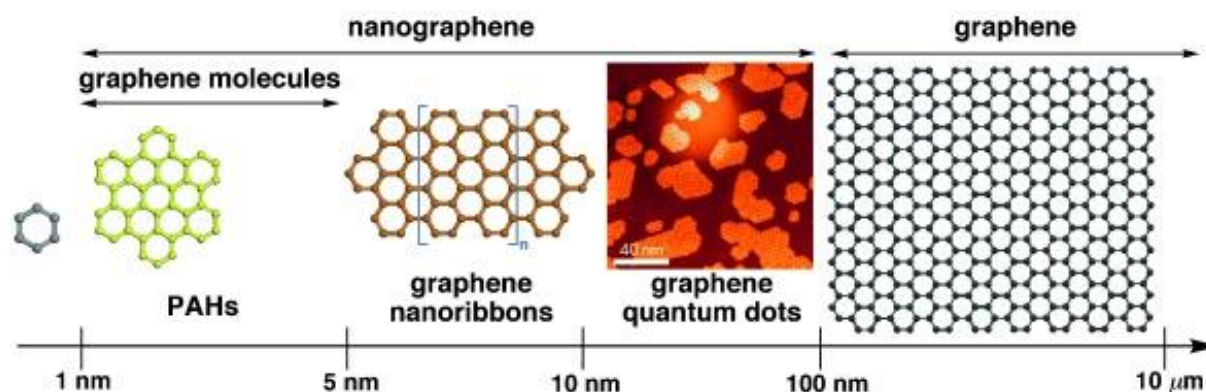
Figure 1.2 Carbon-based structures with sp^2 π-conjugated structures exhibiting different dimensionality; ranging from the smallest aromatic unit up to quasi-0D (PAHs and GQDs), quasi-1D GNRs, and 2D graphene. Image taken with permission from ref. [18] *. Copyright © 2012 WILEY-VCH Verlag GmbH & Co. KGaA.*

Nanographenes have been defined as extended PAHs with sizes less than 10 nm, and some examples of precisely synthesised nanographenes are hexa-peri-hexabenzocoronene and dibenzo[hi,st]ovalene. Extended PAHs have attracted extensive interest in the optoelectronic field, mostly because of their exceptional size-dependent optical properties, such as a high

absorption coefficient and high photoluminescence quantum yield (PLQY) with emission wavelengths which can be further tuned by edge functionalisation. Small organic molecules and extended PAHs can be employed in transistor applications owing to their high intrinsic charge-carrier mobilities. However, in organic thin films, the film morphology strongly affects the charge transport performance.[19] In organic field-effect transistors (OFET), the observed charge mobility correlates with the molecular order and crystallinity of the film.[19] In PAHs and GQDs the molecular interactions that controls the molecular packing are intermolecular Van der Waals interactions, in particular for PAHs there are π-π and C-H - π interactions. The charge transport process in PAHs organic films is defined as "hopping mechanism", in which the charge in localised and is transferred from one molecule to the neighbouring one.

Graphene nanoribbons (GNRs) can be considered as one-dimensional extension of graphene with a length/width aspect ratio higher than 10. Narita et al. extensively expanded this class of carbon nanostructures through the precise synthesis of soluble oligophenylenes which were subsequently planarized by oxidative cyclodehydrogenation.[16,20,21] The GNRs properties strongly depend on their width and edge structure, and GNRs can exhibit zigzag or armchair edge configurations (Figure 1.3).[16,22] Armchair GNRs have width-dependent bandgaps, which are usually larger than those of zigzag GNRs. Zigzag GNRs have very localized edge states that can be further tuned by edge functionalization, e.g. introducing chemical dopants, like oxygen atoms,[23,24] and shows magnetic properties due to the localized electronic states.[22]

Armchair GNR   Zigzag GNR
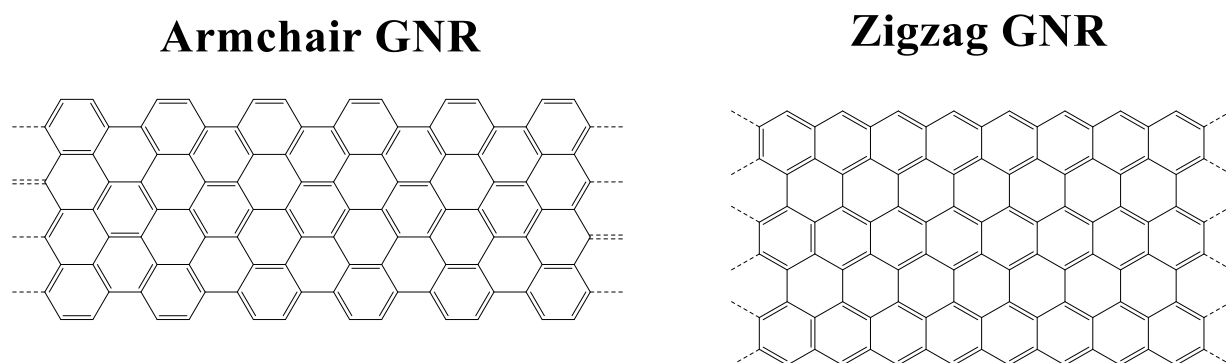
Figure 1.3 Examples of armchair and zigzag graphene nanoribbons.

Owing to the high intrinsic charge carrier mobility of GNRs with finite and controlled bandgaps, field-effect transistor (FET) applications of GNRs are very promising.[22,25] Bottom-up approaches allow the highest degree of control over the GNRs properties and defect density, thus making the most suitable synthetic method of GNR materials for transistor

applications. In contrast to surface-assisted synthesis, solution-synthesised GNRs require functionalization with alkyl chains to improve their solubility and to avoid aggregation in organic solvents. Therefore, currently, most of the reported GNRs for OFET applications are fabricated using surface-assisted methods,[22,26] which do not require a deposition step.[22] Very recently, single-electron transistors have been produced from solutions of molecular graphene nanoribbons, which could open new frontiers for technologies based on quantum electronics.[21]

Based on the applications of such carbon-based systems, their performances are measured in different ways and different material properties are investigated. In light-emitting devices, such as OLED or light-emitting electrochemical cells (LEECs), the desired material performance are oriented on their efficiency, brightness, and colour purity. In solar cell devices, the performance of organic materials depends on the power conversion efficiency and lifetime. Finally, in organic thin-film transistors, the performance is related to the charge carrier mobility, on/off ratio, threshold voltage and transconductance.[14]

1.3 Electrochemistry of polycyclic aromatic molecules

Organic species such as PAHs and heteroaromatic species are typically neutral, and their electrochemical oxidation or reduction generates radical ion species with odd numbers of electrons and paramagnetic properties. From a chemical point of view, radical cations ($R^{\bullet+}$) are electrophiles, whereas radical anions ($R^{\bullet-}$) are nucleophilic species, and in both cases, they are more reactive than their neutral counterparts. Nevertheless, PAHs radical ion reactivity decreases with the extension of the PAH π-system because the extended π-conjugated frontier molecular orbitals (FMOs) are able to better delocalise the charge.[27]

The electrochemical reduction of small polycyclic aromatic hydrocarbons (PAHs) is a well-known process. For many PAHs, the reduction process is chemically reversible, indicating that the radical anions are relatively stable. Moreover, for similar PAHs (acenes and benzenoid PAHs), the half-wave potentials ($E_{1/2}$) have been observed to be linearly correlated with the lowest unoccupied molecular orbital (LUMO) energies, and a decrease in $E_{1/2}$ was observed with an increase in π-conjugation.[28] The stability of PAH radical anions can be exploited in different applications, especially if multiple reduction processes are stable, such as in energy storage applications like Al-based batteries[29,30] or organic redox flow battery.[28] Furthermore,

a stable radical ion is a prerequisite for the application of PAHs as luminophores in electrochemiluminescence (ECL) in order to achieve a bright and stable ECL signal.[31–33]

More interesting, but less investigated than the reduction counterpart, is the electrochemical oxidation of polycyclic aromatic species, mostly because of the stability limitation of their radical cations,[34,35] which in many cases results in electrode fouling. PAHs radical cations are extremely electrophilic and accurate electrochemical characterisation of oxidation processes requires the use of a very sophisticated setup to avoid possible nucleophilic species, such as H_2O, and the ensuing unwanted parasitic processes. The use of airtight electrochemical cells and carefully dried organic electrolytes with non-nucleophilic counterions, such as quaternary alkylammonium salts $R_4N^+X^-$, where X^- can be hexafluorophosphate (PF_6^-) or hexafluoroarsenate (AsF_6^-) anions, is mandatory to avoid reactions of $R^{\bullet+}$ with H_2O, O_2, or other nucleophiles. The solvent is also required to have a low nucleophilicity with a very careful purification steps to remove H_2O traces; in our case, the very reactive radical cations have been investigated with extremely purified CH_2Cl_2.

Different factors can be used to influence the chemical stability of $R^{\bullet+}$. In general, lower temperatures decrease the rate constant of possible follow-up reactions, the use of non-nucleophilic electrolytes and solvents limits undesired reactions, and the rational design of PAHs with protecting groups such as bulky tert-butyl or mesitylene groups can protect reactive positions. Despite the intrinsic instability of $R^{\bullet+}$ can be problematic for the electrochemical characterization studies, such a reactivity can be exploited in organic electrosynthesis, particularly for the C-H activation for oxidative coupling, functionalization and cyclodehydrogenation reactions.[36,37]

1.4 Chemical reactivity of radical ions

In recent years, organic electrochemistry has received increasing interest in the organic chemistry community as a versatile and sustainable method for the synthesis of many organic species, from pharmaceutical molecules to new functional materials.[38–40]

Through electrochemical methods, by applying a suitable potential at the working electrode, we can induce reduction and oxidation reactions, which differently from conventional chemical methods do not require an excess of oxidising or reducing chemical species, but just an electric current. This difference results in a huge benefit from an economic and environmental perspective, because oxidant or reductant-free conditions allow for less waste and avoid the use of toxic organic molecules with an easier separation and purification

workup. Moreover, one of the reagents is the electric current which can be produced by renewable energy sources. Electrochemistry has the advantage of precise control of the driving force via the control of the electrode potential, thus being able to generate highly energetic intermediates in a very facile and precise way.[39]

The applicability of organic electrosynthesis has vastly improved in recent years, and two main branches can be defined depending on the electrochemical reaction: cathodic reduction and anodic oxidation reactions. Under these two categories, there is a multitude of electrochemically induced reactions from the oxidation of alcohols, olefins, arenes, and many other aromatic and heteroaromatic species to the reduction of alkyl or aryl halides, CO_2, and many other species. A very important reaction for the synthesis of new molecules in material science is the activation of the C – H bond, in particular the electrochemical oxidative coupling reaction which has been successfully used for the formation of new carbon–carbon (C-C), carbon–heteroatom (C–X), and heteroatom–heteroatom (X–Y) bonds. Oxidative coupling is at the basis of the electropolymerization of many organic conductive polymers, such as polythiophenes, polyaniline, and polypyrrole. C-H activation via oxidative coupling and intramolecular cyclodehydrogenation of PAHs has been performed using electrochemical methods (Figure 1.4).[41–44]
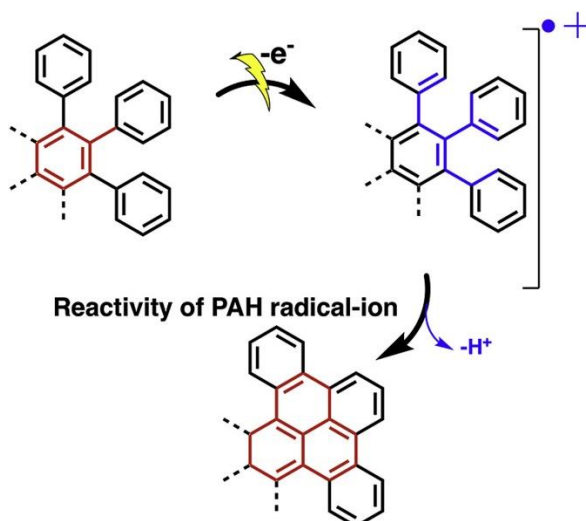

Figure 1.4 Scheme of the direct electrochemical cyclodehydrogenation of oligophenylenes to PAHs involving the reactivity of radical cation.

1.5 Applications

Energy storage

PAHs and carbon nanomaterials have attracted interest in many applications for the energy storage, from supercapacitors to batteries and even as support of catalyst for energy conversion applications. The main advantages of aromatic molecules and graphene derivatives are their exceptional conductivity and charge transport properties, while their cost and weight are significantly lower than those of their inorganic counterparts. Electrochemistry has a central role in many energy storage applications of carbon materials, for example the electropolymerization and deposition of pyrene oligomers have been reported to produce materials with remarkable stability and high specific capacity which have been employed as supercapacitor[45] or as cathode materials for Al-based batteries.[29] Noteworthy, small PAH can be exploited as catholytes in organic redox flow batteries owing to their negative reduction potential and chemically stable radical anion, allowing them to reach outstanding power densities.[28] In the framework of PAH with bowl structures, corannulene has been reported to reversibly store multiple electrons, with an electron capacity ($5C/e^-$) superior to that of pristine graphite ($6C/e^-$) and C_{60}-fullerene ($10C/e^-$). Furthermore, corannulene anions (up to $C_{20}H_{10}^{4-}$) have been observed to generate sandwich complexes with Li^+ and other alkali ion, which potentially, could be exploited as anode material in Li-ion batteries.[46,47]

Photoluminescence and electrogenerated chemiluminescence

The photophysical properties of PAHs are of great interest because of their possible application in organic electroluminescent devices, such as organic light-emitting diodes (OLEDs) or light-emitting electrochemical cells (LEECs), or for imaging and sensing applications. The PAHs and GQDs luminescence properties are tuned by the size and extension of their π-system. Generally, more extended structures have redshifted emission wavelengths compared to smaller molecules. The PAHs luminescence is usually fluorescence with very bright emission and a small Stokes shift, which suggests a negligible geometric change between the ground and excited state. Their photoluminescence quantum yields (PLQY) are also very large. Nonetheless, for planar PAHs such as pyrene, the fluorescence is affected by excimer formation that is a phenomenon in which an aggregate of two PAHs units forms in the excited state, leading to a new broad red-shifted emission with a decreased fluorescence PLQY. Electrogenerated chemiluminescence (ECL) is a luminescence process in

which the excited state of a luminophore is generated by a chemical reaction between electrogenerated reactive intermediates. PAHs are among the first organic luminophores studied in ECL, particularly 9,10-diphenylanthracene, pyrene, and rubrene, which are able to generate stable radical cations and anions and possess a high PLQY. However, the ECL efficiency of PAHs is limited by the spin statistic because during ECL, both the singlet and triplets are populated, but in classic PAHs, only the singlet emits, limiting the ECL efficiency to a maximum of 25% of the PAH PLQY. Nonetheless, in recent years, aromatic molecules with a smaller energy gap between the singlet and triplet states have allowed spin-up conversion from triplet to singlet (thermally activated delayed fluorescence)[48,49] or triplet-triplet annihilation[50] which theoretically could increase the maximum ECL efficiency. ECL is currently exploited in a number of powerful analytical methods and employed in various commercial, clinical, and biological applications.

Organic electronic

Aromatic π-conjugated systems have attracted significant interest as materials for next-generation electronics such as organic electronics. Differently, from classic inorganic solid electronics, organic materials are flexible and tuneable at lower cost for many different electronic applications, such as thin-film organic field-effect transistors, organic photovoltaics, organic light-emitting diodes, and electrochemical transistors. Organic materials have already been employed in many commercial applications, such as OLED technology which is nowadays used in many displays. Some other applications are still in the early stages and are currently limited to academic research. However, the field of organic electronics is rapidly progressing, and new technologies are introduced to the market each year.

Outline of the thesis

In this thesis, we will further understand the complex electrochemical behaviour and chemical reactivity of electrogenerated aromatic molecules, particularly focusing on the chemical reactivity of their radical cations. These electrogenerated species will be the foundation of different applications, such as the electrochemical synthesis of new materials with peculiar electrical properties, i.e. electro-polymerization of semiconductive organic films, or the production of light from chemical reactions between electrogenerated species, i.e. electrogenerated chemiluminescence (ECL) aimed at the search of new species for the development of novel analytical tools.

In the following, the structure of the thesis is outlined:

In Chapter 2, the electrochemical properties and chemical reactivity of electrogenerated species of small aromatic and PAHs molecules are correlated to their molecular structures. In particular, we show how the presence of extended π-conjugation, sp^3 carbons, and contorted structures can influence the redox properties and their reactivity.

Chapter 3 reports the electrochemically induced cyclodehydrogenation of hexaphenylbenzene to hexabenzocoronene and its application as an organic electrochemical transistor, which was made by depositing a thin film of electrochemically self-assembled hexabenzocoronene and comparing its behaviour with that of a solution-processed thin film of unsubstituted hexabenzocoronene. Electrochemically polymerized poly-pyrene and poly-fluorene films were also prepared and tested as organic electrochemical transistors.

Chapter 4 focuses on the electrochemistry and electrogenerated chemiluminescence of heteroaromatic azapyrenes, with different functional groups and positional isomerism of the pyridinic nitrogen atom, that show a remarkable difference in the ECL behaviour and possibly in the excimer formation.

References

1. Wang, X. Y., Yao, X. & Müllen, K. Polycyclic aromatic hydrocarbons in the graphene era. *Sci China Chem* **62**, 1099–1144 (2019).

2. Anthony, J. E. Functionalized Acenes and Heteroacenes for Organic Electronics. (2006) doi:10.1021/cr050966z.

3. Seyler, H., Purushothaman, B., Jones, D. J., Holmes, A. B. & Wong, W. W. H. Hexa-peri-hexabenzocoronene in organic electronics. *Pure and Applied Chemistry* **84**, 1047–1067 (2012).

4. Figueira-Duarte, T. M. & Müllen, K. Pyrene-Based Materials for Organic Electronics. *Chem Rev* **111**, 7260–7314 (2011).

5. Stępień, M., Gońka, E., Żyła, M. & Sprutta, N. Heterocyclic Nanographenes and Other Polycyclic Heteroaromatic Compounds: Synthetic Routes, Properties, and Applications. *Chem Rev* **117**, 3479–3716 (2017).

6. Abdel-Shafy, H. I. & Mansour, M. S. M. A review on polycyclic aromatic hydrocarbons: Source, environmental impact, effect on human health and remediation. *Egyptian Journal of Petroleum* **25**, 107–123 (2016).

7. Mallah, M. A. *et al.* Polycyclic aromatic hydrocarbon and its effects on human health: An overeview. *Chemosphere* **296**, 133948 (2022).

8. Ehrenfreund, P., Rasmussen, S., Cleaves, J. & Chen, L. Experimentally Tracing the Key Steps in the Origin of Life: The Aromatic World. *Astrobiology* **6**, 490–520 (2006).

9. Ito, H., Ozaki, K. & Itami, K. Annulative π-Extension (APEX): Rapid Access to Fused Arenes, Heteroarenes, and Nanographenes. *Angewandte Chemie International Edition* **56**, 11144–11164 (2017).

10. Solà, M. Forty years of Clar's aromatic π-sextet rule. *Front Chem* **1**, 4–11 (2013).

11. Moran, D., Stahl, F., Bettinger, H. F., Schaefer, H. F. & Schleyer, P. v. R. Towards Graphite: Magnetic Properties of Large Polybenzenoid Hydrocarbons. *J Am Chem Soc* **125**, 6746–6752 (2003).

12. Rempala, P., Kroulík, J. & King, B. T. A Slippery Slope: Mechanistic Analysis of the Intramolecular Scholl Reaction of Hexaphenylbenzene. *J Am Chem Soc* **126**, 15002–15003 (2004).

13. Zhai, L., Shukla, R., Wadumethrige, S. H. & Rathore, R. Probing the arenium-ion (ProtonTransfer) versus the cation-radical (Electron Transfer) mechanism of scholl reaction using DDQ as oxidant. *Journal of Organic Chemistry* **75**, 4748–4760 (2010).

14. Liu, Z. *et al.* Small Size, Big Impact: Recent Progress in Bottom-Up Synthesized Nanographenes for Optoelectronic and Energy Applications. *Advanced Science* **9**, (2022).

15. Wu, J., Pisula, W. & Müllen, K. Graphenes as potential material for electronics. *Chem Rev* **107**, 718–747 (2007).

16. Xu, X., Müllen, K. & Narita, A. Syntheses and characterizations of functional polycyclic aromatic hydrocarbons and graphene nanoribbons. *Bull Chem Soc Jpn* **93**, 490–506 (2020).

17. Berresheim, A. J., Müller, M. & Müllen, K. Polyphenylene Nanostructures. *Chemical Review* **99**, 1747–1786 (1999).

18. Chen, L., Hernandez, Y., Feng, X. & Müllen, K. From Nanographene and Graphene Nanoribbons to Graphene Sheets: Chemical Synthesis. *Angewandte Chemie International Edition* **51**, 7640–7654 (2012).

19. Mas-Torrent, M. & Rovira, C. Role of Molecular Order and Solid-State Structure in Organic Field-Effect Transistors. *Chem Rev* **111**, 4833–4856 (2011).

20. Narita, A., Wang, X. Y., Feng, X. & Müllen, K. New advances in nanographene chemistry. *Chem Soc Rev* **44**, 6616–6643 (2015).

21. Niu, W. *et al.* Exceptionally clean single-electron transistors from solutions of molecular graphene nanoribbons. *Nat Mater* **22**, 180–185 (2023).

22. Chen, Z., Narita, A. & Müllen, K. Graphene Nanoribbons: On-Surface Synthesis and Integration into Electronic Devices. *Advanced Materials* **32**, (2020).

23. Nguyen, G. D. *et al.* Atomically precise graphene nanoribbon heterojunctions from a single molecular precursor. *Nat Nanotechnol* **12**, 1077–1082 (2017).

24. Götz, A. *et al.* Band structure modulation by methoxy-functionalization of graphene nanoribbons. *J Mater Chem C Mater* **10**, 4173–4181 (2022).

25. El Abbassi, M. *et al.* Controlled Quantum Dot Formation in Atomically Engineered Graphene Nanoribbon Field-Effect Transistors. *ACS Nano* **14**, 5754–5762 (2020).

26. Bennett, P. B. *et al.* Bottom-up graphene nanoribbon field-effect transistors. *Appl Phys Lett* **103**, (2013).

27. Ueda, H. & Yoshimoto, S. Multi-Redox Active Carbons and Hydrocarbons: Control of their Redox Properties and Potential Applications. *Chemical Record* **21**, 2411–2429 (2021).

28. Wang, G. *et al.* Exploring polycyclic aromatic hydrocarbons as an anolyte for nonaqueous redox flow batteries. *J Mater Chem A Mater* **6**, 13286–13293 (2018).

29. Walter, M., Kravchyk, K. V., Böfer, C., Widmer, R. & Kovalenko, M. V. Polypyrenes as High-Performance Cathode Materials for Aluminum Batteries. *Advanced Materials* **30**, (2018).

30. Kong, D. *et al.* Polycyclic Aromatic Hydrocarbons as a New Class of Promising Cathode Materials for Aluminum-Ion Batteries. *Angewandte Chemie International Edition* **61**, (2022).

31. J.Bard. *ELECTROGENERATED CHEMILUMINESCENCE*. (Marcel Dekker, Inc, 2004).

32. *Analytical Electrogenerated Chemiluminescence*. (Royal Society of Chemistry, Cambridge, 2019). doi:10.1039/9781788015776.

33. Akins, D. L. & Birke, R. L. Energy transfer in reactions f electrogenerated aromatic anions and benzoyl peroxide. Chemiluminescence and its mechanism. *Chem Phys Lett* **29**, 428–435 (1974).

34. Janata, Jiri. *et al.* Concerning the anion and cation radicals of corannulene. *J Am Chem Soc* **89**, 3056–3058 (1967).

35. Schmittel, M. & Burghart, A. Understanding reactivity patterns of radical cations. *Angewandte Chemie (International Edition in English)* **36**, 2550–2589 (1997).

36. Tang, S., Liu, Y. & Lei, A. Electrochemical Oxidative Cross-coupling with Hydrogen Evolution: A Green and Sustainable Way for Bond Formation. *Chem* **4**, 27–45 (2018).

37. Röse, P., Emge, S., König, C. A. & Hilt, G. Efficient Oxidative Coupling of Arenes via Electrochemical Regeneration of 2,3-Dichloro-5,6-dicyano-1,4-benzoquinone (DDQ) under Mild Reaction Conditions. *Adv Synth Catal* **359**, 1359–1372 (2017).

38. Zhu, C., Ang, N. W. J., Meyer, T. H., Qiu, Y. & Ackermann, L. Organic Electrochemistry: Molecular Syntheses with Potential. *ACS Cent Sci* **7**, 415–431 (2021).

39. *Organic Electrochemistry*. (CRC Press, 2000). doi:10.1201/9781420029659.

40. Little, R. D. A Perspective on Organic Electrochemistry. *Journal of Organic Chemistry* **85**, 13375–13390 (2020).

41. Qin, L. *et al.* In Situ Electrochemical Synthesis and Deposition of Discotic Hexa-peri-hexabenzocoronene Molecules on Electrodes: Self-Assembled Structure, Redox Properties, and Application for Supercapacitor. *Small* **11**, 3028–3034 (2015).

42. Zeng, C. *et al.* Electrochemical synthesis, deposition, and doping of polycyclic aromatic hydrocarbon films. *J Am Chem Soc* **143**, 2682–2687 (2021).

43. Ussano, E. Electrochemistry of molecular systems for new nanostructured materials and bioelectronic devices. (University of Bologna, 2016). doi:10.6092/unibo/amsdottorato/7641.

44. Waltman, R. J., Diaz, A. F. & Bargon, J. The Electrochemical Oxidation and Polymerization of Polycyclic Hydrocarbons. *J Electrochem Soc* **132**, 631–634 (1985).

45. Bachman, J. C. *et al.* Electrochemical polymerization of pyrene derivatives on functionalized carbon nanotubes for pseudocapacitive electrodes. *Nat Commun* **6**, 3–4 (2015).

46. Zabula, A. V., Spisak, S. N., Filatov, A. S., Rogachev, A. Y. & Petrukhina, M. A. Record Alkali Metal Intercalation by Highly Charged Corannulene. *Acc Chem Res* **51**, 1541–1549 (2018).

47. Zabula, A. V., Filatov, A. S., Spisak, S. N., Rogachev, A. Y. & Petrukhina, M. A. A main group metal sandwich: Five lithium cations jammed between two corannulene tetraanion decks. *Science (1979)* **333**, 1008–1011 (2011).

48. Fiorani, A., Difonzo, M., Rizzo, F. & Valenti, G. Versatile electrochemiluminescent organic emitters. *Curr Opin Electrochem* **34**, 100998 (2022).

49. Ishimatsu, R. *et al.* Electrogenerated Chemiluminescence of Donor–Acceptor Molecules with Thermally Activated Delayed Fluorescence. *Angewandte Chemie International Edition* **53**, 6993–6996 (2014).

50. Chang, J., Hercules, D. M. & Roe, D. K. The role of the triplet state in the electrochemiluminescence of rubrene. *Electrochim Acta* **13**, 1197–1207 (1968).
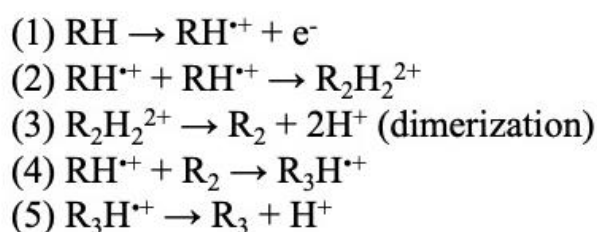
Chapter 2

Electrochemistry of small polycyclic aromatic hydrocarbons and oxidative coupling to organic film
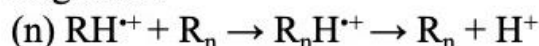
2.1 Introduction:

Polycyclic aromatic hydrocarbons (PAHs) are a class of π-conjugated organic molecules that contains at least two or more fused aromatic rings. We can categorize them as planar, such as triphenylene and pyrene, or curved with a bowl-like shape, as corannulene and sumanene,[1,2] or helically shaped.[3] Generally, PAHs are composed of carbon and hydrogen atoms, we can expand the class of aromatic molecules by incorporating one or more heteroatom in the core structure, in this case we define them as polycyclic heteroaromatic hydrocarbons. Many heteroatoms have been incorporated into PAH structures, nitrogen has been one of the first "dopants", followed by boron, phosphorus and atoms of the 16th group (oxygen, sulphur). The hetero doping has been observed to introduce static dipole moments, edge functionalities[4] and to shift the energies of the frontier molecular orbitals. The presence of heteroatoms could be useful to steer the reactivity of the radical ions towards a selected reaction pathway.

An organic species can undergo electron transfer at the electrode by applying a suitable potential, generating a radical cation if oxidation occurs, or a radical anion for reduction. Radical ions are generally more reactive than neutral molecules and have been extensively used in many organic reactions such as C-H activation, oxidative cyclodehydrogenation and coupling.[5] So far, these reactions required the use of an excess of chemical oxidising or reducing agents. In the last decade, the electrochemical approach has emerged as a sustainable and accessible way where the oxidation or reduction processes occurs directly at the electrode or mediated by a redox active molecule.[6–8] PAHs have been used as precursor for the bottom-up chemical synthesis of extended carbon structure such as graphene nanoribbons and ideally graphene.

Generally, the traditional approach for the extension of PAHs to 1D and 2D structures is based on the polymerization of PAHs precursor through coupling and then cyclodehydrogenation by a chemical oxidiser.[9] Some recent works have tried to perform a bottom-up synthesis of extended carbon structure by electrochemical oxidation of PAHs, through a stepwise coupling of radical cations and cyclodehydrogenation of the oligomers. Planar PAHs, such as triphenylene[10] and pyrene,[11] and bucky-bowl PAHs, such as corannulene,[12] have been reported to generate a conductive film on electrode by coupling of their radical cations. The mechanism (Scheme 2.1) that leads to the formation of a PAH film is similar to the electropolymerization mechanism for thiophene, carbazole, and other heteroaromatic molecules.[13]

$$(1) \ RH \rightarrow RH^{\bullet+} + e^-$$
$$(2) \ RH^{\bullet+} + RH^{\bullet+} \rightarrow R_2H_2^{2+}$$
$$(3) \ R_2H_2^{2+} \rightarrow R_2 + 2H^+ \ (dimerization)$$
$$(4) \ RH^{\bullet+} + R_2 \rightarrow R_3H^{\bullet+}$$
$$(5) \ R_3H^{\bullet+} \rightarrow R_3 + H^+$$

In general
$$(n) \ RH^{\bullet+} + R_n \rightarrow R_nH^{\bullet+} \rightarrow R_n + H^+$$

Scheme 2.1 Reaction mechanism for the electrochemical coupling of radical cations

Cyclic voltammetry is a useful tool for monitoring the electropolymerization process.[14] Generally, the oxidation wave is chemically irreversible with a number of exchanged electrons close to 2.[13] By cycling multiple times, a stepwise increase of the current is observed when the insoluble film, composed of electropolymerized oligomers, deposit on the electrode surface. New surface limited redox processes start to appear in the voltammogram curve, they are typically related to the doping/de-doping of the film coupled with the insertion of counter ions to balance the charged oligomers. The characterisation of the oligomeric species is not an easy and straightforward task due to the small amounts produced, as the electropolymerized film is usually very thin (usually 100-300 nm) and the synthesised oligomers are insoluble in conventional solvents. Therefore, conventional techniques, such as liquid chromatography for separation coupled with mass spectroscopy or NMR, cannot be employed. To analyse the mass of the produced oligomers, we used laser desorption ionisation time-of-flight (LDI-TOF) mass spectroscopy, which employs a laser source to ionise molecular fragments of the film, which are

accelerated by an electric field and the time (of flight) required to reach the detector is proportional to the square root of the mass-to-charge ratio (m/z).

2.2 Outlook:

In this chapter, we analyse the electrochemical behaviour of polycyclic aromatic hydrocarbons (PAHs) and heteroaromatic molecules. In the first part, we analysed a series of extended pyrenes, i.e. benzo[rst]pentaphene, by cyclic voltammetry in different organic solvents. We will observe how bulky substituents, such as mesitylene, can influence the reactivity of the radical ions by protecting the reactive positions. Moreover, we will gain some insight into the oxidative coupling and the electrochemically induced cyclodehydrogenation.

In the second part of the chapter, we analyse the electrochemistry of sumanene, a curved bowl-shaped aromatic molecule, which can be considered as a fragment of C_{60} (buckminsterfullerene) along with corannulene. Furthermore, to better understand the chemical reactivity of sumanene radical ions and to correlate its electrochemical properties with its structure, we also analysed the electrochemical behaviour of some of the sumanene and corannulene fragments, namely triphenylene, fluorene, and acenaphthylene. We will examine how the curvature influences sumanene reactivity and its redox properties compared with those of its planar fragments. At higher potential, oxidative coupling and possibly cyclodehydrogenation occur for these molecules, as well as for corannulene,[12] leading to the formation of insoluble films electropolymerized on the electrode. From the LDI-TOF mass spectroscopy, we will study the different electrogenerated species, providing some insight into the chemical reactivity following electron transfer.

In the third part, we discuss the electrochemical behaviour of heteroaromatic benzo-fused azacorannulene. Moreover, by electrochemical oxidation, we tried to induce the complete closure of five phenyl rings to electrochemically synthesise bowl-shaped azacorannulene from substituted pentaphenyl-pyrroles through intramolecular cyclodehydrogenation. However, a complete study of the products of this oxidation is still underway. Some aspects related to the oxidation mechanism and the chemical nature of the electrosynthesis, at the current state, are just hypothesis and require further analysis in the future.

2.3 Pyrene and extended benzo[rst]pentaphene derivatives

Pyrene (**Pyr**) and more π-extended benzo[rst]pentaphene (**BPP**) derivatives have been characterized by cyclic voltammetry. **BPP** and its derivatives were synthesised by Xu et al. according to a previously reported procedure.[15] Figure 2.1 shows the chemical structures of the molecules, all of them have a pyrene core. **BPP** has two more condensed benzene rings than pyrene, and **BPP** derivatives have mesitylene substituents at position 5 (5-mesitylbenzo[rst]pentaphene, **BPP-M**) or two mesitylene units at position 5 and 8 (5,8-dimesitylbenzo[rst]pentaphene, **BPP-2M**). Lastly, we also investigated a symmetric dimer (8,8'-dimesityl-5,5'-bibenzo[rst]pentaphene, **BBPP-M**) composed of two units of mesitylbenzo[rst]pentaphene which exhibits axial chirality and has two (M) or (P)-enantiomers because the rotation at the C5-C5' bond has a high energy barrier.
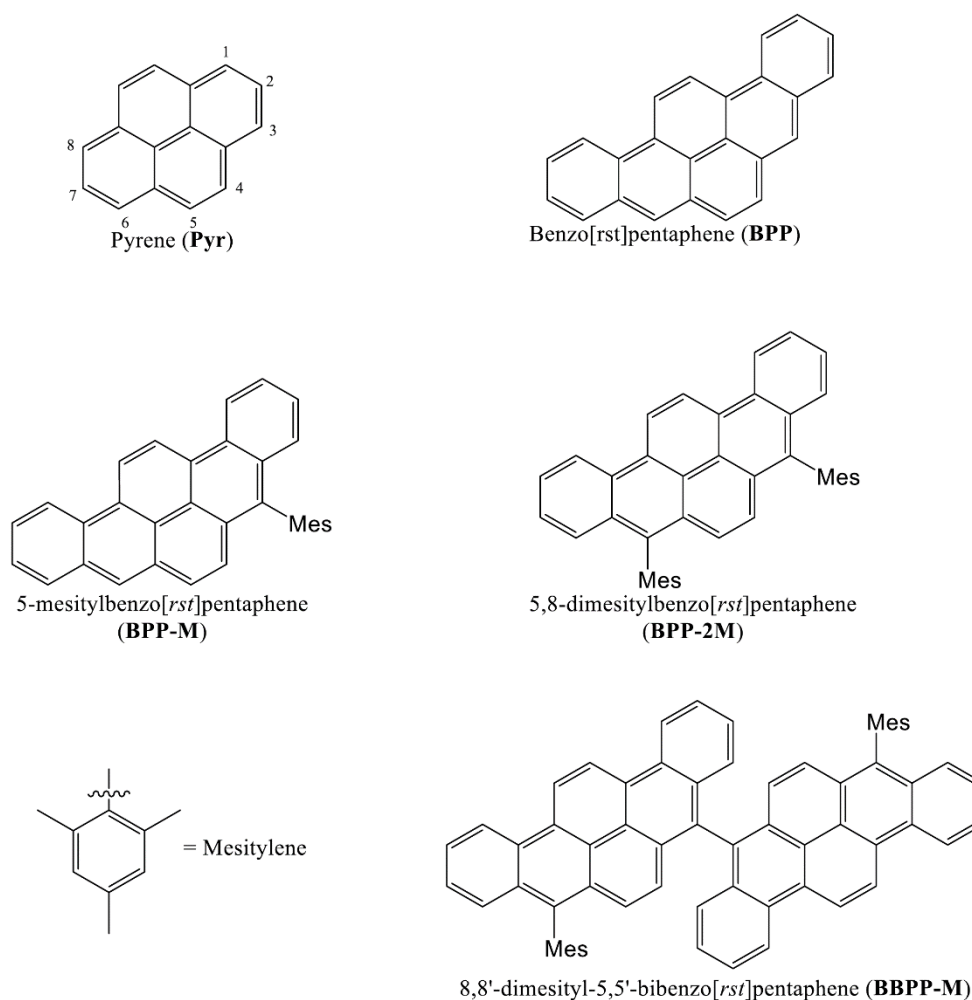

*Figure 2.1 Chemical structures of the investigated pyrene, benzo[rst]pentaphene **BPP**, 5-mesitylbenzo[rst]pentaphene, **BPP-M**, 5,8-dimesitylbenzo[rst]pentaphene, **BPP-2M**, and 8,8'-dimesityl-5,5'-bibenzo[rst]pentaphene, **BBPP-M**.*

2.3.1 Electrochemical characterisation

Cyclic voltammetry (CVs) measurements were carried out in DCM/Bu_4NPF_6 and THF/Bu_4NPF_6, and we decided to report the anodic voltammogram in DCM and the cathodic voltammogram in THF, due to the different stability windows and nucleophilicities of the two solvents. Figure 2.2 shows the CV curve of pyrene in DCM/Bu_4NPF_6. The electrochemical oxidation of pyrene occurs at +1.30V vs. SCE and, under the employed conditions, results in a partially chemically irreversible oxidation. When the applied potential was extended to the second completely irreversible oxidation, new reversible redox processes were observed in the back-scan. The radical cations of pyrene can couple to produce dimers, trimers, and oligomers.[11,13,16] From DFT-calculated electron spin density of pyrene radical cations, it was observed that the most reactive carbon atoms were located at positions 1,3,6 and 8 of pyrene.[13] The poly-pyrene film was observed to have reversible redox-active processes, observed in CV at lower potentials, related to the doping/de-doping of the charged film.
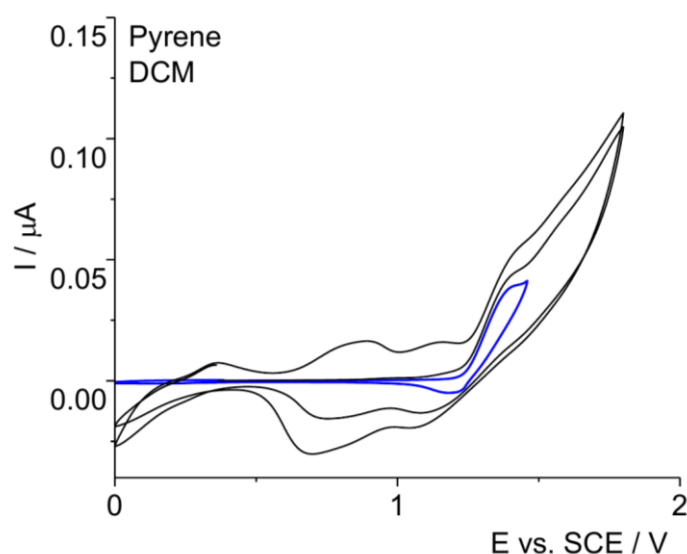

Figure 2.2 Cyclic voltammetry of Pyrene 1.5 mM. Measured at 1 V/s with Pt diameter 2mm working electrode, and SCE as reference electrode at 298 K in 80 mM Bu₄NPF₆/DCM.

Figure 2.3 shows the CVs of **BPP**, and its derivatives. Table 2.1 summarises their redox properties. Based on the similar redox potentials of **BPP** and its derivatives, we expect that the mesitylene side groups are not electrochemically active at the investigated potentials. Thus, all redox processes involve the **BPP** core.
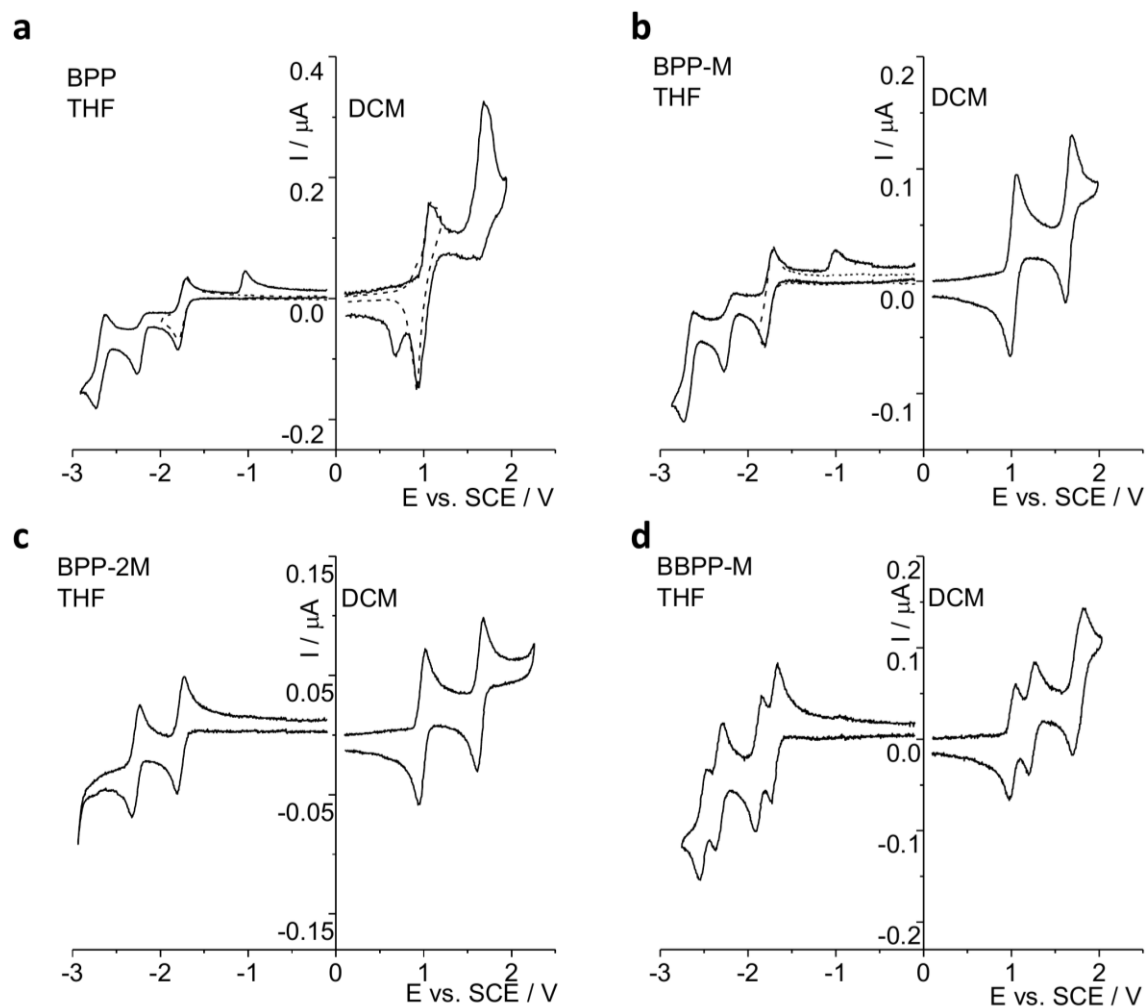
*Figure 2.3 Cyclic voltammetry of (**a**) benzo[rst]pentaphene 0.8 mM, (**b**) 5-mesityl benzo[rst]pentaphene 0.7 mM, (**c**) 5,8-dimesityl benzo[rst]pentaphene 0.6 mM and (**d**) 8,8'-dimesityl-5,5'-bibenzo[rst]pentaphene 0.7 mM (saturated). Measured at 1 V/s with Pt diameter 125 μm and SCE as reference electrode at 298 K in 80 mM Bu₄NPF₆/DCM and 80 mM Bu₄NPF₆/THF.*

Table 2.1: Redox Properties

| Species	Oxidation[a] $E_{1/2}$ vs. SCE / V				Reduction[b] $E_{1/2}$ vs. SCE / V			
Pyr	+1.30[c,f]							
BPP	+1.07	+1.70[c]			-1.75	-2.26[c]	-2.68	
BPP-M	+1.03	+1.66			-1.76	-2.28[c]	-2.68	
BPP-2M	+0.98	+1.64			-1.77	-2.28		
BBPP-M	+1.01	+1.23	+1.71[d]	+1.79[d]	-1.70	-1.88	-2.33	-2.51

Notes: Measured at 298 K with a Pt working electrode disk of 125μm diameter, and SCE as reference electrode at 1V/s. [a](80mM) Bu₄NPF₆/DCM electrolyte solution, [b](80mM) Bu₄NPF₆/THF electrolyte solution, [c] peak potentials are reported for chemically irreversible process, [d] extracted by digital simulation, [f] measured with a Pt working electrode disk of 2 mm diameter in less anhydrous (80mM) Bu₄NPF₆/DCM at 0.1V/s.

Benzo[rst]pentaphene has a more extended π-conjugation than pyrene which also leads to a lower oxidation potential with a potential difference of 0.23 V. From the CV results, we observe that the first oxidation is chemically reversible, even if in the back scan a peaked (not a common diffusion-limited) reduction of the BPP radical cation was observed. This peaked reduction could be caused by an adsorption/desorption phenomenon of the radical cation with the electrode. At a more positive potential, a second chemically irreversible oxidation process was observed which led to the appearance of a new reduction process in the back-scan at a lower potential than the 1st oxidation related to a new chemical species. The reduction of **BPP** in THF shows a first reversible monoelectronic redox process followed by a second chemically irreversible reduction, which also generates a product with an oxidation process in the back scan at -1.0V vs. SCE. A third reduction was observed at -2.68V vs. SCE. Interestingly, this 3rd redox process appears to be partially chemically reversible and seems more than a mono-electronic process, but the current is slightly increased by the onset of solvent reduction and a clear estimation of the number of transferred electron was not possible.

When mesityl substitution is present (**BPP-M**), the oxidation behaviour changes dramatically. In particular, both oxidation processes occur at lower potentials (ca. 40-50 mV) than **BPP**, but they are mostly chemically reversible, at least at 1V/s. The bulky mesitylene group is able to limit and protect the **BPP-M** di-cation from chemical reactions on the time scale of the CV experiment. The reduction behaviour is very similar to that of **BPP** with ca. 20mV more negative reduction potentials.

A second mesitylene substitution did not show any difference in the oxidation behaviour of **BPP-2M**, only ca. 20-50mV less positive potentials. However, the reduction in THF significantly differs from that of **BPP-M**. In particular, the second reduction process becomes completely chemically reversible. We can hypothesise that mesitylene can protect the reactive position of the **BPP-2M** core which is not protected in **BPP-M**. A possible reaction mechanism (Scheme 2.2) involving **BPP** and **BPP-M** di-anions is the electrochemical Birch-like reduction at positions 5 or 8. This reaction does not occur for **BPP-2M** because the two methylene groups protect both positions. The proton donor could be a tetrabutylammonium ion since they are known to be mildly acidic.[17]
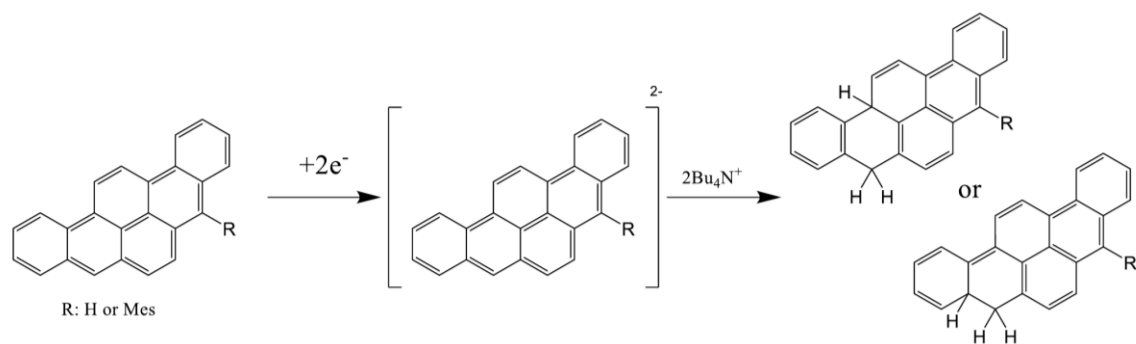
*Scheme 2.2 Proposed reaction mechanism for **BPP** and **BPP-M** dianions. Electrochemical Birch Reactions.*

The dimer (**BBPP-M**) exhibited multiple chemically reversible redox processes. The two enantiomers have the same redox potentials and cannot be distinguished with a common cyclic voltammetry in absence of chiral electrolyte/solvent or functionalized electrode.[18,19] For each oxidation/reduction process, we observed two redox waves with close potentials, one for each **BPP** unit. This behaviour indicates that there is a strong electronic interaction between the two benzo[rst]pentaphene units, because once electron transfer occurs in one unit, a more positive or negative potential (higher energy) is required for the oxidation or reduction of the second unit.[20] The higher energy required is related to the large coulombic repulsion between injected charges.[21] The interaction seems to decrease when **BBPP$^{3+\bullet}$** is further oxidised to **BBPP-M^{4+}**, because the two waves partially overlap. This phenomenon was not observed for the reduction processes. This effect may be due to a decrease in the coulombic repulsion between the **BPP** units in the 4+ state or a different solvation effect. Conformational analysis by DFT (Figure 2.4) showed an increase in the dihedral angle from the initial 90° between the two **BPP** units for the higher oxidised states. The dihedral angle change could explain the potential difference in the electron transfer of the two interacting units because if the angle remained at 90°, the two **BPP** units should interact less. Interestingly, for even oxidised states, namely the +2 and +4 states, there is almost energy degeneracy for the singlet (S) or triplet (T) electronic configurations of the ground state. Further analysis will be required to better understand the differences in the electrochemical behaviour for the 4th oxidation state compared to the others.
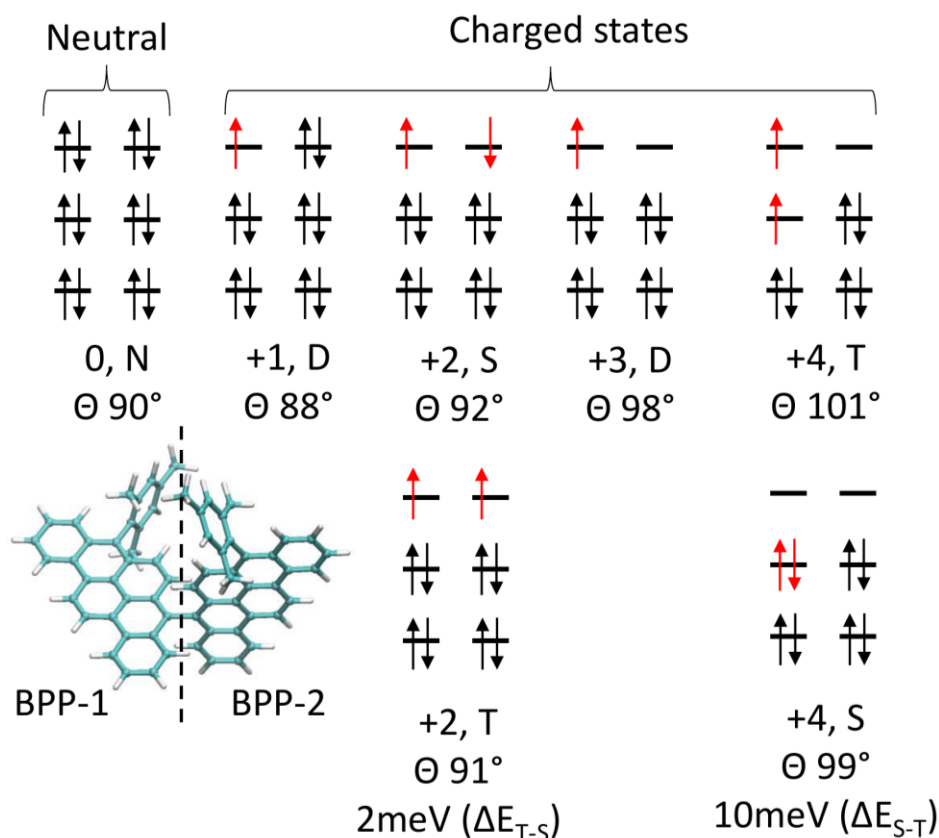
*Figure 2.4 More stable state multiplicities for the oxidation states of **BBPP-M** with dihedral angles between the two **BPP** units. The energy difference (ΔE) between almost degenerates even oxidize state (+2 and +4)*

2.3.2 Electrochemical reactivity

Figure 2.5 shows the CVs in DCM/Bu$_4$NPF$_6$ of **BPP** and derivatives when a more positive potential is applied. For each molecule, we observed a further chemically irreversible multi-electronic oxidation process with the appearance of new redox processes (marked with *****). The current increases between each cycle and the appearance of new reversible redox processes is typical of a redox-active film formation process on the electrode surface. The products of the follow-up chemical reaction after the new oxidation are less soluble in the electrolyte solution and are ultimately deposited on the electrode.

The **BPP** shows the most complex electrochemical behaviour with at least 5 new redox peaks, with the reduction at +0.66V in the back scan which was already present after the second oxidation. These many redox processes may be related to the formation of multiple products from the irreversible oxidation of **BBP** at +2.6V. The other **BPP** derivatives showed simpler electrochemical behaviour with a single new redox process. However, the current increase

between each cycle for **BPP-M** and **BPP-2M** is small, which may suggest that the product of the irreversible oxidation could be partially soluble. **BPP-M** and **BPP-2M** may dimerize and as observed for **BBPP-M**, the dimer is partially soluble and shows two reversible oxidation waves around +1.01 and +1.21V vs. SCE. Interestingly, for the mono-substituted **BPP-M**, this new oxidation product shows a reversible redox process at lower potential (+0.85V vs. SCE) than the 1st oxidations of **BPP-M** and that of **BBPP-M**, which suggests that the oxidised product could have a more π-conjugated structure. Whereas the oxidation product of the double substituted **BPP-2M** has its reversible redox process after the 1st oxidation of **BPP-2M** at +1.1V, with a potential difference of 0.25V when compared to the one of **BPP-M**, suggesting that the two oxidation products of **BPP-M** and **BPP-2M** are quite different in their chemical structures.
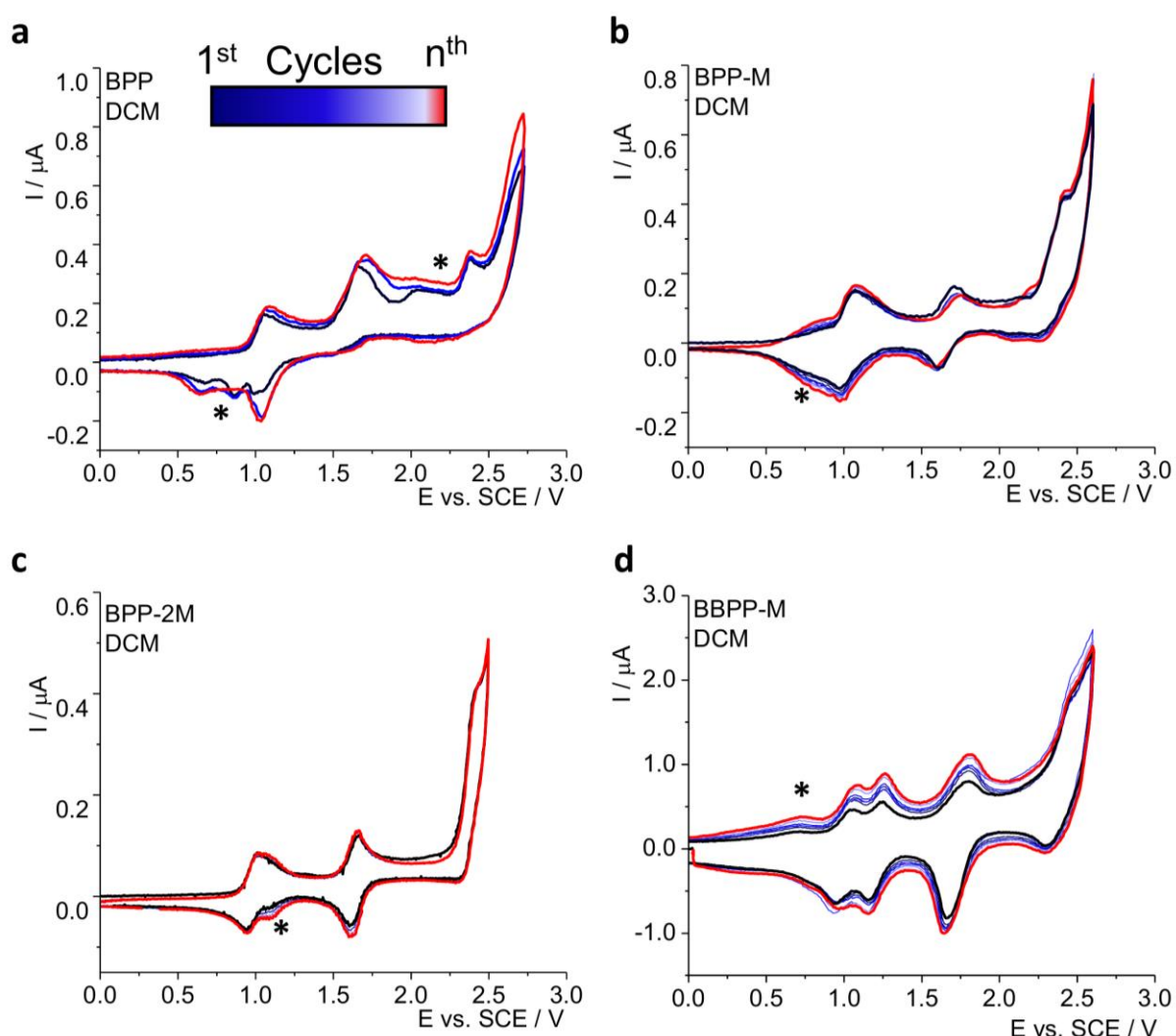

*Figure 2.5 CVs curves with multiple cycles (1st dark to nth light blue and last cycle in red) including the multi-electronic chemically irreversible oxidation of (**a**) BPP 0.8mM, (**b**) BPP-M 0.7mM, (**c**) BPP-2M 0.6mM, and (**d**) BBPP-M 0.7mM (saturated). Measured with working electrode Pt 125 μm diameter, SCE as reference electrode in 80 mM Bu4NPF6/DCM at 1V/s and 298 K.*

The dimer **BBPP-M** showed a single new redox process at a lower potential (0.75V) than its 1st oxidation, suggesting a more π-conjugated molecule. Since **BBPP-M** is already a dimer, we hypothesised that an intramolecular reaction (graphitization) could occur for **BBPP-M** instead of an intermolecular reaction (oligomerization). In particular, new C-C bonds may form within the dimer, leading to a planar and more extended molecule, via the electrochemically induced cyclodehydrogenation (Figure 2.6a). To better understand the chemical nature of the film, we performed laser desorption ionisation – time-of-flight (LDI-TOF) mass spectroscopy of the electrogenerated film of **BBPP-M** deposited on Pt (Figure 2.6b).
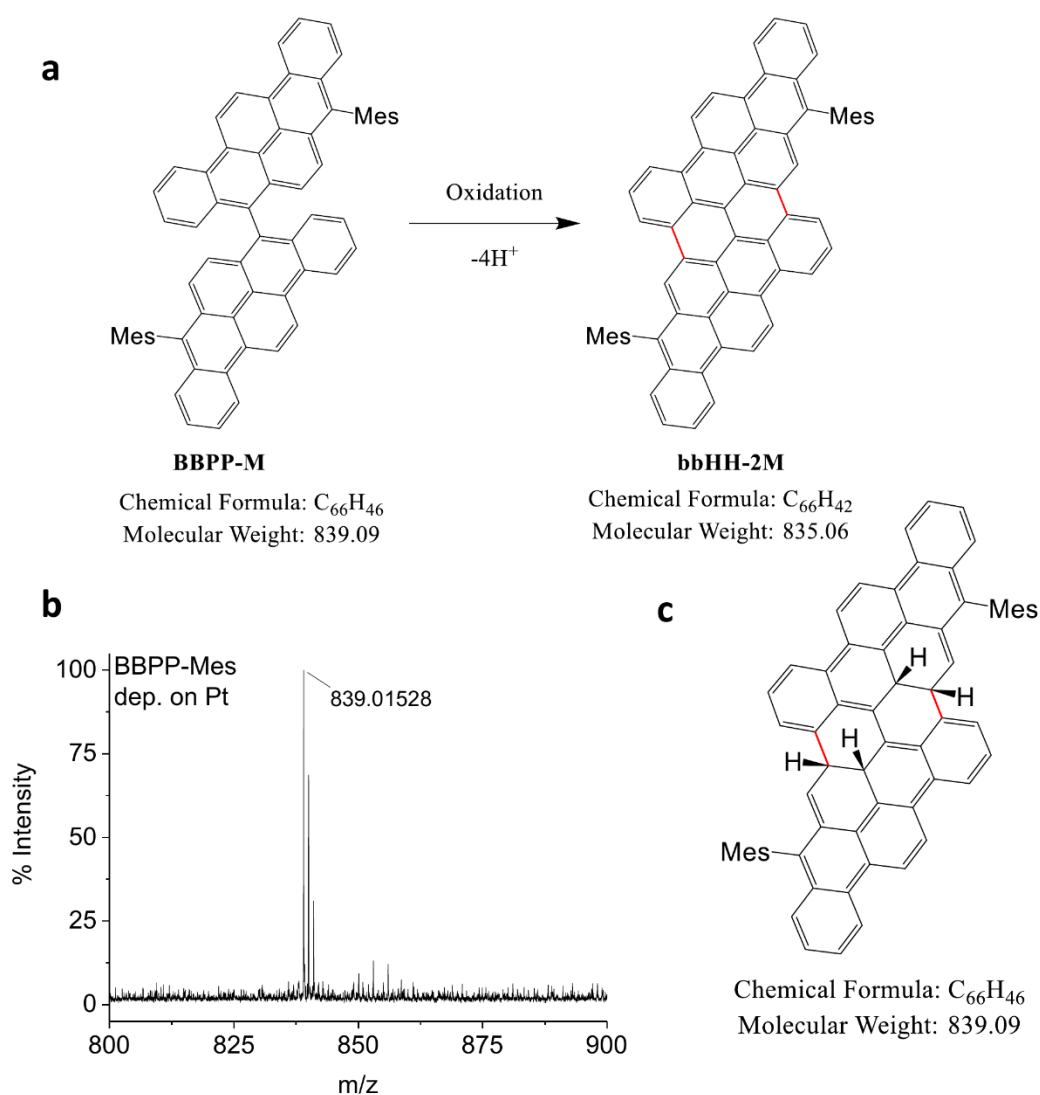

*Figure 2.6 (**a**) Hypothesised mechanism for the oxidative cyclodehydrogenation of **BBPP-M** to the fully closed **bbHH-2M**. (**b**) LDI-TOF spectrum of electrodeposited **BBPP-M** on Pt, at higher m/z values no signal was observed. (**c**) Hypothesised fully closed structure with 4 sp³ carbons.*

However, the observed m/z was equal to that of pristine **BBPP-M** ($C_{66}H_{46}$, 839.09 g/mol). If the complete closure of **BBPP-M** with the formation of 2 new C-C bonds and dehydrogenation occurred, the product, namely 11,22-dimesitylbenzo[fg]benzo[5,6]hexacenohexacene (**bbHH-2M**), would have loss 4 hydrogens and a lower m/z ($C_{66}H_{42}$, 835.06 g/mol) would be observed. Moreover, in order to have complete planarization, the dihedral angle of the two **BPP** units for the oxidised state should increase to 180°, but from DFT conformational analysis of oxidised states of **BBPP-M** the angle remains lower than 180°. Another possibility, that could explain the observed m/z ratio, is a molecule with two new C-C bonds, thus generating a less soluble species, but instead of dehydrogenation the involved hydrogens migrate to form a tetrahydro (sp^3 carbon) product (Figure 2.6c).

2.3.3 Conclusion

The electrochemical characterisation of **BPP** derivatives has been carried out in different organic solvents. At high oxidative potentials, film formation was observed for **BBPP-M**. On the voltammetric basis, we initially hypothesised a complete cyclodehydrogenation of the two **BPP** units, leading to a more planar and π-conjugated structure. However, the LDI-TOF experiment of the film from the electrochemically oxidised dimer showed that the m/z of the fragments were equal to that of the initial molecule.

Further investigation, particularly IR and Raman spectroscopies, is required to better understand the exact chemical nature of the electropolymerized film. We do not think that the film is composed of pristine molecules, since they are soluble in fresh DCM, whereas the film appeared to be highly insoluble in the solvent.

2.4 Electrochemistry of Sumanene and its sub-units

Sumanene ($C_{21}H_{12}$, 4,7-dihydro-1H-tricyclopenta[def,jkl,pqr]triphenylene) and Corannulene ($C_{20}H_{10}$, dibenzo[ghi,mno]fluoranthene) are two bowl-shaped polycyclic aromatic hydrocarbons, which can be viewed as fragments of buckminsterfullerene (C_{60}-I_h)[5,6]fullerene. Corannulene, unlike sumanene, has C_{5v} symmetry with a five-membered ring at the centre and five peri benzo-fused rings. All carbon atoms in corannulene are hybridized sp^2 with 20π electrons, with a bowl depth of 0.87Å and an inversion barrier estimated around 11.5 kcal/mol. From corannulene molecular structure we can identify different smaller fragments, such as acenaphthylene ($C_{12}H_8$, 12π e$^-$), phenanthrene ($C_{14}H_{10}$, 14 π e$^-$), fluoranthene ($C_{16}H_{10}$, 16 π e$^-$), benzo[ghi]fluoranthene ($C_{18}H_{10}$, 18π e$^-$) and benzo[c]phenanthrene ($C_{18}H_{12}$, 18 π e$^-$).

Sumanene has C_{3v} symmetry with a six-membered ring at the centre, three peri-fused benzenic rings (substructure of triphenylene), and three fused five-membered rings. The five-membered rings have one sp^3 carbon each, whereas all the carbon atoms in the six-membered rings are sp^2 with a total of 18π electrons with three Clar rings. Sumanene has a more rigid structure than corannulene, with a bowl depth of 1.11 Å and a higher inversion barrier of 20 kcal/mol.[22] From the sumanene molecular structure, we can identify different fragments, namely fluorene ($C_{13}H_{10}$, 12 π e$^-$) which also has a sp^3 carbon, phenanthrene ($C_{14}H_{10}$, 14 π e$^-$), triphenylene ($C_{18}H_{12}$, 18 π e$^-$), and 4H-cyclopenta[def]triphenylene ($C_{19}H_{12}$, 18 π e$^-$). Triphenylene and 4H-cyclopenta[def]triphenylene are both isoelectronic to sumanene. Because of the strain generated by annulation with the five-membered ring and benzenic rings, corannulene and sumanene are not planar.

In this section, we investigated the electrochemical behaviour of sumanene and the electrochemistry of some of its fragments: 9H-fluorene, triphenylene, and acenaphthylene. The structures of the investigated molecules are shown in Scheme 2.3.
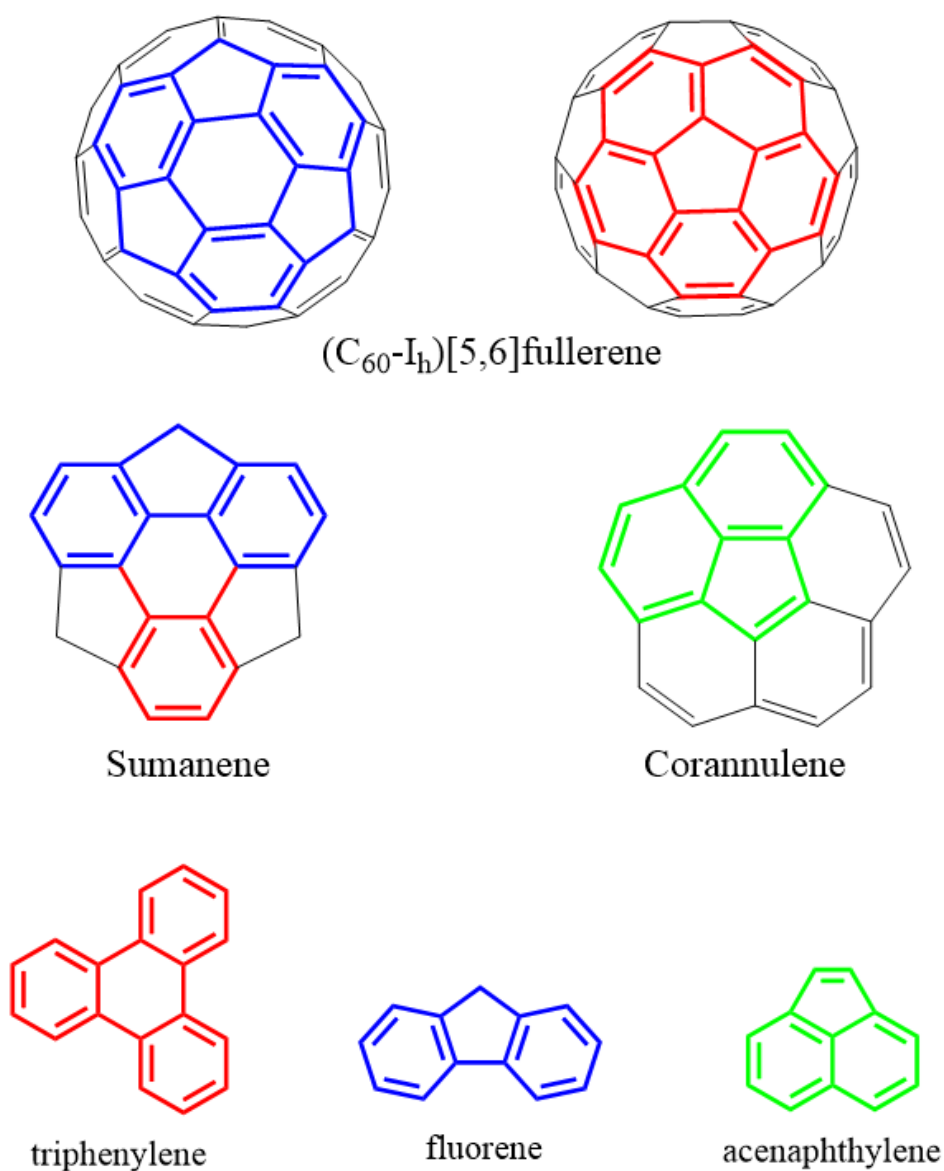
Scheme 2.3 Molecular structures of C$_{60}$ with highlighted fragments of sumanene and corannulene. Investigated fragments: fluorene, triphenylene and acenaphthylene.

2.4.1 Electrochemical characterisation

The electrochemical properties of sumanene, fluorene, and triphenylene were investigated by cyclic voltammetry in DCM/Bu$_4$NPF$_6$ and THF/Bu$_4$NPF$_6$, as shown in Figure 2.7, and their redox properties are reported in Table 2.2.
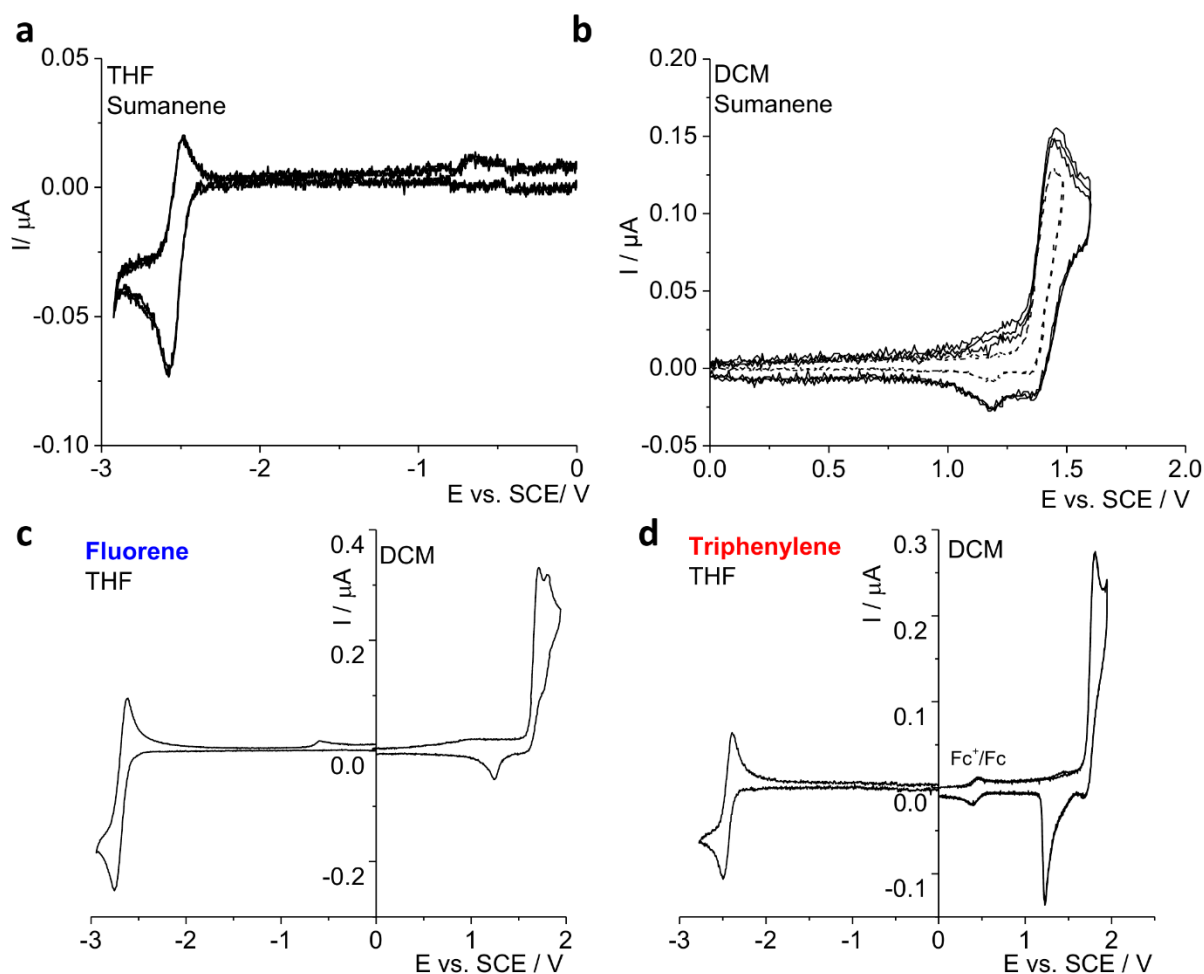
*Figure 2.7 CVs in (**a**) THF/Bu₄NPF₆ (80 mM) and(**b**) DCM/Bu₄NPF₆ (80 mM) of Sumanene 1.39 mM, (**c**) fluorene 1.50 mM, and (**d**) Triphenylene 1.25 mM. Working electrode Pt disk diameter 125 μm, SCE as reference electrode, measured at 1 V/s and 298 K.*

In THF, sumanene shows a partially chemically reversible reduction at 1 V/s, suggesting an EC mechanism with a small kinetic constant for the irreversible chemical reaction. From the digital simulation, we extracted a rate constant (kf) in the range 3-10 s^{-1} and a formal potential of -2.54V vs. SCE, in agreement with previously reported data in DMF.[23]

Fluorene reduction in THF shows a similar electrochemical behaviour with a partially reversible reduction, again suggesting an EC mechanism but with a smaller kf (1.5 s^{-1}) and a more negative reduction potential of -2.69V vs. SCE. Fluorene is expected to have a more negative reduction potential than sumanene because fluorene has a smaller π-conjugation. Sumanene and fluorene, both having sp³ carbons, show a reduction process affected by a following chemical reaction, with sumanene having a higher rate constant. We hypothesise that a chemical reaction

may affect the hydrogen in the sp^3 carbon, and the reaction rate could be enhanced by the curvature of sumanene.

Triphenylene has a similar π-conjugation to sumanene, however its reduction potential ($E_{1/2}$ =-2.45V vs. SCE) is lower than sumanene and it appears completely reversible. The difference between the reduction potentials of sumanene and triphenylene can be explained by the curvature of sumanene, which partially disrupts the π-conjugation and can be considered as a mechanically strained triphenylene.[24,25] Because of its planarity, triphenylene can maximize the overlap between p-orbitals compared to the curved sumanene, thus leading to a less negative reduction potential. Sumanene reduction potential is between the fluorene reduction potential and that of triphenylene, even though sumanene and triphenylene are isoelectronic both with three Clar's ring.

In DCM, sumanene shows a partially chemically irreversible oxidation at a peak potential Ep of +1.45V vs. SCE. At a higher speed rate (10 V/s) the oxidation wave became more reversible. In the back scan, a new small redox peak was observed, as well as a new oxidation process before the onset of the 1st oxidation of sumanene. The pre-wave appeared to increase with multiple cycles, whereas the reduction peak did not increase.

Fluorene oxidation shows a 1st irreversible oxidation with Ep of +1.70V vs. SCE followed by a 2nd irreversible oxidation at Ep +1.80V vs. SCE, while in the back scan a reduction process is observed at Ep +1.24V vs. SCE. The electrochemical behaviour was similar to that of sumanene, except for the 2nd oxidation, which was not present for sumanene and is related to a product of a chemical reaction of the fluorene radical cation after the 1st oxidation.

Triphenylene shows a chemically irreversible oxidation at Ep +1.81V vs. SCE, showing the most positive oxidation potential compared to the other two molecules. Even though triphenylene has a more extended π-conjugation, the three Clar's sextet stabilise the HOMO energy increasing the oxidation potential of triphenylene.[26] In the back scan, a reduction process is observed with a peaked shape, suggesting that an adsorption process may occur, furthermore a new oxidation process before the 1st oxidation of triphenylene is also observed. Based on this evidence, we hypothesised that triphenylene oxidation produces some insoluble products and that dimerization (oligomerization) could occur, as previously reported in literature.[27] These new redox processes could be related to the triphenylene oligomers.

The electrochemical properties of corannulene and acenaphthylene were investigated by cyclic voltammetry in DCM/Bu$_4$NPF$_6$ and THF/Bu$_4$NPF$_6$ (for corannulene), as shown in Figure 2.8, and their redox properties are reported in Table 2.2.

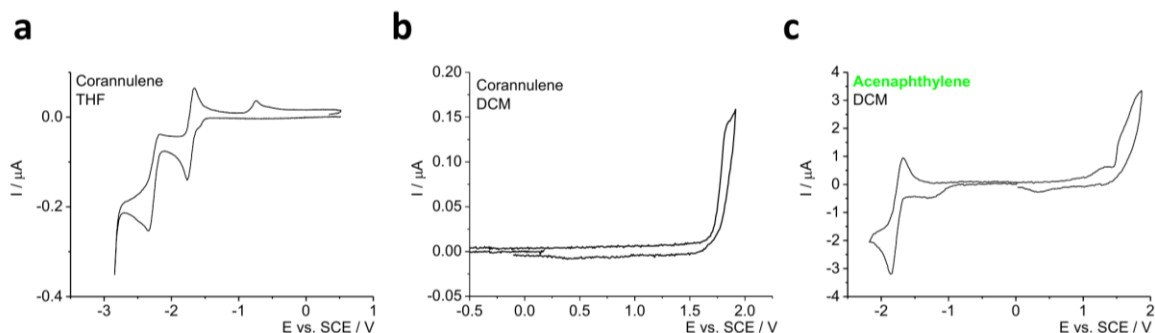*Figure 2.8 CVs in (**a**) THF/Bu$_4$NPF$_6$ (80 mM) and (**b**) DCM/Bu$_4$NPF$_6$ (80 mM) of Corannulene 1 mM. working electrode Pt disk diameter 125 μm, SCE as reference electrode, measured at 1 V/s and 298 K. (**c**) CV in DCM/Bu$_4$NPF$_6$ (80 mM) of acenaphthylene 1 mM, working electrode Pt disk diameter 0.5 mm, SCE as reference electrode. Measured at 1 V/s and 298 K. Corannulene oxidation figure was adapter with permission from ref. [12].*

Corannulene reduction has been thoroughly investigated by Bruno et al. in different electrolytes and solvents,[28] in THF it has two one-electron reduction at 1 V/s and 298 K, with the 2nd one followed by a chemical irreversible reaction with a small rate constant (at 10V/s the 2nd reduction in THF appears chemically reversible). Corannulene appears to be easier to reduce than sumanene and triphenylene.

Acenaphthylene reduction has been investigated in DCM, it shows a one electron chemically reversible reduction. Notably, acenaphthylene reduction occurs at a slightly less negative reduction potential than corannulene even though acenaphthylene has a lower π-conjugation. The lower reduction potential is due to the presence of an external fused cyclopenta moiety which strongly affects the molecular orbital energies, acting as an electron withdrawing substituent. The electron withdrawing effect is so strong on the reduction potentials that acenaphthylene has a 1st reduction shifted of 0.9V toward less negative potential when compared to the naphthalene reduction.[29] The added electron appears to be mainly located in the cyclopenta moiety. In particular, the localised double bond is easily reduced, and a particularly stable radical anion is generated.[30]

Corannulene oxidation has been less studied than its reduction, mostly because of the chemical irreversibility of corannulene oxidation, usually followed by electrode fouling. Bruno et al. has recently reported a comprehensive work on the anodic electrochemical behaviour of

corannulene and the characterisation of the electrogenerated polymeric film from its oxidation.[12] Corannulene is oxidised at E_p +1.86V vs. SCE and is completely irreversible at 1 V/s and at higher scan rates. Corannulene radical cations are extremely reactive with nucleophiles and have been observed to easily dimerise and oligomerize. Using a less nucleophilic solvent (such as liquid SO_2), low temperature, and high scan rate, a 2nd irreversible oxidation wave was observed at 2.5V vs. SCE.

Acenaphthylene in DCM results in a completely irreversible oxidation process at E_p of +1.83V vs. SCE. The voltammogram showed that the oxidation wave was composed of multiple redox processes. After the 1st oxidation, a new redox process was observed in the back scan (+0.5V), this process is related to a newly formed species produced by a follow up reaction of the acenaphthylene radical cation.

Table 2.2: Redox Properties

Species	Oxidation[a] E_p vs. SCE / V		Reduction[b] $E_{1/2}$ vs. SCE / V	
Sumanene	1.45[c]		-2.54	
Fluorene	1.70[c]	1.80[c]	-2.69	
Triphenylene	1.81[c]		-2.45	
Corannulene	1.86[c]	2.50[c]	-1.89	-2.47
Acenaphthylene	1.83[c]		-1.76[a]	

Notes: Measured at 298 K with a Pt working electrode disk of 125μm diameter, and SCE as reference electrode at 1V/s. [a](80mM) Bu_4NPF_6/DCM electrolyte solution, [b](80mM) Bu_4NPF_6/THF electrolyte solution, [c] peak potentials reported for chemically irreversible processes.

2.4.2 Digital Simulation

From the CV analysis, the oxidation of sumanene was not completely irreversible at 1 V/s, this behaviour suggests a small rate constant of the chemical reaction following the 1st oxidation. At higher scan rates, the peak current of the 1st oxidation scales linearly with the square root of the scan rate and the peak potential did not shift with the scan rate (Figure 2.9a). When currents at different scan rates (Figure 2.9b) are reported as dimensionless values (assuming linear diffusion, removing the effect of scan-rate), we can observe that the dimensionless peak current is higher at 1V/s and decreases at higher scan rates, suggesting that the apparent number of exchange electrons decreases. Evidence suggests an ECE mechanism,[31] in which the product of an irreversible chemical reaction is more easily oxidised than sumanene.
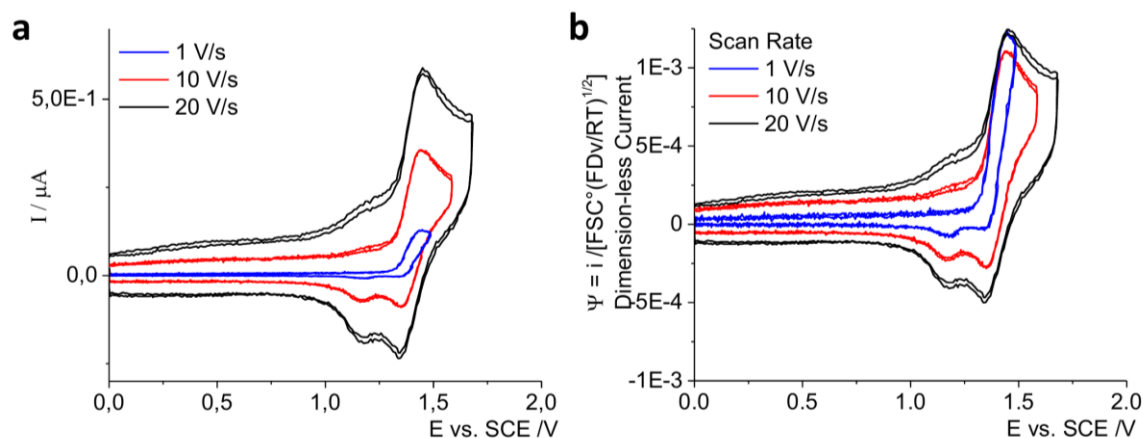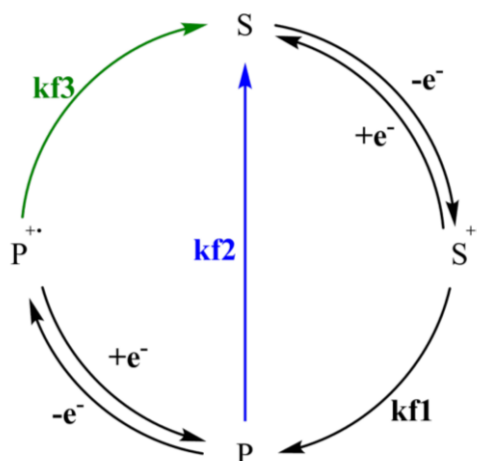
*Figure 2.9 (**a**) Sumanene CVs at 1 V/s, 10, and 20 V/s in DCM/Bu₄NPF₆ with a Pt 125 μm disk diameter as working electrode, SCE as reference electrode. (**b**) Dimensionless current cyclic voltammetry.*

To better understand the mechanism underlying the oxidation of sumanene, we performed three digital simulations of the CV curves. As an initial guess, we started from an **ECE** mechanism, where the first electron transfer is reversible and is followed by an irreversible chemical reaction, in which the product is easily oxidised and reduced in the back-scan at +1.2V. After the ECE mechanism, we simulated two more complex mechanisms, namely **ECCE** or a square mechanism **ECEC**. In the former, the product of the follow-up chemical reaction (**P**) is transformed back into **S** or further oxidized to **P•⁺**. In the latter, square mechanism **P•⁺** is transformed back to the initial molecule (**S**). The mechanisms are schematized in Scheme 2.4 and the simulated CV curves are shown in Figure 2.10.

Scheme 2.4 Simulated reaction mechanism for Sumanene oxidation (black) ECE, blue ECCE and green ECEC (square mechanism)
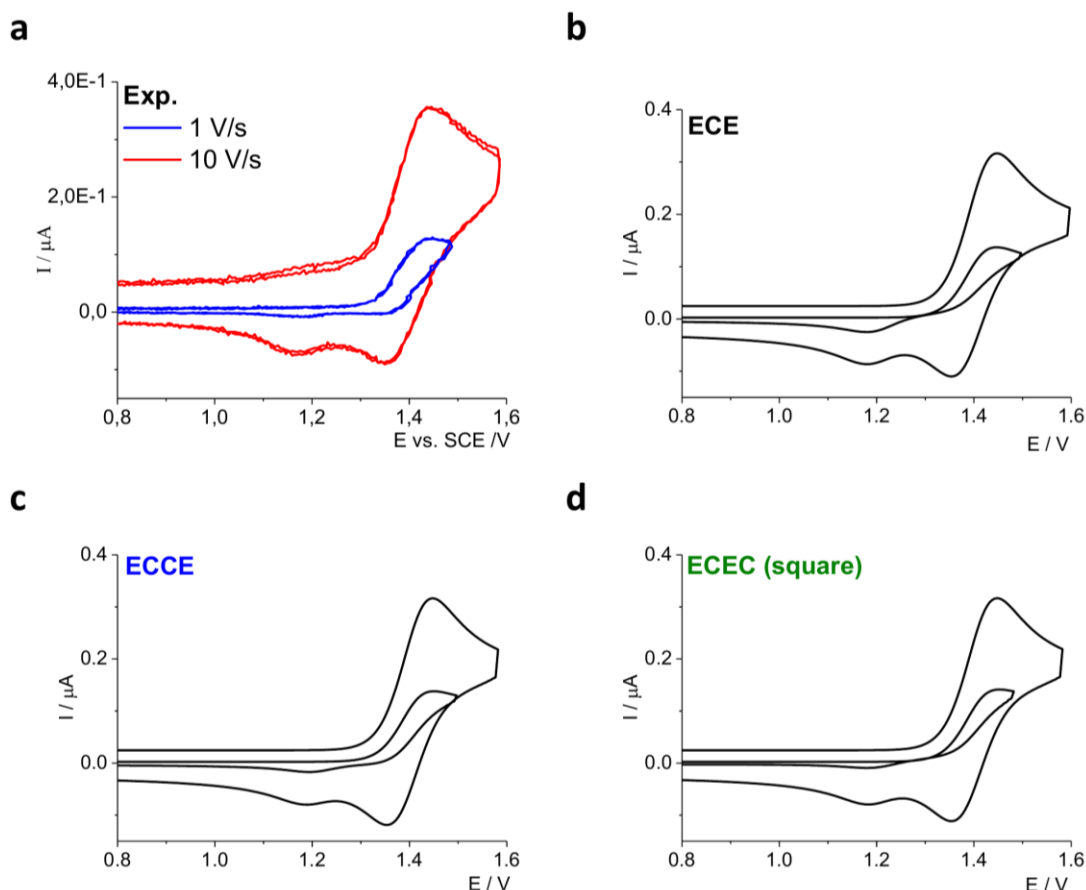
*Figure 2.10 (**a**) Sumanene CVs at 1 and 10 V/s in DCM/Bu$_4$NPF$_6$ with a Pt 125 µm disk diameter as working electrode, SCE as reference electrode. (**b**) ECE simulation with kf1 15s^{-1} at 1 and 10 V/s, (**c**) ECCE simulation with kf1 15 s^{-1} and kf2 30 s^{-1}at 1 and 10 V/s, and (**d**) ECEC (square) simulation with kf1 15 s^{-1} and kf3 5 s^{-1}at 1 and 10 V/s Other simulation parameter [S] 0.43 mM, E°1 +1.4 V, α 0.5, k° 0.1cm/s, E°2 +1.21V, α 0.5, k° 0.1cm/s All the simulations had diffusion coefficients of 10^{-5} cm^2/s and hemispheric diffusion (small disk electrode d=125µm), 298 K, R$_{el}$=5 kΩ and C$_{dl}$=10µF/cm^2.*

From the **ECE** simulation, we observed a good fit with the experimental curve at 10 V/s with a kf1 = 15 s^{-1}, but at lower scan rate the simulated and the experimental CVs are quite different. In particular, at 1 V/s, the simulated oxidation wave results completely irreversible with a crossing in the back scan, moreover the reduction current of the 2nd electron transfer, in the back-scan, resulted higher than the experimental one. These differences suggest a more complicated mechanism. Therefore, we added a competing chemical reaction where **P** is transformed back into the starting molecule. (**ECCE**, pseudo-square mechanism). A good fitting was observed with kf1 = 15 s^{-1} and kf2 = 30 s^{-1} both at 1 V/s and 10 V/s, avoiding the crossing event in the back scan and decreasing the reduction current at 1.2V. Lastly, we simulated a true square mechanism (**ECEC**) where the oxidized product **P$^{•+}$** is transformed back to **S** (kf1 15 s^{-1} and kf3 5 s^{-1}). However, the simulated curves and the experimental one differs significantly

especially at lower scan rate (1 V/s) where a crossing in the CV was observed in the simulation and when we increased kf3 to avoid the crossing, a catalytic S-shaped curve was observed. When we included a DISP process, between $S^{\bullet+}$ and **P**, with a high rate constant (k_{disp} 1000M^{-1}s^{-1}), a significant difference was not observed in the simulated CVs. At the current state, we think that the ECCE (pseudo-square mechanism) better fit the experimental results and could explain the oxidation mechanism of sumanene. The nature of the oxidation products is discussed in the following section.

We performed a digital simulation of the fluorene oxidation to better understand the reaction mechanism. The first guess would be an **ECEC** mechanism (Mechanism 1). However, from the CV analysis we observed that the peak current of the 2nd oxidation is lower than the 1st oxidation peak current, suggesting a more complicated mechanism than **ECEC**. Therefore, we hypothesised two other mechanisms: **ECECC** (mechanism 2) and a more complex **ECECE** (mechanism 3). Reported in Figure 2.11.
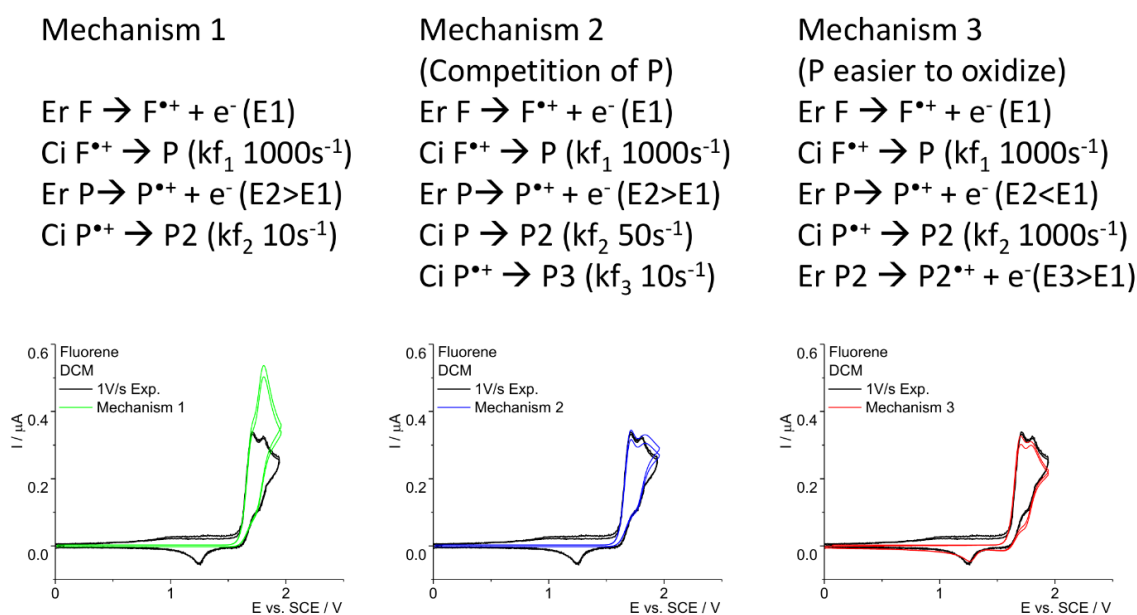
Mechanism 1

Er F $\rightarrow$ F$^{\bullet+}$ + e$^-$ (E1)
Ci F$^{\bullet+}$ $\rightarrow$ P (kf$_1$ 1000s^{-1})
Er P$\rightarrow$ P$^{\bullet+}$ + e$^-$ (E2>E1)
Ci P$^{\bullet+}$ $\rightarrow$ P2 (kf$_2$ 10s^{-1})

Mechanism 2
(Competition of P)

Er F $\rightarrow$ F$^{\bullet+}$ + e$^-$ (E1)
Ci F$^{\bullet+}$ $\rightarrow$ P (kf$_1$ 1000s^{-1})
Er P$\rightarrow$ P$^{\bullet+}$ + e$^-$ (E2>E1)
Ci P $\rightarrow$ P2 (kf$_2$ 50s^{-1})
Ci P$^{\bullet+}$ $\rightarrow$ P3 (kf$_3$ 10s^{-1})

Mechanism 3
(P easier to oxidize)

Er F $\rightarrow$ F$^{\bullet+}$ + e$^-$ (E1)
Ci F$^{\bullet+}$ $\rightarrow$ P (kf$_1$ 1000s^{-1})
Er P$\rightarrow$ P$^{\bullet+}$ + e$^-$ (E2<E1)
Ci P$^{\bullet+}$ $\rightarrow$ P2 (kf$_2$ 1000s^{-1})
Er P2 $\rightarrow$ P2$^{\bullet+}$ + e$^-$(E3>E1)

*Figure 2.11 Oxidation of fluorene (ca. 1.5 mM) in DCM at 1 V/s and simulated cyclic voltammetry. **Mechanism 1** with Simulation parameters: (ECEC) [F] 1.4 mM, E°1 +1.71 V, α 0.5, k° 0.1 cm/s, Ci1 kf$_1$ 1000s^{-1}, E°2 +1.78 V, α 0.5, k° 0.1 cm/s, Ci2 kf$_2$ 10s^{-1};**Mechanism 2** with Simulation parameters: (ECECC) [F] 1.4mM, E°1 +1.71 V, α 0.5, k° 0.1 cm/s, Ci1 kf$_1$ 1000s^{-1}, E°2 +1.78 V, α 0.5, k° 0.1 cm/s, Ci2 kf$_2$ 50s^{-1}, Ci3 kf$_3$ 10s^{-1}; **Mechanism 3** with Simulation parameters: (ECECE) [F] 0.9mM, E°1 +1.71 V, α 0.5, k° 0.1 cm/s, Ci1 kf$_1$ 1000s^{-1}, E°2 +1.25 V, α 0.5, k° 0.1 cm/s, Ci2 kf$_2$ 1000s^{-1}, E°3 +1.78 V, α 0.5, k° 0.1 cm/s; All the simulations have the diffusion coefficients of 10^{-5} cm^2/s and hemispheric diffusion (small disk electrode d=125μm), 1 V/s, 298 K, R$_{el}$ 5000 Ω and C$_{dl}$ 10μF/cm^2.*

In mechanism 2, the product of the 1st chemical reaction (**P**) is oxidised at a higher potential, but there is also a competitive irreversible chemical reaction (**P** could be not stable), this could

explain the small peak current of the 2nd oxidation compared to the 1st one. In mechanism 3, the product of the 1st chemical reaction (**P**) is easier to oxidise than fluorene (typical for the formation of radicals), and the product of the 2nd chemical reaction (**P2**) is oxidised at higher potentials. Further measurements at higher scan rates would help to discriminate between the different mechanisms.

For sumanene and fluorene, we could hypothesize that the 1st irreversible chemical reaction is the deprotonation of the benzylic carbon, which becomes more acidic when the molecule is oxidised to its radical cation. Deprotonation forms a radical and a proton, the radical is usually easier to oxidise than the neutral molecule. The protons, as reported by Bruno et al.,[12] could be solvated by DCM and a reduction of the [DCM-H]$^+$ adduct could be observed appearing with an onset of -2.2V vs. SCE. Reported in Figure 2.12. Due to the high concentration of DCM, the reduction wave did not reach a diffusion-limited regime but appeared like a background solvent reduction. However, DCM reduction (in the absence of H$^+$) appears to occur at more negative potentials (green line).
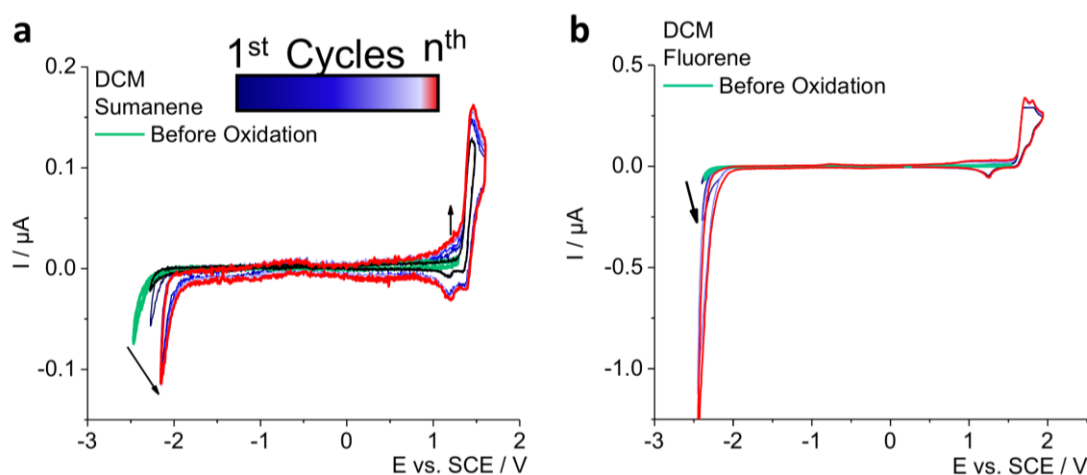
*Figure 2.12 CVs of Sumanene 1.39 mM (**a**) and fluorene 1.5 mM (**b**) in DCM/Bu$_4$NPF$_6$ (80 mM), before (green), and after oxidation. Measured at 298 K and 1 V/s, working electrode Pt disk diameter 125μm, SCE as reference electrode. The arrows indicate the rising of new redox processes after the molecule oxidation.*

Nonetheless, fluorene oxidation has been observed to generate oligomers of polyfluorene, which are not linked by the sp^3 carbon but instead between the benzene units as shown in Scheme 2.5. Therefore, we can expect that the fluorene radical cation could dimerise (in competition with the deprotonation) or that the dimerization of the fluorene radical may induce the migration of H from the sp^2 carbons involved in the new C-C bond, in order to reestablish

aromaticity and returning to a sp^3 CH$_2$. Currently, we cannot distinguish between these two mechanisms.
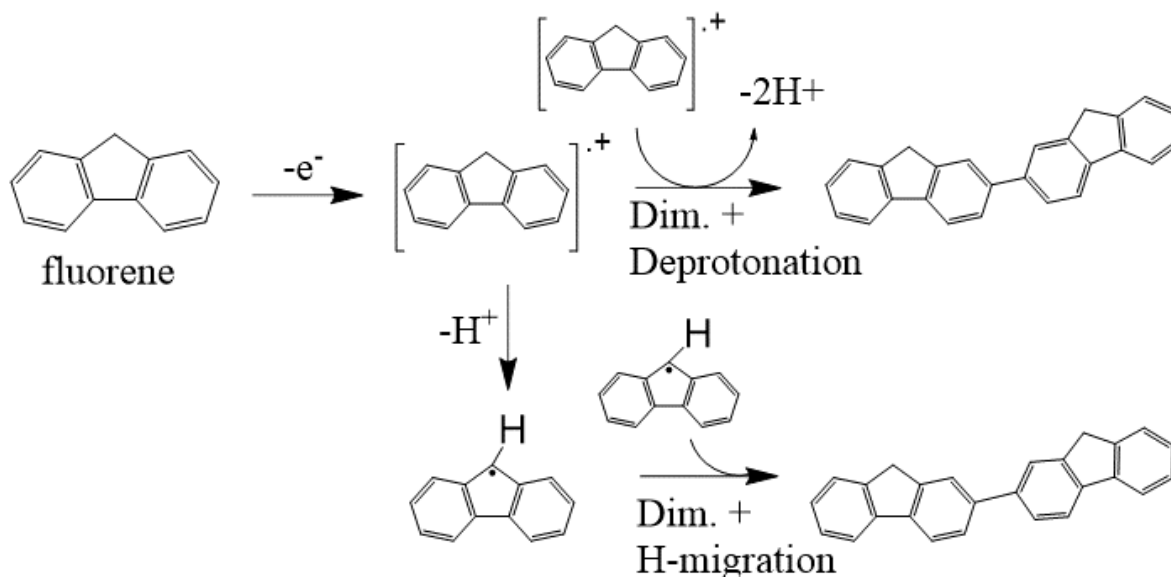
Scheme 2.5 Hypothesised reaction mechanism for fluorene dimerization following dimerization of radical cations and deprotonation pathway or dimerization of radicals (from the deprotonation of the radical cations) and migration of H.

2.4.3 Electropolymerization

Sumanene, corannulene and their fragments, i.e. fluorene, triphenylene and acenaphthylene, shows a film formation process once they are oxidised at higher potentials. For some PAHs, when oxidation occurs in a purified solvent (in absence of H$_2$O or other nucleophiles) with low-nucleophilic solvents and electrolytes, such as DCM/Bu$_4$NPF$_6$, we can observe a dimerization process followed by oligomerization leading to the formation of a (semi) conductive film on the electrode surface. When the film deposition occurs, the current in the cyclic voltammetry will increase because of an increase of the electrode active surface area and capacitance.[13,16] However, the redox wave may have a decrease of the electron transfer kinetics because the film conductivity and charge transport properties are worse than those of the pristine metal electrode, and for very thick films, it could act as a barrier to electron transfer. The conductive film may also exhibit new redox processes, such as the doping of the material (polaron formation), which could be used in different optical and electronic applications. Figure 2.13 shows the CV curves for the electropolymerization of sumanene, fluorene, triphenylene, and acenaphthylene. Corannulene electropolymerization has been thoughtfully investigated by Bruno et al. in similar conditions. Multiple oligomers of corannulene were observed, some of

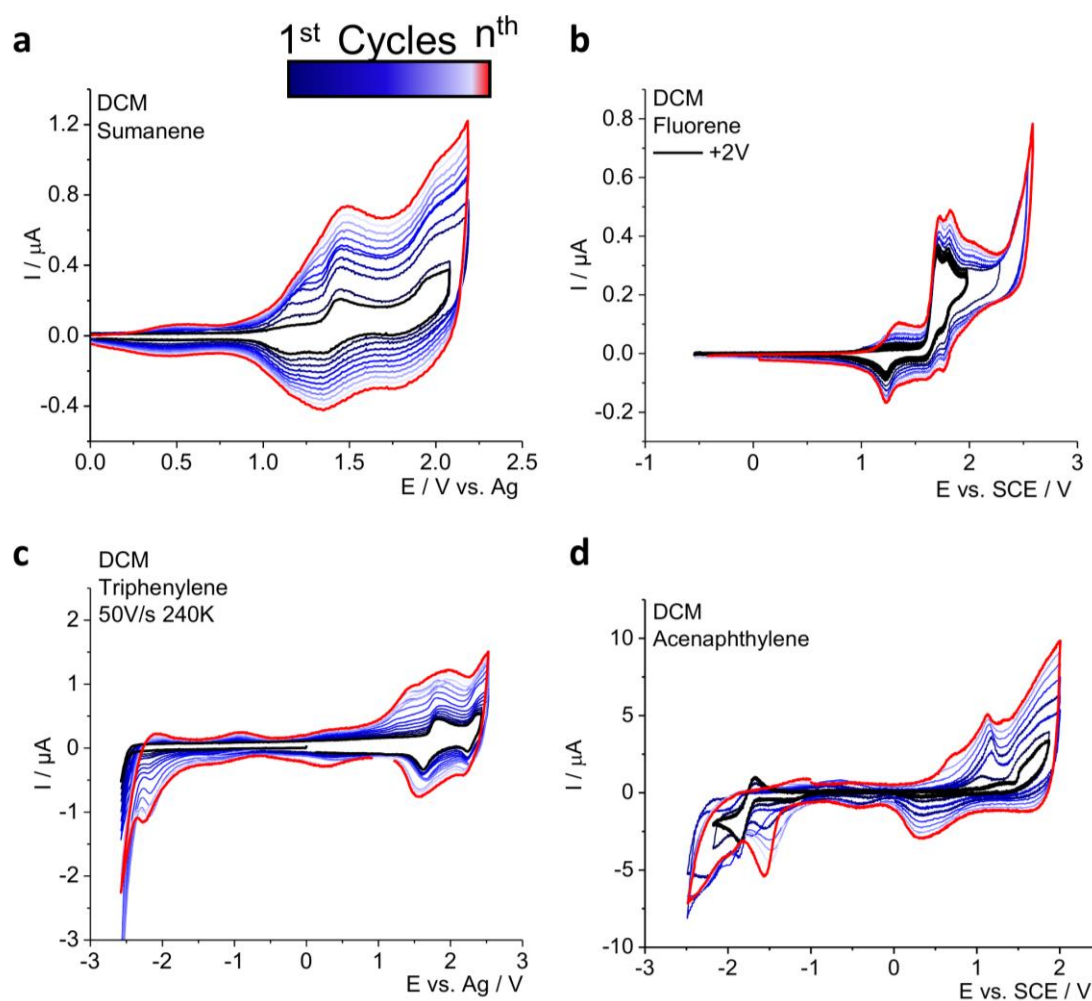them even showed ring closure (cyclodehydrogenation) to more extended and contorted carbon nanostructures.[12]

*Figure 2.13 Electropolymerization of sumanene 1.39 mM (**a**), fluorene 1.5 mM (**b**), triphenylene 1.25 mM (**c**) and acenaphthylene 1 mM(**d**) in DCM/Bu₄NPF₆ (80 mM). Measured at 298 K and 1 V/s, working electrode Pt disk diameter 125μm and 0.5mm for acenaphthylene, Ag quasi-reference electrode or SCE as reference electrode. Measured at 240 K and 50V/s for the electropolymerization of triphenylene.*

Sumanene shows an oligomerization and film deposition that started once a second oxidation wave is reached at +2V vs. SCE. The new oxidation process at +1.2V was already present after the 1st oxidation of sumanene, but greatly enhanced when the 2nd oxidation was reached with a current that increased after each cycle. A new reversible redox process appeared at +0.5V, these two new redox processes may be related to two different species generated by the sumanene oxidation or two doping/de-doping processes when the film is oxidised.

Fluorene showed a small current increase after each cycle and a new oxidation process after the 1st oxidation (black lines). However, film formation is greatly enhanced when a higher potential

is reached (+2.5V vs. SCE, blue lines). However, for the fluorene film there are not new redox wave before 1V vs. SCE. This suggests that the fluorene film requires a very positive potential for the doping of the oligomers.

Triphenylene has already been reported to form a conductive film on the electrode at room temperature,[10] and we observed that electropolymerization is a very fast process for triphenylene because it occurs even at fast scan-rate of 50V/s and low temperature (-60°C). Once again, electropolymerization was enhanced when the 2nd oxidation wave was reached.

Acenaphthylene electropolymerization occurred just after the 1st oxidation was reached, owing to the high reactivity of its radical cation. A steady increase in the current was observed after each oxidative cycle, and three new redox processes were observed. In the positive potential region, a process before acenaphthylene oxidation is observed at +1V, and in the back scan, a reduction process at +0.5V. These new redox waves are probably related to the doping and de-doping processes of positive polarons. In the negative potential region, a new reduction process at -1.5V is observed, moreover the peak potential seems to shift between each cycle. If the process is related to doping of a negative polaron, the shift may indicate an unstable reduction state in our conditions (chemical reactivity) or the film becomes thicker between each cycle, and the reduction becomes more difficult to occur.

The molecules were electropolymerized on the ITO electrode, and the films were characterised by laser desorption ionisation time-of-flight (LDI-TOF) mass spectroscopy. Laser desorption ionisation is necessary because the electropolymerized films are insoluble in conventional solvents, and conventional mass spectroscopy techniques cannot be applied. A matrix could not be added because the produced films were very thin and the total amount of material was relatively low to prepare a mixture with a matrix, as in the conventional matrix-assisted laser desorption ionisation technique. Laser power is an important parameter, which should ideally be as low as possible, because too high power could result in the severe fragmentation of oligomers or unwanted reactions. In fact, the laser power was kept as low as possible to have a sufficiently high signal and a further increase of the laser intensity, in many cases, led to a substantial modification of the fragmentation pattern.

Figure 2.14 shows the LDI-TOF of a pristine film of electropolymerized sumanene on the ITO. The attribution of the observed m/z peaks is quite difficult since sumanene molecular weight is 264.32 g/mol and its linear dimer and trimer would be respectively 526.6 and 788.9 g/mol with a general chemical formula of $[C_{21}H_{11}]n$. However, if we consider multiple ionisation

charges z=2 and z=3 for the observed signal at 258.3 and 256.3 m/z respectively, we would calculate a mass of 512.6 and 774.9 g/mol respectively. These calculated masses differ from those of the linear dimer and trimer of sumanene for just 14 g/mol, such difference could be explained by the fragmentation of a CH_2 unit from the cyclopenta moiety of sumanene. At higher m/z, dimers and trimers with z=1 were not observed. In order to facilitate the ionisation and detection in gas phase, the sumanene film was successively treated with a dilute solution of trifluoroacetic acid (TFA; 5% v/v in a mixture of 75% ACN and 25% H_2O) and the LDI-TOF spectrum of the treated film is reported in Figure 2.14b. As all the samples analysed passed through a pre-vacuum chamber before entering the ionisation chamber, we can expect that the solvent molecules (ACN and H_2O) have been removed before the film is ionised. The number of peaks dramatically increased for the treated sumanene film, in particular we can distinguish at 354.45 m/z the salt of deprotonated TFA^- (113.02 g/mol) and Bu_4N^+ (242.3 g/mol), the linear dimer of sumanene 525.4 m/z and trimer 787.6 m/z. No peaks close to the tetramer mass were observed. The other peaks are more difficult to attribute, nonetheless we cannot exclude that TFA may react with sumanene oligomers in unexpected way thus leading to new m/z peaks.
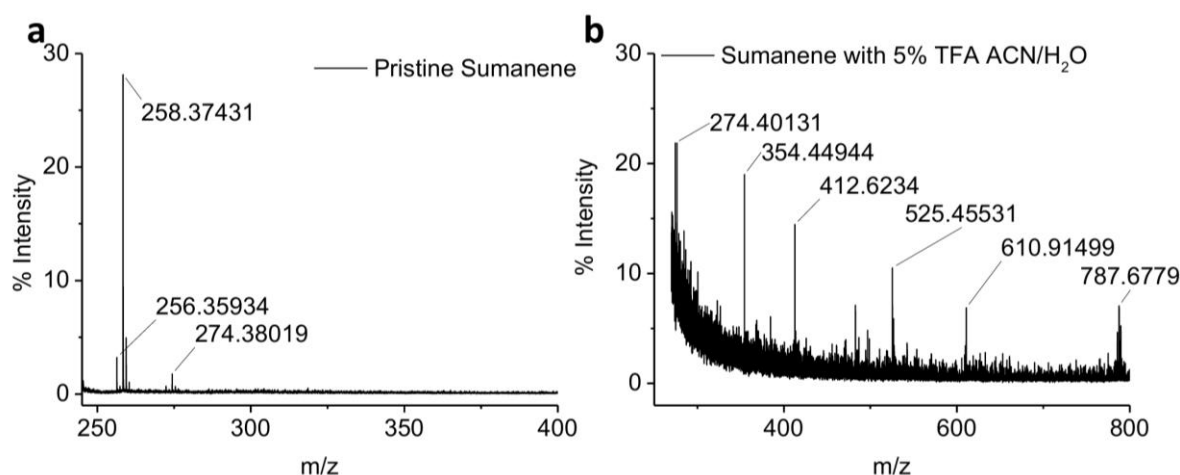
Figure 2.14 LDI-TOF Spectrum of electropolymerized sumanene film on ITO in DCM/Bu_4NPF_6

Figure 2.15 shows the LDI-TOF spectrum of the electropolymerized fluorene film on ITO and we can observe the presence of multiple oligomers. Considering that fluorene (166.22 g/mol) bonds linearly through the sp^2 carbon, the oligomer molecular weight is MW (g/mol) = $166.22 \times n - (2 \times n + 2)$ with a chemical formula of $[C_{13}H_9]n$. The peak at 242.04 m/z is related to the Bu_4N^+ (242.4 g/mol) cation, which is present even though the electropolymerized electrode was repeatedly dipped in pure DCM. Fluorene dimer to octamer can be observed in the

spectrum, suggesting that the electropolymerization of fluorene generates a distribution of oligomers. Some of the low-molecular-weight oligomers, which should be partially soluble in DCM, may remain trapped in the aggregates of longer chain oligomers or they could come from laser fragmentation, leading to the observation of lower m/z units.
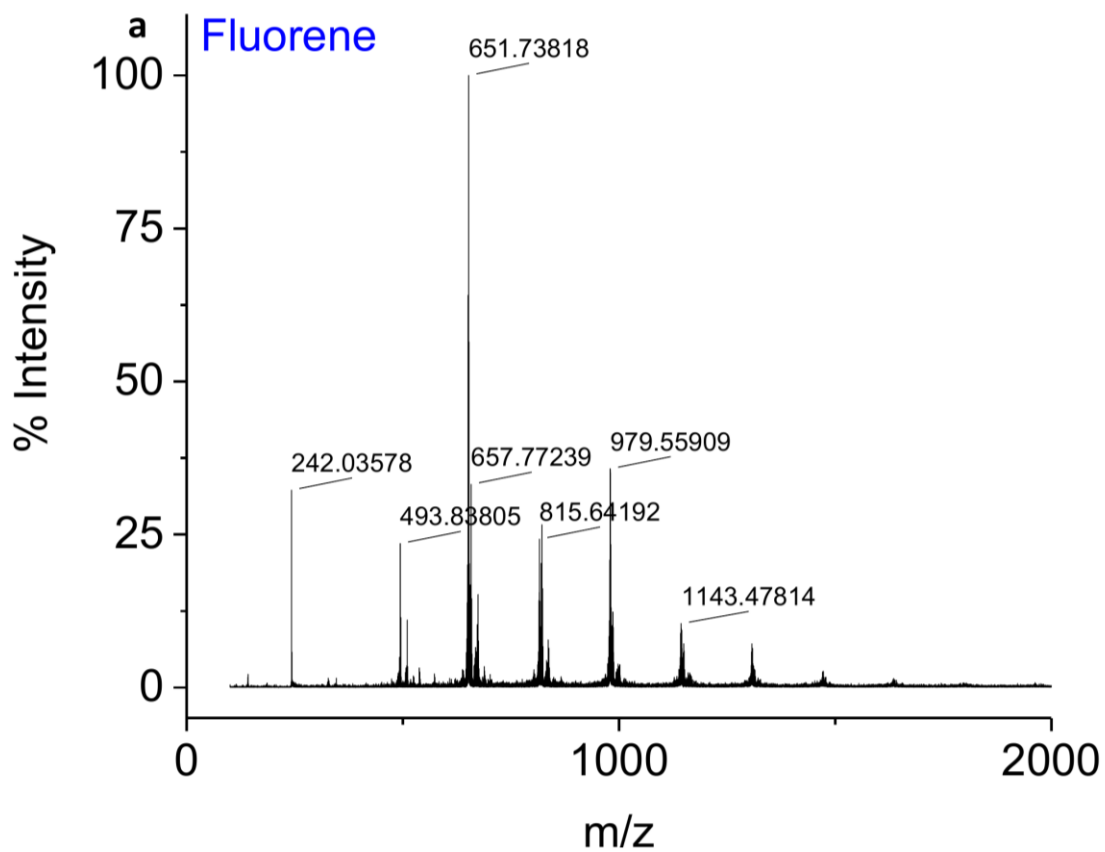
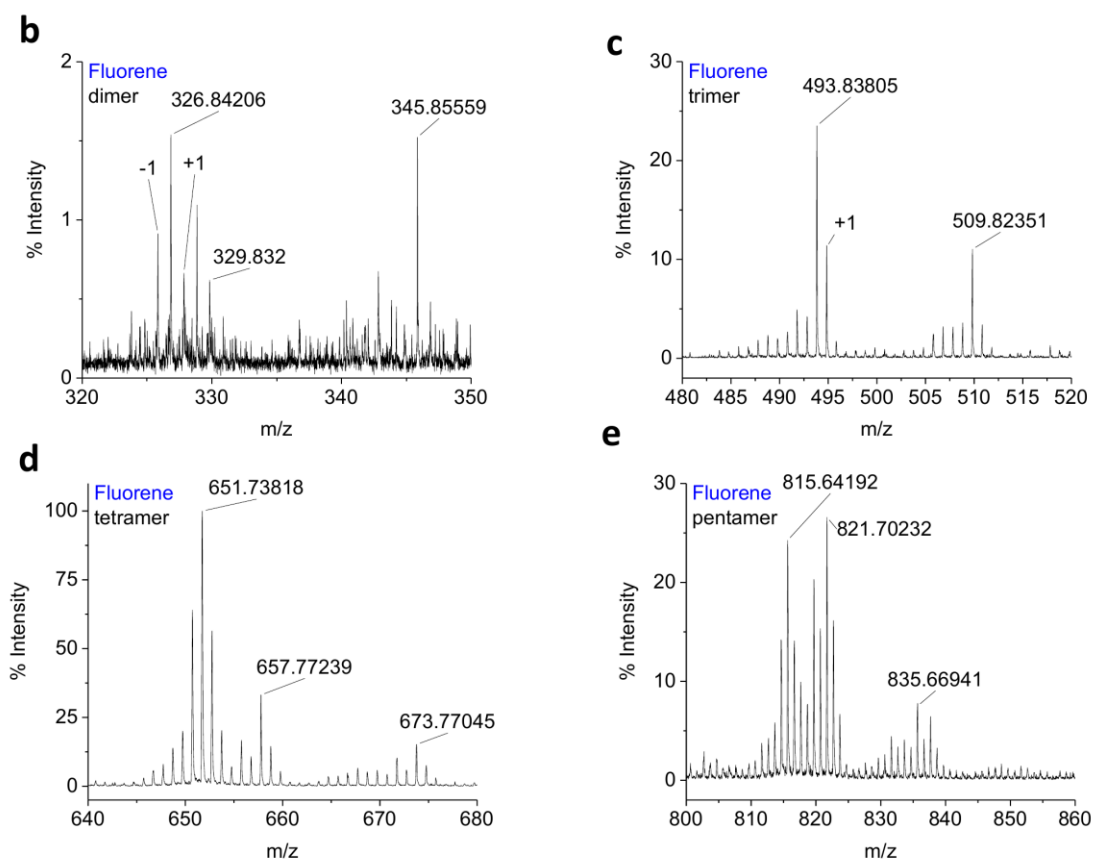*Figure 2.15 LDI-TOF spectra of electropolymerized fluorene on ITO in DCM/Bu₄NPF₆.*

A closer look at the dimer range (320-360 m/z) shows that three different molecules were present, each with their proton clusters. In particular, we observed the fluorene dimer, $C_{26}H_{18}$, 330.4 g/mol (329.8 m/z). Whereas the peak at 326.8 m/z has four less hydrogens than the dimer, suggesting two possibilities: (1) a linear dimer without the sp^3-C hydrogens or (2) the chemical structure is not linear; in particular, the m/z may correspond to a benz[e]indeno[1,2,3-hi]acephenanthrylene, $C_{26}H_{14}$ 326.4 g/mol. The hypothesised molecule can be generated by the ring closure between the benzene carbons of a bifluorenylidene,[32] $C_{26}H_{16}$ 328.4 g/mol (Scheme 2.6). Moreover, this supports the previous hypothesis of a radical formation after deprotonation of the fluorene radical cation with radicals that could couple between the benzylic carbon. Lastly, the peak at a higher m/z (345.8 m/z) could be related to a hydroxy group or ketone group present in the dimer. Also in the longer chain oligomer, ketone or hydroxy groups are present. Fluorene oligomer, with un-protected benzylic carbons, may be subject to oxidation by air or due to some residual H_2O still present in the solution when the film was produced; in fact, H_2O can react as a nucleophile with dimers or fluorene radical cations leading to hydroxy or ketone

groups. In the tetramer and pentamer regions, molecules with m/z values lower than expected (6 m/z less than a linear tetramer/pentamer) were observed, supporting the hypothesis that fluorene oligomerization does not occur exclusively linearly, but more complex structures are produced like a benz[e]indeno[1,2,3-hi]acephenanthrylene dimer(650.8 g/mol) or mixed with fluorene unit.

MW 166.22 g/mol   MW 328.41 g/mol   MW 326.40 g/mol
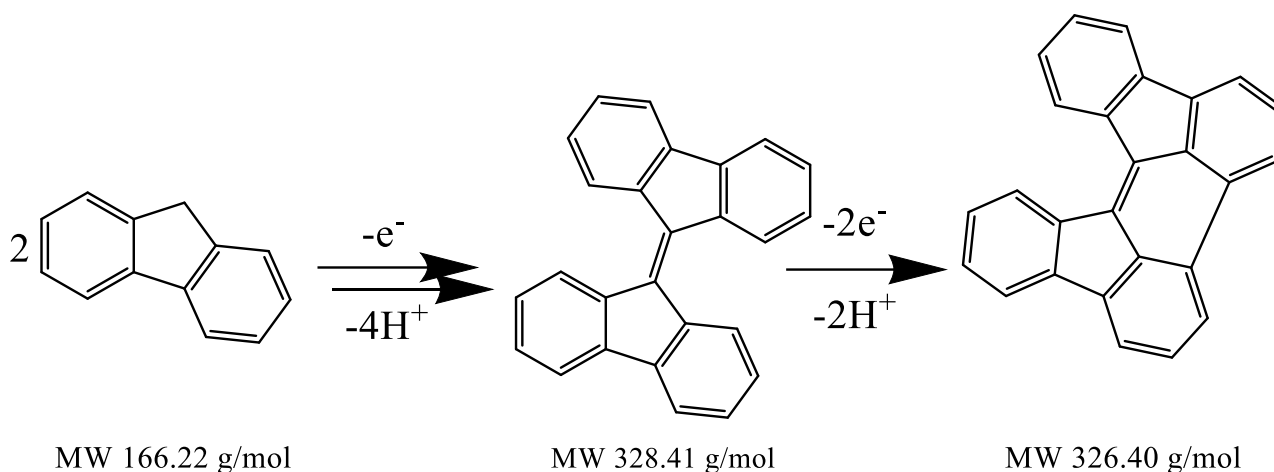
Scheme 2.6 Hypothesized dimerization of fluorene to bifluorenylidene and ring closure to benz[e]indeno[1,2,3-hi]acephenanthrylene

Figure 2.16 shows the LDI-TOF of the electropolymerized triphenylene film on ITO. We can observe that multiple oligomers are present, triphenylene (228.29 g/mol) oligomers bonded linearly would show a MW (g/mol) = 228.29×n –(2×n-2) with a chemical formula of $[C_{18}H_{11}]n$. From the mass spectrum, we recognised the presence of single bonded dimer (454.4 m/z), trimer (680.5 m/z), and tetramer (906.7 m/z).
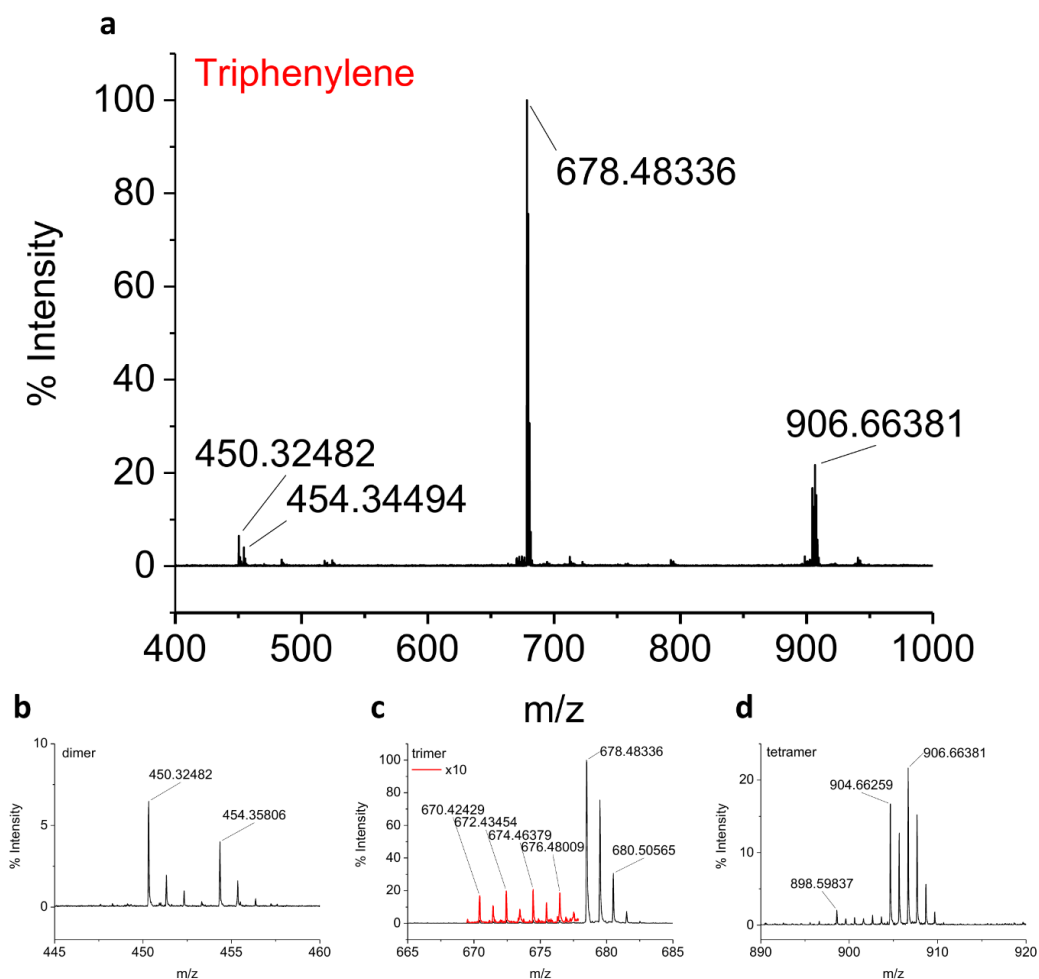
Figure 2.16 LDI-TOF spectra of electropolymerized triphenylene on ITO in DCM/Bu₄NPF₆.

Nonetheless, other structures with lower m/z were observed, particularly in the dimer m/z range (Figure 2.16b) a more intense signal was observed at 450.3 m/z. This structure implies a molecular formula of $C_{36}H_{18}$ which has 4 less hydrogens than the single-bonded dimer. We hypothesised that two more C-C bonds are generated by the electrochemically driven cyclodehydrogenation of triphenylene. Since triphenylene is a highly symmetric molecule, two reactive sites are possible for dimerization, namely position 1 (closer to the fused aromatic ring) and position 2 at the edge (Scheme 2.7), therefore only three possible dimerizations are possible: C1-C1, C1-C2, and C2-C2. The only dimer with a mass of 450.5 g/mol was the one with three new bonds (one C1-C1 and two C1-C2). However, once the dimers are generated, the molecules lose some of their initial symmetry, therefore many reactive positions will not be equal and many different trimers could be formed. The highest molecular weight trimer is the one with three triphenylene units singly bonded between each other (680.8 g/mol). However,

from the LDI-TOF data, trimers with more than three new bonds were observed, some of them have the same mass, but different chemical structures. The only possible trimer with the lowest molecular weight is the fully conjugated one at 670.7 g/mol which, interestingly, was also observed in the mass spectrum. The number of possible tetramers is even higher and many multiple structures are possible.
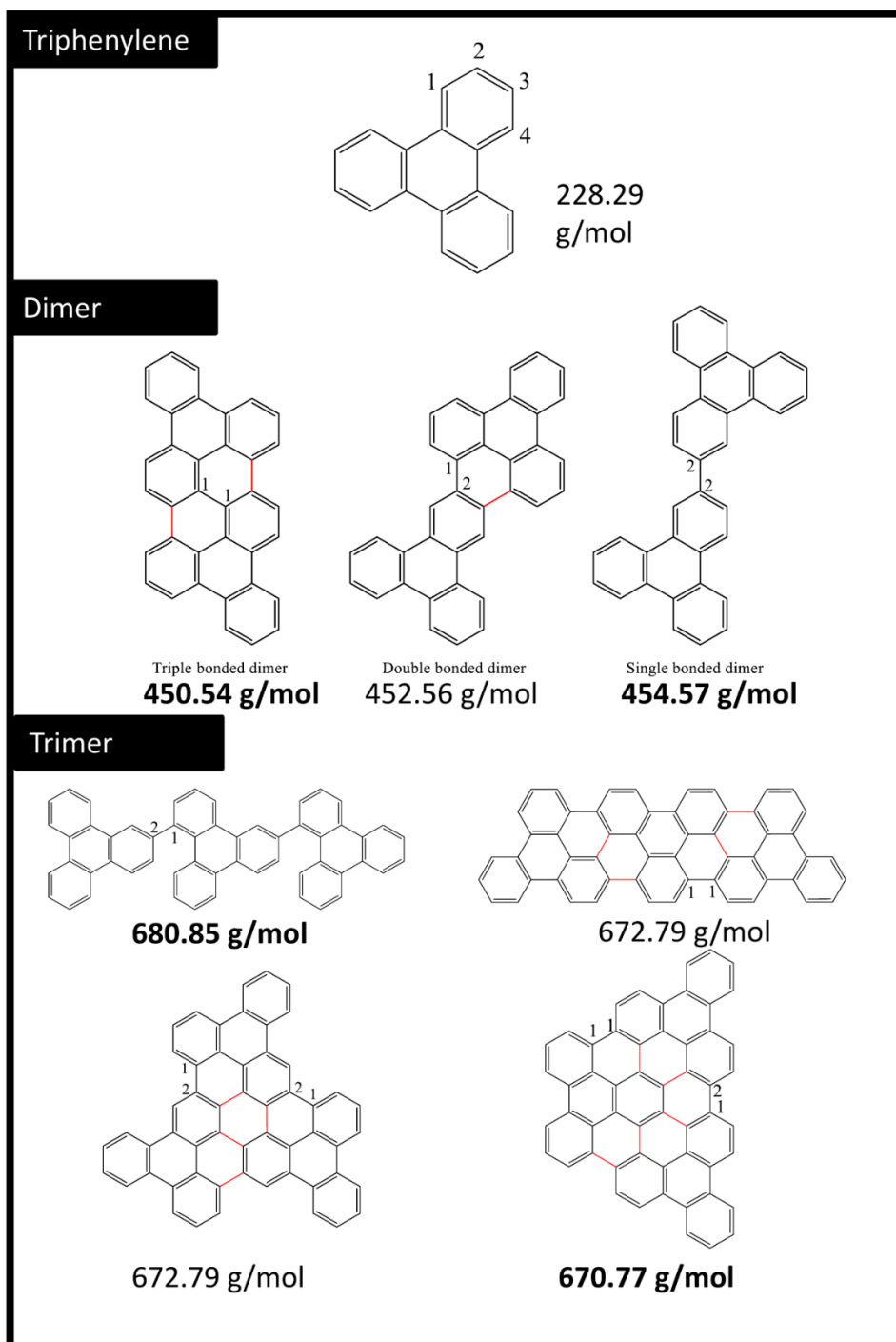
Scheme 2.7 Possible structures of the dimer and trimer of triphenylene with mass observed in the LDI-TOF spectrum. The new bonds, other than those responsible for linear dimers, are highlighted in red.

Figure 2.17 shows the LDI-TOF of the electropolymerized acenaphthylene film on the ITO.
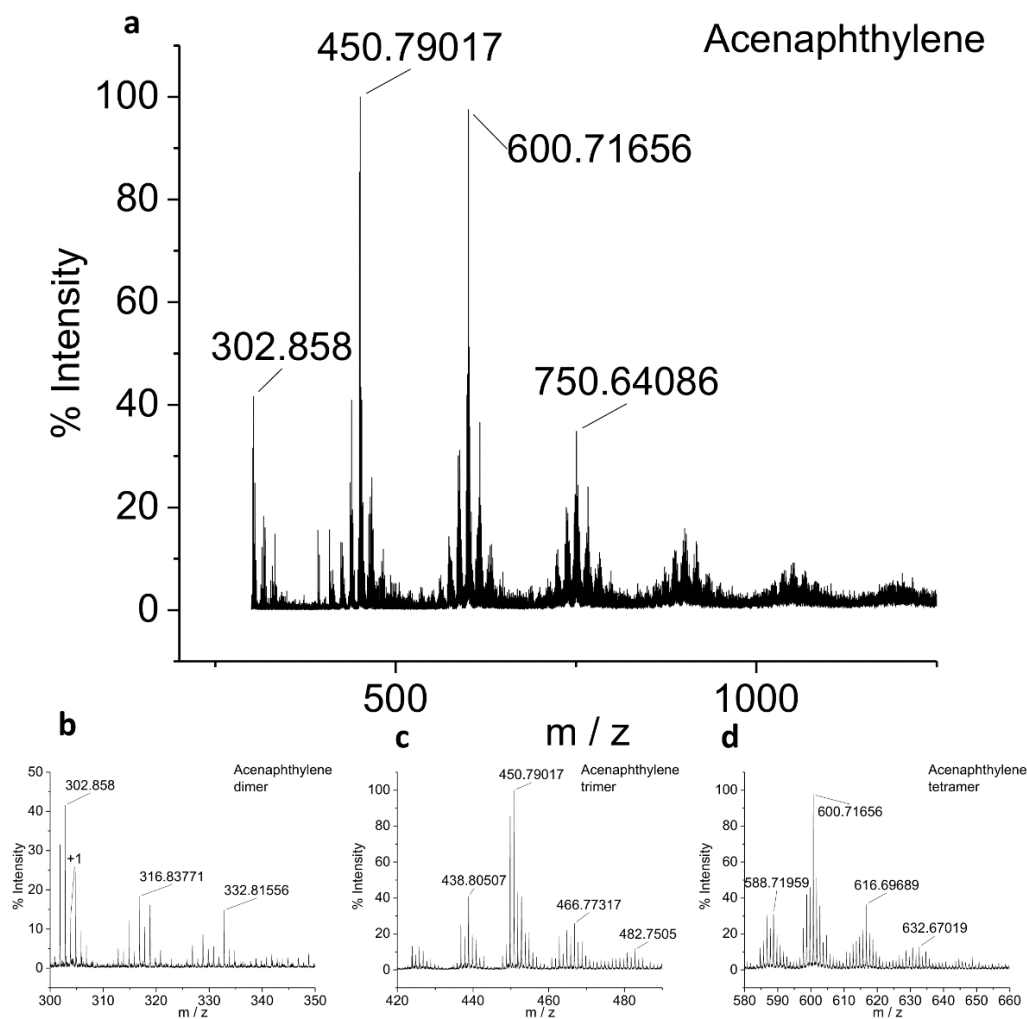
Figure 2.17 LDI-TOF spectra of electropolymerized acenaphthylene on ITO in DCM/Bu₄NPF₆.

The spectrum shows dimer to heptamer of acenaphthylene, and the fragmentation is higher than that of the fluorene spectrum. If linear, the expected oligomer has the chemical formula $[C_{12}H_7]_n$ and MW (g/mol) 152.2×n-(2×n+2). In the region corresponding to dimer range, three molecules can be observed, the linear dimer at 302.8 m/z and two species with +16 and +30 m/z than the dimer. These species could be related to one and two hydroxy or ketone groups. In particular, the central double bond is localised and the corresponding two carbons are more reactive, thus they could be subjected to oxidation (from air) or H_2O (traces present during electropolymerization). The oxidated (hydro or ketone groups) oligomers are also present in the trimer and tetramer regions. Fragmentation of the acenaphthylene units was observed in

the trimer and tetramer zones. In fact, species with m/z less than 12 than the corresponding linear oligomer were observed, suggesting the removal of a carbon atom. This may be related to the higher laser power required for the ionisation of the film, which inevitably brings to partial damages of the film (fragmentation).

2.4.4 Conclusion

Sumanene electrochemistry has been explored in DCM and THF and compared to that of corannulene and to their sub-fragments, namely fluorene, triphenylene and acenaphthylene. We observed that sumanene and its fragments exhibit similar electrochemical behaviour, but because of sumanene curvature we observed a higher redox potentials and increased reactivity of sumanene radical ions. Moreover, these molecules have been observed to generate a conductive film on the electrode when they are oxidised at high potential. These films have been studied by LDI-TOF mass spectroscopy and have shown a distribution of oligomers with different chemical structures, ranging from linear oligomers to more π-conjugated oligomers. In future work, to achieve a more selective synthesis by electrochemically induced cyclodehydrogenation or oxidative coupling, it will be necessary to carefully functionalize the molecular precursor. In this way, the radical cation would have a very localised electron density and the coupling could occur exclusively between well defined reaction sites, making the selective electrosynthesis of extended aromatic molecules feasible.

2.5 Heteroaromatic pentabenzo-azacorannulene and pentaphenyl-pyrrole

In this last section, we discuss the electrochemical behaviour of heteroaromatic curved pentabenzoazacorannulene and two substituted pentaphenylpyrroles. The aim of this investigation was also to evaluate whether pentabenzoazacorannulene could be obtained by the electrochemical oxidation and induced cyclodehydrogenation of these substituted pyrroles; similarly to the reaction occurring with the oxidation of hexaphenylbenzene, which produces the fully closed hexabenzocoronene by planarization of all the phenyl groups. Nonetheless, concerning such substituted pentaphenylpyrroles an important challenge for this electrochemically induced cyclodehydrogenation reaction is a noticeable molecular strain related to the expected curved final structure in contrast with a flat molecule as in the case of the planarization of hexaphenylbenzene.

The investigated molecules are shown in Scheme 2.8: 8-tert-butyl-6b^2-azapentabenzo[bc,ef,hi,kl,no]corannulene (**NCor**), 1-(p-bromophenyl)-2,3,4,5-tetraphenyl-pyrrole (**Br5PhPy**), and 1-tolyl-2,3,4,5-tetraphenylpyrrole (**Tol4PhPy**).

tBu-Pentabenzoazacorannulene (**NCor**)

Pentaphenylpyrrole

X: Br (**Br5PhPy**)
CH$_3$ (**Tol4PhPy**)
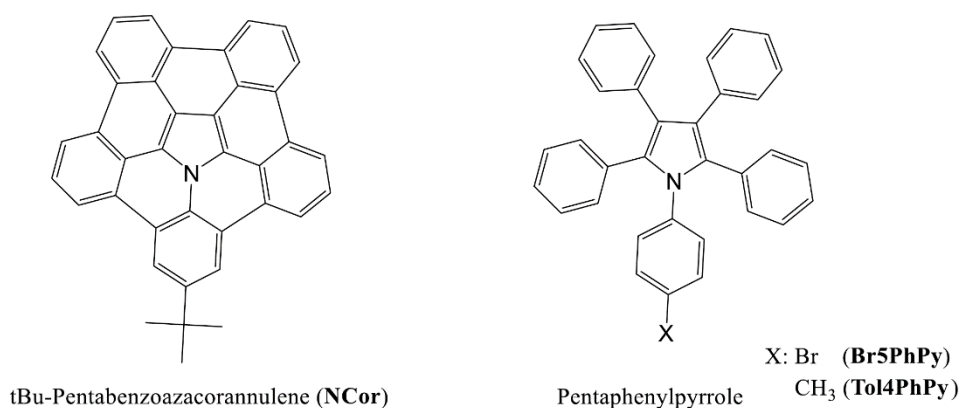
*Scheme 2.8 Molecular structures of 8-tert-butyl-6b^2-azapentabenzo[bc,ef,hi,kl,no]corannulene (**NCor**), 1-(p-bromophenyl)-2,3,4,5-tetraphenylpyrrole (**Br5PhPy**), and 1-tolyl-2,3,4,5-tetraphenylpyrrole (**Tol4PhPy**).*

2.5.1 Electrochemical characterisation

The CV curves of 8-tert-butyl-6b^2-azapentabenzo[bc,ef,hi,kl,no]corannulene (**NCor**) are shown in Figure 2.18. **NCor** was investigated in both THF and DCM/Bu$_4$NPF$_6$ at room T (25°C) and low T (-60°C). The redox properties of **NCor** and pentaphenyl-pyrrole molecules are summarised in Table 2.3.

In THF, **NCor** has two chemically reversible one-electron reductions at E$_{1/2}$ =-1.92V and -2.17V vs. SCE, each with a peak-to-peak potential separation (ΔE$_p$) of 88mV, which suggest a slightly slower electron transfer kinetics. The ΔE$_p$ for ferrocene oxidation under the same conditions was 72mV (higher than the expected 59mV, but the voltammograms were affected by ohmic drop). At more negative potentials, a third reduction appears to be chemically irreversible and its cathodic peak is observed at E$_p$ -2.75V close to the THF background reduction, which increases the observed peak current. At lower temperature (-60°C) the 3rd reduction can be separated by the THF reduction. However, even at low temperature the 3rd reduction remains chemically irreversible and the number of exchanged electrons, extrapolated by the peak current, was close to 2. We hypothesised that the 3rd reduction could be a two-electron process or, more probably an ECE mechanism, where the product of the irreversible chemical reaction is easier to reduce. The products generated following the irreversible 3rd reduction process are oxidized in the back-scan at -1.25 and -0.95V vs. SCE. Furthermore, at a low T, the 1st oxidation of **NCor** was observed in THF. The anodic process appears to be chemically reversible and one electron is transferred, since the peak current is close to that of the 1st reduction. However, the oxidation is affected by a slow electron transfer kinetics because we observed a high peak-to-peak separation, ΔE$_p$ =102mV compared to the 67mV of the 1st reduction in the same voltammogram. The sluggish kinetics could explain the small difference in the peak current between the oxidation and reduction of **NCor** in THF.

In DCM, at 0.5mM, differently from THF, the 1st oxidation in DCM shows two quasi-reversible oxidations with close potentials around 0.75V vs. SCE. The electron transfer kinetics seem even more sluggish (ΔE$_p$ 230mV) than the 1st oxidation in THF at low T, and the peak current was lower than expected. At a more positive potential, a 2nd reversible oxidation was observed at E$_{1/2}$ = 1.40V, the ΔE$_p$ 51 mV was smaller than the expected for a one-electron transfer and the peak current was higher than the first oxidation. This evidence suggests a multi-electron process or an ECE mechanism or a more complex behaviour. Finally, a 3rd oxidation process is observed close to the solvent potential limit, at 2.15V vs. SCE with a ΔE$_p$ of 70mV (closer to the

one expected by one-electron transfer). Nonetheless, the peak current was similar to that of the 2nd oxidation.

At lower temperatures in DCM, the electrochemical behaviour of **NCor** was particularly affected by the temperature change. The two redox processes in the 1st oxidation peak were more separated. Furthermore, the 2nd oxidation wave (+1.4V vs. SCE at 25°C) was particularly affected and it appeared to be split into two oxidation waves with an anodic peak difference of 316mV. The first wave appeared to be chemically reversible, whereas the latter was affected by an irreversible chemical reaction (with a small kinetic constant). The two separated wave have a total peak current similar to that of the 1st oxidation. At a more positive potential, a 4th reversible oxidation process was observed with a peak current which is double that of the previous oxidations. Interestingly, the peak current of the 4th oxidation is similar to that of the 1st reduction (in DCM at low T). Assuming that both redox processes (4th oxidation and 1st reduction) are one-electron transfers, the previous ones (1st, 2nd, and 3rd oxidations) show an apparent number of electrons of ½.
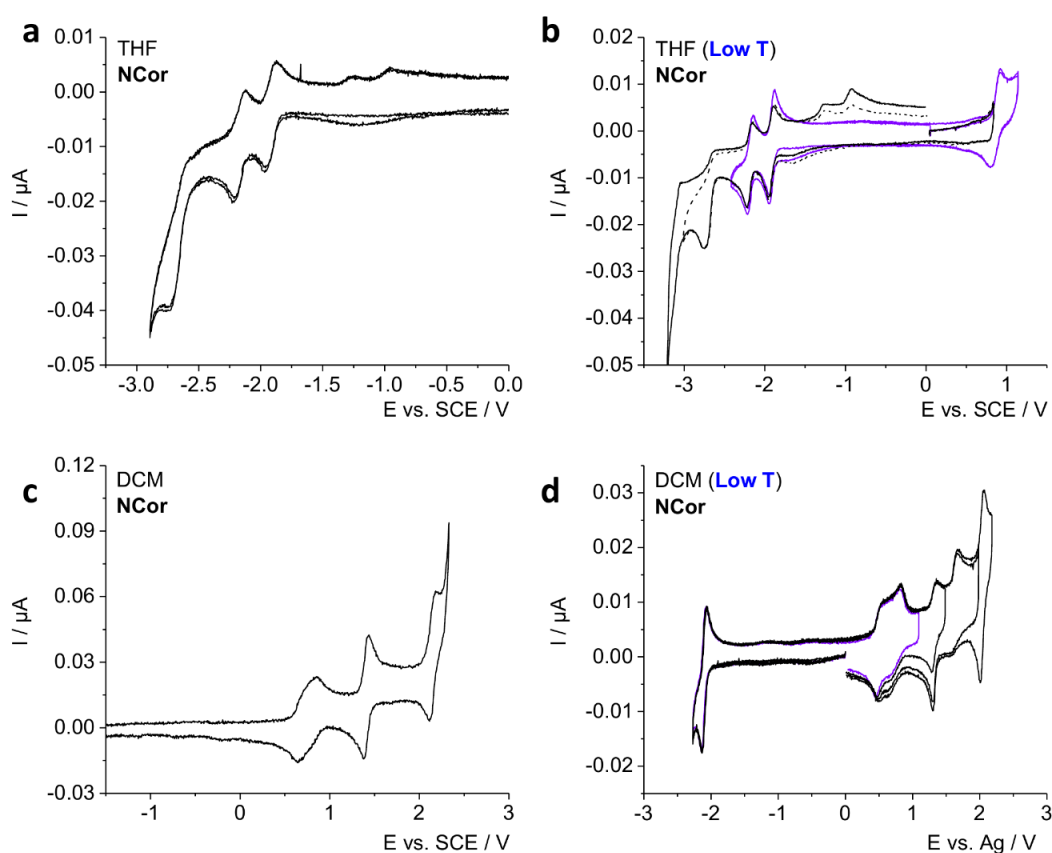
*Figure 2.18 (**a,c**) CVs in DCM/Bu₄NPF₆ (80 mM) and (**b,d**) THF/Bu₄NPF₆ (80 mM) with 8-tert-butyl-6b2-azapentabenzo[bc,ef,hi,kl,no]corannulene 0.5 mM. Working electrode Pt disk diameter 125 µm, Ag wire as quasi-reference electrode or SCE as reference electrode, Measured at 1V/s, 298 K (**a, b**), and 213 K (**c,d**).*

Table 2.3: Redox Properties

Species	Oxidation[a] $E_{1/2}$ vs. SCE / V			Reduction[b] $E_{1/2}$ vs. SCE / V		
NCor	0.75 (0.83)	1.40	2.15	-1.92	-2.17	-2.75c
Tol4PhPy	1.02	1.84c				
Br5PhPy	1.09	1.84c				

Notes: Measured at 298 K with a Pt working electrode disk of 125 μm diameter, and SCE as reference electrode at 1 V/s. [a](80 mM) Bu_4NPF_6/DCM electrolyte solution, [b](80 mM) Bu_4NPF_6/THF electrolyte solution, [c] peak potentials reported for chemically irreversible processes.

To explain the complex anodic behaviour of **NCor**, we hypothesised the presence of an **NCor** dimer resulting from the aggregation of the two units, arranged by π-π interaction or/and cooperative dipolar interactions, they could stack in a concave-convex way. It comes out that the actual concentration of the dimer at the electrode would be half of the analytical concentration of the species. Such a hypothesis would be in line with the electrochemical behaviour at 25°C of the 1st oxidation, for which the two oxidation potentials would be related to a dimeric form of the compound. Once a unit of the dimer is oxidised, an electrostatic effect occurs on the electron transfer of the second unit, resulting in a higher potential required. After the 1st oxidation, the oxidised dimer separates into two oxidised units, thus restoring the analytical concentration of the electroactive species. Thus, the 2nd and 3rd oxidation show both a peak current that is double the current of the 1st one. It is possible to hypothesize that the formation/separation of the dimeric aggregate seems to be a reversible and very fast equilibrium, as in the back scan the cathodic current of the 1st oxidation is also halved.

At low T, the solubility of **NCor** decreases and probably the dimer results to be even more tightly aggregated, remaining in the dimeric form also after the 1st oxidation wave. The 2nd oxidation at +1.4V vs. SCE is now affected by the dimer, showing two redox waves. After the 3rd oxidation, the double-oxidised dimer separates and hence the 4th oxidation has a doubled peak current. Interestingly, the reduction processes do not seem to be affected by the presence of a dimer, or more probably, it separates as soon as the reduction starts, with a fast equilibrium, thus showing a single redox process. Finally, THF may be a better solvent for **NCor**, even at low T, that does not favour the dimeric aggregation and then the oxidation and reduction peak currents are similar.

Further analysis at lower concentration of the **NCor** compound in DCM, at room T, showed that the 1st oxidation becomes a single one electron transfer with a peak current comparable to that of the 2nd oxidation (1e- as well), as shown in Figure 2.19. This evidence supports the hypothesis

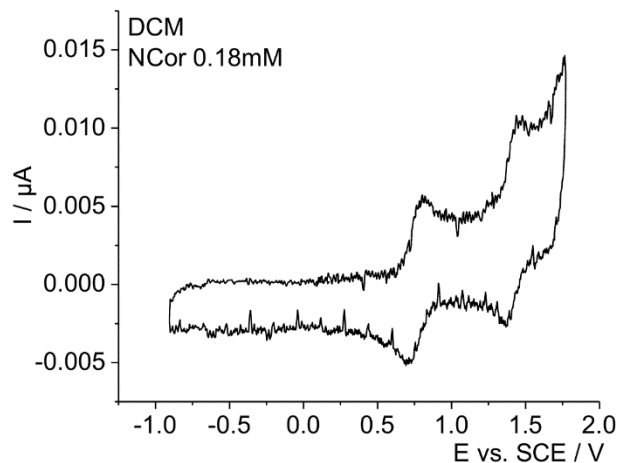of an aggregated dimer at higher concentration in DCM, which instead was not present at lower concentration.

Figure 2.19 CVs curves in DCM/Bu₄NPF₆ (80mM) of 8-tert-butyl-6b2-azapentabenzo[bc,ef,hi,kl,no]corannulene, 0.18mM. Working electrode Pt disk diameter 125μm, SCE as reference electrode, scan rate: 1V/s and T=298 K.

Furthermore, to investigate the eventual occurrence of the electrochemically induced cyclodehydrogenation reaction that leads to the curved pentabenzoazacorannulene. Two pentaphenylpyrrole derivatives, i.e. 1-(p-bromophenyl)-2,3,4,5-tetraphenylpyrrole (**Br5PhPy**) and 1-tolyl-2,3,4,5-tetraphenylpyrrole (**Tol4PhPy**), sketched in Scheme 2.8, have been studied. Figure 2.20 shows their CV curves. The two substituted phenyl-pyrroles show similar electrochemical behaviour in DCM; the species **Tol4PhPy** has a 1st one-electron oxidation process at $E_{1/2}$ of +1.02V vs. SCE with a ΔE_p of 59mV. At more positive potential, a new multi-electronic oxidation process was observed, and the redox wave appeared to be composed of two processes with very close potentials. At a preliminary analysis, the first process, within the second voltammetric wave, seems to have a double current than the latter. The peak potential of the second wave is +1.84V and from the peak current we estimated an apparent number of exchanged electron close to 3.3, even though the electrolyte background current could slightly affect the estimated value. It is worth noting that, in Figure 2.20a, for the second cycle, a new oxidation wave is observed at less positive potentials than the 1st oxidation of **Tol4PhPy**. Such a new redox process suggests that a more conjugated product may have been produced during the whole potential scan of the first cycle. The electrochemical behaviour of **Br5PhPy** has a 1st chemically reversible oxidation at $E_{1/2}$ +1.09V vs. SCE, 70mV more positive than **Tol4NPyr** due to the electron-withdrawing effect of the -Br substituent. At more positive potential, with E_p

+1.84V vs. SCE, **Br5PhPy** has also a multi-electronic oxidation. Similarly to **Tol4NPyr**, it is composed of at least two closely spaced redox waves. In contrast to **Tol4NPyr** (3.3 electrons), the number of exchanged electrons for **Br5PhPy** was estimated from the peak current to be about 4.2 electrons. Moreover, **Br5PhPy** did not exhibit any new redox process after the irreversible oxidation.
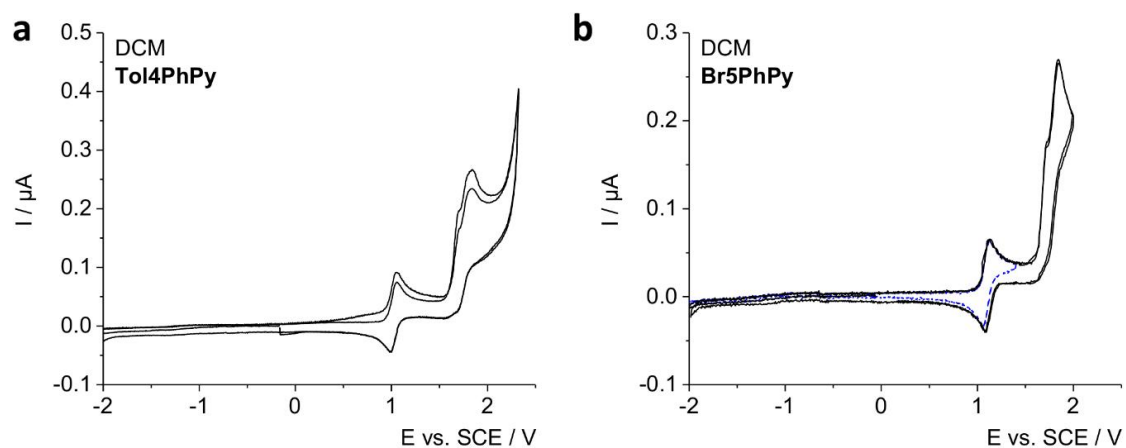
*Figure 2.20 CVs in DCM/Bu₄NPF₆ (80 mM) of (**a**) 1-tolyl-2,3,4,5-tetraphenylpyrrole (**Tol4PhPy**) 0.67 mM and (**b**) 1-(p-bromophenyl)-2,3,4,5-tetraphenylpyrrole (**Br5PhPy**), 0.72 mM. Working electrode Pt disk diameter 125μm, SCE as reference electrode, measured at 1 V/s and 298 K.*

2.5.2 Conclusion

A product is generated by the irreversible chemical reaction following the 2nd multi-electronic reaction of the substituted pentaphenylpyrroles, but there is no indication that the produced species is the fully closed pentabenzoazacorannulene. Even at higher scan rate (5V/s), we did not observe the redox processes related to the pentabenzoazacorannulene. A plausible hypothesis is that only a partial closure of the phenyl ring occurred. Assuming that 2e$^-$ and 2H$^+$ are involved for each new C-C bond, from the number of exchanged electrons, we can hypothesise that only two new bonds are formed. Further investigations and analysis are required to support this hypothesis and understand the nature of the product that is generated by the oxidation of pentaphenyl-pyrroles. Moreover, the strain related to the closure of all the phenyl rings, which would bring to a bowl (curved) structure, could hinder the complete conversion to pentabenzoazacorannulene resulting in only a partial closure.

2.6 References

1.   Nestoros, E. & Stuparu, M. C. Corannulene: a molecular bowl of carbon with multifaceted properties and diverse applications. *Chemical Communications* **54**, 6503–6519 (2018).

2.   Amaya, T. & Hirao, T. A molecular bowl sumanene. *Chemical Communications* **47**, 10524–10535 (2011).

3.   Shen, Y. & Chen, C.-F. Helicenes: Synthesis and Applications. *Chem Rev* **112**, 1463–1535 (2012).

4.   Stępień, M., Gońka, E., Żyła, M. & Sprutta, N. Heterocyclic Nanographenes and Other Polycyclic Heteroaromatic Compounds: Synthetic Routes, Properties, and Applications. *Chem Rev* **117**, 3479–3716 (2017).

5.   Yi, H. *et al.* Recent Advances in Radical C-H Activation/Radical Cross-Coupling. *Chem Rev* **117**, 9016–9085 (2017).

6.   Ripani, L., Bombonato, E., Paolucci, F. & Marcaccio, M. Electron transfer in polyaromatic hydrocarbons and molecular carbon nanostructures. *Curr Opin Electrochem* **35**, 101065 (2022).

7.   Röckl, J. L., Pollok, D., Franke, R. & Waldvogel, S. R. A Decade of Electrochemical Dehydrogenative C,C-Coupling of Aryls. *Acc Chem Res* **53**, 45–61 (2020).

8.   Wang, Y., Zhao, R. & Ackermann, L. Electrochemical Syntheses of Polycyclic Aromatic Hydrocarbons (PAHs). *Advanced Materials* 2300760 (2023) doi:10.1002/adma.202300760.

9.   Wang, X. Y., Yao, X. & Müllen, K. Polycyclic aromatic hydrocarbons in the graphene era. *Sci China Chem* **62**, 1099–1144 (2019).

10.   Hao, Q. *et al.* Electrochemical Polymerization and Properties of Poly(triphenylene), an Excellent Blue-Green-Light Emitter. *The Journal of Physical Chemistry C* **114**, 9608–9617 (2010).

11.   Bachman, J. C. *et al.* Electrochemical polymerization of pyrene derivatives on functionalized carbon nanotubes for pseudocapacitive electrodes. *Nat Commun* **6**, 3–4 (2015).

12.   Bruno, C. *et al.* Wavy graphene sheets from electrochemical sewing of corannulene. *Chem Sci* **12**, 8048–8057 (2021).

13.   Waltman, R. J. & Bargon, J. Electrically conducting polymers: A review of the electropolymerization reaction, of the effects of chemical structure on polymer film properties, and of applications towards technology. *Can J Chem* **64**, 76–95 (1986).

14.   Heinze, J., Frontana-Uribe, B. A. & Ludwigs, S. Electrochemistry of conducting polymers-persistent models and new concepts. *Chem Rev* **110**, 4724–4771 (2010).

15.   Xu, X. *et al.* Synthesis and Characterizations of 5,5′-Bibenzo[rst]pentaphene with Axial Chirality and Symmetry-Breaking Charge Transfer. *Advanced Science* **9**, 2200004 (2022).

16. Waltman, R. J., Diaz, A. F. & Bargon, J. The Electrochemical Oxidation and Polymerization of Polycyclic Hydrocarbons. *J Electrochem Soc* **132**, 631–634 (1985).

17. *Organic Electrochemistry*. (CRC Press, 2000). doi:10.1201/9781420029659.

18. Grecchi, S. *et al.* Widening the Scope of "Inherently Chiral" Electrodes: Enantiodiscrimination of Chiral Electroactive Probes with Planar Stereogenicity. *ChemElectroChem* **7**, 3429–3438 (2020).

19. Vacek, J., Zadny, J., Storch, J. & Hrbac, J. Chiral Electrochemistry: Anodic Deposition of Enantiopure Helical Molecules. *Chempluschem* **85**, 1954–1958 (2020).

20. Qi, H. *et al.* Electrochemistry and electrogenerated chemiluminescence of π-stacked poly(fluorenemethylene) oligomers. multiple, interacting electron transfers. *J Am Chem Soc* **134**, 16265–16274 (2012).

21. Hapiot, P., Kispert, L. D., Konovalov, V. V & Savéant, J.-M. Single Two-Electron Transfers vs Successive One-Electron Transfers in Polyconjugated Systems Illustrated by the Electrochemical Oxidation and Reduction of Carotenoids. (2001) doi:10.1021/ja0106063.

22. Amaya, T. & Hirao, T. Chemistry of sumanene. *Chemical Record* **15**, 310–321 (2015).

23. Zanello, P. *et al.* The electrochemical inspection of the redox activity of sumanene and its concave CpFe complex. *Dalton Transactions* 9192–9197 (2009) doi:10.1039/B910711H.

24. Li, X., Kang, F. & Inagaki, M. Buckybowls: Corannulene and Its Derivatives. *Small* **12**, 3206–3223 (2016).

25. Xu, Q., Petrukhina, M. A. & Rogachev, A. Yu. Stepwise deprotonation of sumanene: electronic structures, energetics and aromaticity alterations. *Physical Chemistry Chemical Physics* **19**, 21575–21583 (2017).

26. Solà, M. Forty years of Clar's aromatic π-sextet rule. *Front Chem* **1**, 4–11 (2013).

27. Hao, Q. *et al.* Electrochemical polymerization and properties of poly(triphenylene), an excellent blue-green-light emitter. *Journal of Physical Chemistry C* **114**, 9608–9617 (2010).

28. Bruno, C. *et al.* Electrochemical and theoretical investigation of corannulene reduction processes. *Journal of Physical Chemistry B* **113**, 1954–1962 (2009).

29. Koper, C., Jenneskens, L. W. & Sarobe, M. Externally-fused cyclopenta moieties in non-alternant CP-PAHs act as peri-substituents. *Tetrahedron Lett* **43**, 3833–3836 (2002).

30. Koper, C., Sarobe, M. & Jenneskens, L. W. Redox properties of non-alternant cyclopenta-fused polycyclic aromatic hydrocarbons: The effect of peripheral pentagon annelationy. doi:10.1039/b312234d.

31. Savéant, J.-M. *Elements of Molecular and Biomolecular Electrochemistry*. (John Wiley & Sons, Inc., 2006). doi:10.1002/0471758078.

32.   Shenhar, R. *et al.* From bifluorenylidene dianion to dibenzo[g,p]chrysene dianion: sensitivity of anisotropy changes to bonding structure. *Journal of the Chemical Society, Perkin Transactions 2* 449–454 (2002) doi:10.1039/b110315f.

Chapter 3

Electrochemical deposition of hexabenzocoronene for organic electrochemical transistor

In collaboration with

Prof. J. Zaumseil and Dr. E. Fresta (Heidelberg University)

3.1 Introduction

Hexa-peri-hexabenzocoronene

Since the development of graphene materials, polycyclic aromatic hydrocarbon (PAH) chemistry has attracted enormous interest in the organic and material science fields, from a new synthetic approach for the synthesis of extended π-conjugated molecules to functional materials with broad applications, ranging from optoelectronic to organic electronic.[1] PAHs can be considered as molecular subunits of graphene. However, differently from graphene, owing to their molecular nature, PAH-based materials are semiconductors with non-zero band gap and size-dependent optical and electronic properties. Traditional π-extended PAHs preparation requires at least two synthetic steps: first, the formation of soluble precursors with the desired functional groups, and second, ring closure (planarization process) to generate the fused PAHs. The Scholl reaction is by far the most used synthetic method for the ring closure step, it is an acid-catalysed oxidative condensation of aryl groups which allows the formation of many sp² C−C bonds between the unfunctionalized aryl moieties of the polyphenylene precursors. Although the Scholl reaction mechanism is still not fully understood, it is reported to proceed via a radical cation pathway or an arenium cation pathway (Scheme 3.1).
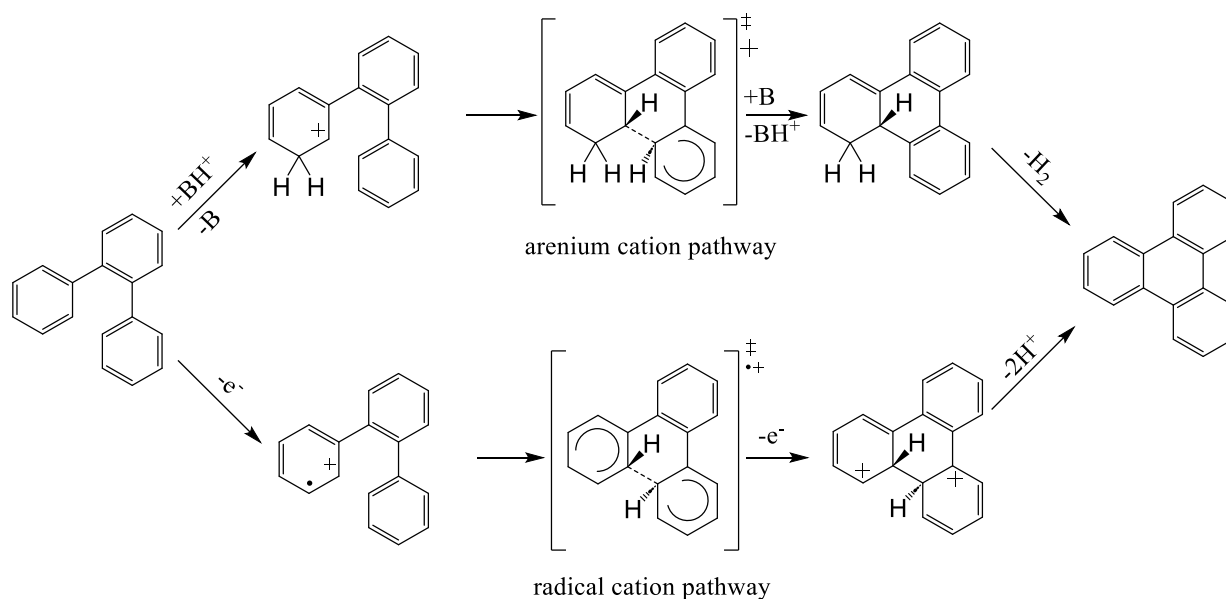
Scheme 3.1 Arenium cation and radical cation mechanisms for the cyclodehydrogenation of o-terphenyl to triphenylene Adapted with permission from ref. [2]. *Copyright © 2006, American Chemical Society*

In the radical cation pathway, R$^{\bullet+}$ acts as an electrophile, reacting with an electron-rich position of the adjacent aromatic ring forming a new C-C bond, followed by a further oxidation step, and finally by a deprotonation step to restore the aromaticity. In the arenium cation pathway, the initial step is the protonation of an aryl group by an acid (BH$^+$), leading to an electrophilic cation which reacts with a nucleophilic position of a nearest aromatic ring, forming a new C-C bond. The new condensed arenium cation is then deprotonated by the conjugated base (B) and loses H$_2$ to restore the aromaticity of the system.[3]

Hexa-peri-hexabenzocoronene (**HBC**) is an all-benzenoid PAHs with 7 Clar's sextets and has been successfully synthesised from hexaphenylbenzene by oxidative cyclodehydrogenation using chemical oxidisers such as FeCl$_3$ or 2,3-dichloro-5,6-dicyano-1,4-benzoquinone (**DDQ**) (Scheme 3.2).[3–5]
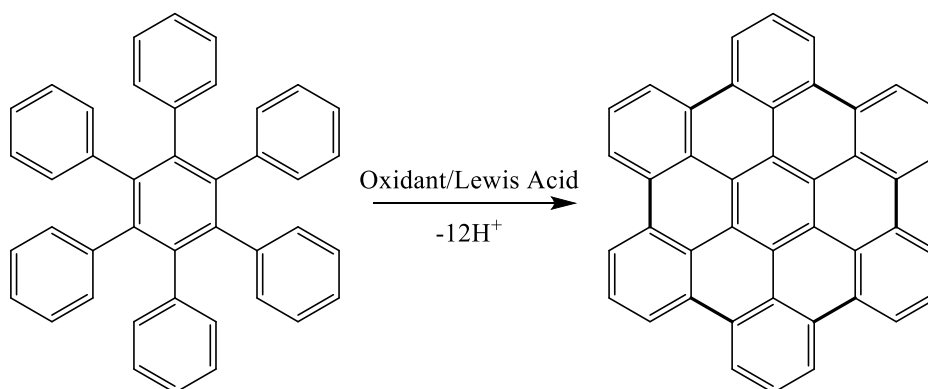
*Scheme 3.2 Chemical synthesis of hexabenzocoronene (**HBC**) from hexaphenylbenzene*

HBC and larger planar PAHs show poor solubility in most common organic solvents but, by functionalising the initial polyphenylene precursor with alkyl groups, it is possible to process substituted **HBC** by solution methods. However, groups such as alkyl groups can affect the crystal morphology and the π–π interaction between **HBC** units, thus ultimately influencing the electrical properties of **HBC** thin films. Unsubstituted **HBC** can be alternatively deposited by vacuum deposition at high temperatures leading to **HBC** thin films.[6] The single-crystal X-ray structure of unsubstituted **HBC** showed strong π–π interactions and a flattened-out herringbone packing (γ motif) because of the high C/H ratio with an interplanar distance between the aromatic cores of 3.42 Å.[7] Solubilising groups such as long alkyl chains on the outer phenyl rings allowed the preparation of devices with substituted **HBC** films by solution deposition methods. Functionalized **HBC** remains planar and forms columnar structures, similarly to the unsubstituted **HBC**, but as a drawback resulted in an insulating columnar arrangement due to the segregation of the alkyl chains between the **HBC** columns. A problem of such morphology are defects in the columnar arrangement which can negatively affect the film charge carrier mobility along the stacking direction while the charge mobility perpendicular to the stacking direction is suppressed by the alkyl chains[8]. Owing the strong π–π interactions of **HBC**, that leads to a columnar structure, substituted **HBC** films has been found to have an high intrinsic charge carrier mobility up to 1.1 $cm^2V^{-1}s^{-1}$, which was measured by the pulse-radiolysis time-resolved microwave conductivity technique.[9] Owing to the semiconductive properties of **HBC**, interest in this discotic PAH has increased in the field of organic electronics (OFET and OLED). In the transistor field, particularly in OFETs applications, hole mobility (μ_h) of **HBC** has been observed to range from 10^{-6} to 10^{-2} $cm^2V^{-1}s^{-1}$. Due to **HBC** insolubility, thin films of unsubstituted **HBC** were obtained by vacuum deposition,

and a hole mobility of 3.3×10^{-2} cm^{2}V^{-1}s^{-1} was extracted by OFETs measurements. XRD measurements of the vacuum-deposited **HBC** thin film showed herringbone packing with the π-stacking direction parallel to the substrate ("edge-on"). In thin-film OFETs, charge transport is strongly influenced by the film morphology and crystallinity in addition to the local intermolecular interactions.[10] Aligned substituted **HBC** films have been reported to have the highest hole mobility, ranging from 10^{-2} cm^{2}V^{-1}s^{-1} for zone-cast **HBC-C$_{12}$**[9] to a maximum of 0.083 cm^{2}V^{-1}s^{-1} for brush-coated **HBC-1,3,5-Ph-C$_{12}$**.[11] In general, substituted **HBC** shows a strong anisotropy in the charge carrier mobility with a higher mobility in the **HBC** column direction and about two orders of magnitude higher mobility than that with unoriented films.[11] Nevertheless, for unsubstituted **HBC** the charge mobilities of unoriented films were higher than those of unoriented substituted **HBC** films because the intercolumn charge mobility of unsubstituted **HBC** has a lower barrier than the alkyl-substituted **HBC**. The alky-substituted **HBC** has assembled columns separated by the alkyl chains that act as insulated wires.[8]

Electrochemical cyclodehydrogenation

Scholl reactions require stoichiometric amounts of chemical oxidants and typically occur in the presence of acids. Alternatively, cyclodehydrogenation of a soluble polyphenylene precursor can be achieved by electrochemical methods. In recent years, organic electrochemistry has gained considerable interest as a greener alternative for the straightforward synthesis of PAHs via electro-oxidative coupling and/or cyclodehydrogenation reaction.[12–14] Electrochemical synthesis can be achieved by direct or indirect methods (Figure 3.1).[15–17] In the first case, by applying a suitable potential, the PAH precursor is directly oxidised at the electrode, the 1st step is the generation of radical cations, which then react as previously shown in the Scholl mechanism via the radical cation pathway. Differently from the direct method, the second strategy is based on the oxidation that occur by the use of a mediator, oxidized at the electrode or already present in its redox active form. Indirect methods use a redox mediator which must be stable in the oxidised/reduced state, and the homogeneous electron transfer must be kinetically and thermodynamically favourable. In one case, the 1st step is the activation by electrochemical oxidation of the redox mediator which then homogenously oxidises the PAHs precursor. Such an indirect method involves the use of catalytic amount of a redox-active mediator. In the second case, the redox mediator is already in its active form and does not require activation by electrochemical

oxidation, an example is **DDQ**. Stoichiometric or excess amounts of **DDQ** have already been used in the traditional Scholl reaction for the synthesis by oxidative cyclodehydrogenation of **HBC**. However, in electrochemically mediated cyclodehydrogenation with **DDQ**, the reaction occurs as soon as **DDQ** is added to the PAH precursor, but the reduced **DDQH₂** can be regenerated by electrochemical oxidation at the electrode requiring just catalytic amount of **DDQ**.
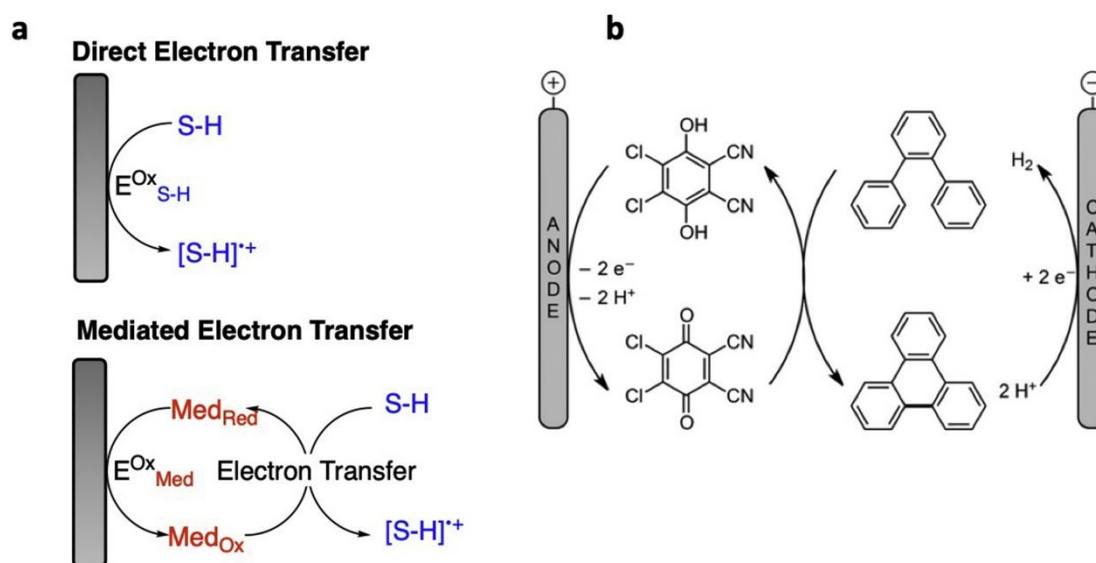
*Figure 3.1 Electrochemical direct (**a**) and mediated (**b**) redox and catalytic oxidation of PAH precursors (SH). Figure adapted from ref.[15] with permission from Elsevier 2022 and adapted from [18] with permission from the American Chemical Society.*

The electrochemical cyclodehydrogenation of hexaphenylbenzene to hexabenzocoronene has been studied in our group using a Pt and ITO electrodes[19] and reported by Ma et al.[20] under similar conditions. It was reported that the electrochemical oxidation of hexaphenylbenzene via the electrochemically induced cyclodehydrogenation induces the complete closure of the six phenyl rings with the formation of six new sp^2-sp^2 C-C bonds, leading to the planar hexabenzocoronene (**HBC**). The complete closure of hexaphenylbenzene to **HBC** via electrochemical synthesis was confirmed by MALDI mass spectroscopy, Raman spectroscopy, and IR spectroscopy on an ITO electrode. Similarly, electrochemical intramolecular cyclodehydrogenation has been reported for o-terphenyl to triphenylene by direct oxidation[19] or as reported by Röse et al. catalysed by **DDQ** which was electrochemically regenerated at the electrode.[18] Electrochemical catalysed cyclodehydrogenation with **DDQ** has also been

successfully achieved for **HBC** synthesis.[18] Recently, Ma et al. also reported the electrochemical synthesis of PAHs that are more extended than **HBC**[21,22] which led to the self-assembly of PAHs to form nanofibres with a defined molecular alignment over the electrode surface. The reactivity of radical cations can also occur intermolecularly by oxidative coupling to form dimers, and cyclodehydrogenation (intramolecular) of the dimers has been observed to occur if two reactive positions are in close proximity. Bruno et al. reported the oligomerisation and cyclodehydrogenation of corannulene units via direct electrochemical oxidation.[23] Triphenylene has also been reported to oligomerise and by cyclodehydrogenation to form more π-conjugated structures.[24]

Organic electrochemical transistor

A transistor is a device made of a semiconductor, a dielectric and metal electrodes, which allows the control of charge flow in a solid-state device. Organic semiconductive materials have attracted interest in the transistor field because of their lower cost, flexibility, tunability of the electronic properties and ease of fabrication compared to inorganic semiconductors. Organic field-effect transistors (OFETs) are composed of π-conjugated molecules or conductive polymers. Their working principle is based on field-effect doping upon application of a suitable voltage between the gate electrode and the semiconducting material, when they are separated by a dielectric material. This gate voltage produces a strong electric field that induces doping near the semiconductor surface. Depending on the major charge carrier, we can define the organic material as an *n-type* semiconductor, where electrons are the major carriers, or *p-type*, where holes are the major charge carriers. An organic electrochemical transistor (OECT) is also made of an organic semiconductor, metal electrodes, and, unlike OFETs, an electrolyte that acts as the gating medium. The semiconductor and the gate electrode are immersed in the electrolyte. An OECT is based on the electrochemical doping of an organic semiconductor with ions from the electrolyte that are injected inside the organic film, influencing the doping state and conductivity. The OECT operation relies on the mixed (ionic and electronic charge) conduction properties of the organic material in the channel, which is controlled by the gate voltage (V_G). A current can flow from the source to the drain electrode and the current magnitude is controlled by the drain voltage (V_D). The drain current is proportional to the doping level (quantity of mobile electrons or holes) in the channel. A typical structure of an OECT is shown in Figure 3.2.
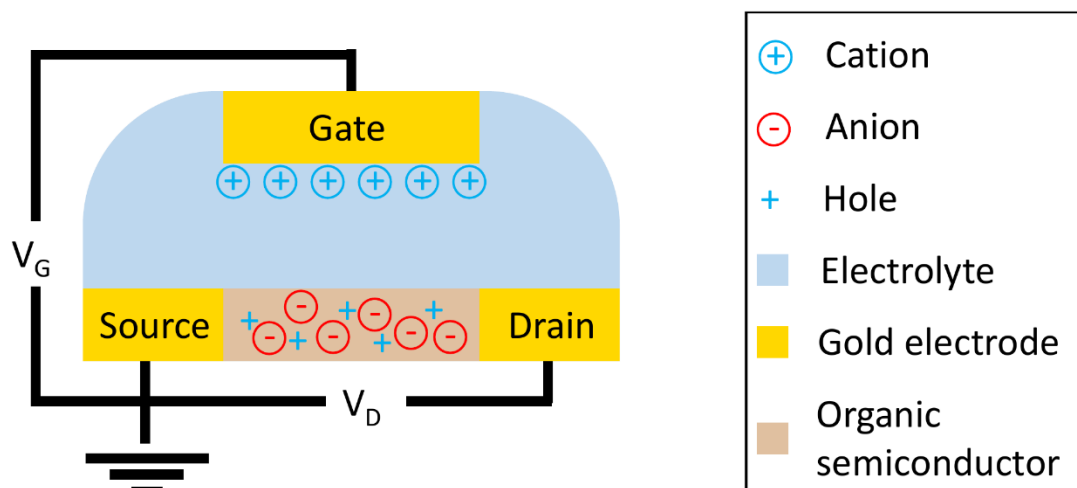
Figure 3.2 Sketch of an organic electrochemical transistor with a doped film (V_G <0) for a p-type organic semiconductor in accumulation mode.

An important feature that differentiates OECT from OFETs or electrolyte-gated field-effect transistors is that doping occurs over the entire volume of the channel. Theoretically, ions can penetrate the entire volume of the organic film; therefore, the channel capacitance depends linearly on the width, length, and thickness of the organic film. Depending on the organic material, OECTs can work in two distinct modes: in depletion mode, such as PEDOT:PSS, where a drain current can flow without a gate voltage. When a suitable gate voltage is applied, ions are injected inside the channel, compensating the already present counterions (compensating doping), the film is de-doped and charge injection does not occur anymore, decreasing the number of charge carriers. Alternatively, in accumulation mode, the OECT results undoped in the absence of a gate voltage and the drain current does not flow. When a suitable potential is applied, polarons are formed (electrochemical doping) in the organic film and counterions are injected inside the film, resulting in a drain current. For p-type organic semiconductors in accumulation mode, the doping occurs when a negative gate voltage (V_G) is applied, oxidised states are generated in the organic film and anions migrate from the electrolyte to balance the charge in the channel, thus generating a capacitor element (C_H). The ionic and electronic circuits of a OECT are shown in Figure 3.3.
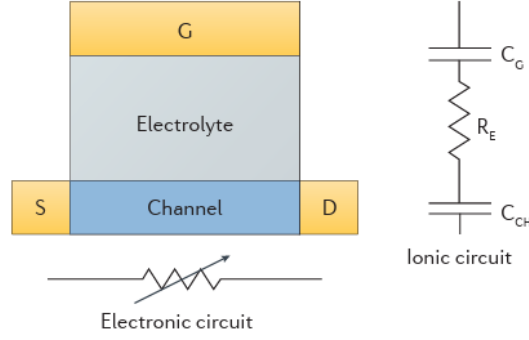
Figure 3.3 Sketch of the ionic and electronic circuits of a OECTs. The electronic circuit is modelled as a resistor with a resistance that varies with gate voltage. The ionic circuit is composed of two capacitors corresponding to the channel, C_{CH}, and gate, C_G, and a resistor corresponding to the electrolyte, R_E, in series. Figure taken with permission from ref.[25]. Copyright © 2018, Macmillan Publishers Limited.

If the anions are able to intercalate inside the film, the (volumetric) capacitance C* depends on the volume of the organic film. Otherwise, when the anions do not intercalate and form a double layer (electrolyte-gated transistor), the capacitance C depends only on the exposed surface of the organic film. For OECT, the product of charge mobility (µ) and volumetric capacitance (C*) is the figure of merit which characterizes different organic materials. The channel current (I_D) is monitored by applying a source–drain voltage (V_D) and source-gate voltage (V_G). The I_D is proportional to the number of mobile charge carriers and their mobility. The transconductance (g_m), i.e. the first derivative of the drain current on the gate voltage at fixed drain voltage, is another important parameter which quantifies the amplification of the transistor. Transistors have two regimes, depending on V_D: a linear regime where I_D scales linearly with the drain voltage and a saturation regime where a maximum I_D is achieved and becomes independent of V_D. For the saturation regime of OECT, I_D and g_m follow the equations reported below,[26,27] adapted by Bernards and Malliaras from a model for metal-oxide semiconductor field-effect transistor (MOSFET).

$$I_D^{Sat} = \frac{Wd}{2L} \times \mu_{OECT} C^* \times \left[\frac{(V_{Th} - V_G)^2}{V_{Th}} \right] \qquad (1)$$

$$g_m = \left(\frac{\partial I_D}{\partial V_G} \right)_{sat} = \frac{Wd}{L} \times \mu_{OECT} C^* \times |(V_G - V_{Th})| \qquad (2)$$

Where W and L are the width and length of the channel, respectively, d is the film thickness, μ_{OECT} is the charge carrier mobility, C* is the volumetric capacitance, V_G is the gate voltage, and V_{Th} is the threshold voltage. As can be seen from Equation (2), the transconductance is

geometry dependent. Therefore, a more accurate estimation of the product $\mu_{OECT} \times C^*$ should be performed by fitting the transconductance for multiple transistors with different channel geometries (width and length).

The electrical characterisation of an organic material for OECT can be analysed by performing transfer curves,[25,28] where the drain current (I_D) is recorded while V_D is fixed, and V_G is scanned at a fixed scan rate. From a transfer curve, we can extract the transconductance g_m from the derivate $\left(\frac{\partial I_D}{\partial V_G} \right)_{sat}$ at saturation regime, the ON-OFF ratio from I_D in the ON and OFF states, the threshold potential (V_{Th}) from the extrapolation of the $\sqrt{I_D}\ vs.\ V_G$, and ultimately, knowing the geometric parameters of the channel width (W), length (L) and film thickness (d), the product of charge mobility and volumetric capacitance (μC^*). High ON/OFF ratios are essential for biosensor response, as it improves the signal-to-noise (SNR) ratio of the device. The output curves show the evolution of I_D, probed as a function of V_D, for various V_G values. The pinch-off voltage, i.e. the voltage of the linear-to-saturation regime transition, can be extrapolated by the output curve.

The state of the art of OECT materials are semiconductive polymers of the polythiophene family functionalized with different groups (Figure 3.4 and Table 3.1). The most studied is PEDOT:PSS, a polymer mixture of monomer and ionomer poly(3,4-ethylenedioxythiophene) and poly(styrene sulfonate), which shows a μC^* of 47 ± 6 $Fcm^{-1}V^{-1}s^{-1}$ and has been the top performing material in the OECT field for a long time. However, because of the sulfonate groups, PEDOT:PSS operates in depletion mode. The PEDOT:PSS performance as OECT material were surpassed by a glycolated bithiophene-thienothiophene polymer, p(g2T-TT),[29] which operates in accumulation mode with a hole mobility close to that of PEDOT:PSS but almost five times higher volumetric capacitance (C^*), which translates to a product μC^* of 261 ± 6 $Fcm^{-1}V^{-1}s^{-1}$. However, more recently a crystalline PEDOT:PSS surpassed the glycolated p(g2T-TT) μC^* of almost 2 times.[30,31]

Nowadays PEDOT:PSS is the most widely used conducting polymer for OECT, mostly due to its high electronic and ionic conductivity, long-term stability, processability in H_2O and biocompatibility, which makes PEDOT:PSS suitable for bioelectronic and implanted OECT applications. Conducting polymer are highly versatile since they can be blended and mixed with other components,[32] for example polyethylene glycol or antibacterial agents, to produce

composites with mixed electrical-ionic conductivity and functional properties, such as stretchability,[33,34] self-healing,[35,36] and antibacterial properties.[37,38]

New OECT materials with improved performance should be tailored to enhance hole mobility with increased C* to enhance the transconductance, while improving or adding functional properties depending on the OECT application, e.g. biosensor, bioelectronic, neuromorphic device, memory storage and many other applications in different physical and medical fields.
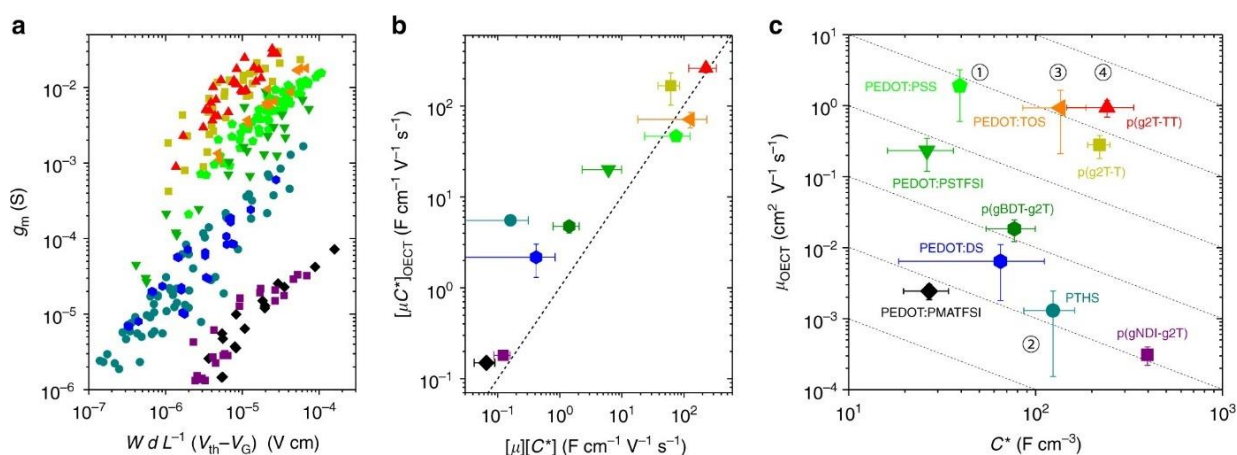

Figure 3.4 (a) Transconductance (gm) of OECTs of different materials as a function of channel geometries in saturation regime. (b) the product of the charge mobility and the volumetric capacitance, [μC]$_{OECT}$, as a function of the product of μ $_{OECT}$ and C* determined independently, [μ][C*]. (c) μ$_{OECT}$ vs. C* map of ten reported materials. Figure reprinted with permission from ref. [39] licensed under a Creative Commons Attribution 4.0 International License. Copyright Springer Nature 2017.*

Table 3.1 State of the art of organic electrochemical transistor materials

Material/Formulation	C* (Fcm^{-3})	μOECT (cm^{2}V^{-1}s^{-1})	[μC]OECT (Fcm^{-1}V^{-1}s^{-1})
p(g2T-TT)	241 ± 94	0.94 ± 0.25	261 ± 29
p(g2T-T)	220 ± 30	0.28 ± 0.10	167 ± 65
PEDOT:TOS [VPP]	136 ± 50	0.93 ± 0.72	72 ± 14
PEDOT:PSS+ EG	39 ± 3	1.9 ± 1.3	47 ± 6
PEDOT:PSTFSILi100	26 ± 10	0.23 ± 0.11	20.0 ± 1.6
PTHS + EG	124 ± 38	0.0013 ± 0.0011	5.5 ± 0.1
p(gBDT-g2T)	77 ± 23	0.018 ± 0.006	4.8 ± 0.7
PEDOT:DS + EG	65 ± 46	0.0064 ± 0.0046	2.2 ± 0.9
p(gNDl-g2T)	397	0.00031 ± 0.00009	0.18 ± 0.01
PEDOT:PMATFSILi80	27 ± 7	0.0024 ± 0.0006	0.15 ± 0.01

Notes: p(g2T-T), p(g2T-TT) and p(gBDT-g2T) are glycolated thiophene, thiophene-thienothiophene and BDT-thiophene based polymers, respectively. TOS, PSS, PSTFSILi100 and PMATFSILi80, and DS, are various molecular, polymeric, and biological anionic dopants complexed with PEDOT, namely tosylate, poly(styrene sulfonate), (trifluoromethylsulfonyl)sulfonylimide (styrenic or methacrylic backbone, with a molar mass 100 or 80 kDa and Li+ as the counter ion), and dextran sulfate, respectively. p(gNDI-g2T) is a glycolated naphthalene diimide based polymer, which is a n-type semiconductor. PTHS is a thiophene-based conjugated

3.2 Outlook

In this chapter, we investigate the electrochemical cyclodehydrogenation of hexaphenylbenzene to hexa-peri-hexabenzocoronene (**HBC**) and the deposition of self-assembled **HBC** on interdigitated gold electrodes with a channel length of 5 μm. The electro synthesised and deposited (**eChem.**) **HBC** film was characterised using microscopy (optical and AFM) and Raman spectroscopy. Finally, the **eChem HBC** film was studied as a p-type semiconducting material in organic electrochemical transistors in pure deionised H_2O and ionic liquids during my stay at *Heidelberg University in the group of Prof. Jana Zaumseil and with Dr. Elisa Fresta*. To obtain a benchmark for a comparison of **eChem. HBC**, we prepared **HBC** films using different solution-processing methods, i.e. drop casting, aerosol jet printing, and Langmuir-Blodgett, with a dispersion of commercially available **HBC**. The solution-processed **HBC** films were characterised by microscopy and Raman spectroscopy and tested as organic electrochemical transistors in ionic liquid.

In this study, we show that the electrochemical approach for the synthesis and self-assembly of **HBC** from a soluble precursor allows the preparation of **HBC** films for transistor applications in one synthetic step.

Additional PAHs were electrochemically polymerized, namely poly-pyrene and poly-fluorene, and tested as electrochemical transistor, although with inferior performance than the **HBC** films. In the last part of the chapter, we report the characterisation of the poly-pyrene and fluorene films in ionic liquid.

Result and discussion:

3.3 Electrochemical deposition

The electrochemical properties of hexaphenylbenzene were investigated by cyclic voltammetry in DCM/Bu$_4$NPF$_6$, as shown in Figure 3.5.
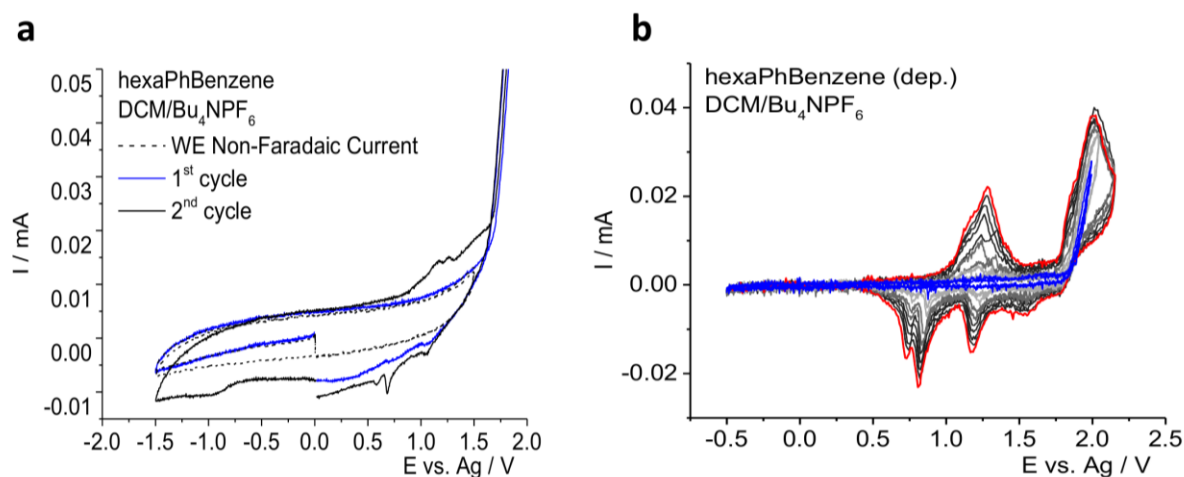

*Figure 3.5 Cyclic voltammetry of (**a**) the first two cycles of hexaphenylbenzene 1.18 mM in DCM/Bu$_4$NPF$_6$ 80mM, measured at 1 V/s and 298 K, and (**b**) Cyclic voltammetry of electro-deposition via oxidation of hexaphenylbenzene 1.18 mM in DCM/Bu$_4$NPF$_6$ 80mM. The first two cycles are coloured in blue, followed by a grey scale from light to dark, and the last cycle is red. Measured at 0.4 V/s at 298K. with Au interdigitated electrode 1.8 mm x 5µm x 30 pairs (total surface 0.54 mm^2). The potentials are reported vs. Ag (quasi-reference electrode) which has been observed to be stable in DCM during the potential scan and for several experiments.*

The onset of hexaphenylbenzene oxidation occurred at +1.7V vs. Ag (QRE), with a completely chemically irreversible oxidation without a diffusion-limited peak current at a scan rate of 1 V/s. After the 1st oxidation, during the backward scan we observed an increase of the non-faradaic current compared to that before the hexaphenylbenzene oxidation (dashed line) and the appearance of new redox processes related to some electrogenerated products produced by the chemically irreversible oxidation. This evidence suggests an electrodeposition process of an organic film. The increase of the non-faradaic current could be caused by an increase of the electrochemically active surface area or by an increase in the double-layer capacitance. New peaks are observed in the voltammogram: two oxidations at +1.17 and +1.26V and, in the reverse scan three reductions at +1.04, +0.68 and +0.59V. These processes are related to the new electrogenerated species which accumulate on the electrode surface.

When hexaphenylbenzene was potentio-dynamically oxidised for several subsequent cycles, a clear film formation was observed. Figure 3.5b shows the electrodeposition of HBC on a new

interdigitated electrode. The increasing current in each cycle reflected the growth of the organic film. The CV changed slightly during the electrodeposition. The oxidation of hexaphenylbenzene remained chemically irreversible, but a diffusion-limited peak was observed at Ep +2.00V. A crossing in the back-scan was present in the first and second cycles of CV but disappeared after a few cycles. Furthermore, the onset of the oxidation decreased with the appearance of a new redox process before the hexaphenylbenzene oxidation. The two processes below 1.5V, related to two different redox states, merged and partially overlapped, with an onset oxidation of +1.03V vs. Ag (QRE). From the CV curve, we observed that the oxidation peak showed symmetrical anodic and cathodic waves with very close peak potentials at +1.2V vs. Ag (QRE), even though the reduction peak current and charge were lower than the oxidation peak. Such electrochemical behaviour is related to a surface-limited process of a redox-active thin film and, most likely, it is related to the doping and de-doping of the organic film. Two very sharp and peaked reduction processes are observed below 1V, which could be related to a different de-doping processes or the removal of PF_6^- anions from the film requires a potential lower than +1.2V. Similar to conducting polymers, we can also hypothesise that each intermediate during the electrochemical cyclodehydrogenation, owing to their more extended π-conjugation than hexaphenylbenzene, is easier to oxidise. During the electrochemical oxidation of hexaphenylbenzene they will be in their oxidised state and they will be reduced during the back scan of the CV.

HBC films were electrochemically synthetised and deposited on two Au 5 × 5 μm (30 pairs) interdigitated electrodes by short-circuiting (with a Cu foil) both the two interdigitated branches. The working electrode was changed under an Ar gas flow with positive pressure to avoid any eventual contamination by O_2 and H_2O from air. The CV curves of the hexaphenylbenzene oxidation did not change after the electrode was replaced with a new one.

Figure 3.6 shows an interesting feature of the CV for the 1st cycle of hexaphenylbenzene oxidation. A voltammetric loop (crossing) was observed in the reverse sweep when the potential was reversed after (about 200mV) the onset potential of hexaphenylbenzene oxidation.
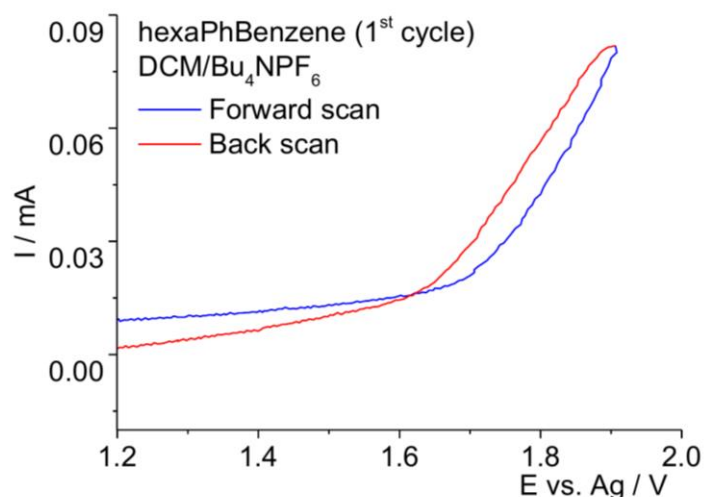
Figure 3.6 Cyclic voltammetry of the first cycles of hexaphenylbenzene oxidation, forward scan is blue and the back scan in red. Measured at 1 V/s and 298 K with Au interdigitated electrode 1.8 mm x 5µm x 30 pairs (total surface 0.54 mm². The potentials are reported vs. Ag (quasi-reference electrode) which has been observed to be stable in DCM during the potential scan and for several experiments.

Crossing in cyclic voltammetry for the electropolymerization of conductive polymers is often attributed to a nucleation step, which occurs only in the first cycles and with a freshly polished electrode, and to the three-dimensional growth of the polymer.[40–42] The observed loop in CV for the electropolymerization of the conductive polymer was initially attributed to the nucleation and growth steps because the observed behaviour was similar to the CV response for the electrodeposition of metal on a different substrate, where an overpotential is necessary for the nucleation and growth of the metal crystals[43]. However, Heinze et al. proposed a different explanation for the crossing event in the electropolymerization of chain-forming conductive polymers such as polythiophene and polypyrrole. Heinze's proposed mechanism is an autocatalytic oxidation of the monomer catalysed by the homogeneous comproportionation of the oxidised oligomer (Oligo^{n+}) with the neutral monomer (Scheme 3.3) which generates a loop in the CV[44,45]. The resulting reduced species (Oligo$^{(n-1)+}$) are re-oxidised at the electrode during the back-scan, thus resulting in an increased anodic current.
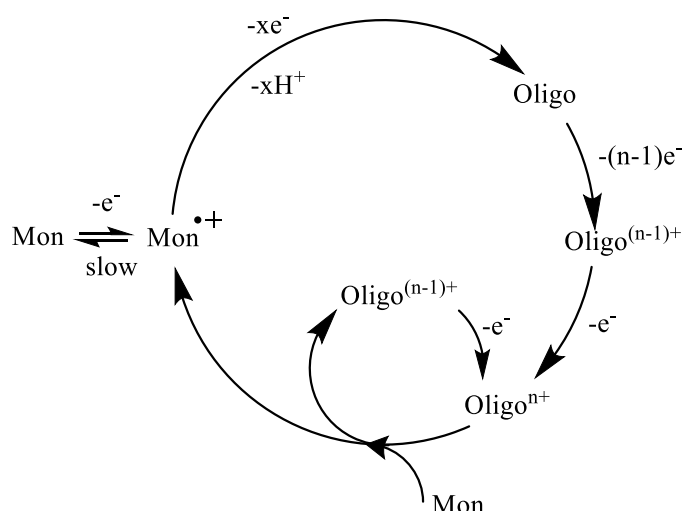
Scheme 3.3 Proposed comproportionation mechanism by Heinze et al. for the oligomerization of conductive polymers and the related loop in CV.

Following the Heinze model, two requisites are necessary. First, the redox potentials of the $Oligo^{n+}/Oligo^{(n-1)+}$ pair and that of the starting monomer $Mon/Mon^{\bullet+}$ must be close. Second, the heterogeneous rate constant of monomer oxidation must be sluggish, enabling the homogeneous oxidation of monomers by comproportionation to occur. Thermodynamically, the comproportionation reaction is unfavourable, because $E°(Mon/Mon^{\bullet+})$ is generally higher than $E°(Oligo^{n+}/Oligo^{(n-1)+})$, but since $Mon^{\bullet+}$ is rapidly consumed by dimerization and $Oligo^{(n-1)+}$ is re-oxidised, the equilibrium is constantly shifted towards the right side of the reaction.

$$Oligo^{n+} + Mon \rightleftarrows Oligo^{(n-1)+} + Mon^{\bullet+} \quad \text{Comproportionation reaction (1)}$$
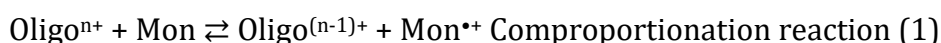
A third possible explanation for the loop event in CV is a slow follow-up reaction with an ECE mechanism, where the product of the follow-up reaction is easier to oxidise than the monomer, but the rate constant of the chemical reaction is sluggish.[46] The increased anodic current in the reverse sweep results from the oxidation of this product. In some cases, the deprotonation step after the dimerization reaction has been observed to be sluggish,[47] even though the driving force for the deprotonation of a charged dimer is the re-aromatization of the molecule. Because hexaphenylbenzene oxidation does not produce linear oligomers but instead an intramolecular cyclodehydrogenation reaction occurs, we hypothesise that this third explanation could better explain the hexaphenylbenzene oxidation mechanism.

3.4 Film Characterisation

The electrodeposited **HBC** films were characterised by optical microscopy in bright-field mode. The optical images of the two electrodes were similar. Figure 3.7 shows the optical images of the **HBC** film electro-deposited on an interdigitated electrode in bright-field mode at 20x and 100x magnifications.
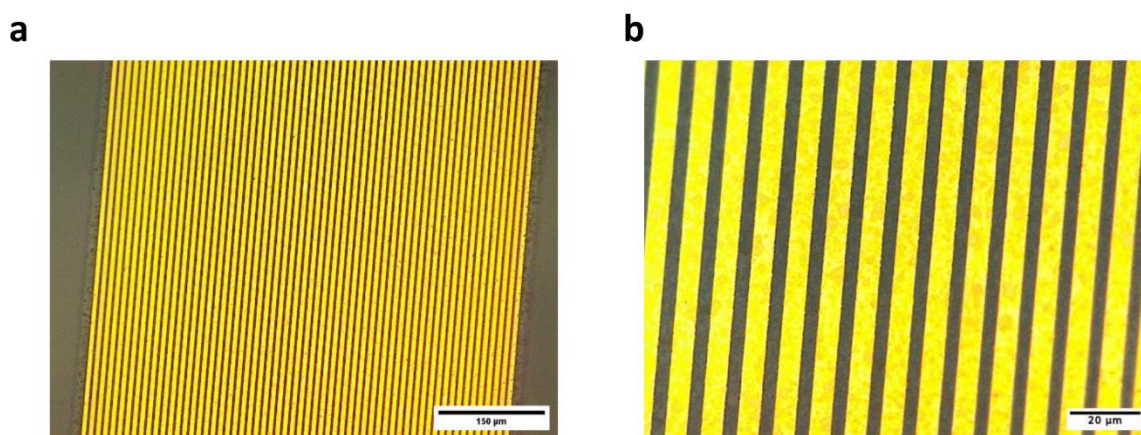
*Figure 3.7 Optical images in bright-field mode at (**a**) 20x magnification and (**b**) 100x magnification of the 1ˢᵗ electrochemical deposited **HBC** film on an interdigitated 5 μm channel length × 5 μm Au electrode, 30 pairs (59 channels) and 1.8 mm channel width.*

The electrodeposited **HBC** appeared to be homogeneously deposited over the entire electrode area; in particular, **HBC** appeared to be present inside the entire channel area (5 μm × 1.8 mm) between the two Au electrode branches. The electrodeposition extended to an average of 13 μm beyond the last gold electrode. At 100x magnification, an edge effect between the Au and glass was not observed, even if the Au electrode thickness is 150 nm higher than the glass substrate. Small darker spots are observed dispersed over the entire **HBC** film, although the reason behind these spots is still not completely clear, we hypothesise that these spots could be denser **HBC** areas.

The morphologies of the electrochemically deposited **HBC** films were characterised by AFM measurements. Figure 3.8 shows the AFM images and line profiles of the electrodeposited films.
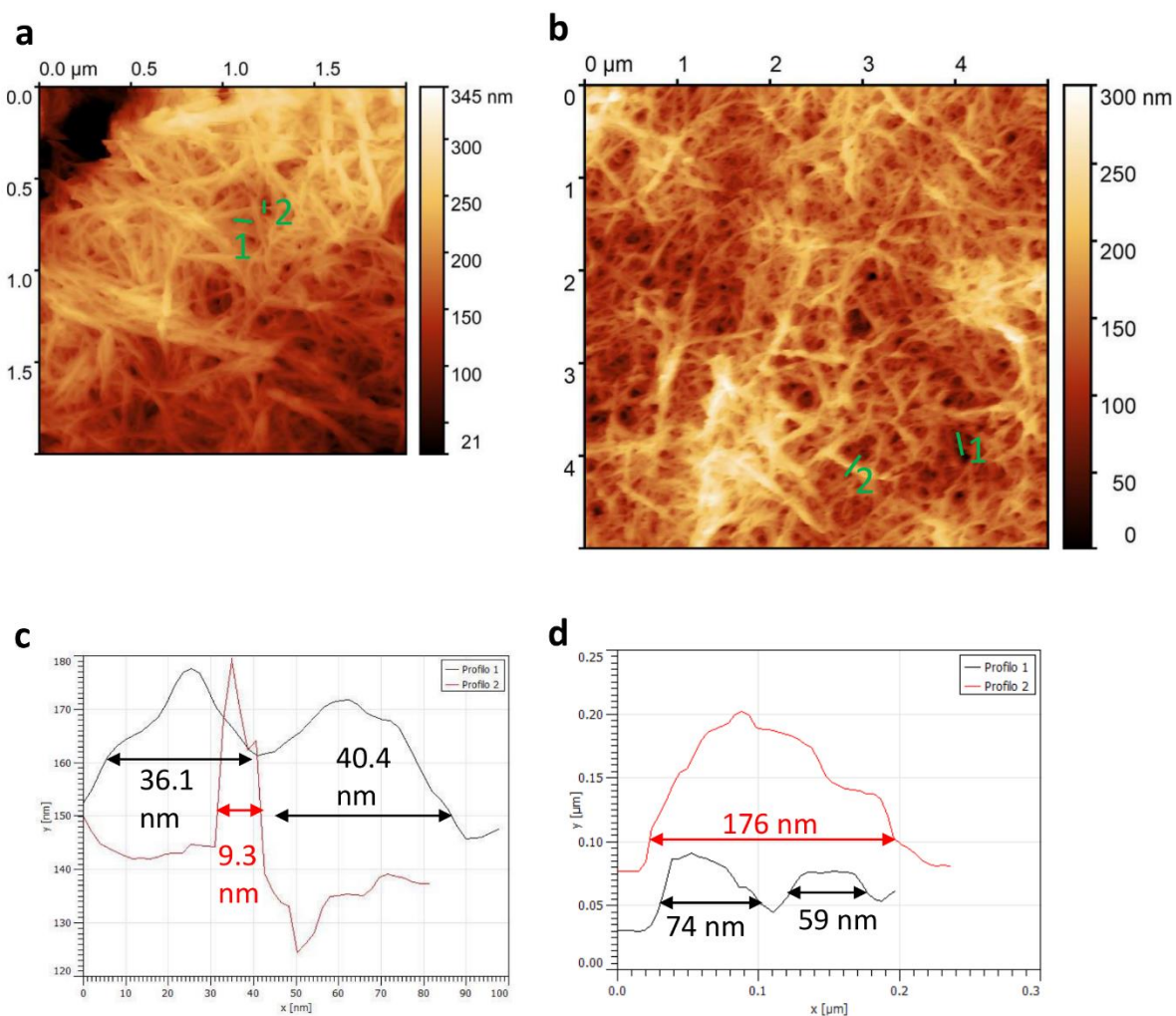
*Figure 3.8 AFM images inside the channel (**a**) of the 1st electrodeposited **HBC** film with 2 × 2 µm area and (**b**) of the 2nd electrodeposited **HBC** film with 5 × 5 µm area. Peak force amplitude 80 nm, scan rate 0.3 µm/s, T 298 K. (**c**) Selected profile lines of **HBC** fibres in the 1st **HBC** film and (**d**) profile lines of the 2nd **HBC** film.*

The electrochemically deposited **HBC** films show a randomly oriented highly intertwined nanofibre structure with fibre connections which extend throughout all the channel length (5µm). The nanofibres, in turn, resulted from the aggregation of rod-like smaller aggregates. A single fibre is composed of multiple rods, and depending on the number of rods aggregates the fibres have different widths and heights. Moreover, each rod aggregate was the product of multiple columnar crystals from the self-assembly of **HBC** units via π–π stacking. Electrogenerated **HBC** forms close-packed columns with an oblique packing between stacked **HBC** units with a herringbone packing. From HR-TEM measurements of **echem**. **HBC**,[19] a column width of 1.02 nm was observed from the diffraction pattern (Figure 3.9) and considering a calculated **HBC** length of 1.13 nm (from the XRD data of **HBC** single crystal[7]) we

73

can estimate an angle of 25°, calculated as $\alpha = \cos^{-1}\left(\frac{HBC\ length}{Column\ length}\right)$, which is smaller compared to the 48° respect to the (010) plane observed in **HBC** single crystal. We hypothesise that at least 9 **HBC** columnar crystals form a single rod-like aggregate for the smallest observed in Figure 3.8c profile 2. We expect even more **HBC** columnar crystals to be present in wider rods.
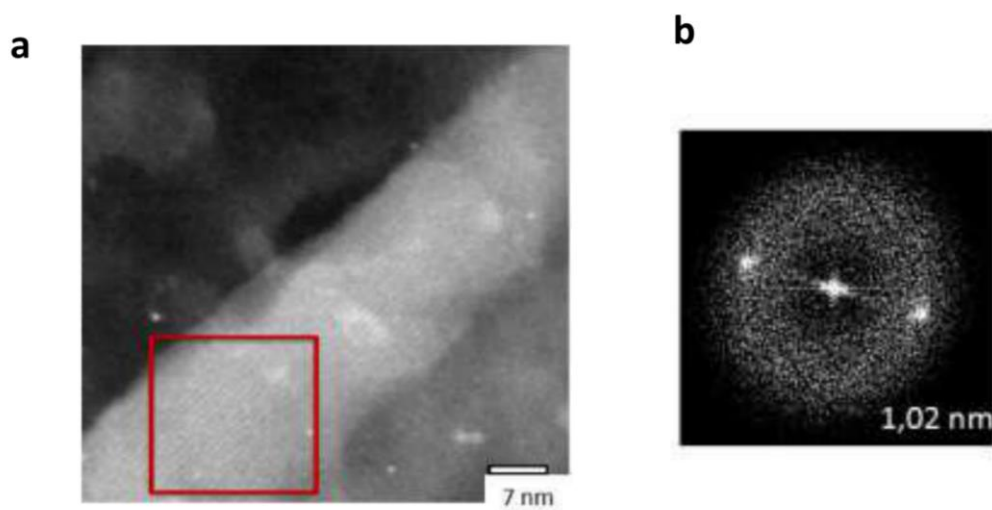
*Figure 3.9 (**a**) HR-TEM image of **echem. HBC** rod and (**b**) diffraction pattern from the red square box. Image taken from ref.* [19]

Microscopically, the electrochemically deposited **HBC** films were inhomogeneous, as there were zones with different aggregate densities, resulting in different film thicknesses. Comparing the two **HBC** films, we can observe that the density of the nanofibres was higher in the first electrodeposited **HBC** film. However, owing to the inhomogeneous nature of these films and the small scanned areas of the AFM images, further analysis is necessary to compare the fibre densities of the two films. An average film thickness was calculated by making a scratch on the **HBC** film on gold and measured by AFM, the resulting thickness is 116 nm. Nonetheless, we can expect that deviation from this average value is high due to the film inhomogeneity.

The electrochemically deposited **HBC** film was characterised by confocal Raman spectroscopy and compared to commercially available **HBC** deposited by drop-casting and aerosol jet printing (AJP) (see the following sections). Figure 3.10 shows the Raman spectra of the **HBC** films. All of them showed a strong fluorescence background with the 532 nm laser; therefore

background subtraction was applied to the data. The background curve was obtained by masking the Raman peaks and fitting the rest of the data with a 2nd order polynomial law, after which the fitted polynomial was subtracted from the raw data and the Raman peaks were normalised.
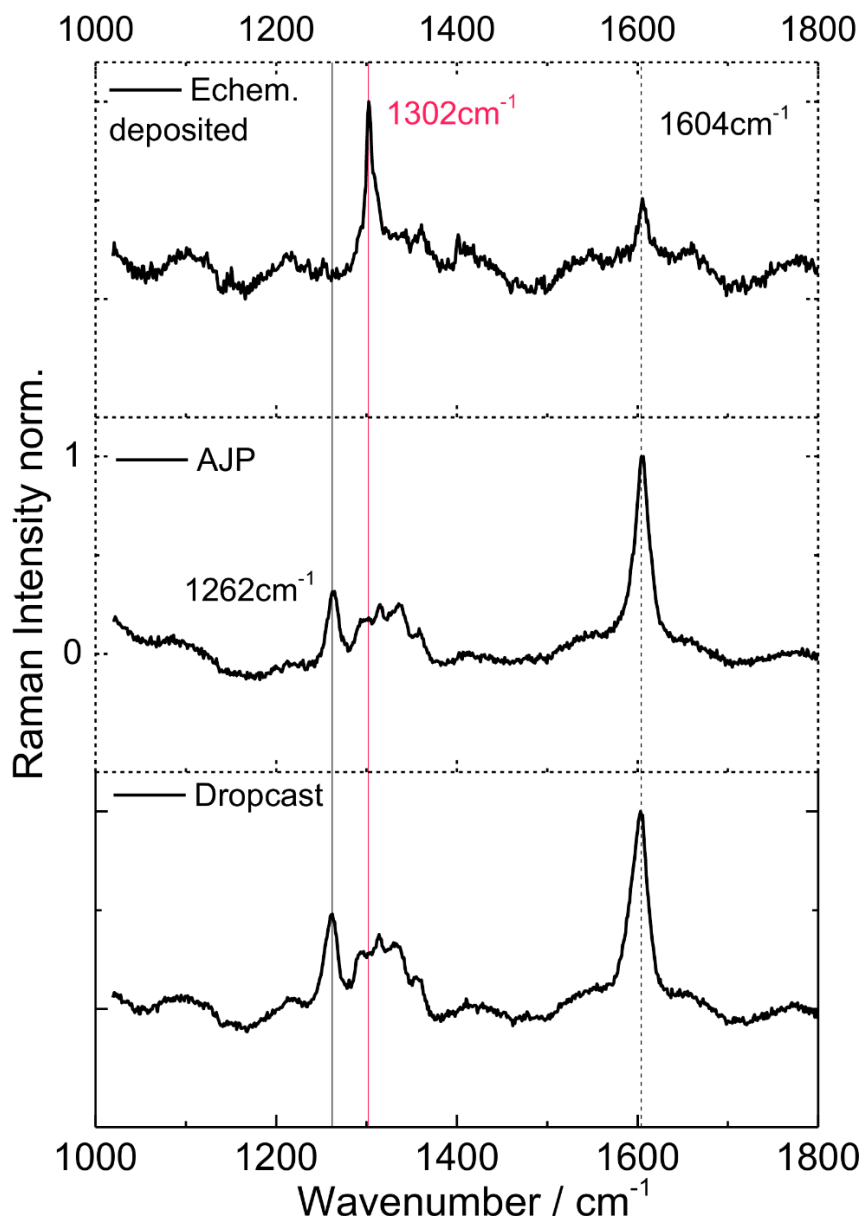
*Figure 3.10 Background-subtracted Raman spectra of (**top**) electrochemically deposited **HBC** film, (**centre**) aerosol jet-printed synthesised **HBC** film, and (**bottom**) drop-cast **HBC** film. Measured in confocal mode with 20x magnification focussing on the surface of the film with a 532 nm laser at 5 % power. Integration time 0.1 s for 10 pulses. For the electrochemically deposited **HBC** film, the spectrum was recorded at ten different spots and averaged. Selected wavenumbers have been highlighted with a black full line (1262 cm-1), red line (1302 cm-1) and dashed line (1604 cm-1)*

The electrochemically deposited **HBC** showed two well recognisable Raman peaks in the spectrum. The D band at 1302 cm^{-1} corresponds to the totally symmetric vibration (A$_{1g}$) and involves the in-phase ring breathing of all seven Clar rings coupled with the C-C shrinking of the bonds with the collective in-plane bending of the C-H bonds. The G band at 1604 cm^{-1} corresponds to the doubly degenerate vibration (E$_{1g}$) and involves C-C stretching mainly in the external part of the molecule coupled with collective in-plane C-H bending.[48–50] The D(1302 cm^{-1})/G (1604 cm^{-1}) ratio was 1.96. Further Raman peaks of the electrochemically deposited **HBC** could be hidden by the high noise.

The two solution-deposited films (drop-cast and AJP) with commercial **HBC** showed similar Raman spectra, suggesting that the two different deposition methods did not alter the **HBC** chemical structure. However, a significant difference was observed when compared with the Raman spectra of the electrochemically deposited **HBC**. In particular, in the D peak region, more peaks were observed, with the most intense D band at 1262 cm^{-1}, followed by four more peaks at 1297 cm^{-1}, 1315 cm^{-1}, 1336 cm^{-1} and 1358 cm^{-1}. The G band was observed at 1604 cm^{-1} like the electrochemically deposited **HBC**. The D(1262 cm^{-1})/G (1604 cm^{-1}) ratio was also very different from that of the **echem. HBC**, 0.31 and 0.48 for the AJP and drop-casted **HBC** films, respectively. Further studies are currently undergoing to explain the nature of the difference in the Raman spectra of the electrochemically deposited **HBC** and the synthesised (commercial) **HBC**. We do not think that the chemical nature of the two **HBC** is different, since the complete closure of the hexaphenylbenzene via the electrochemical cyclodehydrogenation was confirmed by MALDI-TOF mass spectroscopy on ITO.[19]

3.5 Solution processed HBC films

HBC films have been prepared using different solution-processing methods, namely drop-casting, aerosol jet printing, and Langmuir-Blodgett. Nonetheless, **HBC** is rather difficult to process using solution methods due to its very poor solubility in common organic solvents. Among the organic solvents, halogenated solvents and amides showed better dispersion capability toward **HBC**, leading to the lowest aggregation in solution.[51] In particular, we chose to use 1,2-dichlorobenzene (**DCB**) for aerosol jet printing, because of its higher **HBC** solubility and lower evaporation temperature (178-180 °C) among the reported halogenated solvents and 1,2,4-trichlorobenzene for the drop-casting method. Whereas for the Langmuir-Blodgett technique, THF was used due to its lower vapour pressure. The procedure for the ink

preparation is reported in the experimental section. Figure 3.11 shows the optical images (a,b,c) at 20x magnification, (d,e,f) at 100x of the solution-processed film, and (g,h) AFM images. Drop cast (left column), aerosol jet printing (central column), and Langmuir-Blodgett (right column).
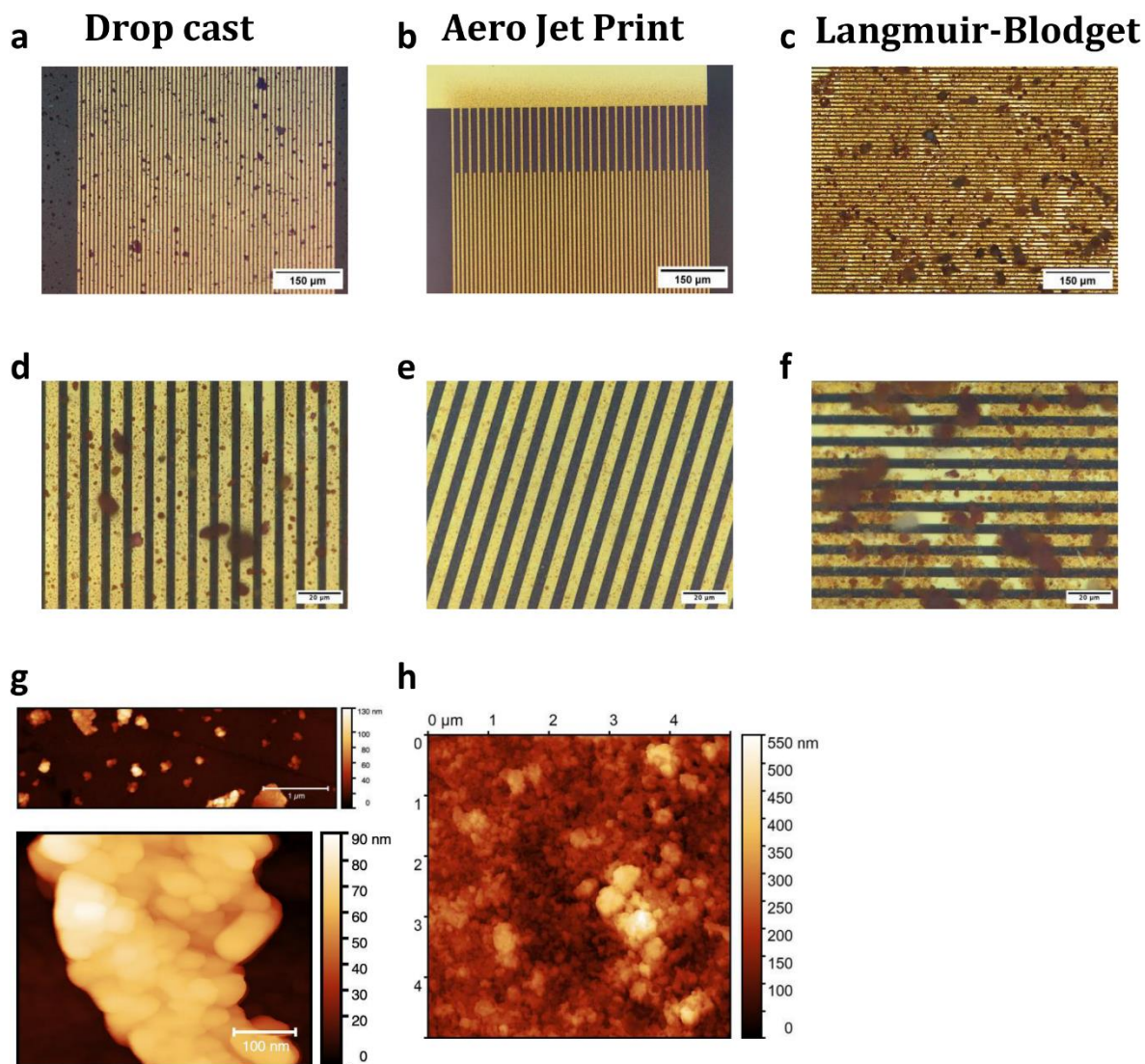
*Figure 3.11 Optical images in bright-field mode of **HBC** film (**a,d**) electrochemically deposited at 20x and 100x magnification, (**b,e**) aerosol jet printed at 20x and 100x magnification, and (**c,f**) Langmuir-Blodgett at 20x and 100x magnification. AFM images of (**g**) drop-cast **HBC** on glass on a low crystal density zone and (**h**) aerosol jet-printed **HBC** inside the channel.*

The optical images (a and d) of the drop-casted **HBC** film showed microsized crystals dispersed over the entire electrode surface, some of which were longer than 5 μm and connected both the source and drain electrodes. The film was not homogeneous and exhibited a large distribution of crystal sizes. Probably, some crystals were already present in the **HBC**

dispersion in 1,2,4-trichlorobenzene and acted as seeds during the solvent evaporation, increasing the crystal size during the **HBC** deposition. From the AFM image (6g) of the drop-cast **HBC** film for a region with low crystal density, we observed that nanosized aggregates were present on the glass substrate, but a monolayer of **HBC** was not present. These aggregates were composed of smaller **HBC** crystals of different sizes and shapes. A rod shape aggregate or fibres were not observed in the drop-casted **HBC** film, even though the solvent evaporation was relatively slow and could allow the self-assembly process to occur.

The aerosol jet printed **HBC** film showed a better coverage over the electrode area, **HBC** was successfully deposited over both source and drain electrodes and inside the channel area between the two electrodes. Smaller aggregates were observed as darker spots in the optical images. From the AFM image (h), we observed a completely covered electrode with thicker regions which corresponds to the darker spots observed in the optical image. However, a clear self-assembly of **HBC** into rod-like crystals or fibres was not observed. In fact, the aggregates had many different shapes and sizes, resulting in a very different film morphology compared to the electrochemically deposited and drop-cast films. This difference could be related to the very fast solvent evaporation during the printing process, resulting in the very rapid deposition of **HBC** which was not able to self-assemble or form crystals and resulted in an amorphous phase.

Lastly, the Langmuir-Blodgett **HBC** film showed the highest inhomogeneity among the **HBC** films, showing very large polycrystalline aggregates dispersed over the electrode and some film cracks that could have arisen during the H_2O evaporation or from a suboptimal film formation of the dispersed **HBC** in the initial step. In fact, unlike the usual Langmuir-Blodgett technique, in which the molecules are slowly compressed to form a homogeneous film,[52] we allowed **HBC** to freely diffuse over the H_2O surface while THF evaporated. Since **HBC** prefers non-polar interactions, it tends to interact with itself and forms a film which was not very homogeneous because of the aggregation phenomenon. AFM of the Langmuir-Blodgett deposited **HBC** film was not recorded because of the extreme inhomogeneity and roughness of the film with very large aggregates.

Spin coating and spray coating were also tested with **DCB** as a solvent, but they resulted in very poor film coverages, with small aggregates dispersed over the entire device surface. Moreover, no connection between the source and drain electrodes was achieved, making the spin-coated and spray-coated **HBC** films unsuitable for transistor applications.

3.6 Electrochemical transistor

The electrochemically (**eChem.**) deposited **HBC** films were tested as organic electrochemical transistors (OECT). The OECT was gated with deionised H_2O on top of the substrate and a reference electrode (Ag/AgCl) was immersed close to the gold-side gate to independently measure the applied gate voltage (V_G). Before the measurements, the **HBC** films were conditioned with 5 cycles of transfer curves. However, during the cycling we noticed a decrease in the drain current and a shift of the curve during the conditioning. Currently, it is not clear if the **HBC** film is not very stable in H_2O or if other effects occur. Figure 3.12 shows the transfer curves in deionised H_2O of the two **eChem.** deposited **HBC** films and the transconductance (g_m) normalized by the channel length (5 μm) and width (1.8 mm x 59 channels).
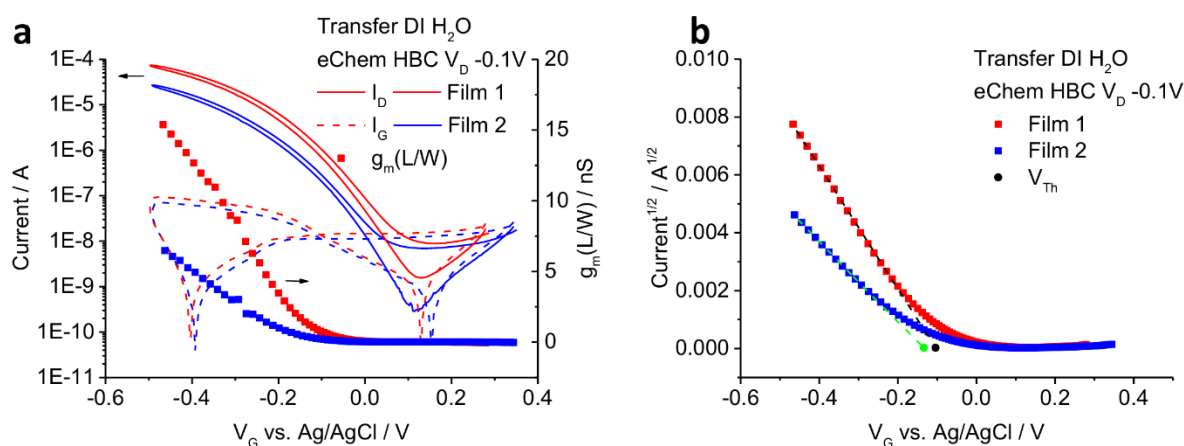
*Figure 3.12 (**a**) Transfer curves at drain voltage V_D -0.1 V of (red) 1st electrodeposited **HBC** film and (blue) 2nd electrodeposited **HBC** film. With full line is reported the absolute value of the drain current (I_D) in logarithmic scale and with the dashed line the absolute value of the leakage gate current (I_G) in log scale. On the right y axis is reported the transconductance ($g_m = \frac{\partial I_D}{\partial V_G}$) normalized for the channel's length/width ratio. (**b**) Transfer curves of the two electrodeposited film with the square root of the drain current with the linear fitting (dashed lines) to extrapolate the threshold voltage (circles). Measured in pure de-ionised H_2O with Au side gate electrode and Ag/AgCl as external reference electrode, at 298 K and 10 mV/step with 0.05s/step integration time.*

The transfer curves were recorded with a constant drain voltage (V_D -0.1 V) very close to the saturation regime. The drain current and transconductance of the eChem film 1 (red) were always higher than those of the second **HBC** film (blue). The transconductance of the first film reached significantly higher values, 2.5–3 times, compared to that of the 2nd film and the threshold voltage (V_{Th}) was lower for the film 1 (-0.10 V vs. Ag/AgCl) compared to the V_{Th} of the 2nd film (-0.13 V vs. Ag/AgCl). A maximum transconductance was not observed, probably higher gate voltages were required to observe a maximum, but to avoid electrochemical

reactions or severe degradation of the film we limited the potential window. The difference in performance between the two **eChem** deposited **HBC** films could arise from some water contamination when the electrochemical cell was opened (under a positive flow of Ar), during the preparation (see above) to change the working electrode, thus affecting the electrochemical cyclodehydrogenation of hexaphenylbenzene. Or an alternative explanation is the lower density of **HBC** fibres in the 2nd film, as observed in the AFM images, that could lower the volumetric capacitance and decrease the connection points between the **HBC** fibres responsible for charge transfer between **HBC** aggregates. Figure 3.13 shows the transfer curves at different drain voltages (V_D) for the film 2 in DI H_2O and for film 1 in ionic liquid (EMimFAP) in glovebox.
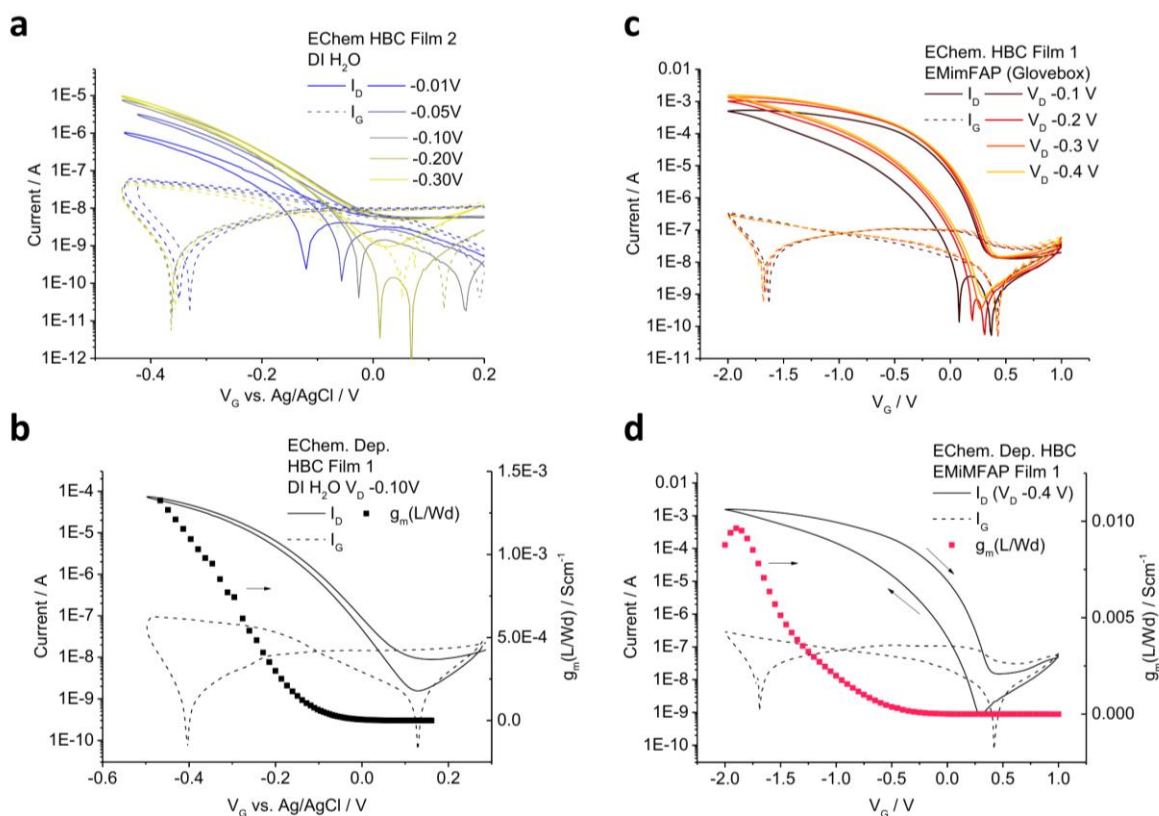
*Figure 3.13 (**a**) Transfer curves at different drain voltage V_D from -0.01 to -0.30 V of the 2nd electrodeposited HBC. (**b**) Transfer curve at V_D -0.1 V of the 1st electrodeposited HBC film with its normalized transconductance. Measured in pure de-ionised H_2O with Au side gate electrode and Ag/AgCl as external reference electrode, at 298 K and 10 mV/step with 0.05s/step integration time. (**c**) Transfer curves at different drain voltage V_D from -0.10 to -0.40 V of the 1st electrodeposited **HBC**. (**d**) Transfer curve at V_D -0.4 V of the 1st electrodeposited **HBC** film with its normalized transconductance. Measured in EMimFAP ionic liquid in glovebox with a Pt wire vertically placed as the gate electrode and without an external reference electrode, at 298 K and 10 mV/step with 0.05s/step integration time. With full line is reported the absolute value of the drain current (I_D) in logarithmic scale and with the dashed line the absolute value of the leakage gate current in log scale. On the right y axis is reported the transconductance ($g_m = (\partial I_D/\partial V_G)$) normalized for the channel's length/(width and film thickness) ratio.*

As expected, at higher drain voltages, a higher drain current was observed until the saturation regime was reached. In deionised H_2O, a saturation regime was reached after V_D -0.1 V. The maximum transconductance in DI H_2O normalized by the channel geometric parameter and film thickness (d 116 nm) was 1.35 mScm^{-1}, which corresponds for the saturation regime to a $[\mu C^*]_{OECT}$ of 3.65 mFcm^{-1}s^{-1}V^{-1}. The ON-OFF ratio in the forward scan was 5×10^4.

In glovebox, the device was gated with ionic liquid on top of the substrate. A reference electrode was not used to avoid H_2O contamination, and a Pt wire was placed vertically close to the **HBC** film and used as the gate electrode. In the EMimFAP ionic liquid, the measurement was carried out inside a glovebox to exclude the presence of H_2O, allowing to reach more negative gate voltages. The drain currents were one order of magnitude higher than those in DI H_2O, but the saturation regime was reached at more negative drain voltages. The threshold voltage was also more negative V_{Th} -0.44 V, but it should be noted that it was not measured by an external reference electrode. Moreover, a larger hysteresis in the drain current between the forward and backward scans was observed in the ionic liquid than in DI H_2O at the same voltage scan rate. These differences could be explained by the larger ions of EMimFAP compared to those present in H_2O, thus the ion mobilities will differ and could affect the measured threshold voltage, capacitance (C^*) and induce a larger hysteresis. The ON-OFF ratio in the forward scan was 2×10^6, whereas in the back scan, the OFF current increased and the ratio decreased to 10^5. The maximum transconductance in EMimFAP normalized by the channel geometric parameter and film thickness (d = 116 nm) was 9.63 mScm^{-1}, which corresponds for the saturation regime (V_D -0.4V) to a $[\mu C^*]_{OECT}$ of 6.64 mFcm^{-1}s^{-1}V^{-1}, which is almost two times the value in DI H_2O. Figure 3.14 shows the output curve of **eChem HBC** film 1 gated with EMimFAP measured in glovebox.
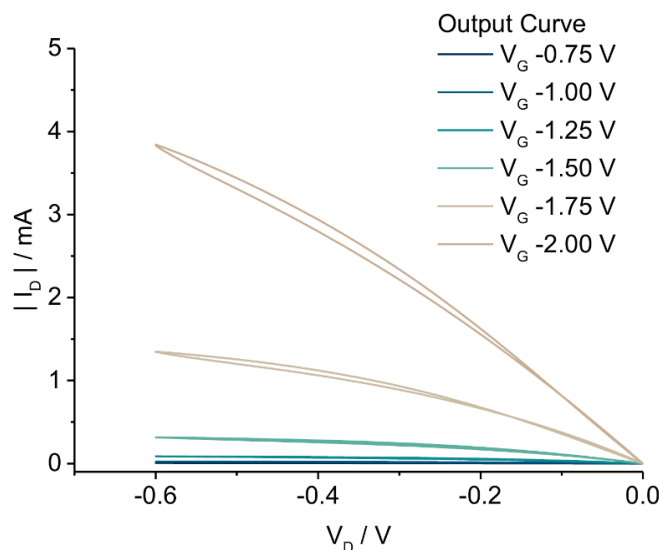
*Figure 3.14 Output curves (with the absolute value of the drain current) at different gate voltages V_G from -0.75 V to -2.00 V of the 1st electrochemically deposited **HBC** film. Measured in EMimFAP ionic liquid in glovebox with Pt wire vertically placed as gate electrode and without an external reference electrode, at 298 K and 10 mV/step with 1 s/step integration time.*

The Output curve did not show a clear linear-to-saturation transition, especially at higher gate voltages, for this reason the pinch-off voltage cannot be correctly defined. This effect could be related to a too low drain voltages, even though V_D= -0.6V is a relatively high value for an OECT. An alternative reason for this trend could be attributed to a more complex electrochemical behaviour of the **HBC** film. We can rule out that the unreached saturation regime is due to **HBC** degradation at high drain voltages, as a similar shape is observed in the reverse sweep. Additionally, it was not a kinetic effect because of the very slow scan rates used, that is, 10 mV/s. Currently, this effect on **HBC** films is still not completely understood.

Figure 3.15 shows the transfer curves of the solution-processed **HBC** films in the EMimFAP ionic liquid. The drain currents (I_D, full line) of the drop-cast (a) and **AJP HBC** (b) films are comparable to the leakage gate currents (I_G, dashed line), resulting in negligible charge transport inside the material channel. Interestingly, the Langmuir-Blodgett **HBC** film (Figure 3.15c) showed some degree of charge transport, although with very poor performance.

*Figure 3.15 Transfer curves at different drain voltage V_D from -0.01 (black) to -0.1 V (red) of the (**a**) drop casted HBC film, (**b**) Aerosol jet printed HBC film. (**c**) Transfer curve at different drain voltage V_D from -0.1 to -0.3 V of the Langmuir-Blodgett HB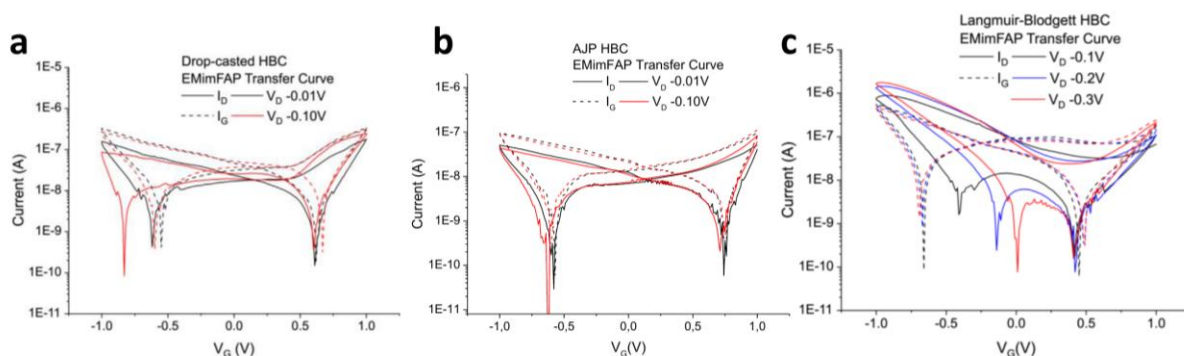C film Measured in EMimFAP ionic liquid outside the glovebox with Pt wire vertically placed as gate electrode and without an external reference electrode, at 298 K and 10 mV/step with 0.05 s/step integration time. With full line is reported the absolute value of the drain current (I_D) in logarithmic scale and with the dashed line the absolute value of the leakage gate current in log scale.*

The poor performance of the solution-processed **HBC** (obtained from chemical synthesis) films as OECTs is most likely related to the poor film homogeneity and the absence of self-assembly of the **HBC** in fibres, as in the **eChem. HBC** film. It is likely that the doping process occurs, but the charge transport between the film is severely inefficient or absent if the **HBC** film is not well connected from the source to the drain.

3.7 Conclusion

The electrochemical synthesis of hexa-peri-hexabenzocoronene from the soluble precursor hexaphenylbenzene produced **HBC** films with a thickness of approximately 100 nm, which completely covered the electrode and the 5 μm channel. From the optical images, the electrodeposition, in principle, can cover channel lengths up to 10 μm with a limit of approximately 15 μm. The electrosynthesised **HBC** deposits in self-assembled structures with an intertwined randomly oriented pattern made of polycrystalline aggregates and fibres. This reticulated structure is beneficial for OECT applications because it allows easier ion mobility and a larger surface area than very crystalline **HBC**. The electrochemical approach allowed the synthesis and deposition in a single step starting from a soluble precursor, this strategy showed a better film morphology and better performance than the drop-cast or Langmuir-Blodgett **HBC** films. Good **HBC** coverage was also achieved with aerosol jet printing methods, but poor crystallinity and the absence of self-assembly led to poor OECT performance. A further step is the comparison of OECT (**eChem**. prepared **HBC**) performance with that of

vacuum-deposited **HBC** films, which should be used as a reference benchmark. Nonetheless, we can expect that the electrochemical method provides a more intertwined structure, whereas via vacuum deposition, the **HBC** film is denser and more compact with many grain boundaries,[6] which could interfere with the ion and charge mobility inside the film.

3.8 Electrochemical transistor of electropolymerized poly-pyrene and poly-fluorene

Pyrene is known to electro-polymerize when its radical cations are generated at the electrode via an oxidative coupling of radical cations.[53,54] The pyrene oligomers deposited on the electrode give rise to new reversible redox processes, related to the doping and de-doping of the poly-pyrene film, that occur with an onset potential of +0.7V vs. Ag at less positive potentials than the 1st oxidation of pyrene. The CV curve of pyrene electro-polymerization on interdigitated electrode is shown in Figure 3.16a, whereas Figure 3.16b and 3.16c show the optical (at 100x magnification) image and the scanning electron microscopy results of the electropolymerized pyrene film, respectively. We can observe that poly-pyrene is deposited within the gap (channel) between the Au electrodes, but an edge effect is observed at the Au/channel interphase that may be related to the detachment of the poly-pyrene film. At present, a clear explanation for this phenomenon is still under investigation, and we can hypothesise that the poly-pyrene film is particularly rigid, and the doping phenomenon could lead to some mechanical stress, particularly at the Au/channel interphase, which ultimately causes cracking of the organic film. Moreover, Figure 3.16d shows the AFM image of the poly-pyrene film taken on glass 2 μm from the last Au electrode (note: it was not recorded inside the channel due to the very thick edge). Poly pyrene films are composed of many small spherical aggregates of pyrene oligomers with similar radii. However, the coverage is not complete, and there are some areas where the poly-pyrene aggregates are not well connected. Finally, Figure 3.16e shows the transfer curve of the poly-pyrene film in EMimFAP electrolyte. Unfortunately, charge injection or charge transfer was not observed, and the drain current was comparable to the leakage current (gate current). We believe that the edge effect at the Au/channel interphase may interfere with the charge injection from the source and/or that the poly-pyrene aggregates, not very well connected inside the channel (see the AFM data

above), hamper the charge transfer within the organic film, ultimately leading to a non-working device.

*Figure 3.16 (**a**) Cyclic voltammetry of pyrene 2.0 mM in DCM/Bu₄NPF₆ 80mM, measured at 0.4 V/s and 298 K with Au interdigitated electrode 1.8 mm x 5μm x 30 pairs (total surface 0.54 mm²). The potentials are reported vs. Ag (quasi-reference electrode) which has been observed to be stable in DCM during the potential scan and for several experiment. (**b**) Optical image at 100x magnification in bright-field mode of the poly-pyrene film on Au interdigitated electrode. (**c**) Scanning electron microscopy image at 5 kV (30 kX magnification) of the Au/channel interphase of a new poly-pyrene film. The film was treated with thin gold sputtering process before the image. (**d**) AFM image of poly-pyrene film from a zone 2 μm from the last gold electrode which should be representative of the film inside the channel. (**e**) Transfer curve at V$_D$ -0.4 V of the electropolymerized poly-pyrene film. Measured in EMimFAP ionic liquid outside the glovebox with Au side gate electrode and without an external reference electrode, measured at 298 K and 10 mV/step with 0.05 s/step integration time. With full line is reported the absolute value of the drain current (I$_D$) in logarithmic scale and with the dashed line the absolute value of the leakage gate current in log scale.*

The electropolymerization of fluorene, was investigated in chapter 2, in this section we report the film characterization of poly-fluorene electrochemically deposited on an interdigitated Au

electrode. Figure 3.17a shows the CV curve of fluorene during the electropolymerization in DCM/Bu$_4$NPF$_6$. Differently from **HBC** and poly-pyrene CV curves, the voltammetric pattern for the polymerization of fluorene does not show an evident current increase between each cycle. A new redox process related to the doping/de-doping occurred at an onset potential of +0.9 V vs. Ag, whereas with the Pt working electrode, in chapter 2, it was observed at +1.1 V vs. SCE, which is a relatively high potential for a doping process. After rinsing the electrode by immersion in a clean DCM solution, the optical images at 100x magnification were recorded and reported in Figure 3.17b in bright-field (BF) mode (top) and in fluorescence mode with a UV source (bottom). We can observe that the darker spots in the BF mode are related to the poly-fluorene film, which in some cases cover both electrode and, most important, the channel. A clearer view of the poly-fluorene film can be observed in fluorescence mode where the poly-fluorene had a green fluorescence. Alkyl-substituted poly-fluorene has been reported to show a blue fluorescence in solid-state and we can reasonably expect that the unsubstituted poly-fluorene should have a blue fluorescence as well.[55] However, we observed a green wavelength fluorescence of the electropolymerized fluorene, which has been reported to be originated by oxidised groups in the poly-fluorene such as hydroxy or ketone groups (fluorenone),[56] or excimer emission, or as observed in the LDI-TOF measurements in chapter 2, the electropolymerization of fluorene could produce more π-conjugated species by intramolecular reactions that could have a green emission.

Nonetheless, the coverage and homogeneity of the poly-fluorene film is very poor and could be the result of a partial solubilisation of the lower molecular weight oligomers during the electrode cleaning with a fresh solution of DCM. Therefore, only the longer poly-fluorene chain that formed big polymer bundles remained on the electrode. One of the poly-fluorene bundles was investigated by AFM as shown in Figure 3.17c and 3.17d. The poly-fluorene aggregate was on top of the gold electrode and showed an amorphous structure that extends beyond 5 μm. A line profile was extracted (Figure 3.17d) over one of the highest regions of the poly-fluorene and showed a maximum height of 480 nm which changed drastically depending on which part was sampled. We observed that the poly-fluorene bundles are randomly dispersed over the entire electrode area and that the microstructure of the aggregate is very inhomogeneous.

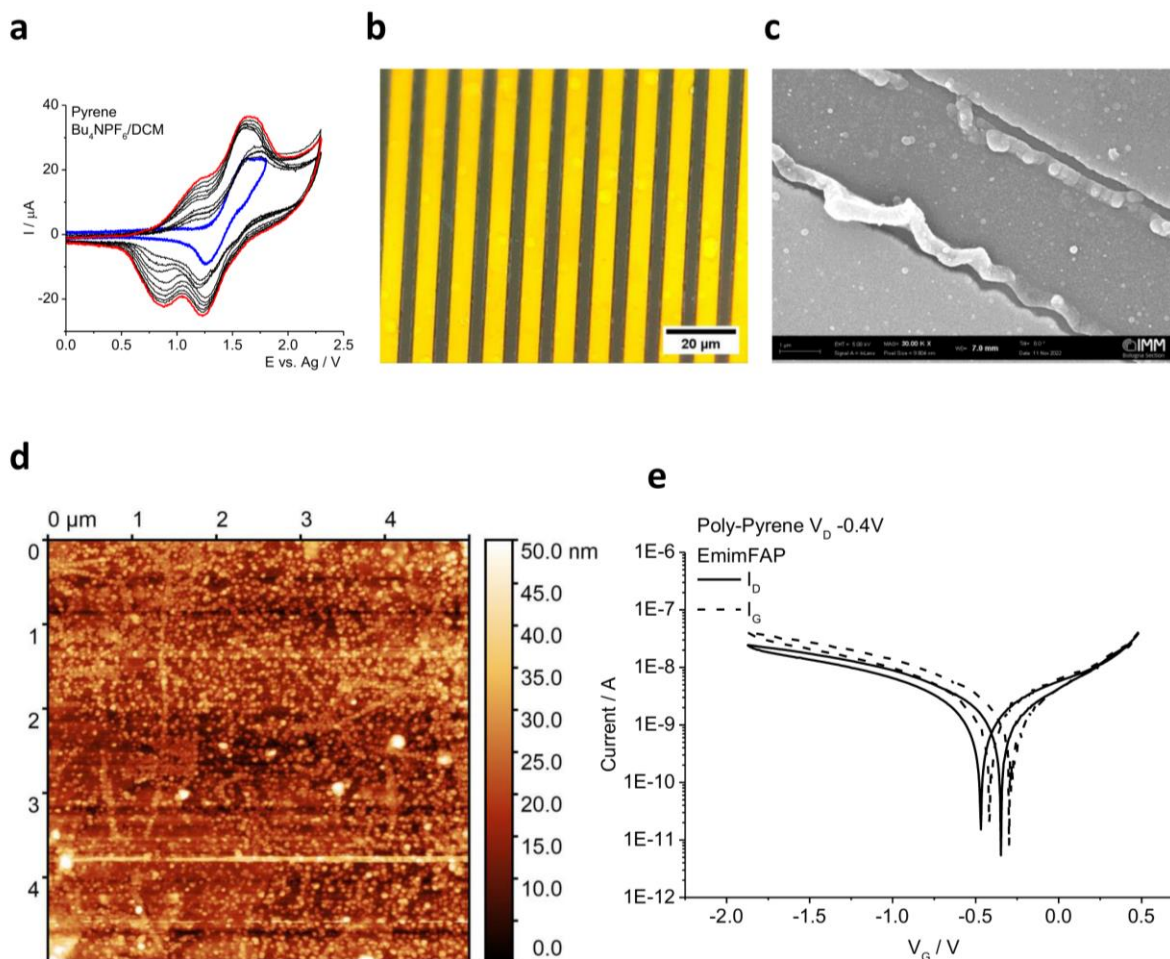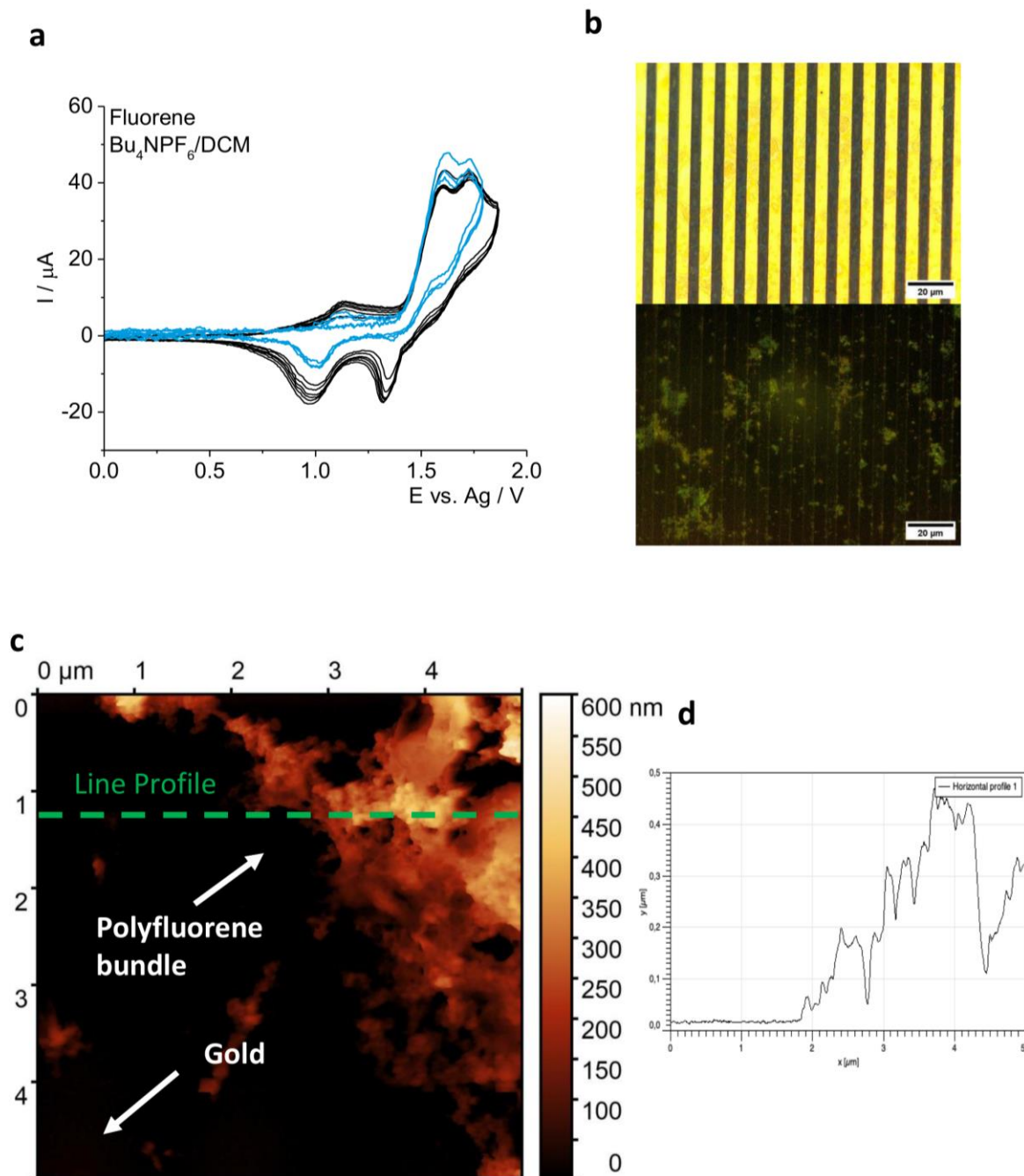*Figure 3.17 (**a**) Cyclic voltammetry of fluorene 2.65 mM in DCM/Bu₄NPF₆ 80mM, measured at 0.4 V/s and 298 K with Au interdigitated electrode 1.8 mm x 5µm x 30 pairs (total surface 0.54 mm²). The potentials are reported vs. Ag (quasi-reference electrode) which has been observed to be stable in DCM during the potential scan and for several experiment. (**b**) Optical image at 100x magnification in bright-field mode (top) and fluorescence mode (bottom) of the poly-fluorene film on Au interdigitated electrode. (**c**) AFM image of poly-fluorene film over the gold electrode. (**d**) Profile line (green line) of the AFM image.*

Poly-fluorene film was characterized as OECT with EMimFAP as electrolyte in glovebox, in order to reach more negative gate voltages and exclude H_2O from the electrolyte. The transfer curves of poly-fluorene are reported in Figure 3.18, from which we extracted a threshold voltage of -1.42 V which is very negative, but in agreement with the observed doping process in CV at high potentials. The ON-OFF ratio at V_D -0.3V is 2.6×10^5 and a maximum transconductance normalized for the channel width and length of 80 nS. However, it is worth to note that the entire electrode was not covered with the poly-fluorene film as observed by the optical microscopy, thus the normalized transconductance value is underestimated. For the same reason, we could not estimate the product of the mobility and volumetric capacitance.
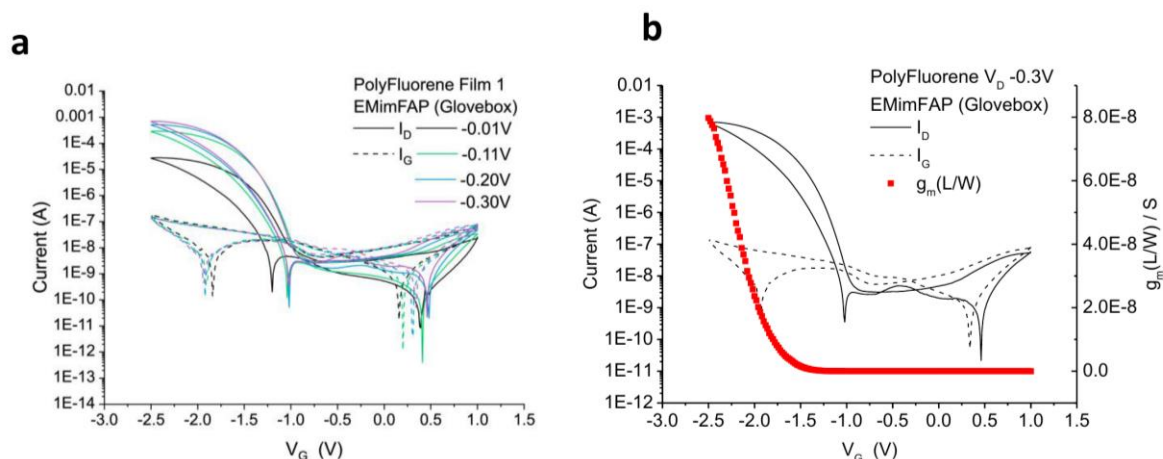
*Figure 3.18 Transfer curves (**a**) at V_D from -0.01V to -0.3 V of the electropolymerized poly-fluorene film. (**b**) at V_D -0.3 V with its normalized transconductance. Measured in EMimFAP ionic liquid in glovebox with Pt vertically placed gate electrode and without an external reference electrode, measured at 298 K and 10 mV/step with 0.05 s/step integration time. With full line is reported the absolute value of the drain current (I_D) in logarithmic scale and with the dashed line the absolute value of the leakage gate current in log scale. Normalized transconductance reported as scatter plot with red symbol.*

Lastly, the output curve of the poly-fluorene film was recorded with EMimFAP as electrolyte inside the glovebox and shown in Figure 3.19. Until V_G = -1.5V, the I_D was comparable to the leakage current, which is in agreement with the very negative threshold voltage. A hysteresis was observed in the back-scan at negative gate voltage which could be related to a too high scan rate. The pinch-off voltage, which is the voltage at which there is the transition from linear to saturation regime, was easier to measure than the **HBC** film and was -0.3V at V_G = -2.0V.
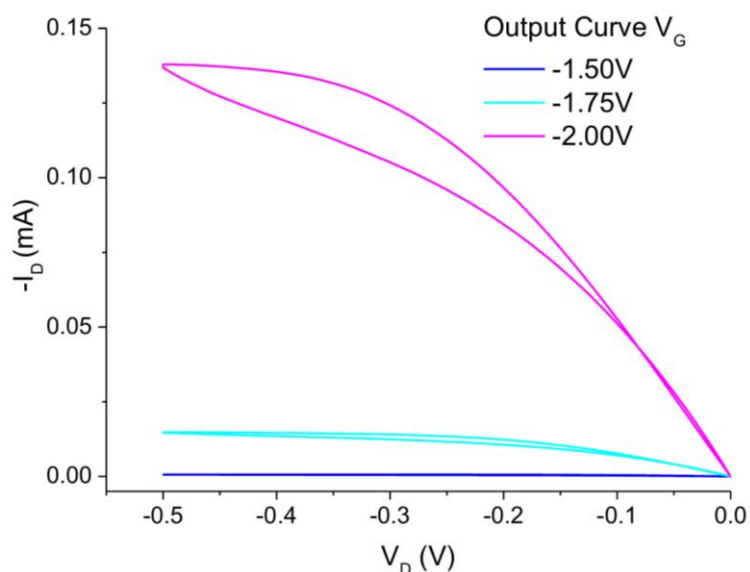
Figure 3.19 Output curves (with the negative value of the drain current) at different gate voltages V_G from -1.50 V to -2.00 V of the electropolymerized poly-fluorene film. Measured in EMimFAP ionic liquid in glovebox with Pt wire vertically placed as gate electrode and without an external reference electrode, at 298 K and 10 mV/step with 0.1 s/step integration time.

3.9 Conclusion

Two further examples of electropolymerized films, namely poly-pyrene and poly-fluorene, have been reported. The poly-pyrene film was composed of spherical aggregates, which were not homogeneously dispersed over the entire channel area. Moreover, a thicker poly-pyrene film was observed at the interphase with the Au/channel, which detached from the Au electrode. For these reasons we think that the poly-pyrene film did not work as OECT in our experiments. A more controlled electropolymerization is required to produce a better quality film of poly-pyrene for transistor applications.

Differently from poly-pyrene, the poly-fluorene film worked as OECT. However, the film was inhomogeneous and aggregated as very thick (over 500 nm) amorphous bundles of poly-fluorene. Moreover, the green fluorescence is not expected for a linear poly-fluorene film and further characterization are required to understand this phenomenon. As OECT, poly-fluorene showed very negative threshold voltage that makes it unusable in aqueous electrolyte due to the limited potential stability window of H_2O. The transconductance was very low compared to the state of the art of semiconductive material for OECT, however further improvement could be achieved both with functional groups and with a better control of the electropolymerization and deposition processes.

3.10 References

1. Wang, X. Y., Yao, X. & Müllen, K. Polycyclic aromatic hydrocarbons in the graphene era. *Sci China Chem* **62**, 1099–1144 (2019).

2. Rempala, P., Kroulik, J. & King, B. T. Investigation of the mechanism of the intramolecular Scholl reaction of contiguous phenylbenzenes. *Journal of Organic Chemistry* **71**, 5067–5081 (2006).

3. Rempala, P., Kroulík, J. & King, B. T. A Slippery Slope: Mechanistic Analysis of the Intramolecular Scholl Reaction of Hexaphenylbenzene. *J Am Chem Soc* **126**, 15002–15003 (2004).

4. Feng, X., Wu, J., Enkelmann, V. & Müllen, K. Hexa-peri-hexabenzocoronenes by efficient oxidative cyclodehydrogenation: The role of the oligophenylene precursors. *Org Lett* **8**, 1145–1148 (2006).

5. Berresheim, A. J., Müller, M. & Müllen, K. Polyphenylene Nanostructures. *Chemical Review* **99**, 1747–1786 (1999).

6. Keil, M. *et al.* Influence of the Morphology on the Electronic Structure of Hexa- *p eri* -hexabenzocoronene Thin Films. *J Phys Chem B* **104**, 3967–3975 (2000).

7. Goddard, R., Haenel, M. W., Herndon, W. C., Krueger, C. & Zander, M. Crystallization of Large Planar Polycyclic Aromatic Hydrocarbons: The Molecular and Crystal Structures of Hexabenzo[bc,ef,hi,kl,no,qr]coronene and Benzo[1,2,3-bc:4,5,6-b'c']dicoronene. *J Am Chem Soc* **117**, 30–41 (1995).

8. Seyler, H., Purushothaman, B., Jones, D. J., Holmes, A. B. & Wong, W. W. H. Hexa-peri-hexabenzocoronene in organic electronics. *Pure and Applied Chemistry* **84**, 1047–1067 (2012).

9. Pisula, W. *et al.* A zone-casting technique for device fabrication of field-effect transistors based on discotic hexa-perihexabenzocoronene. *Advanced Materials* **17**, 684–689 (2005).

10. Mas-Torrent, M. & Rovira, C. Role of Molecular Order and Solid-State Structure in Organic Field-Effect Transistors. *Chem Rev* **111**, 4833–4856 (2011).

11. Lin, F. J., Chen, H. H. & Tao, Y. T. Molecularly Aligned Hexa- peri-hexabenzocoronene Films by Brush-Coating and Their Application in Thin-Film Transistors. *ACS Appl Mater Interfaces* **11**, 10801–10809 (2019).

12. *Organic Electrochemistry*. (CRC Press, 2000). doi:10.1201/9781420029659.

13. Zhu, C., Ang, N. W. J., Meyer, T. H., Qiu, Y. & Ackermann, L. Organic Electrochemistry: Molecular Syntheses with Potential. *ACS Cent Sci* **7**, 415–431 (2021).

14. Little, R. D. A Perspective on Organic Electrochemistry. *Journal of Organic Chemistry* **85**, 13375–13390 (2020).

15. Ripani, L., Bombonato, E., Paolucci, F. & Marcaccio, M. Electron transfer in polyaromatic hydrocarbons and molecular carbon nanostructures. *Curr Opin Electrochem* **35**, 101065 (2022).

16. Wang, Y., Zhao, R. & Ackermann, L. Electrochemical Syntheses of Polycyclic Aromatic Hydrocarbons (PAHs). *Advanced Materials* 2300760 (2023) doi:10.1002/adma.202300760.

17. Sauermann, N., Meyer, T. H., Qiu, Y. & Ackermann, L. Electrocatalytic C-H Activation. *ACS Catal* **8**, 7086–7103 (2018).

18. Röse, P., Emge, S., König, C. A. & Hilt, G. Efficient Oxidative Coupling of Arenes via Electrochemical Regeneration of 2,3-Dichloro-5,6-dicyano-1,4-benzoquinone (DDQ) under Mild Reaction Conditions. *Adv Synth Catal* **359**, 1359–1372 (2017).

19. Ussano, E. Electrochemistry of molecular systems for new nanostructured materials and bioelectronic devices. (University of Bologna, 2016). doi:10.6092/unibo/amsdottorato/7641.

20. Qin, L. *et al.* In Situ Electrochemical Synthesis and Deposition of Discotic Hexa-peri-hexabenzocoronene Molecules on Electrodes: Self-Assembled Structure, Redox Properties, and Application for Supercapacitor. *Small* **11**, 3028–3034 (2015).

21. Zeng, C. *et al.* Electrochemical synthesis, deposition, and doping of polycyclic aromatic hydrocarbon films. *J Am Chem Soc* **143**, 2682–2687 (2021).

22. Zeng, C. *et al.* Electrochemical Deposition of a Single-Crystalline Nanorod Polycyclic Aromatic Hydrocarbon Film with Efficient Charge and Exciton Transport. *Angewandte Chemie - International Edition* **110016**, (2021).

23. Bruno, C. *et al.* Wavy graphene sheets from electrochemical sewing of corannulene. *Chem Sci* **12**, 8048–8057 (2021).

24. Hao, Q. *et al.* Electrochemical polymerization and properties of poly(triphenylene), an excellent blue-green-light emitter. *Journal of Physical Chemistry C* **114**, 9608–9617 (2010).

25. Rivnay, J. *et al.* Organic electrochemical transistors. *Nature Reviews Materials 2018 3:2* **3**, 1–14 (2018).

26. Bernards, D. A. & Malliaras, G. G. Steady-State and Transient Behavior of Organic Electrochemical Transistors. *Adv Funct Mater* **17**, 3538–3544 (2007).

27. Rivnay, J. *et al.* High-performance transistors for bioelectronics through tuning of channel thickness. *Sci Adv* **1**, (2015).

28. Ohayon, D., Druet, V. & Inal, S. A guide for the characterization of organic electrochemical transistors and channel materials. *Chem Soc Rev* **52**, 1001–1023 (2023).

29. Giovannitti, A. *et al.* Controlling the mode of operation of organic transistors through side-chain engineering. *Proceedings of the National Academy of Sciences* **113**, 12017–12022 (2016).

30. Kim, S.-M. *et al.* Influence of PEDOT:PSS crystallinity and composition on electrochemical transistor performance and long-term stability. *Nat Commun* **9**, 3858 (2018).

31. Kim, Y. *et al.* Strain-Engineering Induced Anisotropic Crystallite Orientation and Maximized Carrier Mobility for High-Performance Microfiber-Based Organic Bioelectronic Devices. *Advanced Materials* **33**, (2021).

32. Yang, Y., Deng, H. & Fu, Q. Recent progress on PEDOT:PSS based polymer blends and composites for flexible electronics and thermoelectric devices. *Mater Chem Front* **4**, 3130–3152 (2020).

33. Lu, B. *et al.* Pure PEDOT:PSS hydrogels. *Nat Commun* **10**, 1043 (2019).

34. Zhang, S. *et al.* Tuning the Electromechanical Properties of PEDOT:PSS Films for Stretchable Transistors And Pressure Sensors. *Adv Electron Mater* **5**, (2019).

35. Li, Y., Zhou, X., Sarkar, B., Gagnon-Lafrenais, N. & Cicoira, F. Recent Progress on Self-Healable Conducting Polymers. *Advanced Materials* **34**, (2022).

36. Li, Y. *et al.* Autonomic Self-Healing of PEDOT:PSS Achieved Via Polyethylene Glycol Addition. *Adv Funct Mater* **30**, (2020).

37. Talikowska, M., Fu, X. & Lisak, G. Application of conducting polymers to wound care and skin tissue engineering: A review. *Biosens Bioelectron* **135**, 50–63 (2019).

38. Rahimzadeh, Z., Naghib, S. M., Zare, Y. & Rhee, K. Y. An overview on the synthesis and recent applications of conducting poly(3,4-ethylenedioxythiophene) (PEDOT) in industry and biomedicine. *J Mater Sci* **55**, 7575–7611 (2020).

39. Inal, S., Malliaras, G. G. & Rivnay, J. Benchmarking organic mixed conductors for transistors. *Nat Commun* **8**, 1767 (2017).

40. Asavapiriyanont, S., Chandler, G. K., Gunawardena, G. A. & Pletcher, D. The electrodeposition of poly-N-methylpyrrole films from aqueous solutions. *J Electroanal Chem Interfacial Electrochem* **177**, 245–251 (1984).

41. Downard, A. J. & Pletcher, D. A study of the conditions for the electrodeposition of polythiophen in acetonitrile. *J Electroanal Chem Interfacial Electrochem* **206**, 147–152 (1986).

42. Noftle, R. E. & Pletcher, D. The mechanism of electrodeposition of composite polymers including polypyrrole. *J Electroanal Chem Interfacial Electrochem* **227**, 229–235 (1987).

43. Fletcher, S. *et al.* The response of some nucleation/growth processes to triangular scans of potential. *J Electroanal Chem Interfacial Electrochem* **159**, 267–285 (1983).

44. Heinze, J., Frontana-Uribe, B. A. & Ludwigs, S. Electrochemistry of conducting polymers-persistent models and new concepts. *Chem Rev* **110**, 4724–4771 (2010).

45. Heinze, J., Rasche, A., Pagels, M. & Geschke, B. On the origin of the so-called nucleation loop during electropolymerization of conducting polymers. *Journal of Physical Chemistry B* **111**, 989–997 (2007).

46. Savéant, J.-M. *Elements of Molecular and Biomolecular Electrochemistry*. (John Wiley & Sons, Inc., Hoboken, NJ, USA, 2006). doi:10.1002/0471758078.

47. Heinze, J., John, H., Dietrich, M. & Tschuncky, P. σ-"Dimers" – key intermediates and products during generation and redox switching of conjugated oligomers and polymers. *Synth Met* **119**, 49–52 (2001).

48. Negri, F., Castiglioni, C., Tommasini, M. & Zerbi, G. A Computational Study of the Raman Spectra of Large Polycyclic Aromatic Hydrocarbons: Toward Molecularly Defined Subunits of Graphite †. (2002) doi:10.1021/jp0128473.

49. Maghsoumi, A. *et al.* Edge chlorination of hexa-peri-hexabenzocoronene investigated by density functional theory and vibrational spectroscopy. *Physical Chemistry Chemical Physics* **18**, 11869–11878 (2016).

50. Castiglioni, C., Mapelli, C., Negri, F. & Zerbi, G. Origin of the D line in the Raman spectrum of graphite: A study based on Raman frequencies and intensities of polycyclic aromatic hydrocarbon molecules. *J Chem Phys* **114**, 963–974 (2001).

51. Hughes, J. M. *et al.* High quality dispersions of hexabenzocoronene in organic solvents. *J Am Chem Soc* **134**, 12168–12179 (2012).

52. Oliveira, O. N., Caseli, L. & Ariga, K. The Past and the Future of Langmuir and Langmuir–Blodgett Films. *Chem Rev* **122**, 6459–6513 (2022).

53. Bachman, J. C. *et al.* Electrochemical polymerization of pyrene derivatives on functionalized carbon nanotubes for pseudocapacitive electrodes. *Nat Commun* **6**, 3–4 (2015).

54. Waltman, R. J., Diaz, A. F. & Bargon, J. The Electrochemical Oxidation and Polymerization of Polycyclic Hydrocarbons. *J Electrochem Soc* **132**, 631–634 (1985).

55. Leclerc, M. Polyfluorenes: Twenty years of progress. *J Polym Sci A Polym Chem* **39**, 2867–2873 (2001).

56. Honmou, Y. *et al.* Single-molecule electroluminescence and photoluminescence of polyfluorene unveils the photophysics behind the green emission band. *Nat Commun* **5**, 4666 (2014).

Chapter 4

Electrochemiluminescence of heteroaromatic azapyrene

In collaboration with

Prof. N. Zaccheroni, Dr. E. Giovannetti, Prof. F. Negri, Prof. D. Fazzi (University of Bologna)

Prof. P Langer (Rostock University)

4.1 Introduction

Pyrene and azapyrenes

Pyrene is the simplest peri-fused polycyclic aromatic hydrocarbon (PAH) with 16 π electrons and a completely planar structure. Pyrene is used as a building block for many organic materials due to its versatile electronic properties,[1] such as p-type charge transport, or as fluorescent probe due to its photophysical properties.[2] Peri-fused heteroaromatic analogues of pyrene, such as azapyrenes,[3–5] diazapyrenes[6–8] and up to the tetraazapyrene,[9] have recently received a growing interest in the material science community owing to their photophysical and electronic properties, such as high fluorescence quantum yield and intense blue wavelength emission. Doping pyrene with a nitrogen atom can significantly influence the frontier orbital energies and increases the electron-acceptor ability of the molecule, making it a promising candidate for non-fullerene n-type semiconductive materials.[6,10] The photophysical properties of pyrene have been extensively studied, pyrene shows a high fluorescence quantum yield with an exceptionally long-lived singlet excited state, and the possibility to form excimers and exciplexes via π–π interactions. The UV/vis spectrum of pyrene shows four bands with a fine vibronic structure: a weak band at 372 nm related to the symmetry-forbidden $S_0 \rightarrow S_1$ transition (Platt nomenclature, L_b), two allowed bands at 334 and 272 nm, $S_0 \rightarrow S_2$ (L_a) and $S_0 \rightarrow S_3$ (B_b), respectively, and a strongly allowed band at 243 nm, $S_0 \rightarrow S_4$ (B_a).[11] Pyrene can easily form excimers in solution at concentrations higher than 10^{-5} M,

giving rise to a broad structureless emission band centred at 480 nm. The monomer/excimer emission is concentration-dependent and the ratio decreases at higher pyrene concentrations (increase of the excimer). Electrochemically, pyrene undergoes a chemically reversible reduction in aprotic solvent at -2.08V vs. SCE and a chemically irreversible oxidation with a peak potential E_p +1.30V vs. SCE in CH_2Cl_2, followed by a film-forming process on the electrode, related to the formation of poly-pyrene oligomers.[12,13] The HOMO and LUMO orbitals of pyrene have their largest coefficients at the 1,3,6,8-positions. Therefore, functional groups or heteroatom doping, that can affect the π-orbitals at these positions, can strongly influence the electronic properties of pyrene.[1] In comparison, the functional groups or doping at the 2,7-positions of pyrene, do not strongly interact with the HOMO and LUMO, because they are placed at the nodal planes of both these frontier molecular orbitals (FMO), but instead interact with the HOMO–1 and LUMO+1 of pyrene.

Figure 4.1 reports the FMOs and energies calculated at the B3LYP/6-31G(d,p) level for pyrene, 2-azapyrene, 1-azapyrene and 5,9 phenyl derivatives. When one or more nitrogen atoms are incorporated in the pyrene core, a change in the photophysical properties occurs. In particular, with increasing number of nitrogen atoms there is a lowering of the frontier orbital energies (HOMO and LUMO) and a decrease of the optical gap.[3,4,14] However, for the same number of heteroatoms, the electronic properties are strongly influenced by the position of the nitrogen atoms. Molenda et al. showed that for 5,9-diphenyl-2-azapyrene and 5,9-diphenyl-1-azapyrene, a stronger effect on the electronic properties was observed when nitrogen directly contributed to the frontier molecular orbitals (FMOs), like in 1-azapyrene, whereas N-doping had a smaller effect when nitrogen was placed in the nodal plane of the FMOs like in the 2-azapyrenes.[3,4]
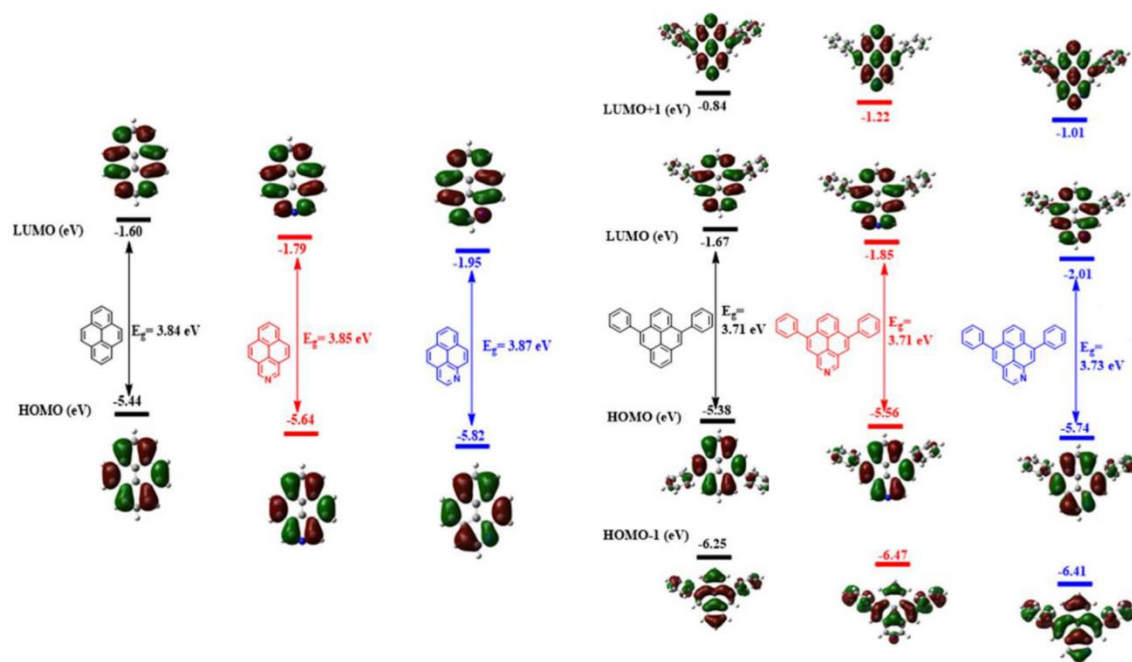
Figure 4.1 Frontier molecular orbitals and energies of pyrene, 2-azapyrene, 1-azapyrene, 5,9-diphenylpyrene, 5,9-diphenyl-2-azapyrene, and 5,9-diphenyl-1-azapyrene. Calculated at the TD-DFT B3LYP/6-31G/d,p) level of theory using a polarisable continuum model of dichloromethane for the solvent effect. Adapted with permission from [3]. Copyright 2022, American Chemical Society.

Introduction of the electrogenerated chemiluminescence

Electrogenerated chemiluminescence (ECL) is a luminescence process in which the excited state of a luminophore is generated by homogeneous electron transfer (ET) between reactive intermediates produced by an electrochemical reaction at the electrode surface.[15,16]

The first studied ECL mechanism involved the ET between an oxidised and a reduced species, both of them were generated by a double potential step. This method is called "ion-annihilation" and follow a general mechanism as sketched in Scheme 4.1.

$$A - e^- \rightarrow A^{\bullet+} \qquad \text{(electrochemical oxidation)} \qquad (1)$$

$$A + e^- \rightarrow A^{\bullet-} \qquad \text{(electrochemical reduction)} \qquad (2)$$

$$A^{\bullet+} + A^{\bullet-} \rightarrow A^* + A \qquad \text{(ion-annihilation)} \qquad (3)$$

$$A^* \rightarrow A + h\nu \qquad \text{(light emission)} \qquad (4)$$

Scheme 4.1 ECL Ion-annihilation mechanism, energy sufficient S-Route

Many PAHs, such as rubrene and diphenyl-anthracene, were some of the first organic luminophores studied in ECL.[15,16] These PAHs undergo a chemically reversible one-electron oxidation and reduction. Moreover, their ion annihilation is energetically sufficient to populate the single excited state. An "energy-sufficient" system has an enthalpy ($\Delta H°$) of annihilation (electron transfer) reaction which is higher than the singlet excited state energy (E^{S1}). The enthalpy of reaction can be estimated from the standard potentials, which are usually approximated to the half-wave potential,[15,17] as $-\Delta H^0 = E^o(D^{·+}, D) - E^o(A^{·-}, A) - T\Delta S^0$, where the entropic contribution $T\Delta S^0$ at 298 K is estimated as 0.1 ± 0.1 eV.[16] An energy sufficient system, i.e. $|-\Delta H°| > E^{S1}$, is referred to follow a "S-Route" ECL mechanism.

Two different chemical species, a donor and an acceptor, can also generate ECL, in particular, the acceptor (A) is reduced and the donor (D) is oxidised. In this case the ECL mechanism remains the same as the classic ion-annihilation, but it is called "mixed annihilation" system. This method is useful when one radical ion is not chemically stable for the classic ion-annihilation approach thus a different species is added. However, even with the mixed system, it is important that the energy requirement is satisfied in order to populate the singlet state (S-Route) of the luminophore. Generally, the populated excited state is the one with a singlet energy (E^{S1}) closer to $\Delta H°$, assuming that energy transfer phenomenon is not present.[16]

When the energy requirement is not met, i.e. $|-\Delta H°| < E^{S1}$, the system is defined as "energy deficient" and the observed ECL involves triplet intermediates. The ECL mechanism is called T-Route.[18,19] T-Route mechanism may occur also in energy sufficient systems in the so called "ST-Route", where both the excited states, that are statistically produced, contribute to the ECL.

A more recent alternative to ion annihilation to generate ECL is the use of a sacrificial co-reactant. A co-reactant is a chemical species that, once oxidised or reduced, generates a highly reactive intermediate that can react with the luminophore in different ways to produce the excited state. We can classify the co-reactant as "oxidative-reduction" and "reductive-oxidation".[16,20] In the former case, the co-reactant is oxidised at the electrode and generates a strong reducing intermediate, such in the case of tripropylamine (**TPrA**) or oxalate ($C_2O_4^{2-}$). In the latter case, the co-reactant is reduced and generates a strong oxidating intermediate, as in the case of benzoylperoxide (**BPO**)[16,21] or peroxydisulfate ($S_2O_8^{2-}$). A very important characteristic of the co-reactant method is that ECL can be generated in a single potential step which can, in principle, last for several seconds without significantly decreasing the ECL

signal. The use of a co-reactant allows ECL to be performed in aqueous media, thus exploiting the technique to many, already commercially available, analytical applications.

Mechanism of co-reactant BPO in ECL

As previously mentioned, **BPO** is a reductive-oxidation co-reactant that can be directly reduced at the electrode. **BPO** is irreversibly reduced in ACN with a peak potential of -1.23V vs. SCE, generating at the electrode an oxidant radical, benzoyloxy radical (PhCOO$^\bullet$), and benzoate anion (PhCOO$^-$) as result of the O-O bond cleavage. **BPO** reduction and bond cleavage have been reported as stepwise mechanism in early reports of ECL by **BPO**.[16,21] However, Maran et al. reported that for many peroxides[22] and perbenzoates,[23] a concerted mechanism occurred via dissociative electron transfer.[24] The benzoate radical is a reactive intermediate that can be further reduced at the electrode to benzoate anion or can react with the luminophore in different ways. PhCOO$^\bullet$ is a strong oxidant species and the PhCOO$^-$/PhCOO$^\bullet$ couple has been reported to have a standard reduction potential of +1.5V vs. SCE.[16] ECL of various PAHs in the presence of **BPO** occurs when the applied potential is sufficient to generate the luminophore radical anion. The simplest ECL mechanism with **BPO** is S-Route, observed in energy-sufficient systems, where the enthalpy of homogeneous electron transfer between PhCOO$^\bullet$ (E° PhCOO$^-$/PhCOO$^\bullet$) and A$^{\bullet-}$ (E° A$^{\bullet-}$/A) is larger than the singlet energy ($|-\Delta H°| > E^{S1}$).

$$BPO + e^- \rightarrow PhCOO^\bullet + PhCOO^- \qquad \text{(BPO D-ET)} \qquad (1)$$

$$A + e^- \rightarrow A^{\bullet-} \qquad \text{(luminophore reduction)} \qquad (2)$$

$$PhCOO^\bullet + A^{\bullet-} \rightarrow {}^1A^* + PhCOO^- \qquad \text{(homogenous ET)} \qquad (3)$$

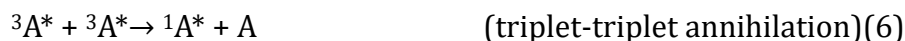$${}^1A^* \rightarrow A + h\nu \qquad \text{(fluorescence)} \qquad (4)$$

Scheme 4.2 BPO S-Route ECL Mechanism

The **BPO** ECL mechanism is sometimes more complex than the S-Route mechanism, and triplet or secondary reactions may be involved. In particular, if the system is energy-deficient, homogeneous ET can produce triplet excited states, which can undergo triplet-triplet

annihilation or quenching. Moreover, because PhCOO• is an oxidant species, it can homogenously oxidise the luminophore to its radical cation, when $E°(PhCOO^-/PhCOO^•) > E°(A/A^{•+})$, and the produced radical cation can undergo ion-annihilation[25] or degradation if not stable (Scheme 4.3).

$$PhCOO^{•}+ A^{•-}\rightarrow {}^3A^* + PhCOO^- \qquad \text{(triplet formation ET)} \qquad (5)$$

$${}^3A^* + {}^3A^*\rightarrow {}^1A^* + A \qquad \text{(triplet-triplet annihilation)} \quad (6)$$

$${}^3A^* + Q\rightarrow A + Q^* \qquad \text{(triplet quenching)} \qquad (7)$$

$$PhCOO^{•}+ A\rightarrow A^{•+} + PhCOO^- \qquad \text{(radical-cation formation)} \quad (8)$$

$$A^{•+} + A^{•-}\rightarrow {}^1A^* + A \qquad \text{(ion-annihilation)} \qquad (9)$$

$$A^{•+} \rightarrow P \qquad \text{(radical-cation degradation)} \quad (10)$$

Scheme 4.3 BPO Triplet formation (T-Route) and oxidation ECL mechanism

When the **BPO** concentration is much higher than the luminophore concentration, triplet quenching or radical cation formation reactions are favoured over the triplet-triplet annihilation, resulting in an ECL which is mainly generated by the ion-annihilation reaction.[16]

Role of triplet state in energy deficient systems

When the enthalpy of the electron transfer reaction is smaller than the energy of the lowest singlet excited state but higher than the energy of the triplet state of the luminophore, triplets can be generated at the electrode surface with subsequent triplet-triplet annihilation as the ECL mechanism when fluorescence is observed. PAH triplets have longer lifetimes than inorganic complex luminophores, therefore they are usually more subject to quenching from species such as radicals and traces of oxygen which are not completely removed, for this reason phosphorescence is generally not observed in ECL of PAHs at 298K. Nonetheless, triplet quenching competes with the triplet-triplet annihilation mechanism which can occur with a high rate constant.[18] Alternatively, fluorescence can be observed when triplet states, if close to the energy of the singlet state, exhibit thermally activated delayed fluorescence.[26] However, this kind of "reverse" intersystem crossing requires that ΔE(triplet-singlet) is

relatively small which is generally not true for many π-conjugated PAHs. In principle, a triplet mechanism can be experimentally identified by adding a triplet quencher to the solution with a triplet energy around 0.2 eV lower than the luminophore triplet energy. However, the quencher must be chosen such that it is not electrochemically active at the scanned potentials and it is chemically inert with the electrogenerated radical and radical ions.
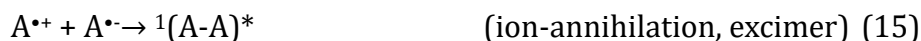
Excimer formation in ECL

In addition to the usual fluorescence, a broad structureless emission band at a wavelength higher than that of fluorescence is common for many planar PAHs, particularly in ECL. In fact, pyrene exhibits a second emission band which is attributed to its excimer.[27–29] In the case of pyrene, an excimer was observed both in the PL and ECL. During photoluminescence, an aggregate in the excited state can be generated by the close interaction of a molecule in the excited state with another molecule in the ground state, if the two molecules are the same the aggregate is defined as "excimer", whereas if the two molecules are different the aggregate is defined as "exciplex". Usually, an excimer has a lower energy than the molecule alone and is stable exclusively in the excited state. Upon relaxation to the ground state (which has a completely dissociative potential energy curve), with the emission of a photon ($h\nu_2$) with a lower energy than single molecule fluorescence, the aggregate dissociates (Scheme 4.4) showing an emission band of the excimer which is broad and structureless.

$$A + h\nu \rightarrow 1A^* \qquad \text{(Absorption)} \qquad (11)$$

$$A^* + A \rightarrow (A\text{-}A)^* \qquad \text{(Excimer formation)} \qquad (12)$$

$$(A\text{-}A)^* \rightarrow (A\text{-}A) + h\nu_2 \qquad \text{(Excimer emission)} \qquad (13)$$

$$(A\text{-}A) \rightarrow 2A \qquad \text{(Disaggregation)} \qquad (14)$$

Scheme 4.4 Excimer formation in photoluminescence

During ECL, excimers can be generated by more pathways than in photoluminescence. Because ECL is localised in the proximity of the electrode surface, there is a reaction layer where the concentration of the excited state is very high which can favour excimer formation.

Alternatively, ECL can be generated by both ion-annihilation and triplet-triplet annihilation reactions.[16,30,31] In these cases, excimer emission may be observed in the ECL (Scheme 4.5) but not in the PL.

$$A^{\bullet+} + A^{\bullet-} \rightarrow {}^1(A\text{-}A)^* \qquad \text{(ion-annihilation, excimer)} \quad (15)$$

$${}^3A^* + {}^3A^* \rightarrow {}^1(A\text{-}A)^* \qquad \text{(TTA, excimer)} \qquad (16)$$

Scheme 4.5 Excimer formation in ECL (E-Route) mechanism

Excimer emission has also been observed in co-reactant ECL, although it is less common than ion-annihilation ECL. Bard et al. reported an excimer emission of pyrenophanes exclusively observed in ECL by using **BPO** as co-reactant.[25] In such a work, the pyrenophanes were directly oxidised by PhCOO•, that led to a large amount of excimer, via ion-annihilation. Furthermore, the difference in the monomer/excimer ratio between similar pyrenophanes was explained by the different lifetime of the radical cation, where a longer lifetime would increase the probability of excimer formation.

4.2 Outlook

In this chapter, we investigate the electrochemical behaviour of a series of heteroaromatic pyrenes with a pyridinic nitrogen in the pyrene core. In particular, we analyse the effects on the electrochemical properties of different substituents and of the nitrogen positions on two constitutional isomers. The chemically irreversible oxidation processes of the azapyrene are further analysed with the characterisation of its oxidised products by UV/vis spectroscopy, and mass spectroscopy. In the second part of this chapter, the electrochemiluminescence of azapyrenes is analysed by ion annihilation and with sacrificial co-reactants. In particular, the ECL mechanism with **BPO** as co-reactant is analysed in order to understand the non-trivial formation of an excimer for only one type of isomer. A proposed mechanism is then proposed for ECL with **BPO**.

Results and discussion:

The electrochemical, photophysical properties and electrochemiluminescence of a series of 5,7,9-substituted 2-azapyrene (naphtho[2,1,8-def]isoquinoline) and 1-azapyrene (5,9-diphenylnaphtho[2,1,8-def]quinoline) derivatives were investigated. Their molecular structures are shown in Scheme 4.6. The synthesis was carried out in the Langer group at Rostock University according to the reported procedure.[3,4]
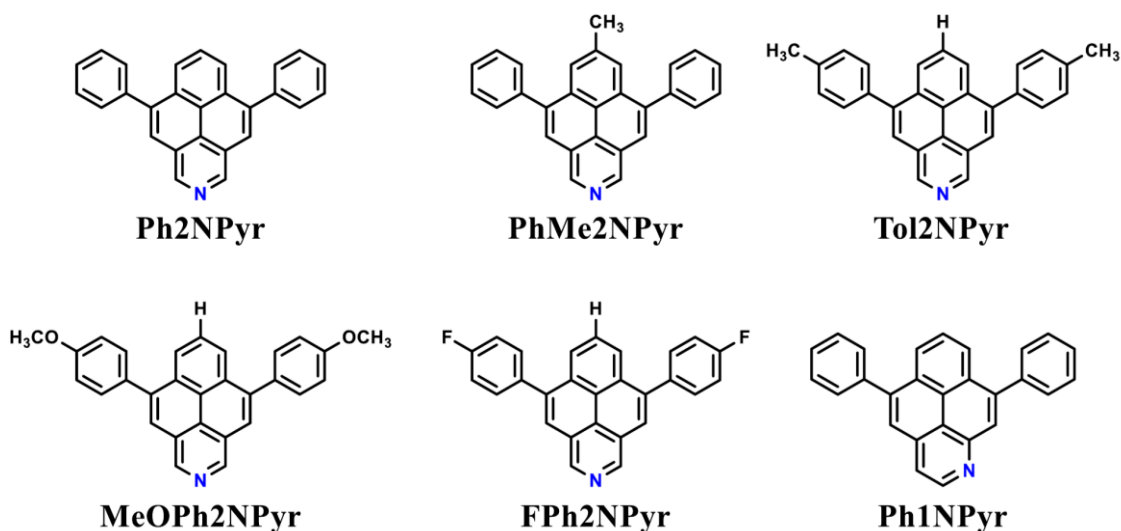
Scheme 4.6 Chemical structure of naphtho[2,1,8-def]isoquinoline derivatives and 5,9-diphenylnaphtho[2,1,8-def]quinoline

4.3 Electrochemical characterization

Cyclic voltammetry (CVs) measurements were performed in Bu_4NPF_6/DCM and Bu_4NPF_6/THF. Figure 4.2 shows the CVs curves of azapyrenes in THF, and their redox potentials are summarised in Table 4.1. The electrochemical behaviours of the various derivatives of the 2-azapyrenes are very similar between each other; thus, only the cyclic voltammetry of 5,9-diphenyl-2-azapyrene (**Ph2NPyr**) is extensively described.

In THF, the first reduction process of **Ph2NPyr** appeared both chemically and electrochemically reversible, with an $E_{1/2}$ potential of -1.89 V vs. SCE. Azapyrenes, because of the pyridinic nitrogen heteroatom in its pyrene structure, are more easily reduced than pyrene ($E_{1/2}$ -2.08 V vs. SCE in DMF). At more negative potentials, a chemically irreversible second reduction process was observed with a peak potential (E_p) of -2.45 V vs. SCE. The

chemical irreversibility of the 2nd reduction produces a new species that shows a new oxidation process in the backward scan at approximately -0.8 V.
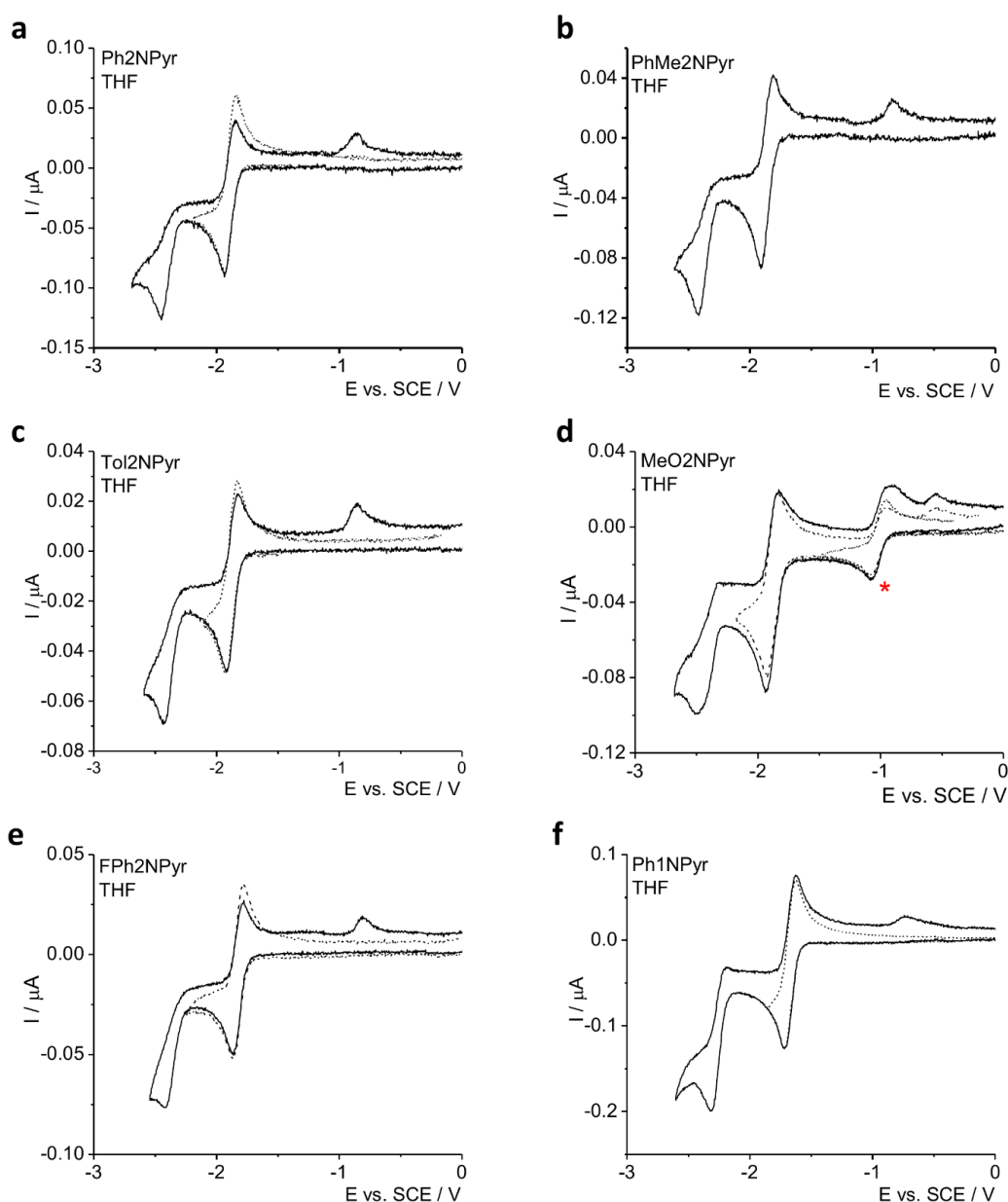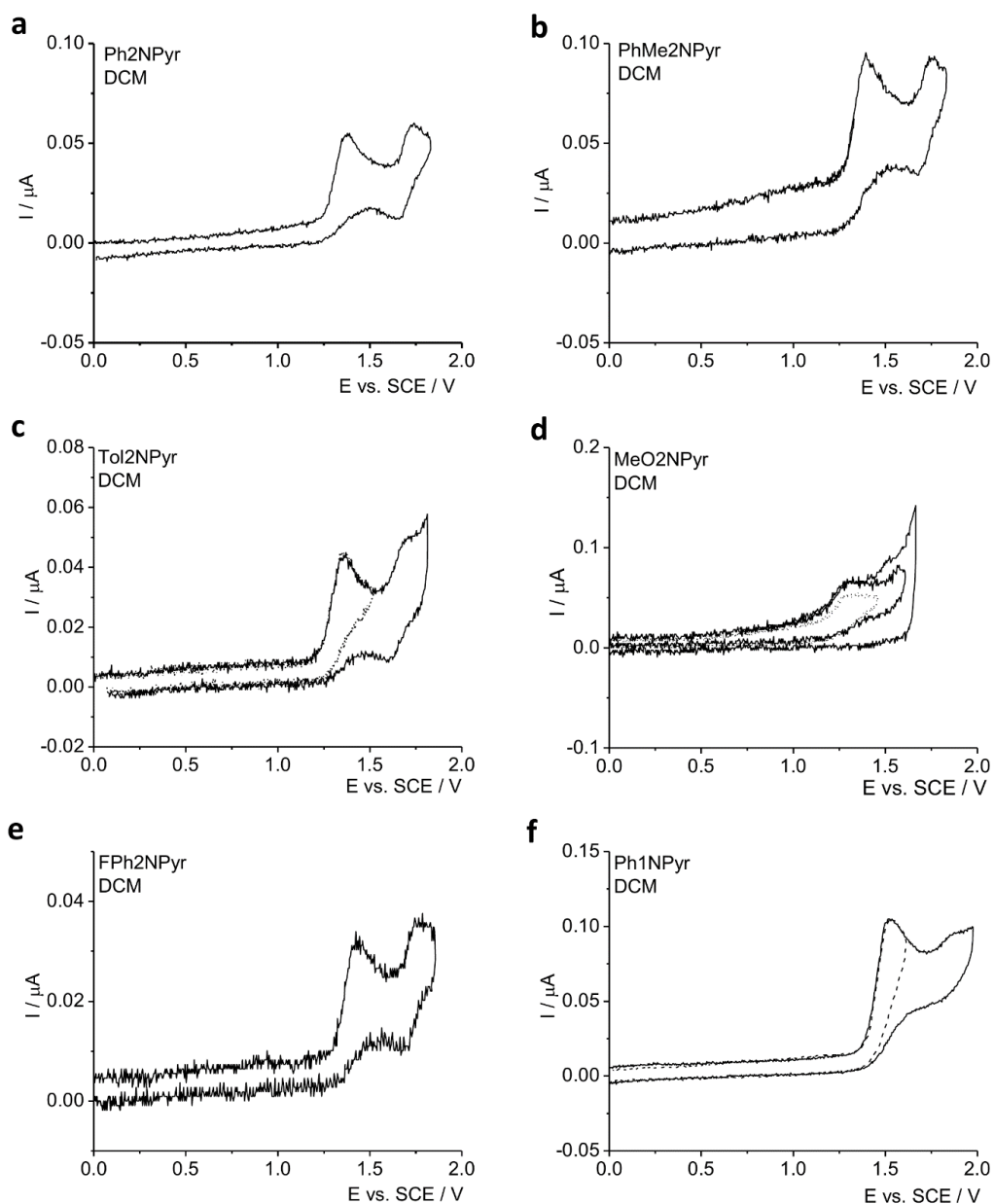

*Figure 4.2 Cyclic voltammetry of (**a**) **Ph2NPyr** 0.91 mM, (**b**) **PhMe2NPyr** 0.90 mM, (**c**) **Tol2NPyr** 0.45 mM, (**d**) **MeOPh2NPyr** 0.95 mM, (**e**) **FPh2NPyr** 0.74 mM, and (**f**) **Ph1NPyr** 1.00 mM. Measured at 1 V/s at 298 K in 80 mM Bu₄NPF₆/THF with Pt disk diameter 125 μm as working electrode and SCE as reference electrode. The red asterisk for **MeOPh2NPyr** is related to a different species always present together with the methoxy azapyrene, probably it is a degradation product.*

Figure 4.3 shows the CVs curves of the azapyrenes in DCM. In DCM, the first oxidation process of **Ph2NPyr** was chemically irreversible, with an anodic peak potential (E_p) of +1.37 V vs SCE. Such irreversibility remained even at higher scan rates, up to 50V/s and low temperatures,

down to -60°C (Figure 4.4), indicating that the generated radical cation undergoes a follow-up irreversible chemical reaction with a high rate constant. Besides, at more positive potential, a chemically reversible second oxidation process was observed at +1.70 V vs SCE, with an anodic peak current (i^{pa}) that was approximately half of that of the first oxidation. Our hypothesis is that the second oxidation process is related to a product of the first irreversible electron transfer. The chemical identity of the product is discussed in the following section.

*Figure 4.3 Cyclic voltammetry of (**a**) **Ph2NPyr** 0.91 mM, (**b**) **PhMe2NPyr** 0.90 mM, (**c**) **Tol2NPyr** 0.45 mM, (**d**) **MeOPh2NPyr** 0.95 mM, (**e**) **FPh2NPyr** 0.74 mM, and (**f**) **Ph1NPyr** 1.00 mM. Measured at 1 V/s at 298 K in 80 mM Bu₄NPF₆/DCM with Pt disk diameter 125 μm as working electrode and SCE as reference electrode.*

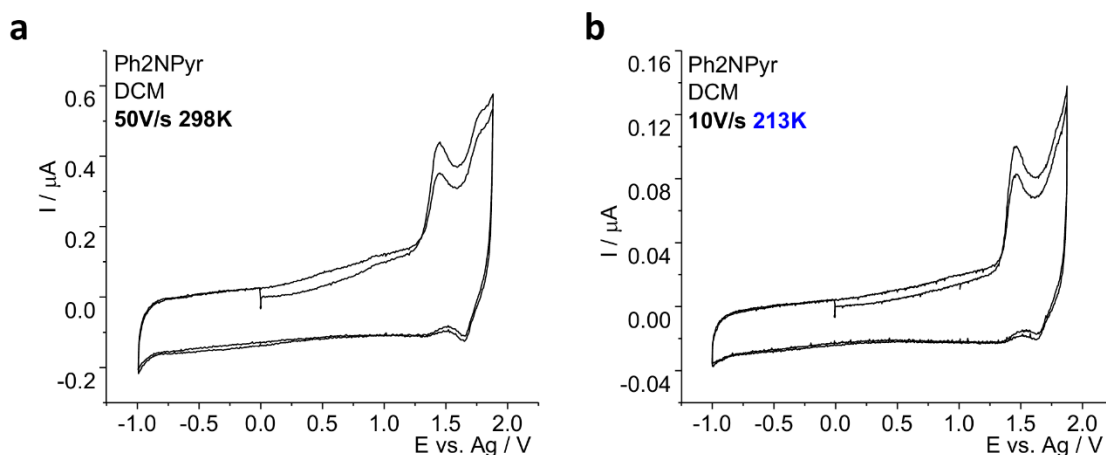*Figure 4.4 Cyclic voltammetry of **Ph2NPyr** 0.91 mM. Measured at 50 V/s and 298 K (**a**) or 10 V/s and 213 K (**b**) in Bu4NPF6/DCM with Pt disk diameter 125 μm as working electrode and SCE as reference electrode.*

Table 4.1: Redox Properties

Species	Oxidation[a] E^p vs. SCE / V		Reduction[b] $E_{1/2}$ vs. SCE / V	
Ph2NPyr	1.37[c]	1.70	-1.89	-2.45[c]
PhMe2NPyr	1.39[c]	1.71	-1.86	-2.42[c]
Tol2NPyr	1.35[c]	1.65	-1.88	-2.43[c]
MeOPh2NPyr	1.31[c]	1.54[c]	-1.88	-2.49[c]
FPh2NPyr	1.42[c]	1.72	-1.83	-2.42[c]
Ph1NPyr	1.53[c]	1.89	-1.67	-2.31[c]

Notes: Measured at 298 K with a Pt disk of 125μm diameter as working electrode and SCE as reference electrode at 1V/s. [a](80mM) Bu4NPF6/DCM electrolyte solution, [b](80mM) Bu4NPF6/THF electrolyte solution, [c] Peak potentials reported for chemically irreversible processes.

In general, for 2-azapyrenes, the presence of electron-donating substituents in the phenyl groups, such as CH_3 or CH_3O, leads to lower oxidation potentials compared to **Ph2NPyr**, whereas the effect is negligible for the reduction potentials. Electron-withdrawing groups such as F substituents increase the oxidation potential and shifts the reduction potential toward less negative values compared to **Ph2NPyr**. The only difference was observed for **MeOPh2NPyr** in THF which showed an additional reduction process. This unexpected process (highlighted by an asterisk) was related to a different electro-active species, probably generated by degradation of azapyrene. This species was successfully separated by thin-layer chromatography with silica (this molecule has a higher polarity than **MeOPh2NPyr**), although the exact nature of this species is still not completely understood. We suspect that protonation

could have occurred, even though it was not clear if pyridinic nitrogen was involved or if hydrolysis of the methoxy group had occurred.

A stronger influence on the redox potentials was observed for two regioisomers (positional isomers), 2-azapyrene (**Ph2NPyr**) and 1-azapyrene (**Ph1NPyr**). The first oxidation peak potential of **Ph1NPyr** is 150mV more positive than that of **Ph2NPyr**, and the first reduction process of **Ph1NPyr** is 220mV less negative in THF. Changing the nitrogen position strongly influenced the HOMO and LUMO energies. In 2-azapyrene, the N atom is located in the nodal plane of both the HOMO and LUMO, which has a moderate effect on the electronic properties of the pyrene core. The nitrogen of 1-azapyrene directly contributes to the frontier orbitals, strongly influencing the frontier orbital and lowering the HOMO and LUMO energies. This modulation of the HOMO and LUMO energies was directly reflected in the oxidation and reduction potentials. In addition, the chemical reactivity of the radical cation seemed to be affected by the different positions of the nitrogen atom, as a lower i^{pa} of the 2nd oxidation was observed for **Ph1NPyr** compared to the 2nd oxidation of **Ph2NPyr**.

4.4 Characterisation of the oxidised species

To better understand the anodic electrochemical behaviour and reactivity of azapyrene radical cations, we performed spectroelectrochemical measurements for the oxidation of **Ph2NPyr** in Bu_4NPF_6/DCM at -15°C and preparative-scale electrolysis in Bu_4NPF_6/DCM at room T in order to produce enough oxidised species for further characterisation. The initial oxidation mechanism is probably an EC mechanism with a fast kinetic rate of the chemical reaction. The first oxidised product was stable during spectroelectrochemical measurements with an orange/red colour. Figure 4.5 shows the absorption spectra evolution during the spectroelectrochemical measurements.
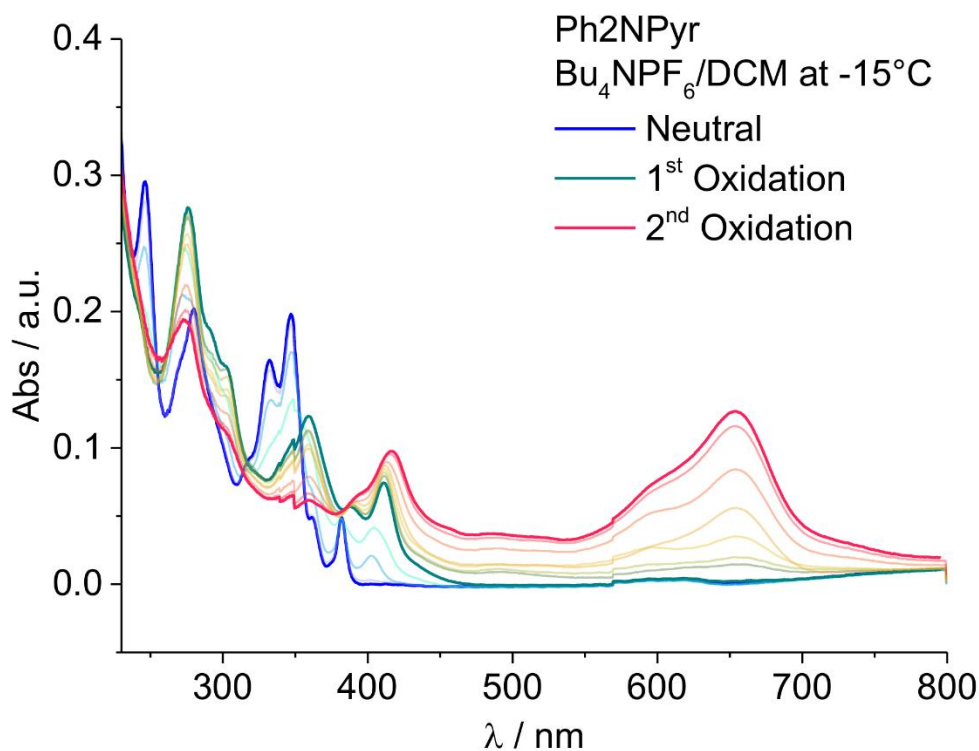
*Figure 4.5 Spectro-electrochemistry of 0.61mM **Ph2NPyr** in Bu₄NPF₆/DCM at -15°C, blue line with an applied potential of 0V vs. SCE, green +1.53V vs. SCE, red +2.03V vs. SCE. Working electrode Pt mesh, Reference electrode Ag/AgCl separated with a glass frit. Cell optical pathway 0.3mm. Scan rate 454 nm/min, baseline corrected.*

Neutral **Ph2NPyr** showed electronic transitions with well-defined vibrational progression, with electronic excitations similar to those of pyrene. However, in contrast to pyrene, the pyridine nitrogen significantly increased the intensity of the dipole-forbidden (for pyrene [32]) transition $S_0 \rightarrow S_1$ (^1L_B) at 383 nm, which for pyrene is associated with the HOMO $\rightarrow$ LUMO+1 and HOMO-1 $\rightarrow$ LUMO electronic transitions. At higher energies, **Ph2NPyr** showed an intense $S_0 \rightarrow S_2$ transition (^1L_A) at 348 nm, which for pyrene is associated with the HOMO $\rightarrow$ LUMO and HOMO-1 $\rightarrow$ LUMO+1. Two other electronic transitions were observed at 280 and 246 nm.

When +1.53 vs. SCE was constantly applied to the working electrode, **Ph2NPyr** was irreversibly oxidised and rapidly transformed into a different species. The new species showed different electronic transitions than **Ph2NPyr**. A new band appeared at 410 nm, suggesting the presence of a more conjugated structure than that of the precursor. Moreover, the L_A band red-shifted to 360 nm and became less intense without vibronic progression. The $S_0 \rightarrow S_3$ band blue-shifted to 276 nm with some vibronic progression, whereas the band at 246 nm disappeared completely.

Reaching +2.03V vs. SCE, a second oxidation occurred, which was reversible and probably related to a charged (cation or radical cation) species. The absorption spectrum showed a higher baseline in the 230-800 range, a new broad band at 590-650 nm, and a red-shifted transition at 416 nm. The band at 360 nm partially disappeared and the band at 276 nm decreased. It is likely that electrochemical oxidation was incomplete, and the two species coexisted at that potential. An isosbestic point was observed at 384 nm.

After the spectroelectrochemical measurements, the electrogenerated species were characterised ex-situ by photoluminescence (PL) measurements, shown in Figure 4.6. However, multiple species were present in the solution, namely **Ph2NPyr**, the oxidised species from the 1st oxidation and likely some product of the 2nd oxidation, which may not be completely reversible in the experimental timescale of spectroelectrochemical measurements (from minutes to tens of minutes). Two new emission bands were observed, one centred at 545 nm and the other at 650 nm. The very intense emission of **Ph2NPyr** is not shown in Figure 4.6. The excitation spectrum (dashed brown line) with an emission wavelength of 545 nm is similar to the absorption spectrum of the 1st oxidation except that the maxima are slightly red-shifted at 425, 370, and 290 nm. The emission band at 650 nm is related to a different molecule which was likely produced during the second or further oxidation, probably some soluble oligomers. The same oligomers can be observed in the absorption spectrum by magnifying 10-times the absorption between 470 and 650 nm range. (see below, for the electropolymerization section).
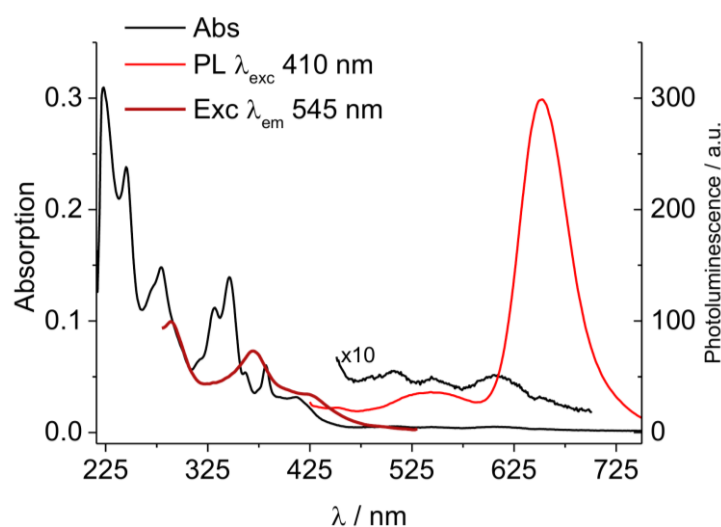

*Figure 4.6 Absorption (black) and photoluminescence spectra (red line with λexc 410 nm) and excitation spectra (dashed brown with λem 545 nm) of a recovered solution of **Ph2NPyr** in DCM after the spectroelectrochemistry measurement.*

Further analysis was conducted by preparative-scale electrolysis to better characterise the oxidised species after the 1st oxidation of **Ph2NPyr**. The electrochemical cell was saturated with Ar and kept under a slow and steady positive flux of inert gas to avoid mainly oxygen and H_2O contamination from air as much as possible. The solution was kept under stirring and a constant potential was applied vs. a quasi-reference Ag wire. Because the potential of the quasi-reference electrode slightly drifted during electrolysis, we performed CVs with a GC electrode to monitor the oxidation potential shift of **Ph2NPyr** and to correct the applied potential during electrolysis. The electrolysis lasted for 9h. During electrolysis, the colour of the solution changed from light yellow to red (Figure 4.7b). Figure 4.7c shows the charge (Q-Q_0) in Coulombs vs. time and the applied potential vs. the quasi-reference electrode during electrolysis. From the total charge (0.289 C), assuming that one electron is transferred for each oxidation of **Ph2NPyr**, we can estimate that 3.1×10^{-6} mol of **Ph2NPyr** was transformed to the oxidised product with a conversion percentage of 40%. CV curves were recorded before and after electrolysis (Figure 4.7d). No new redox processes were observed in the voltammograms before the 1st oxidation of **Ph2NPyr**, while the 2nd oxidation peak current increased, due to the oxidation of the accumulated product occurring at a higher potential with respect to the pristine **Ph2NPyr**. Furthermore, we observed a 36% decrease in the peak current of the 1st oxidation, which is in agreement with the estimated 40% conversion from the calculated charge. The small discrepancy between the conversion percentages could be attributed to a slight evaporation of DCM during electrolysis, thus increasing the **Ph2NPyr** concentration, which affected the peak current evaluation.
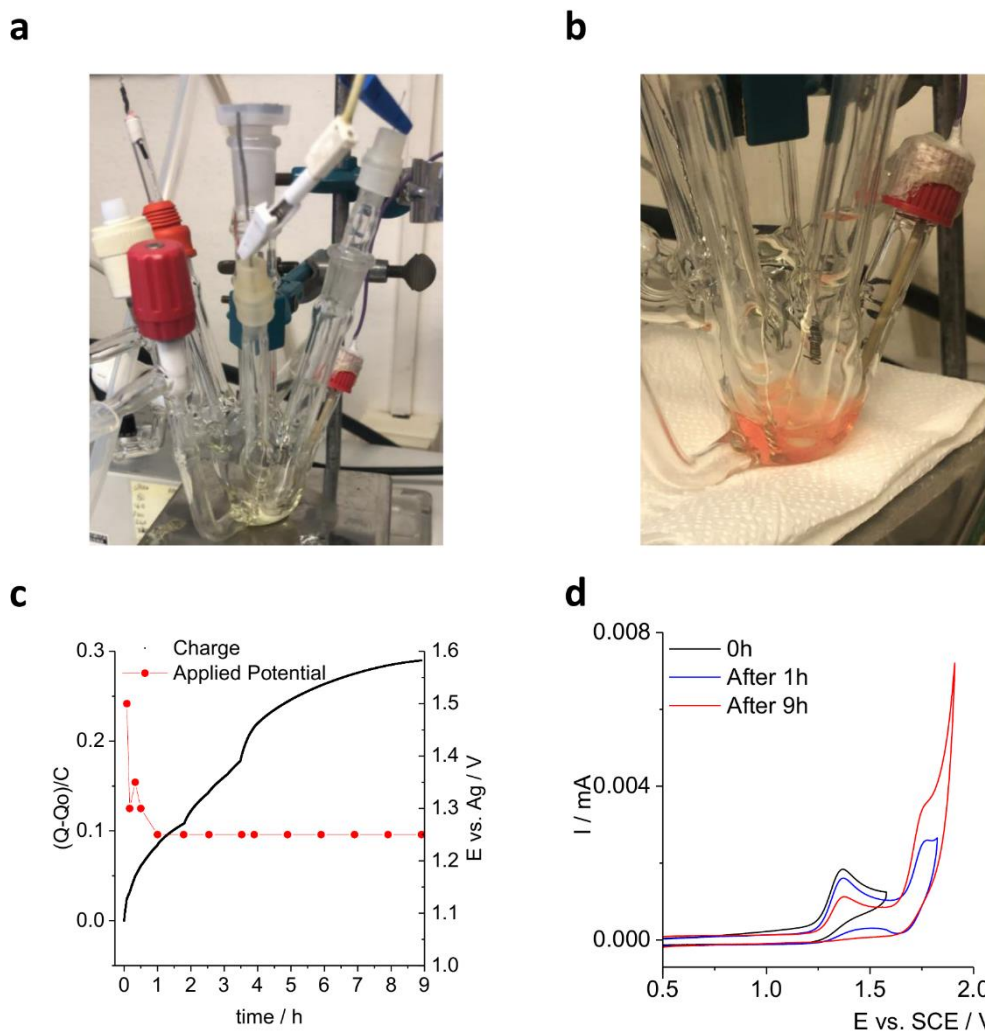
*Figure 4.7 Electrochemical cell for preparative-scale electrolysis (**a**) before and (**b**) after 9h of electrolysis. **Ph2NPyr** 1 mM in 80 mM Bu_4NPF_6/DCM at 298 K. A completely immersed Pt sheet (rectangle geometry) was used as the working electrode for electrolysis, and a glassy carbon disk (diameter 1 mm) was used as the working electrode for CV measurements at 200 mV/s. An Ag wire was used as the quasi-reference electrode and a Pt spiral separated with a glass frit was used as the counter electrode. (**c**) Total charge vs. time and vs. potential (Ag QRE). (**d**) CV before, during, and after electrolysis.*

The electrolysis products were separated by column flash chromatography using silica gel with 1:1 ethyl acetate/cyclohexane as eluents. The separated product of the 1st oxidation was characterised by UV/vis absorption, photoluminescence, and electron-spray ionisation (ESI) mass spectroscopy. In Figure 4.8 the UV/vis and PL spectra of the oxidised species are reported.
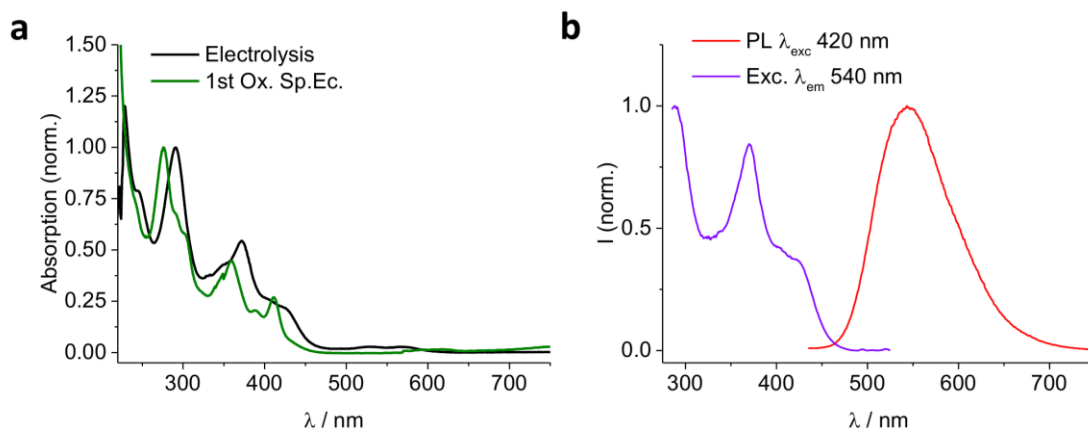
110

*Figure 4.8 (**a**) UV-Vis Absorption of the separated product after the oxidative electrolysis of **Ph2NPyr** (black) and absorption of the Ph2NPyr 1st oxidation during spectroelectrochemistry in Bu₄NPF₆/DCM (green), (**b**) PL (red λexc 420 nm) and excitation spectra (purple line) with λem 540 nm. Solvent DCM. Note: the spectroelectrochemistry experiment was carried out at 258 K, whereas the absorption and excitation spectra were recorded at 298 K.*

The absorption spectrum of the separated oxidised species had a very similar absorption bands as the spectrum of the oxidised species in spectroelectrochemistry (Figure 4.5), except for a redshifted wavelengths of ca. 10 nm for the entire spectrum. Moreover, the same shift was observed in the excitation spectrum of the recovered solution after the spectroelectrochemistry experiment (Figure 4.6). All these facts evidence that the oxidised products after electrolysis and during the spectroelectrochemical experiment are the same species.

The PL spectrum of the oxidatively electrolysed species shows a broad emission band centred at 545 nm. The excitation spectrum was similar to the absorption spectrum, confirming that the excited state was the same. The same emission was observed in Figure 4.6 from the solution recovered after the spectroelectrochemical experiment, confirming that the 1st band at 545 nm was indeed the emission of the 1st oxidation product. The emission at 650 nm, which was not present in the electrolysed solution, was related to a product of a further oxidation that occurred at a more positive potential during the spectroelectrochemistry measurement.

The solution after the electrolysis contained three species: the unreacted **Ph2NPyr**, the oxidation product and the electrolyte Bu₄NPF₆. Figure 4.9a shows the thin layer chromatography (TLC), with the same eluent used for chromatography, before the separation (**M**) and after separation of the species (**A**) and (**B**). In particular, species (**A**) showed a blue emission and a Rf similar to that of pure **Ph2NPyr**, whereas the green/yellow emitting species

(**B**) results to be more polar than **Ph2NPyr** (lower Rf) and is related to the product of the oxidative electrolysis. When the solvent was evaporated from the separated product (**B**), part of the electrolyte (Bu4NPF6) was still present. Unfortunately, Bu_4N^+ cations are a problem for ESI mass spectroscopy, because they suppress the ionisation of the product, and a better separation through silica chromatography was not possible because the electrolyte couldn't be seen in TLC. For this reason, before injection in the mass spectrometer, liquid chromatography with a short C_{18} column was used to separate the electrolyte from the species (**B**).

Figure 4.9b shows the ESI mass spectrum of the oxidation product after separation.
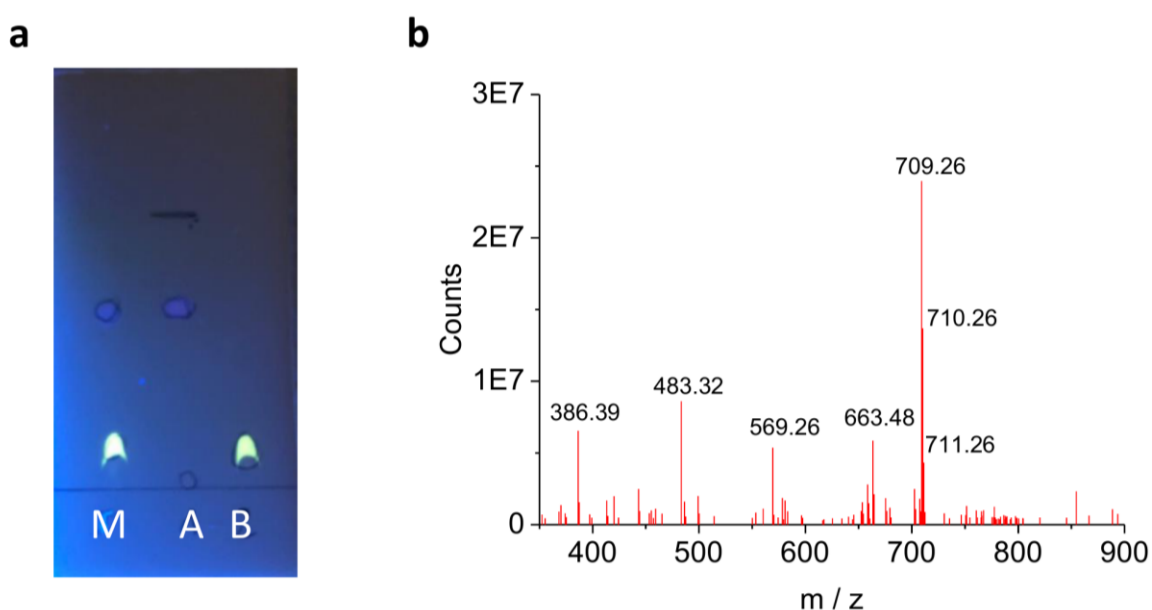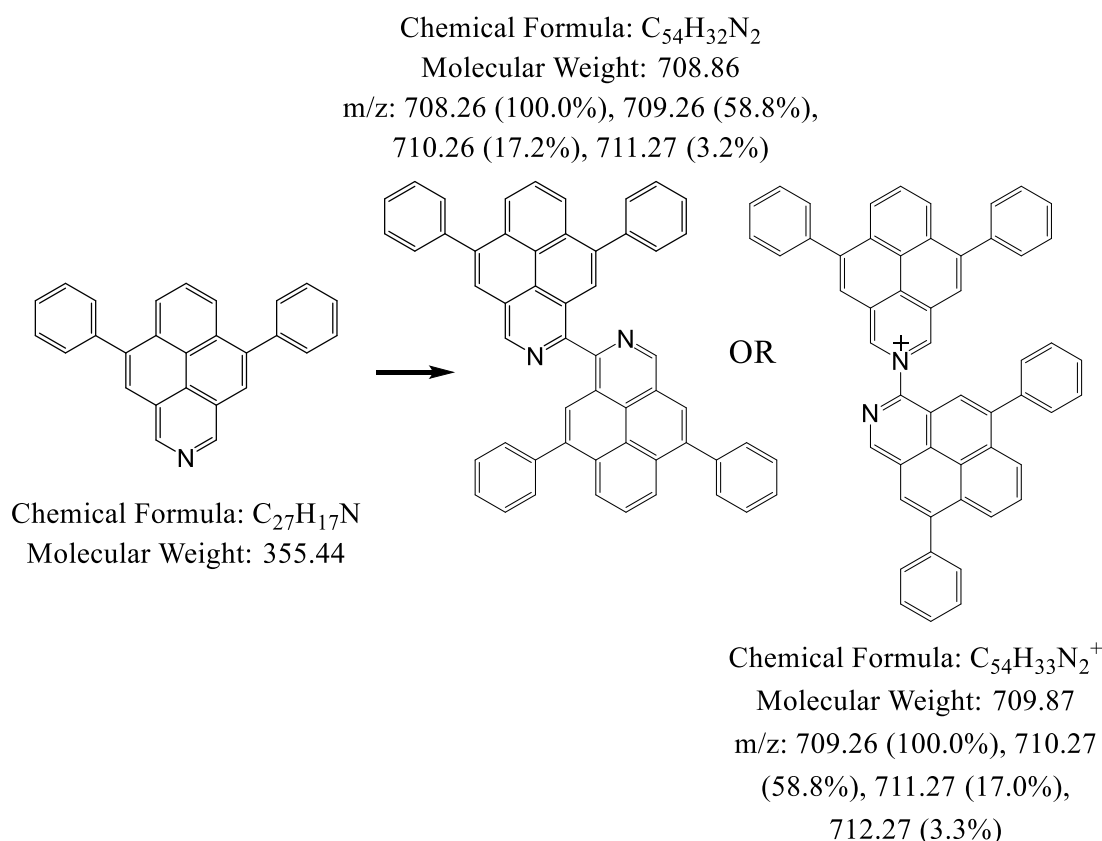

*Figure 4.9(**a**) TLC with SiO2 of the solution after oxidative electrolysis of **Ph2NPyr** (M) before separation. (A) and (B) are two different chemical species separated with silica chromatography. Eluent cyclohexane/ethyl acetate (1:1). (**b**) Electron-spray ionisation mass spectroscopy of the oxidation product of **Ph2NPyr** (species B) after separation with liquid chromatography (C18 column) and ACN/H2O as liquid phase.*

From the mass spectrum, we observed the absence of **Ph2NPyr** which would show a m/z peak close to its molecular weight (355.44 g/mol), whereas the most intense peak was that at 709.26 m/z, which corresponds to a linear dimer of **Ph2NPyr** (Scheme 4.7). From the m/z analysis of the two possible dimers, namely **C-C dimer** or the charged **C-N dimer**, we can hypothesise that the observed m/z could be a proton adduct of the **C-C dimer** (708.26 + 1 m/z, [**C-C dimer**+H]$^+$) or directly the positively charged **C-N dimer** (709.26 m/z). Unfortunately, adducts with K^+ or Na^+ were not present to help identify which dimer was produced by the oxidation of **Ph2NPyr**.

Chemical Formula: $C_{54}H_{32}N_2$
Molecular Weight: 708.86
m/z: 708.26 (100.0%), 709.26 (58.8%),
710.26 (17.2%), 711.27 (3.2%)

OR

Chemical Formula: $C_{27}H_{17}N$
Molecular Weight: 355.44

Chemical Formula: $C_{54}H_{33}N_2^+$
Molecular Weight: 709.87
m/z: 709.26 (100.0%), 710.27
(58.8%), 711.27 (17.0%),
712.27 (3.3%)

*Scheme 4.7 Sketch of the oxidation of **Ph2NPyr** with the two possible dimers which couple with two C atoms (**C-C dimer**) or with a N and a C atom (**C-N dimer**). In the **C-C dimer** there is the loss of two hydrogens and the dimer is neutral, whereas in the **C-N dimer** there is the loss of a single hydrogen and the dimer is positively charged.*

At the moment, the most plausible hypothesis concerning the product of the oxidation of **Ph2NPyr** is that one positively charged, i.e., the **C-N dimer**. As further support to our hypothesis, we know that the PL of this dimer is strongly red-shifted compared with that of **Ph2NPyr**. Moreover, from the CV analysis of **Ph2NPyr**, the dimer was oxidised at a higher potential than **Ph2NPyr**, which suggests an already charged species. From TLC, the dimer is less polar, and Rf is less than half that of **Ph2NPyr**. Moreover, reactive positions for the dimerization close to the phenyl ring are less likely because they are sterically protected. The opposite position far from the nitrogen, in the chemical structure, is also less likely to react; in fact, a dimer was observed (from CV) also for **PhMe2NPyr** where a methyl group should protect that carbon.

Furthermore, acridine, which is a nitrogen-doped anthracene, has been reported to form a green-emitting quaternary salt from the coupling of two acridine molecules via N and C atoms via electrochemical oxidation.[33] A similar reaction could also occur during the oxidation of azapyrenes. At the moment, this evidence suggests a **C-N dimer**; however, further analyses

such as IR spectroscopy and quantum chemical calculations will be carried out to better identify the oxidation product.

4.5 Electropolymerization

At a higher positive potential, **Ph2NPyr** showed a further irreversible oxidation process (Figure 4.10) similarly to the other azapyrene derivatives. For each azapyrene, oxidation resulted in film formation on the electrode surface, which was probably related to an electropolymerization process of azapyrenes forming chain-oligomers. New surface limited redox process appeared in voltammogram (highlighted by a *) at +0.4V and +1.0V vs. SCE and such processes could be related to the doping/de-doping mechanism of the film. Two reduction waves were observed in the potential range 1.5-2.0V. At this stage. it is not clear if these reductions were related to a de-doping process of the film or a diffusion-limited reduction of soluble (low molecular weight) oxidised oligomers.
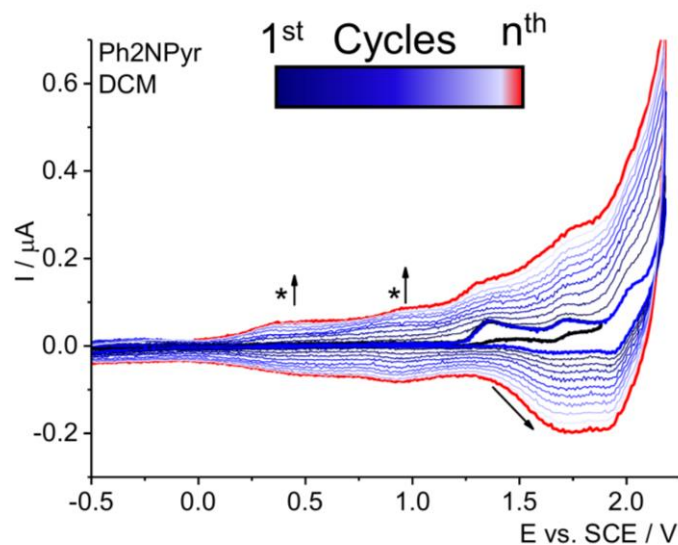

*Figure 4.10 Cyclic voltammetry of **Ph2NPyr** 0.91 mM. Measured at 1 V/s and 298 K with a Pt disk diameter of 125 μm as working electrode and SCE as reference electrode in 80 mM Bu$_4$NPF$_6$/DCM. Multiple cycles are reported with a blue scale, the last cycle is in red.*

The species **Ph2NPyr** was electropolymerized on ITO electrode in Bu$_4$NP$_6$/DCM and the film thus obtained was immersed in fresh DCM in order to remove the excess of electrolyte, soluble species and the unreacted **Ph2NPyr**. Then, the film was analysed by laser desorption

ionisation time-of-flight mass spectroscopy (LDI-TOF) and the spectrum is reported in Figure 4.11.
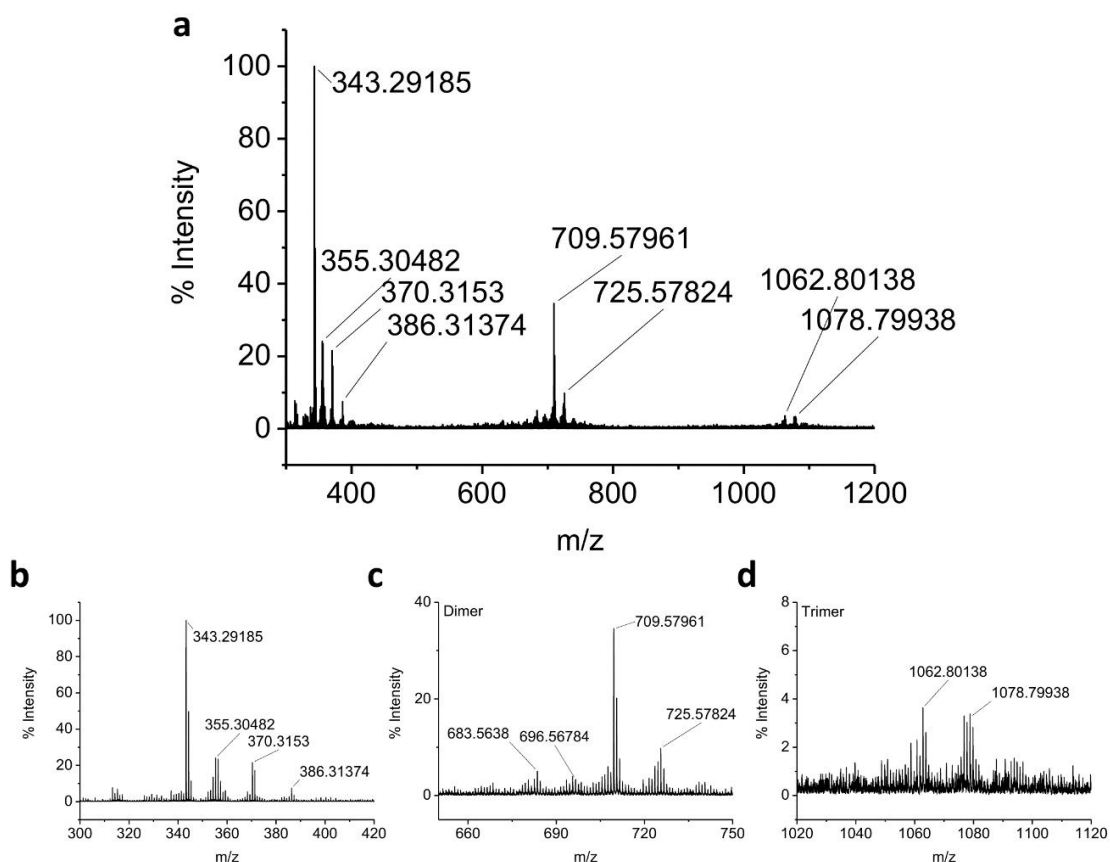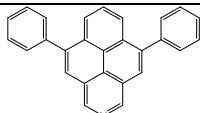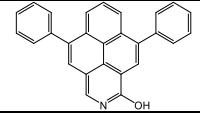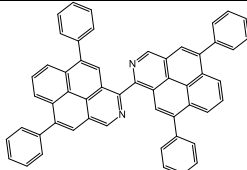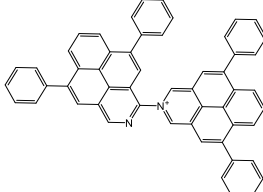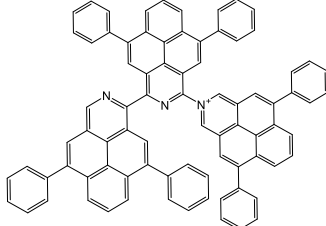

*Figure 4.11 LDI-TOF of electropolymerized **Ph2NPyr** on ITO (**a**) full m/z range, (**b**) precursor m/z range, (**c**) dimer m/z range, and (**d**) trimer m/z range. Relevant m/z values are highlighted, in particular **Ph2NPyr** MW is 355.44 g/mol, the linear **C-C dimer** MW 708.86 g/mol, the linear **C-N dimer** is 709.87 g/mol and a linear C-C-C trimer is 1062.29.*

In the mass-to-charge ratio (m/z) range from 300 to 1200, we observed different fragments of the **Ph2NPyr** electropolymerized film. In particular, between 300 and 420 m/z (Figure 4.11b) we recognize the presence of the pristine **Ph2NPyr** fragment (355.44 g/mol) at 355.3 m/z, the other fragments at higher m/z are related to chemically oxidised species with one or two hydroxy groups, in fact we observed fragments with m/z +16 and +31 than pristine **Ph2NPyr**. We hypothesised that the fragment of the **Ph2NPyr** film presented a hydroxy groups as a post-oligomerization reaction products. In fact, the film could maintain some positive trapped charges when the sample is drawn out of the cell and the contact with O_2 and H_2O from air can allow such a process; alternatively, but less probable, some residual and very small quantity of H_2O could be present in the electrolyte solution during the electropolymerization, which can act as a nucleophile toward the **Ph2NPyr** radical cation or oligomers. The reason why we

observed fragments at a lower mass than that of pristine **Ph2NPyr** (-12 m/z) is related to fragmentation of the oligomers due to the laser power required for ionisation and lack of a matrix. A table of the observed fragments with the proposed structures is reported below in table 4.2.

Table 4.2: Observed fragments and proposed structures

Observed m/z	Calculated m/z	Fragment Structures
355.30	355.14	
370.31	371.13	
709.57	708.26	
709.57	709.26	
1062.8	1062.38	

In the dimer range of m/z from 650 to 750, we observed at least four different fragments; the most intense is that at 709.6 m/z which is related to a dimeric species of **Ph2NPyr**. In particular, if there is a coupling of 2 sp^2 C, we would have a linear dimer with a chemical formula of $[C_{54}H_{32}N_2]$ and a MW of 708.86 g/mol. Instead, if the coupling occurs between a pyridinic nitrogen and an sp^2 C, we would have a positively charged dimer with an additional hydrogen, i.e., $[C_{54}H_{33}N_2]^+$ and a MW of 709.86, which is very similar to the value observed in the mass spectrum. Again, we observed chemically oxidised species with one hydroxy group and +16 m/z (725.6 m/z) compared to the dimer. Those at lower m/z than the dimer are related to fragmentation with the loss of carbon atoms. Finally, in the trimer (m/z range from

1020 to 1120) we observed very low signals, but we can recognise at least two species: at 1062.8 a linear trimer of **Ph2NPyr**, even though it is not possible to distinguish whether the bond is between N-C or C-C or a combination of the two. At a higher m/z, we observed a fragment of the trimer with one hydroxy group at 1078.8 m/z.

4.6 Electrochemiluminescence

The electrochemiluminescence (ECL) of the azapyrenes was investigated in Bu_4NPF_6/ACN electrolyte solution. However, all azapyrene derivatives showed poor solubility in relatively polar solvents such as ACN. In particular, we estimated a limit of solubility, by adding small solvent aliquots to a known amount of species, that is 0.9mM for **Ph2NPyr** and 0.6mM for **Ph1NPyr**. The ECL of **Tol2NPyr**, which has the highest fluorescence quantum yield among the 2-azapyrenes[4] and electrochemical properties similar to those of **Ph2NPyr**, was initially investigated by ion annihilation. Figure 4.12 shows the CV and chronoamperometry (CA) measurements during the ion annihilation experiment with **Tol2NPyr**. The ECL signal was absent in CV, and it was exclusively observed in CA when the radical anion was generated before the radical cation. Moreover, the ECL in CA during ion annihilation showed a very fast decay of the signal. This behaviour is in agreement with the high chemical reactivity of the radical cation, which did not live enough to diffuse and annihilate with the radical anion. Unfortunately, the ECL signal was too low to record an ECL spectrum via ion annihilation.

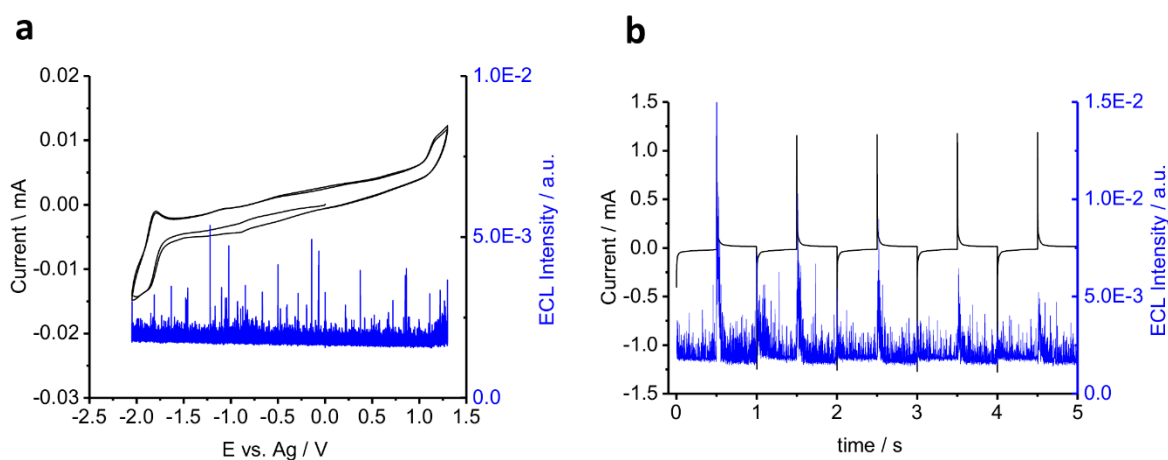*Figure 4.12 (**a**) CV of **Tol2NPyr** 0.52 mM (saturated) in 80mM Bu_4NPF_6/ACN at 400 mV/s and ECL signal (in blue). (**b**) CA E1 -2.15 V for 500 ms and E2 +1.45 V for 500 ms. Measured with a Pt disk with a diameter of 2 mm as working electrode oriented in front of the PMT, Ag wire as quasi-reference electrode. Measured in a dark box at 298 K. Amplification of the PMT: 650 V.*

Since the radical anion of the azapyrene derivatives was observed to be always more stable than the radical cation, also in Bu₄NPF₆/ACN electrolyte solution, we decided to use a sacrificial co-reactant, namely benzoyl-peroxide (**BPO**) or a peroxydisulfate salt (($Bu_4N)_2S_2O_8$) for the ECL generation. Once reduced, both the co-reactants generate a highly reactive (oxidant) radical which reacts with the luminophore radical anion to produce the luminophore excited state.

Figure 4.13 shows the CV-ECL and spectrum of **Ph2NPyr** in a slightly saturated solution (0.97mM) in Bu₄NPF₆/ACN with 5.6 mM **BPO**. The CV curve showed a first chemically irreversible reduction of the **BPO** at -1.25V followed at more negative potentials by the reduction of **Ph2NPyr**. The peak current of the **BPO** reduction was higher than that of the **Ph2NPyr** reduction due to the higher concentration. As soon as the luminophore was reduced, the ECL signal (blue) started to increase and partially continued to increase during the back-scan. The ECL spectrum were obtained using a double-step potential experiment with a frequency of 10 Hz. This method results in a segmented spectrum with many spikes but provides a lower amount of degradation products and a partial recovery of the luminophore concentration at the electrode surface. The upper envelope was highlighted and a continuous ECL spectrum was thus obtained. The ECL spectrum of **Ph2NPyr** showed two ECL emissions centred at 394 nm and 508 nm. The first band at lower λ was less intense than the second band and closely matched the PL spectrum (red line). It is worth noting that, the second broad band at higher λ was not observed in the PL spectrum.
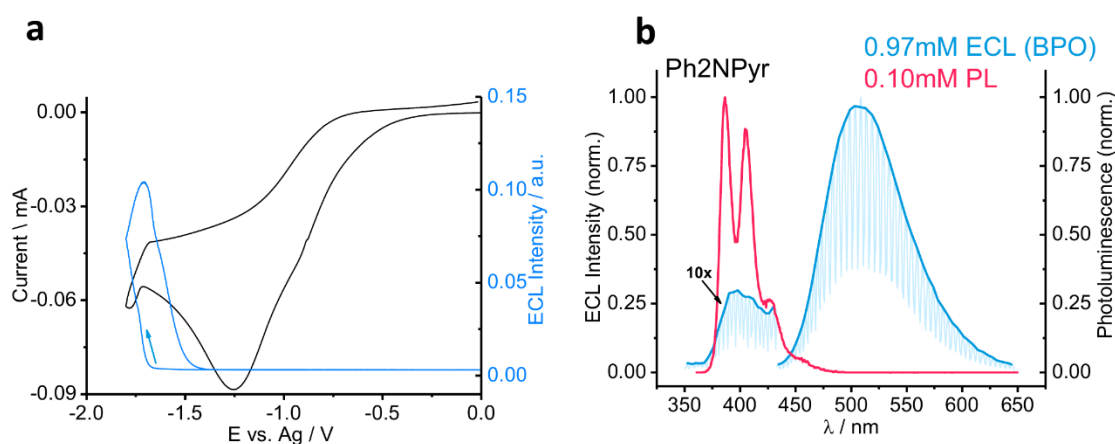
*Figure 4.13 (**a**) CV-ECL of **Ph2NPyr** 0.97 (saturated) in Bu₄NPF₆/ACN and 5.6mM **BPO**. Measured at 250mV/s and 298 K with a Pt disk of diameter 2 mm as working electrode, Ag wire as quasi reference electrode. Measured in a dark box, amplification of the PMT 650 V. (**b**) ECL and PL spectra of **Ph2NPyr**, the ECL spectrum was recorder with a double potential step (E1 -1.9 V and E2 0 V with 100 ms each). Amplification of the PMT 750 V, integration time of 150 ms, and monochromator speed rate of 600 nm/min.*

The ECL spectra of the other 2-azapyrene derivatives, reported in Figure 4.14, showed similar ECL behaviour to **Ph2NPyr** with a double-wavelength emission which was not observed in PL. The difference in the ratio between the two emission bands could be related to the different solubility limits of the functionalized 2-azapyrenes (different concentrations of luminophores) or could be specific to their molecular structures. More polar groups such as methoxy or fluorine groups on the phenyl rings showed a higher $I(\lambda 400)/I(\lambda 508)$ ratio, with **MeOPh2NPyr** having the emission at lower wavelengths more intense than the one at higher λ, even at saturated luminophore concentrations.

A plausible hypothesis to understand the origin of such two ECL emission bands could be found in the formation of excimers during the ECL process with BPO as co-reactant.
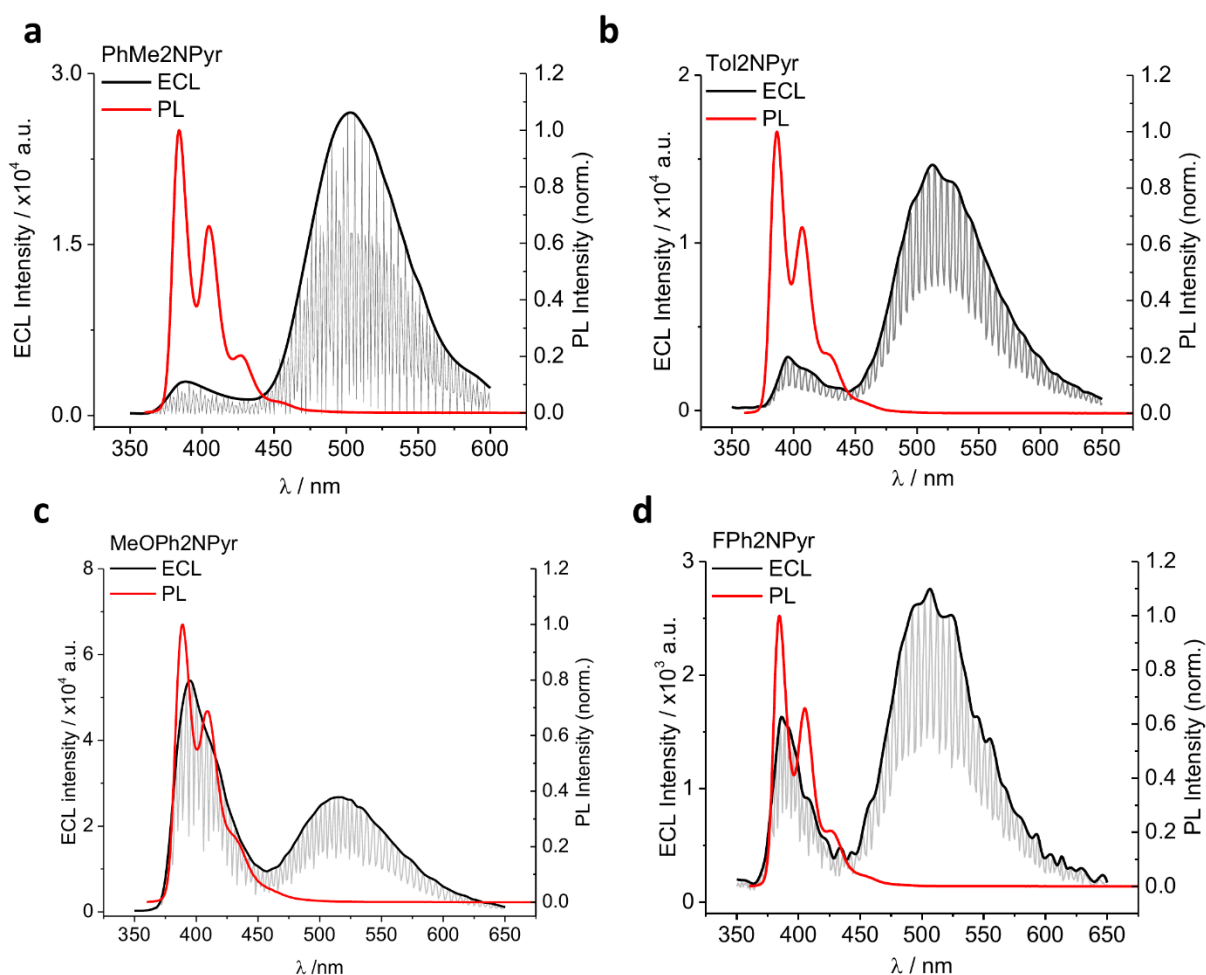
*Figure 4.14 ECL and PL spectra of (**a**) **PhMe2NPyr** 0.89 mM (saturated) and 5.5 mM **BPO**, (**b**) **Tol2NPyr** 0.52 mM (saturated) and 3.1 mM **BPO**, (**c**) **MeOPh2NPyr** 0.92 mM (saturated) and 5.4 mM **BPO** and (**d**) **FPh2NPyr** 0.46 mM (saturated) and 2.41 mM **BPO** in 80 mM Bu_4NPF_6/ACN. Measured with a Pt disk of diameter 2 mm as working electrode and Ag wire as quasi-reference electrode. The ECL spectra were recorded using a double potential step. Measured in a dark box, amplification of the PMT 750 V, integration time 150 ms, and monochromator speed 600 nm/min.*

Excimer emission is usually concentration dependant. Therefore, we measured the ECL spectra at different **Ph2NPyr** concentrations while keeping the **BPO** concentration constant. Figure 4.15 shows the ECL spectra of **Ph2NPyr** in Bu$_4$NPF$_6$/ACN (0.08M) at different luminophore concentrations. When the concentration was decreased from saturated to 0.22mM, the ECL spectrum changed. In particular, the ratio of the two band maxima, i.e. $I_{ECL}(\lambda^{394})$/ $I_{ECL}(\lambda^{508})$ ratio increased, and the monomer emission band became the dominant emission. A concentration-dependent experiment was also performed for the photoluminescence of **Ph2NPyr**. Although strong self-absorption and internal filter phenomena occurred at higher concentrations, the PL spectra (Figure 4.15d) did not show a longer wavelength emission at higher concentrations. In contrast to pyrene, the longer-wavelength emission attributed to an excimer of azapyrene was generated only during the ECL experiment.
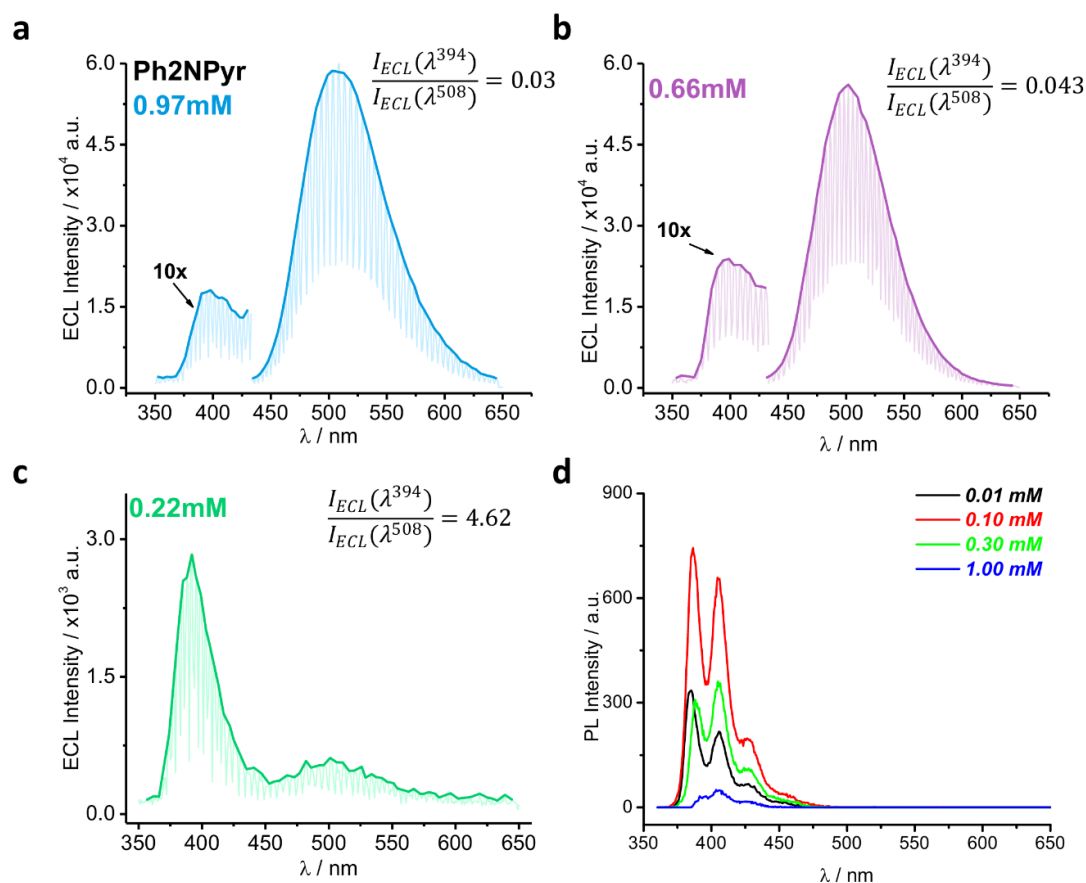
*Figure 4.15 ECL spectra of **Ph2NPyr** and 5.6 mM **BPO** in 80 mM Bu$_4$NPF$_6$/ACN, at (**a**) 0.97 mM (saturated) (**b**) 0.66 mM, and (**c**) 0.22 mM. (**d**) PL of **Ph2NPyr** in ACN at increasing concentration. ECL was measured with a Pt disk with a diameter of 2 mm as the working electrode and Ag wire as quasi-reference electrode. The ECL spectra were recorded using a double potential step. Measured in a dark box, amplification of the PMT 750 V, integration time 150 ms, and monochromator speed 600 nm/min.*

The ECL behaviour of the other azapyrene isomer, **Ph1NPyr**, is reported in Figure 4.16. It shows the ECL spectrum of **Ph1NPyr** 0.49mM with **BPO** in Bu4NPF6/ACN compared with its PL spectrum. Interestingly, even at a concentration close to the saturation limit, **Ph1NPyr** showed only a single ECL emission band which closely matched the PL emission band. This behaviour is significantly different from that of the isomers 2-azapyrenes and is probably related to a different ECL mechanism occurring for **Ph1NPyr**. Moreover, under similar conditions, the ECL signal of **Ph1NPyr** is more than one order of magnitude lower than the ECL signal of **Ph2NPyr** (0.66mM). From the reported fluorescence quantum yields in DCM, **Ph2NPyr** (φ 0.34) should emit more than **Ph1NPyr** (φ 0.20),[3,4] but it does not explain the remarkable difference in the ECL intensity. The PL and ECL properties of the investigated azapyrenes are summarised in Table 4.3.
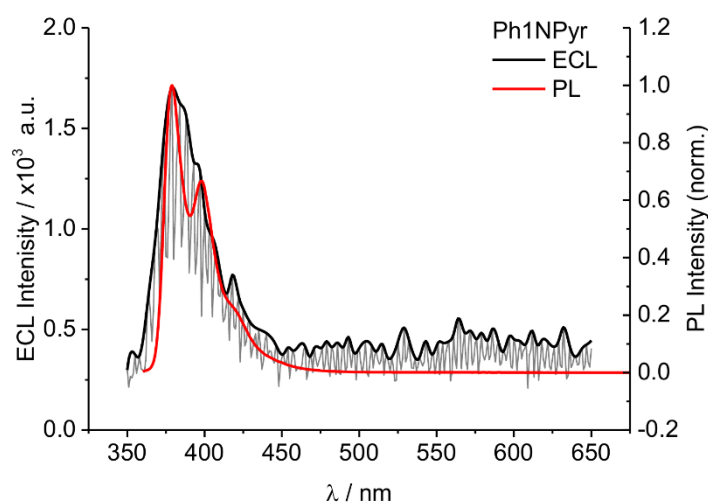

*Figure 4.16 ECL and PL spectra of **Ph1NPyr** 0.49 mM and 5.3 mM **BPO** in 80 mM Bu4NPF6/ACN. Measured with a Pt disk of diameter 2 mm as working electrode and Ag wire as quasi-reference electrode. The ECL spectra were recorded using a double potential step. Measured in a dark box, amplification of the PMT 750 V, integration time 150 ms, and monochromator speed 600 nm/min.*

Table 4.3: PL and ECL Properties

Species	λ_{Em1}^{PL}(nm)[a]	λ_{Em2}^{PL}(nm)[a]	λ_{Em3}^{PL}(nm)[a]	λ_{Em1}^{ECL}(nm)[b]	λ_{Em2}^{ECL}(nm)[b]	E^{S1}(eV)[c]	$-\Delta H_{Ann.}^{ECL}$(eV)[d]	$-\Delta H_{BPO}^{ECL}$(eV)[e]
Ph2NPyr	385	405	427	394	508	3.24	3.13	3.29
PhMe2NPyr	384	404	426	388	503	3.24	3.12	3.26
Tol2NPyr	387	407	428	395	513	3.22	3.10	3.28
MeOPh2NPyr	389	409	433	396	515	3.21	3.06	3.28
FPh2NPyr	385	405	427	387	507	3.24	3.12	3.23
Ph1NPyr	379	398	421	379	X	3.29	3.07	3.07

Notes: ECL was measured at 298 K with a Pt WE disk of 2 mm diameter and Ag quasi-reference electrode. PMT Voltage of 750V, integration time of 150ms and 600 nm/min were used. [a] Diluted solution in DCM. [b](80mM)

Energy analysis of the homogenous ion annihilation reaction of azapyrenes between radical cations and radical anions results in an ECL energy-deficient system because the enthalpy of the reaction is lower than the energy required to populate the singlet excited state. This deficiency is around 0.12 eV for most of the 2-azapyrene, whereas it has a higher value for 1-azapyrene (0.22 eV). However, even if the energy to populate the singlet excited state is insufficient, ion annihilation can lead to the formation of triplet states (T-Route) which can undergo triplet-triplet annihilation (TTA) to generate the singlet excited state or excimer formation (E-Route).

When **BPO** is used as a sacrificial co-reactant, an oxidant radical is generated by the dissociative electron transfer of **BPO**, namely, PhCOO$^\cdot$. This radical has been reported to have an estimated reduction potential $E_{1/2}$(PhCOO$^-$,PhCOO$^\cdot$) of +1.5V vs. SCE. Similarly to ion annihilation, we calculated the enthalpy of reaction for the homogenous electron transfer between PhCOO$^\cdot$ and the azapyrene radical anion and compared to the energy requirement for the singlet excited state. We observed that the 2-azapyrene molecules, except for **FPh2NPyr**, have an enthalpy of reaction higher than that of E^{S1}. Therefore, we can reasonably expect that the reaction will populate the singlet excited state (S Route). The reaction energy for **FPh2NPyr** and especially for **Ph1NPyr**, was lower than the energy required to populate the singlet state E^{S1}, which could explain the lower ECL intensity observed for the two azapyrenes. Moreover, despite the two azapyrenes resulted in an energy-deficient mechanism with TTA mechanism for the emission at higher energy, only **FPh2NPyr** exhibited excimer emission, whereas **Ph1NPyr** had just its fluorescence emission. This remarkable difference, assuming that both **FPh2NPyr** and **Ph1NPyr** follow a T-Route mechanism and both are able to form an excimer under the right conditions, allow to exclude the TTA mechanism as responsible for the excimer formation, otherwise the excimer should be observed also for **Ph1NPyr** during ECL with BPO.

The ECL of **Ph2NPyr** was also tested using $(Bu_4N)_2S_2O_8$ as the sacrificial co-reactant. We chose to use a bis(tetrabutylammonium)peroxydisulfate salt to improve the solubility of peroxydisulfate in ACN, and the experimental procedure to prepare $(Bu_4N)_2S_2O_8$ is reported in the experimental section. In contrast to **BPO**, $S_2O_8^{2-}$ is not directly reduced at the electrode in aprotic ACN but is instead homogeneously reduced by the azapyrene radical anion, **Ph2NPyr•⁻**, in a redox catalytic mechanism. The $SO_4^{•-}$ radical anion, produced by the cleavage of the O-O bond of reduced $S_2O_8^{•3-}$, is a highly oxidant intermediate with an estimated reduction potential ≥+3.15V vs. SCE.[16] We chose to use a low concentration of $S_2O_8^{2-}$ (4.2mM) because it was reported to act as a quencher for triplet excited states, such as for the ECL of $[Ru(bpy)]^{2+}$.[34] Figure 4.17 shows the CV-ECL and ECL spectra of **Ph2NPyr** with $(Bu_4N)_2S_2O_8$ in Bu_4NPF_6/ACN.
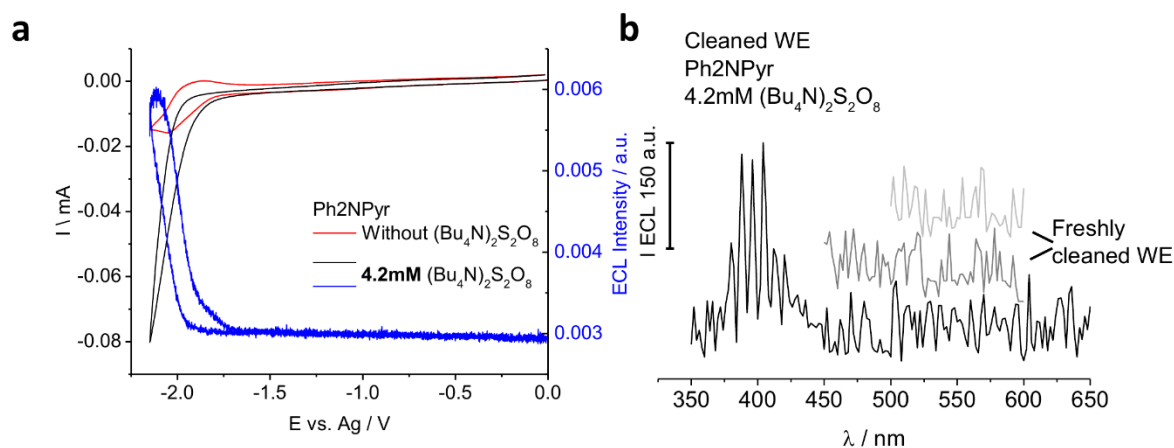
*Figure 4.17 (**a**) CV-ECL of **Ph2NPyr** 0.97 (saturated) in Bu₄NPF₆/ACN without (red) and with 4.2 mM (Bu₄N)₂S₂O₈. Measured at 250mV/s and 298 K with a Pt disk of diameter 2 mm as working electrode and Ag wire quasi-reference electrode. Measured in a dark box, amplification of the PMT 650 V. (**b**) ECL spectra of **Ph2NPyr**, the ECL spectrum was recorder with a double potential, before each ECL spectrum the working electrode was mechanical polished and dried under vacuum. Amplification of the PMT 750 V, integration time 150 ms, and monochromator speed rate 600 nm/min.*

The CV curve shows a catalytic mechanism for the reduction of $S_2O_8^{2-}$ by the **Ph2NPyr** radical anion, once the reduction occurred, the ECL signal increased. Comparing the ECL signal in the CV to that from **BPO** as a co-reactant, we observed a lower intensity when $S_2O_8^{2-}$ was used as a co-reactant. Moreover, the signal was observed to decrease significantly between repeated cycles because of electrode passivation. However, the original ECL intensity and current values were restored by cleaning the Pt working electrode.

Studies reported in literature concerning the ECL of several PAH in ACN/benzene and $S_2O_8^{2-}$ as co-reactants demonstrated that ECL is initiated by the electrochemical reduction of PAH and that the excited state can be produced by ion-annihilation between the luminophore radical ions, in which the radical cation is generated by homogeneous oxidation by $SO_4^{\bullet-}$.[16,35] In our condition, we observed electrode passivation, and we can suppose that at 4.2mM of $S_2O_8^{2-}$, the homogeneous oxidation of **Ph2NPyr** includes processes at higher oxidation states for which the electro-polymerization of the azapyrene occurs on the electrode surface. Becker at el. [35] observed an electrode-filming phenomenon for the ECL of rubrene in the presence of $S_2O_8^{2-}$ as well, which led to a decrease in the catalytic current and ECL signal.

The ECL spectrum exclusively showed fluorescence emission at 400 nm, although a very weak ECL signal was recorded. Because electro-polymerization occurred during the recording of the ECL spectrum, which could lead to a decrease in the ECL signal, we performed ECL spectra with precaution of limiting the scanned wavelengths and cleaning the WE before each spectrum. However, even for a freshly cleaned WE and starting to record the spectrum at 500 nm, excimer emission was not observed. We hypothesise that the singlet excited state of **Ph2NPyr** is generated by the classic S-Route by the reaction of **Ph2NPyr•-** with $SO_4^{\bullet-}$, whereas **Ph2NPyr•+** is further oxidised by additional $SO_4^{\bullet-}$, leading to electro-polymerization (Scheme 4.8). Further analysis at lower co-reactant concentrations is required to better understand the ECL mechanism with $S_2O_8^{2-}$ and trying to avoid electropolymerization phenomenon.

$$NPyr + e^- \rightarrow NPyr^{\bullet-} \qquad \text{(electrochemical reduction)} \quad (1)$$

$$NPyr^{\bullet-} + S_2O_8^{2-} \rightarrow NPyr + S_2O_8^{\bullet 3-} \qquad \text{(homogeneous reduction)} \quad (2)$$

$$S_2O_8^{\bullet 3-} \rightarrow SO_4^{\bullet-} + SO_4^{2-} \qquad \text{(Intermediate formation)} \quad (3)$$

$$NPyr^{\bullet-} + SO_4^{\bullet-} \rightarrow {}^1[NPyr]^* + SO_4^{2-} \qquad \text{(Singlet "S-Route" ECL)} \quad (4)$$

$$NPyr + SO_4^{\bullet-} \rightarrow NPyr^{\bullet+} + SO_4^{2-} \qquad \text{(homogeneous oxidation)} \quad (4b)$$

$$NPyr^{\bullet+} \rightarrow P \qquad \text{(radical cation degradation)} \quad (5b)$$

$$P + nSO_4^{\bullet-} \rightarrow \text{oligomers} \qquad \text{(oligomerisation)} \quad (6b)$$
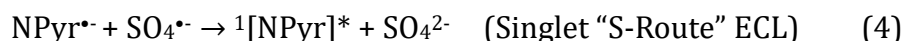
*Scheme 4.8 Proposed reaction mechanism for ECL of **Ph2NPyr** with $S_2O_8^{2-}$ as a sacrificial co-reactant with ECL S-Route mechanism. Reactions "b" involve homogenous oxidation of **Ph2NPyr** by $SO_4^{\bullet-}$ which leads to electrode fouling.*

4.7 Understanding the ECL Mechanism with BPO

The electrochemiluminescence with **BPO** as co-reactant showed a double wavelength emission for all the 2-azapyrene derivatives which was dependent on the luminophore concentration, with the longer wavelength emission not observed in PL even at comparable concentration used in ECL experiments. **Ph1NPyr** exhibited an ECL spectrum that agreed with its PL spectrum and did not show any excimer emission. The enthalpy of reaction for **Ph1NPyr** is lower than the energy required to populate the singlet excited state. Therefore, triplet formation (T-Route) and then TTA are responsible for the ECL of **Ph1NPyr** with **BPO**.

To better understand the mechanism of the ECL of 2-azapyrenes, we evaluated the different possible pathways that could lead to a longer wavelength emission, such as a different chemical species from side reactions with **BPO** or from radical cation decomposition products. Alternatively, different excimer routes, such as triplet–triplet annihilation to excimer for 2-azapyrenes or ion-annihilation, in which the radical cation was generated by the homogeneous oxidation with PhCOO$^{\bullet}$.

We can exclude the emission from the decomposition product (dimer) of **Ph2NPyr$^{\bullet+}$** because, as we previously observed, the PL maximum of this product was centred at 545 nm, whereas the ECL maximum was at 508 nm. However, the dimer generated by the coupling of **Ph2NPyr$^{\bullet+}$** was observed to be present in the ECL solution by analysing ex-situ the PL spectrum of the recovered solution after the ECL experiment. The PL spectrum of the recovered solution of **Ph2NPyr** with **BPO** in Bu$_4$NPF$_6$/ACN after ECL is shown in Figure 4.18. The dimer generated by the oxidation of **Ph2NPyr** could be produced at the counter electrode when the reduction of **Ph2NPyr** and **BPO** occurs at the working electrode or PhCOO$^{\bullet}$ can homogenously oxidise **Ph2NPyr** to its radical cation which then dimerise. Nonetheless, the ECL band at higher wavelengths did not correspond to the dimer PL. Moreover, the excitation spectrum of the emitting species at 560 nm closely match the absorption spectrum obtained by the oxidative electrolysis (Figure 4.8).
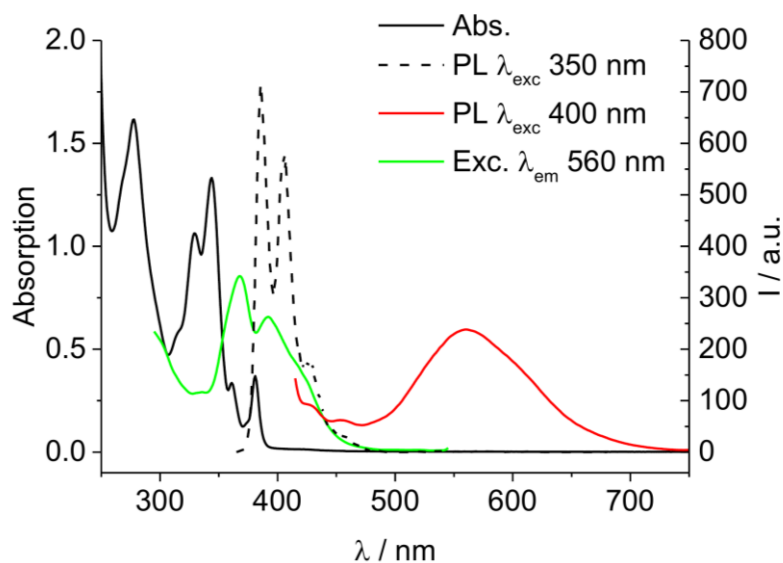
*Figure 4.18 Absorption (black full line), PL (black dashed line λexc 350 nm) and (red line λexc 400 nm) spectra, and excitation (green line λem 560 nm) spectrum of **Ph2NPyr** and **BPO** in the Bu₄NPF₆/ACN of the solution recovered after the ECL experiment.*

An unexpected side reaction can occur between **BPO** or PhCOO• and 2-azapyrene. Therefore, we performed ECL experiments, as shown in Figure 4.19, with increasing **BPO** concentration while keeping the **Tol2NPyr** and Bu₄NPF₆ concentrations fixed. However, we did not observe any significant change in the ECL spectrum with the **BPO** concentration (except for a general lower ECL emission with lower **BPO** concentration), which instead would be expected for a second-order chemical reaction. We ruled out that the longer λ emission was related to a different chemical species.
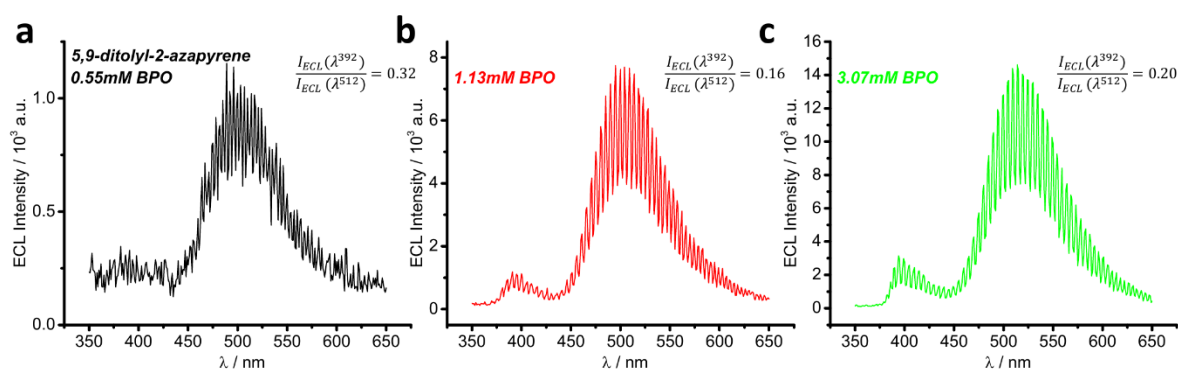
*Figure 4.19 ECL Spectra of **Tol2NPyr** 0.52 mM in the Bu₄NPF₆/ACN with (**a**) 0.55 mM, (**b**) 1.13 mM, and (**c**) 3.07 mM of **BPO**. ECL was measured with a Pt disk with a diameter of 2 mm as working electrode and Ag wire as quasi-reference electrode. The ECL spectra were recorded using a double potential step. Measured in a dark box, amplification of the PMT 750 V, integration time 150 ms, and monochromator speed 600 nm/min.*

Triplet and triplet-triplet annihilation have been proposed to produce excimers. However, we did not observe any excimer for **Ph1NPyr**, and from the enthalpy of reaction with **BPO**, the energy for most of the 2-azapyrene was sufficient to populate the singlet excited state. We expected that the triplet should not play a role in the excimer formation of 2-azapyrenes.

Finally, excimer formation could be produced by ion-annihilation, in which the radical cation was generated by homogeneous oxidation by PhCOO$^{\bullet}$. As observed from the enthalpy of ion-annihilation in Table 4.3, the mechanism is energy-deficient and cannot populate the singlet excited state, but an excimer with a lower excited state energy could be generated in a very efficient process when the two radical ions are in close proximity in a contact radical ion pair by an attractive electrostatic interaction. To confirm this hypothesis, we performed ion-annihilation of **PhMe2NPyr** and through a 455 nm cut-off high band pass filter we removed the emission from the fluorescence during ECL.

Figure 4.20 shows the chronoamperometry ECL for a double-step potential without (a) and with the 455 nm filter (b) and with a mixed ion annihilation system (c).
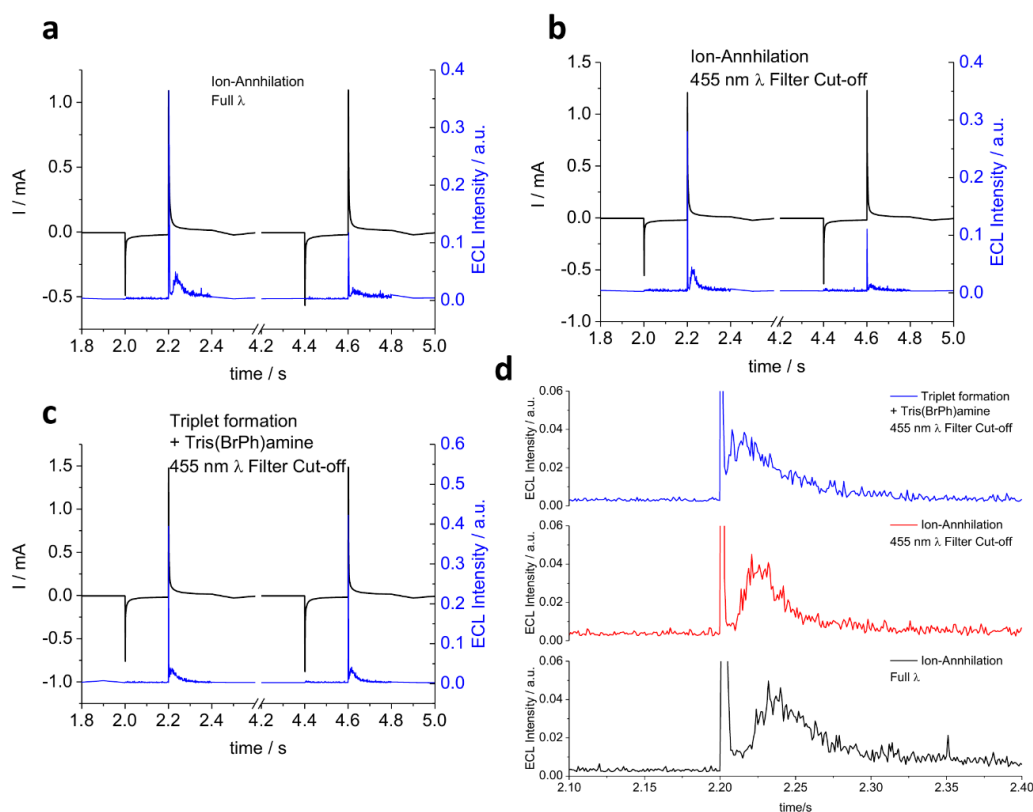
*Figure 4.20 CA-ECL of **PhMe2NPyr** 0.6mM in 80 mM Bu4NPF6/ACN without (**a**) and (**b**) with a 455 nm high-band-pass filter. (**c**) CA of **PhMe2NPyr** 0.6 mM and tris(bromophenyl)amine 0.6 mM with a 455 nm high-band-pass filter. (**d**) Comparison of ECL decay during the 1st ECL pulse. ECL was measured with a Pt disk with a diameter of 2 mm as working electrode and Ag wire as quasi-reference electrode. Each potential step lasted for 200 ms. Amplification of the PMT 650 V.*

During ion-annihilation, ECL emission with λ higher than 455 nm was observed, confirming the presence of the excimer. The second double-step pulse at 4.6s showed a lower ECL intensity than the 1st pulse, probably because the working electrode started to passivate by the less soluble azapyrene dimer formed during the chemically irreversible oxidation or because some platinum oxide was produced at the electrode surface.

Interestingly, for the 1st pulse at 2.2s, we observed (Figure 4.20d) a very intense ECL spike which rapidly decreased after 6 ms (without filter, black) and 4 ms (with 455 nm filter, red). At longer times, a delayed ECL emission raised after 9-14ms and decreased after 100 ms (without filter) or 70 ms (with 455 nm filter). Moreover, the decay of the delayed ECL had two different behaviours when the 455 nm filter was mounted or not. In particular, we observed a clear single exponential decay behaviour when the filter was mounted. Whereas, without the filter, the decay was less steep and could be the result of multiple ECL mechanisms. Further analysis is required to explain the exact nature of this delay. At the moment, we hypothesise that the spiked ECL signal is related to an excited state produced close to the electrode, then the observed very rapid decay could be caused by a quencher generated at the proximity of the electrode. A delayed ECL is then observed because ECL occurs far from the electrode surface in order to not quench. We can exclude that the delayed ECL was due to triplet–triplet annihilation to the singlet excited state (fluorescence) because this behaviour was also observed when the 455 nm filter was mounted. Further studies are required to elucidate the exact mechanism underlying the delayed ECL emission.

In order to exclude the formation of an excimer by the triplet-triplet annihilation mechanism, we added tris(bromophenyl)amine to the solution. Mixed ion annihilation (Figure 4.20c) involved the stable radical cation of the amine and the stable radical anion of **PhMe2NPyr**. Again, the enthalpy of reaction would not be sufficient to populate the singlet excited state of **PhMe2NPyr** and triplets would be generated. However, we observed an ECL emission with λ > 455 nm. At the moment, we cannot distinguish whether TTA leads to the excimer formation of **PhMe2NPyr** or if the higher λ is related to an exciplex between the amine and **PhMe2NPyr**. Tris-tolylamine has been reported to forms exciplexes with many PAHs.[16] The ECL signal for mixed-ion annihilation was more intense and stable between successive pulses, with a sharp spike and a shorter delayed emission. However, the signal was not sufficiently intense to record an ECL spectrum to distinguish between an excimer or an exciplex.

A sketch of the proposed ECL mechanism with **BPO** for 2-azapyrenes is shown in Figure 4.21.
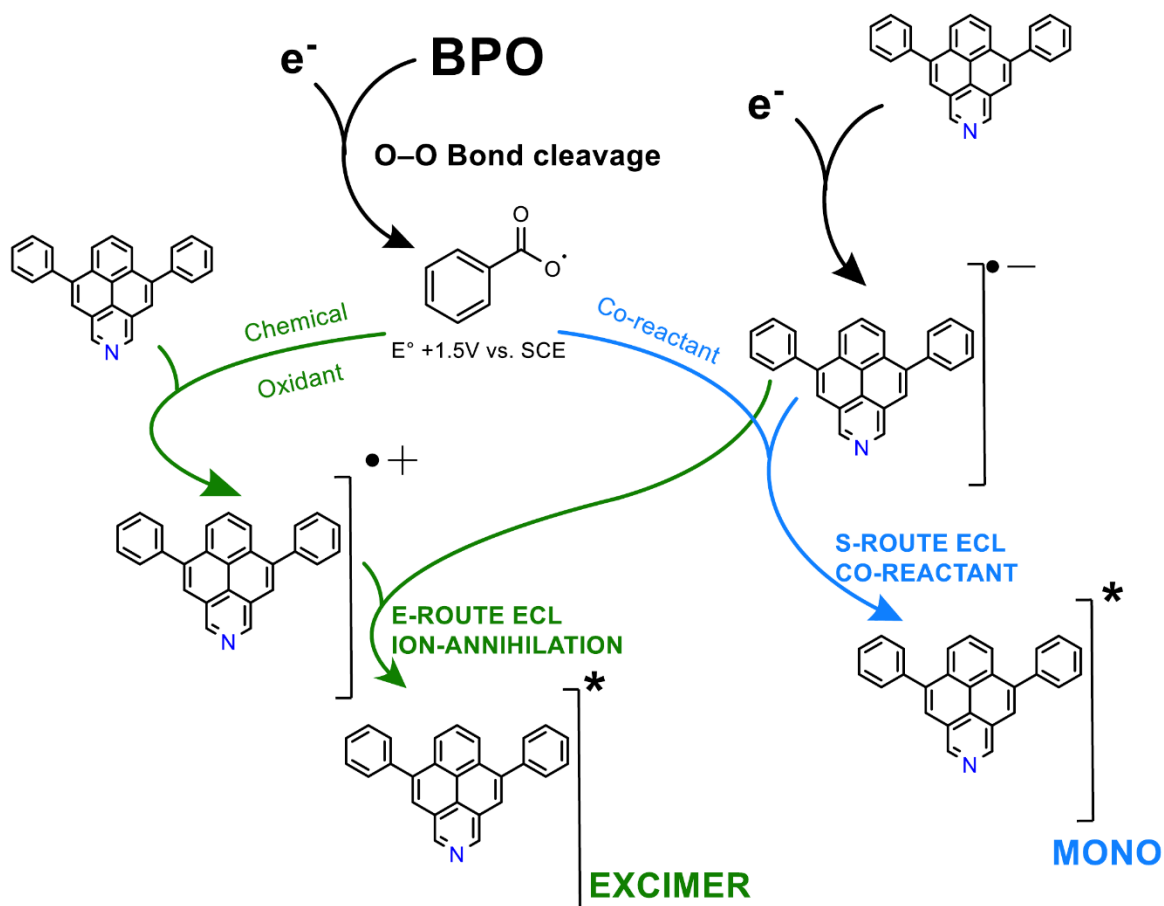
*Figure 4.21 Proposed ECL mechanism of 2-azapyrenes with **BPO** via two competing pathways. The S-route leads to monomer (fluorescence) emission. E-Route leads to excimer emission via ion annihilation.*

Such a mechanism involves two competing pathways, where PhCOO$^•$ acts either as a co-reactant (reactive intermediate) or as a chemical oxidiser. In the former pathway, the classical S route mechanism occurs where PhCOO$^•$ reacts with the **Ph2NPyr** radical anion and the singlet excited state is produced, which then emits at 400 nm. In the latter pathway, PhCOO$^•$ (in excess) reacts with neutral **Ph2NPyr**, and **Ph2NPyr$^{•+}$** is homogenously produced very close to the electrode. In the same potential step at the electrode, **Ph2NPyr$^{•-}$** is electrochemically produced and the ion-annihilation between the two radical ions is favoured because they are produced in close proximity in the same potential step, and because of favourable electrostatic interactions the excimer is produced which will emit at 508 nm.

The above mechanism would explain the concentration dependency of the excimer because both the homogenous reaction between PhCOO• and **Ph2NPyr** and ion annihilation will depend on the **Ph2NPyr** concentration. This mechanism explains why the excimer was not observed in PL, since its non-trivial formation involves radical ions of 2-azapyrenes which are not produced during photoluminescence. Finally, this mechanism would explain the single ECL emission for **Ph1NPyr** because its oxidation potential is higher than the reduction potential of PhCOO•, therefore the homogenous oxidation could not occur for **Ph1NPyr**.

To support the last statement regarding **Ph1NPyr** which does not form an excimer when **BPO** is used as co-reactant, we performed ion-annihilation of **Ph1NPyr** in Bu_4NPF_6/ACN without (a) and with (b) a 455 nm high-band pass cutoff filter, as shown in Figure 4.22.
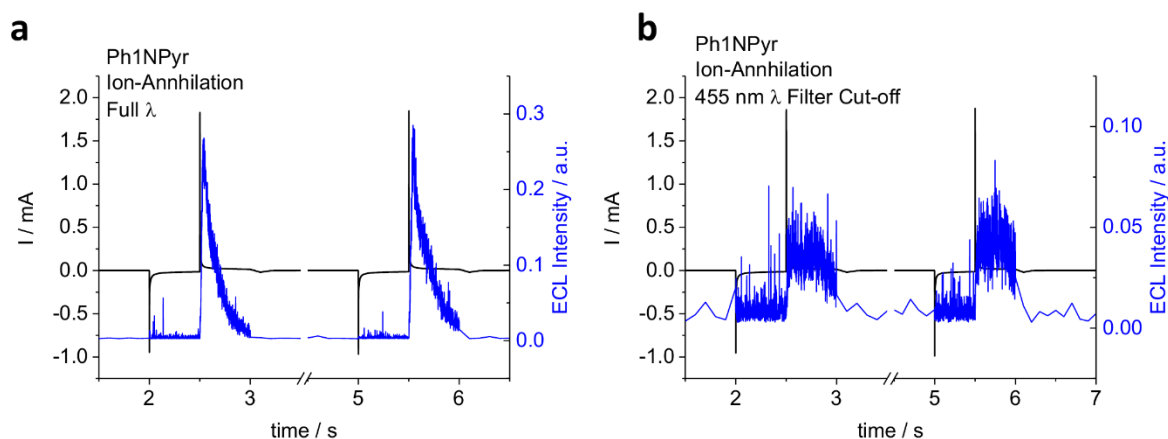
*Figure 4.22 CA-ECL of **Ph1NPyr** 0.8mM (sat.) in 80 mM Bu_4NPF_6/ACN without (**a**) and (**b**) with a 455 nm high-band-pass filter. ECL was measured with a Pt disk with a diameter of 2 mm as working electrode and Ag wire as quasi-reference electrode. Each potential step lasted for 500 ms. Amplification of the PMT 750 V.*

We observed a higher ECL intensity without the filter which can be explained by the fact that the detector is closer to the working electrode and via the TTA mechanism, there is monomer emission (fluorescence) similar to the ECL with **BPO**. On the other hand, when the 455 nm filter is placed in front of the photomultiplier tube, a lower ECL signal is observed during ion annihilation with an emission wavelength higher than 455 nm. This evidence suggests that an excimer can be produced via the ion-annihilation of **Ph1NPyr** and supports the hypothesis that with **BPO**, PhCOO• cannot homogeneously oxidise **Ph1NPyr**, and for this reason, the excimer of **Ph1NPyr** was not observed in the ECL with **BPO**.

Further evidence for the mechanism reported in Figure 4.21 was obtained by performing ECL with **BPO** in DMF or THF, as shown in Figure 4.23. In the above solvents, the electrolyte anodic stability potential window is narrower than the 1st oxidation of **Tol2NPyr**, and PhCOO• is more likely able to oxidise the solvent, for which the concentration is order of magnitude that of **Tol2NPyr**. The ECL emission in the above solvents was strongly reduced compared to that one in ACN, and a single emission band corresponding to **Tol2NPyr** PL was observed. Excimer emission was mostly absent because radical cation formation via homogeneous electron transfer was suppressed. The band at 552 nm in THF could be related to a degradation product of **Tol2NPyr** or to a small amount of excimer.
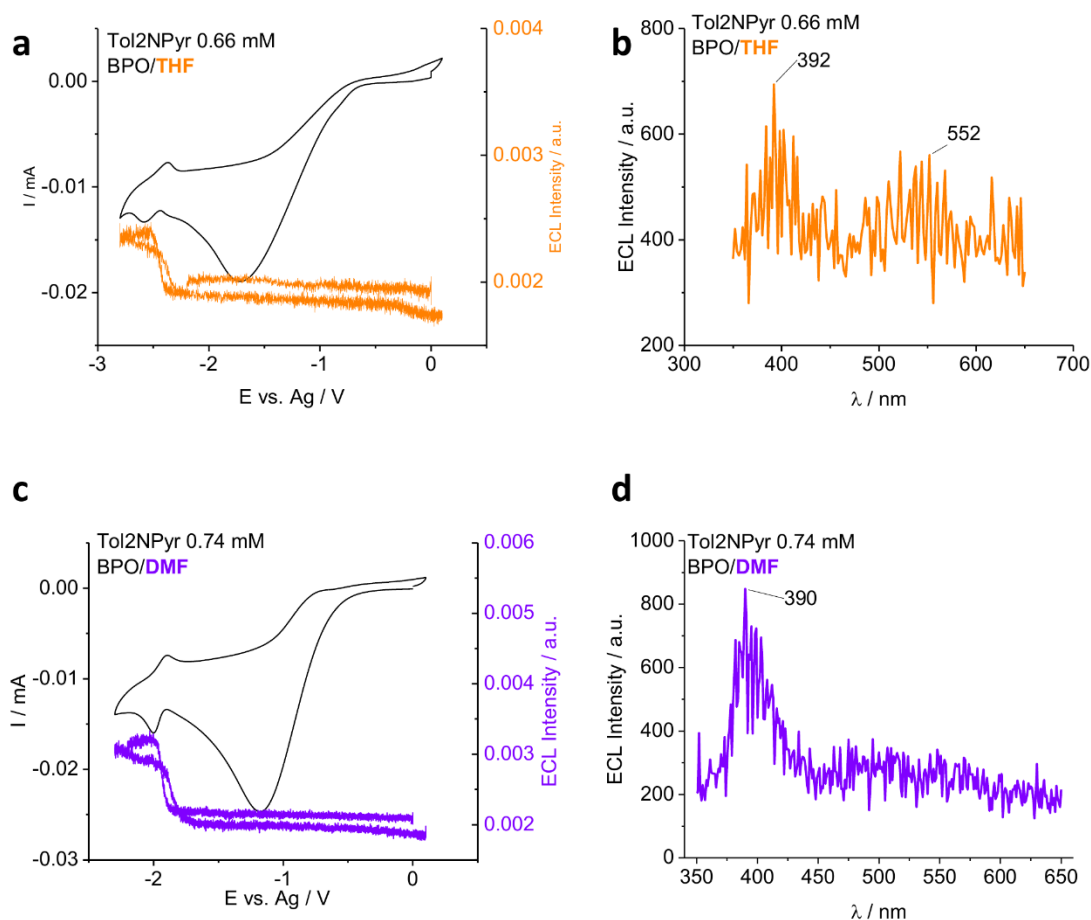
*Figure 4.23 (**a**) CV-ECL of **Tol2NPyr** 0.66 mM in Bu₄NPF₆/THF and 3.5 mM **BPO**. (**b**) ECL spectrum of **Tol2NPyr** with **BPO** in Bu₄NPF₆/THF, (**c**) CV-ECL of **Tol2NPyr** 0.74 mM and 3.5 mM **BPO** in Bu₄NPF₆/DMF and (**d**) ECL spectrum of **Tol2NPyr** with **BPO** in Bu₄NPF₆/DMF. CV were measured at 200mV/s and 298 K with a Pt disk with a diameter of 2 mm as working electrode and Ag wire as quasi-reference electrode. Measured in a dark box, amplification of the PMT 650 V. ECL spectra were recorded using a double potential step. Amplification of the PMT 750 V, integration time 150 ms, and monochromator speed rate 600 nm/min.*

4.8 Conclusion

The electrochemical characterisation of a series of substituted azapyrenes showed the effect of the nitrogen position on the electrochemical properties of heteroaromatic polycyclic molecules. When nitrogen directly contributes to the HOMO and LUMO, the frontier orbital energies decrease. The reactivity of the **Ph2NPyr** radical cation has been explored, and the oxidised product was characterized. At the current state, we hypothesise that a positively charged **C-N dimer** is produced by the oxidative coupling of azapyrene radical cation. Further studies such as IR spectroscopy will help to confirm our hypothesis. At more positive potential, electropolymerization of **Ph2NPyr** occurs and the same dimer was observed to be present as fragment from the film.

Finally, the electrochemiluminescence of azapyrene was studied using different sacrificial co-reactants. Excimer emission, which is not present in PL, was observed for 2-azapyrene, and a reaction mechanism was proposed for **BPO** as a co-reactant. This mechanism can also explain the difference observed in the ECL behaviour of the two positional isomers, **Ph2NPyr** and **Ph1NPyr**, because PhCOO$^•$ from the dissociative electron transfer of BPO could only oxidise the 2-azapyrenes. The nitrogen position was the major contributor to the different ECL behaviours.

References:

1. Figueira-Duarte, T. M. & Müllen, K. Pyrene-Based Materials for Organic Electronics. *Chem Rev* **111**, 7260–7314 (2011).

2. Feng, X., Hu, J., Redshaw, C. & Yamato, T. Functionalization of Pyrene To Prepare Luminescent Materials—Typical Examples of Synthetic Methodology. *Chemistry – A European Journal* **22**, 11898–11916 (2016).

3. Vardanyan, A., Boldt, S., Villinger, A., Ehlers, P. & Langer, P. Synthesis and Properties of 1-Azapyrenes. *Journal of Organic Chemistry* **87**, 11296–11308 (2022).

4. Molenda, R., Boldt, S., Villinger, A., Ehlers, P. & Langer, P. Synthesis of 2-Azapyrenes and Their Photophysical and Electrochemical Properties. *Journal of Organic Chemistry* **85**, 12823–12842 (2020).

5. Tucker, S. A., Acree, W. E. & Tanga, M. J. Polycyclic Aromatic Nitrogen Heterocycles. Part II: Effect of Solvent Polarity on the Fluorescence Emission Fine Structure of Three Azapyrene Compounds. *Appl Spectrosc* **45**, 57–60 (1991).

6. Nakazato, T. *et al.* The reductive aromatization of naphthalene diimide: a versatile platform for 2,7-diazapyrenes. *Chemical Communications* **54**, 5177–5180 (2018).

7. Han, Y. *et al.* Synthesis, Characterization, and Properties of Diazapyrenes via Bischler-Napieralski Reaction. *Journal of Organic Chemistry* **84**, 3953–3959 (2019).

8. Mukherjee, A. *et al.* 2,7-Diazapyrenes: a brief review on synthetic strategies and application opportunities. *RSC Adv* **12**, 9323–9341 (2022).

9. Geib, S. *et al.* 1,3,6,8-tetraazapyrenes: Synthesis, solid-state structures, and properties as redox-active materials. *Journal of Organic Chemistry* **77**, 6107–6116 (2012).

10. Stępień, M., Gońka, E., Żyła, M. & Sprutta, N. Heterocyclic Nanographenes and Other Polycyclic Heteroaromatic Compounds: Synthetic Routes, Properties, and Applications. *Chem Rev* **117**, 3479–3716 (2017).

11. Merz, J. *et al.* Pyrene Molecular Orbital Shuffle—Controlling Excited State and Redox Properties by Changing the Nature of the Frontier Orbitals. *Chemistry – A European Journal* **23**, 13164–13180 (2017).

12. Heinze, J., Frontana-Uribe, B. A. & Ludwigs, S. Electrochemistry of conducting polymers-persistent models and new concepts. *Chem Rev* **110**, 4724–4771 (2010).

13. Bachman, J. C. *et al.* Electrochemical polymerization of pyrene derivatives on functionalized carbon nanotubes for pseudocapacitive electrodes. *Nat Commun* **6**, 3–4 (2015).

14. Omura, Y., Tachi, Y., Okada, K. & Kozaki, M. Synthesis and Properties of Nitrogen-Containing Pyrenes. *J Org Chem* **84**, 2032–2038 (2019).

15. Richter, M. M. Electrochemiluminescence (ECL). *Chem Rev* **104**, 3003–3036 (2004).

16. J.Bard. *ELECTROGENERATED CHEMILUMINESCENCE*. (Marcel Dekker, Inc, 2004).

17. Bard, A. J. & Faulkner, L. R. *Electrochemical methods: fundamental and applications*. (Wiley, 1980).

18. Freed, D. J. & Faulkner, L. R. Mechanisms of Chemiluminescent Electron-Transfer Reactions. I. The Role of the Triplet State in Energy-Deficient Systems. *J Am Chem Soc* **93**, 2097–2102 (1971).

19. Chang, J., Hercules, D. M. & Roe, D. K. The role of the triplet state in the electrochemiluminescence of rubrene. *Electrochim Acta* **13**, 1197–1207 (1968).

20. *Analytical Electrogenerated Chemiluminescence*. (Royal Society of Chemistry, 2019). doi:10.1039/9781788015776.

21. Akins, D. L. & Birke, R. L. Energy transfer in reactions f electrogenerated aromatic anions and benzoyl peroxide. Chemiluminescence and its mechanism. *Chem Phys Lett* **29**, 428–435 (1974).

22. Donkers, R. L., Maran, F., Wayner, D. D. M. & Workentin, M. S. Kinetics of the reduction of dialkyl peroxides. New insights into the dynamics of dissociative electron transfer. *J Am Chem Soc* **121**, 7239–7248 (1999).

23. Antonello, S. & Maran, F. The Role and Relevance of the Transfer Coefficient α in the Study of Dissociative Electron Transfers: Concepts and Examples from the Electroreduction of Perbenzoates. *J Am Chem Soc* **121**, 9668–9676 (1999).

24. Antonello, S. & Maran, F. Intramolecular dissociative electron transfer. *Chem Soc Rev* **34**, 418 (2005).

25. Lai, R. Y. *et al.* Electrogenerated Chemiluminescence. 74. Photophysical, Electrochemical, and Electrogenerated Chemiluminescent Studies of Selected Nonplanar Pyrenophanes. *J Phys Chem A* **108**, 376–383 (2004).

26. Fiorani, A., Difonzo, M., Rizzo, F. & Valenti, G. Versatile electrochemiluminescent organic emitters. *Curr Opin Electrochem* **34**, 100998 (2022).

27. Kihara, T., Sukigara, M. & Honda, K. Electrochemil uminescence of pyrene in acetonitrile. *J Electroanal Chem Interfacial Electrochem* **47**, 161–166 (1973).

28. Fleet, B., Kirkbright, G. F. & Pickford, C. J. The electrogenerated chemiluminescence of pyrene and some related compounds. *J Electroanal Chem Interfacial Electrochem* **30**, 115–121 (1971).

29. Lai, R. Y. *et al.* Electrogenerated Chemiluminescence. 74. Photophysical, Electrochemical, and Electrogenerated Chemiluminescent Studies of Selected Nonplanar Pyrenophanes. *J Phys Chem A* **108**, 376–383 (2004).

30. Choi, J. P. *et al.* Electrogenerated Chemiluminescence. 76. Excited Singlet State Emission vs Excimer Emission in Ter(9,9-diarylfluorene)s. *Journal of Physical Chemistry B* **107**, 14407–14413 (2003).

31. Suk, J., Wu, Z., Wang, L. & Bard, A. J. Electrochemistry, electrogenerated chemiluminescence, and excimer formation dynamics of intramolecular π-stacked 9-

naphthylanthracene derivatives and organic nanoparticles. *J Am Chem Soc* **133**, 14675–14685 (2011).

32. Shirai, S. & Inagaki, S. Ab initio study on the excited states of pyrene and its derivatives using multi-reference perturbation theory methods. *RSC Adv* **10**, 12988–12998 (2020).

33. Yasukouchi, K., Taniguchi, I., Yamaguchi, H. & Arakawa, K. Anodic oxidation of acridine in acetonitrile. *J Electroanal Chem Interfacial Electrochem* **121**, 231–240 (1981).

34. Bolletta, F., Juris, A., Maestri, M. & Sandrini, D. Quantum yield of formation of the lowest excited state of Ru(bpy)2+3 and Ru(phen)2+3. *Inorganica Chim Acta* **44**, L175–L176 (1980).

35. Becker, W. G., Seung, H. S. & Bard, A. J. Electrogenerated chemiluminescence: Part XLIII. Aromatic hydrocarbon/peroxydisulfate systems in acetonitrile-benzene solutions. *J Electroanal Chem Interfacial Electrochem* **167**, 127–140 (1984).

Conclusion and outlook

The framework of my doctoral project has been the study of the reactivity of electrogenerated polycyclic aromatic radical ions, particularly focussed on the radical cation and its oxidative coupling and intramolecular cyclodehydrogenation.

In the second chapter of this thesis, we studied the electrochemical behaviour of a series of extended polycyclic aromatic hydrocarbons based on benzo[rst]pentaphene, showing the effect of bulky functional groups on reducing the chemical reactivity of radical ions by protecting the reactive positions. Through electrochemical oxidation of a benzo[rst]pentaphene dimer at a rather highly positive potential, a film formation process was observed and it has been supposed that cyclodehydrogenation could take place between its units; nevertheless, mass spectroscopy confuted our initial hypothesis. Further studies are still ongoing to elucidate the chemical nature of the electrogenerated film deposited on the electrode. Curved and bucky-bowl aromatic molecules are another class of polycyclic aromatic species, with interesting electrochemical behaviours, that were investigated to understand their electrochemically induced reactivity. One of these curved polyaromatics studied is Sumanene, which is a curved bowl-shaped molecule isoelectronic to triphenylene with sp^3 carbons similar to fluorene, investigated together with its smaller fragments. Sumanene, and its fragments as well, showed electrochemical oxidative coupling of their radical cations to multiple chemical structures, which deposit on the electrode, ranging from linear oligomers to more π-conjugated species. Finally, in the same chapter, a heteroaromatic bowl-shaped pentabenzo-azacorannulene was electrochemically characterised, showing interesting differences in its electrochemical behaviour depending on temperatures and solvents. We attributed this behaviour to an aggregate present in DCM and at low temperatures, which may be formed by the concave-convex stacking of two azacorannulene units, which disaggregate upon electron transfer. Pentaphenylpyrrole derivates, considered as precursors of azacorannulenes, were also electrochemically studied, since we were particularly interested in the electrochemical cyclodehydrogenation of the pyrroles that would be converted into curved pentabenzo-azacorannulene if all the phenyl rings are cyclized. The data so far obtained of the oxidation

product are not consistent with the redox process of the pentabenzo-azacorannulene during the voltammetric timescale and hence with the occurrence of a complete cyclodehydrogenation process. Nonetheless, further analysis, such as CV at higher scan rates with a smaller ultramicroelectrode and preparative-scale electrolysis, will help to identify the oxidation product of pentaphenylpyrrole.

In the third chapter of this thesis, we describe the electrochemical cyclodehydrogenation of hexaphenylbenzene to prepare self-assembled hexabenzocoronene directly on an interdigitated electrode which was subsequently studied as an organic electrochemical transistor. The electrochemical method proved to be successful and superior for the preparation of HBC from a soluble precursor, and better transistor performance was obtained with electrochemical deposition than with other solution-processable methods. Nonetheless, the electrochemical preparation and deposition of oligomers of pyrene and fluorene on interdigitated electrodes showed poor performance for transistor applications, showing that controlling the chemical nature and electrodeposition of the organic film is crucial for device fabrication. As perspective, it will be important to understand how different parameters such as solvent, electrolyte, and electrode material during electropolymerization and deposition can affect the organic film morphology and its electrical and optical properties.

In the study of physical chemical properties of polyaromatic and heteroaromatic compounds also the electrochemiluminescence of some species have been studied and reported in the fourth chapter, where the electrochemical and electrogenerated chemiluminescence of heteroaromatic azapyrene derivatives are discussed. It has been showed that the nitrogen position can strongly affect the electronic properties of the molecule by tuning the HOMO and LUMO energies. Moreover, we further investigated the product of the chemically irreversible oxidation of azapyrene, finding that a dimer is generated by the coupling of azapyrene radical cations; concerning this aspect, research is still ongoing to understand whether in the dimer the linkage is between two C atoms or the pyridinic N and a C atom. The electrogenerated chemiluminescence of 2-azapyrenes with co-reactant benzoylperoxide (BPO) showed a double ECL emission, particularly fluorescence and excimer emission. We demonstrated that the excimer of 2-azapyrenes, which was not observed in photoluminescence, resulted from ion-annihilation of the azapyrene radical cations and anions. In particular, during ECL with BPO, the 2-azapyrene radical cation is generated by homogeneous oxidation upon reaction with the benzoyloxy radical (PhCOO$^•$), whereas the azapyrene radical anion is electrogenerated by a direct reduction at the electrode. Instead, 1-azapyrene ECL showed only the fluorescence

emission produced by triplet-triplet annihilation because ECL with BPO was energy-deficient. Moreover, the excimer of 1-azapyrene was not observed with BPO because the radical PhCOO$^\bullet$ could not oxidise 1-azapyrene, whereas ion-annihilation could produce the excimer.

In summary, this thesis concerns the different electrochemical behaviours of polycyclic aromatic molecules, where the reactions of electrogenerated species are the *red thread* that connects every aspect of my project, from unconventional methods for the synthesis of carbon nanostructures, which can be used in electrochemical transistors, to novel organic emitters in ECL showing unexpected optical and electrochemical properties.

Experimental section

Material and device fabrication

Electrochemical grade tetrabutylammonium hexafluorophosphate (Bu$_4$NPF$_6$), pyrene, acenaphthylene, fluorene, triphenylene, benzoylperoxide (BPO), hexaphenylbenzene, acetonitrile (ACN), dimethylformamide (DMF), dichloromethane (DCM), tetrahydrofuran (THF), 1-ethyl-3-methylimidazolium tris(perfluoroethyl)trifluorophosphate) ionic liquid (EMimFAP), hexabenzocoronene (HBC) and other reagents were purchased from Sigma-Aldrich or Merck Millipore and used as received unless otherwise stated.

Benzo[rst]pentaphene and its derivatives were synthesised by Dr. Xu in the Akimitsu Narita group (Okinawa Institute of Science and Technology Graduate University, Japan), according to the procedure reported in literature,[1] and used as received. Sumanene was synthesized by Toru Amaya group (Nagoya City University, Japan) according to the procedure reported in literature[2] and used as received. Fluorene was purified by sublimation under vacuum and condensate on a custom-made glass sublimation apparatus. Pentaphenylpyrrole derivatives were synthesised by Dr. Bombonato E. and Dr. Ronchi P. (Chiesi Farmaceutici S.p.a.), according to the procedure reported in literature.[3] Pentabenzoazacorannulene was synthesized by Shingo Ito group (Nanyang Technological University, Singapore) according to the procedure reported in literature.[4] Corannulene was synthesized by Scott group (Boston College, USA) according to the reported procedure[5] and used as received. (Bu$_4$N)$_2$S$_2$O$_8$ was easily prepared in H$_2$O from K$_2$S$_2$O$_8$ and Bu$_4$NHSO$_4$ and extracted with DCM according to the reported procedure.[6] (note: use a low temperature at rotavapor to avoid persulfate decomposition from the cleavage of the O-O bond). Azapyrene derivatives were synthesized by Langer Group (Rostock University, Germany) according to the procedure reported in literature.[7,8]

Dry dichloromethane (DCM) was prepared by refluxing DCM over B$_2$O$_5$ in an inert atmosphere (Ar) for at least 48h and distilled in a Schlenk flask over 3 Å activated molecular sieves. The molecular sieves were activated at 320°C for 48h, then Ar was removed by placing the Schlenk flask under vacuum at 210°C for at least 5-7 days. After preparing the Schlenk flask, DCM can

be distilled, keeping the Ar atmosphere in order to avoid H_2O contamination. Distilled DCM was kept in a Schlenk flask with activated molecular sieves for at least 5 days and stored protected from light. Separately, a second smaller Schlenk flask with alumina super I neutral (ICN Biomedicals) was prepared and activated by heating to a maximum of 200°C under vacuum. Finally, DCM was distilled from the Schlenk flask with molecular sieves to the Schlenk flask with activated Al_2O_3 with a trap-to-trap distillation using liquid N_2 to condense the DCM vapours in the second flask.

Dry tetrahydrofuran (THF) was prepared by refluxing THF over Na fragments, previously cleaned from oxides, and washed with THF. THF was refluxed for at least 7 days in an inert atmosphere (Ar), and then distilled over a 250mL round-bottom flask with 1 g of benzophenone and 2 g of solid Na under an Ar atmosphere. The THF solution was again refluxed under stirring for at least 7 days. THF was distilled in a Schlenk flask with 1 g of anthracene, 3 g of Na, and a stirring bar under an Ar atmosphere to avoid H_2O contamination. The THF solution was kept under stirring for at least 7 days and protected from light. Anthracene dianion is a powerful reducing agent and has a blue colour, if H_2O or O_2 enters or is already present the solution will turn green. Finally, THF was transferred under Ar atmosphere in a second smaller Schlenk flask with a magnetic stirring bar. When trap-to-trap distillation of THF into the electrochemical cell with liquid N_2 occurs the anthracene salt is not distilled.

HBC devices were prepared using different solution processing methods, even though it is more accurate to define them as HBC dispersions. In particular, HBC films were deposited on a 5x5 µm Micrux interdigitated Au electrode (Figure 1)
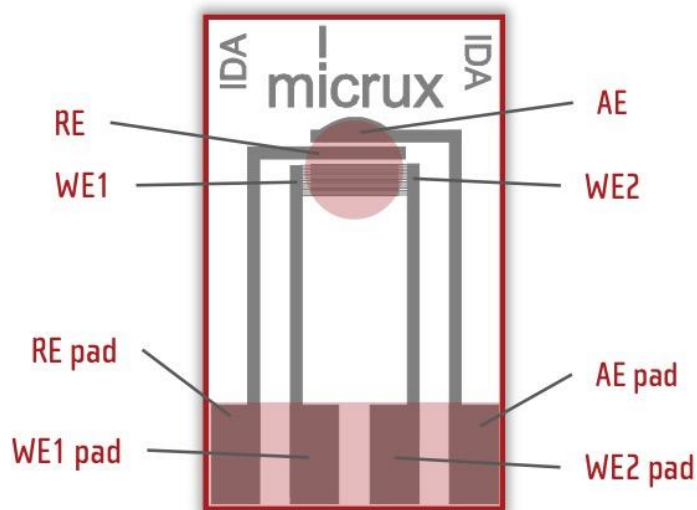
Figure 1 Interdigitated Au electrode with 30 gold pairs electrode, gold RE and gold AE

The HBC ink (0.5 mg/mL) for the drop casting has been prepared by stirring the dispersion for 5 h in hot 1,2,4-trichlorobenzene (110 °C) and deposited 5 µL of the hot HBC dispersion on a heated (110 °C) interdigitated Au electrode. The HBC drop was kept on the heated interdigitated electrode covered with a Petri dish and allowed to slowly evaporate. Drop casting was repeated twice for a total of 5 µg of deposited HBC.

The HBC ink (0.1 mg/mL) for the aerosol jet printing (AJP) has been prepared by sonicating for 30 min a dispersion of HBC (300 µL of a 0.5 mg/mL HBC dispersion in DCB), 1,2-dichlorobenzene (1.14 mL) and 5 % v/v of terpineol (60 µL of a solution 1:1 with DCB) to adjust the dispersion viscosity. The total volume of the ink was 1.5 mL. The ultrasonic atomiser was set to 470 mA and was cooled with H_2O at 15 °C. A good aerosol was produced with the reported ink parameters. The plate and the interdigitated electrode were heated to 250 °C in order to evaporate the DCB solvent once printed. A nozzle of 125 µm was used, nitrogen was the carrier gas with a sheath flow of 9 ccm (0.12 psi) and an aerosol flow of 27 ccm (0.45 psi). The flow speed was set to 0.5 mm/s and 9 repeated prints were performed. Between each printing, the electrode was cleaned with THF and iPrOH, as well as the PTFE tubes with acetone, in order to remove condensed droplets. The printing area was a rectangular area (2.0x0.6 mm) with horizontal and vertical lines with 25 µm spacing between each line.

The HBC ink for Langmuir-Blodgett (LB) was prepared by sonication (for 1 h) a dispersion of HBC 5 mg/ml in THF. The beaker was filled with deionised H_2O to a certain level, and then the LB setup with the cleaned interdigitated electrode was placed inside the beaker completely

immersed in H_2O. A top layer of purified hexane (750 μL) was added, followed by 250 μL of the HBC dispersion. Hexane and THF were allowed to evaporate while the HBC formed a film floating over the H_2O layer. Once a film was produced, although with some aggregates, the LB setup was carefully lifted from the H_2O, depositing the HBC film once H_2O evaporated on the electrode.

Electrochemical characterisation and electropolymerization

Electrochemical experiments in dried solvent were carried out in an airtight single-compartment cell using a platinum disk with a diameter of 125 μm as the working electrode (WE), a Pt spiral as the counter electrode (CE), and a silver spiral as a quasi-reference electrode (QRE). The drift of the quasi-reference electrode was small during the time required for the experiment and was subsequently corrected for each voltammogram. The $E_{1/2}$ potentials were measured as the averages of the cathodic and anodic peak potentials and by digital simulation in the case of non-Nernstian or overlapping processes. The corrected potential values were determined by adding ferrocene (Fc) as an internal standard at the end of each experiment. The ferrocenium/ferrocene couple ($Fc^{+/0}$) standard potential (at 298 K) was +0.42 V vs SCE, i.e., the aqueous saturated calomel electrode in DCM and +0.58 V vs. SCE in THF. The electrochemical cell was cleaned with a 1:1 H_2SO_4 (98%), HNO_3 (60%) concentrated acid solution for at least 3h, then the cell was rinsed several times with deionised H_2O to remove excess acid, and then dried in a laboratory oven at 80°C. The Pt CE was cleaned by immersion in the same acid solution for at least 30 min, then the CE was rinsed several times with deionised H_2O, sonicated in deionised H_2O for few minutes and rinsed several times with deionised H_2O and acetone. The WE was mechanically polished with alumina slurry (Buehler) with decreasing granulometry (1, 0.3 and 0.1 μm). Between each polishing step, the WE was rinsed with deionised H_2O and sonicated for a few minutes. Finally, the electrode was rinsed several times with deionised H_2O and acetone. The Ag wire was mechanically polished with alumina slurry 0.3 μm, rinsed with deionised H_2O, sonicated for a few minutes, and then rinsed several times with deionised H_2O and acetone.

The cell containing the supporting electrolyte was dried under vacuum at 100–110 °C for at least 48 h prior to each experiment. Before performing the trap-to-trap distillation of the solvent, the pressure measured in the electrochemical cell was typically 1×10^{-5} mbar. The electroactive compound was added 30 min prior the solvent distillation. Voltammograms were

recorded using a custom-made fast and low-current potentiostat controlled by an AMEL Mod. 568 programmable function generators. The potentiostat was interfaced to a Nicolet Mod. 3091 digital oscilloscope and the data were transferred to a personal computer by the program Antigona. Digital simulations of the CV curves were performed by Antigona utilising the best-fitting procedure of the experimental curves recorded at different scan rates.

The preparative-scale electrolysis was carried out in a custom-made single-compartment electrochemical cell, using a Pt foil as WE for the electrolysis or a glassy carbon (GC) disk with a diameter of 1 mm for cyclic voltammetry; a Pt spiral as the CE was kept separated by a custom-made glass cylinder with a glass frit at the end. Oxygen was removed before electrolysis by stirring and bubbling with Ar inside the solution. During electrolysis, the solution was stirred and the flux of Ar was maintained above the solution. Voltammograms and electrolysis signals were obtained using a Biologic SP300 potentiostat.

The electropolymerization experiment was carried out using the same setup of the electrochemical characterisation, but with a small indium-titanium-oxide transparent electrode as the WE or an interdigitated Au electrode by Micrux with 59 pairs of 1.8mm length (106.2 mm in total), 5 μm width and 5 μm gap between the pairs. WE was sonicated in H_2O, EtOH, and acetone for 1 min each and rinsed several times with the corresponding solvent. The electropolymerized film was washed several times in fresh DCM after preparation and in isopropanol before AFM and electrical characterisation.

Photophysical characterisation

Absorption spectra were recorded using a Cary 5 (Varian) baseline corrected. The scan rate was 454 nm/min at 298 K, with fully open slits. Alternatively, UV–vis absorption spectra were recorded with a PerkinElmer l40 spectrophotometer using quartz cells with a path length of 1.0 cm. Luminescence spectra were obtained using a PerkinElmer LS-50 or Edinburgh FLS920 spectrofluorometer equipped with a Hamamatsu R928 phototube.

Electrical characterisation

Electrical characterisation of the films was carried out in deionised H_2O or EMimFAP (1-ethyl-3-methylimidazolium tris(perfluoroethyl)trifluorophosphate) ionic liquid, using a vertically placed Ag/AgCl (KCl 0.1M) as the reference electrode (RHD Instrument Micro-reference) and a

gold side gate or a vertically placed Pt wire as the gate. The interdigitated electrode was placed inside an All-in-one PEEK electrochemical cell by Micrux and connected to an Agilent 4155C semiconductor parameter analyser. Measurements are generally carried out in air, and when the gate voltages are very negative, the measurements are carried out in a glovebox.

Spectroelectrochemistry

UV/vis spectroelectrochemical studies were carried out in a homemade optically transparent thin layer electrode (OTTLE) cell built according to the design of Yellowlees et al.[9]. The path length is 0.3 mm. Temperature control was achieved with a special cell holder with quartz windows, in which two nitrogen fluxes at room T and one cooled by passing through a dewar with liquid N_2 were regulated with two needle valves. The working electrode was a Pt gauze with good optical transparency, and an AgCl coated Ag wire was used as the reference electrode and was separated by the solution with a glass frit. A Pt wire was used as the CE and kept far from the WE to avoid the diffusion of the species generated at the CE. The electrochemical cell was cleaned as the one for the electrochemical characterisation. WE and CE were immersed in the same acidic solution (H_2SO_4/HNO_3) for at least 1h and rinsed several times with deionised H_2O and acetone. The electrolyte, electroactive species, and solvent were inserted under an inert atmosphere (Ar), and the cell was closed (partially air-tight). The potentials were applied using an Amel model 552 potentiostat, and the current was recorded using a HP multimeter. The spectra were recorded using a Cary 5 (Varian) baseline corrected. The scan rate was 454 nm/min, with fully open slits.

Electrochemiluminescence

A one-compartment, three-electrode airtight cell with high-vacuum O-rings and glass stopcocks was used for the ECL measurements. A Pt side-oriented 2 mm diameter disk sealed in glass was used as the working electrode, a Pt spiral was used as the counter electrode, and the reference electrode was a quasi-reference Ag wire. The electrodes were cleaned using the same procedure as for electrochemical characterisation. The electrochemical cell was cleaned by immersion in a concentrated KOH/EtOH solution for at least 30 min, thoroughly rinsed with de-ionised H_2O, and immersed in a concentrated aqueous HCl solution for at least 30 min. Finally, the cell was rinsed several times with deionised H_2O to remove excess acid and then dried in a laboratory oven at 80°C. ECL measurements were performed in ACN with Bu_4NPF_6

as the supporting electrolyte, and the cell containing the supporting electrolyte and co-reactant was dried under vacuum at 10^{-2} mbar at room temperature for at least 1h prior to the experiment. The electroactive species was added at least 15 min before solvent introduction. Solid and ACN were added under an inert atmosphere by fluxing Ar inside the cell. To remove Ar and other gases (such as O_2) from the vapour phase, we carefully applied vacuum in the cell containing ACN, leading to a saturated ACN vapour phase inside the cell.

The voltammograms and amplified ECL signals were recorded using a Biologic SP300 potentiostat. The ECL signal generated was measured with a photomultiplier tube (PMT, Hamamatsu R4220p) placed close to the cell and in front of the working electrode inside a homemade dark box. A voltage in the range 650–750 V was supplied to the PMT. The light/current/voltage curves were recorded by collecting the pre-amplified PMT output signal using an ultralow noise Acton research model 181.

ECL spectra were recorded by inserting the same PMT into a dual-exit monochromator (ACTON RESEARCH model Spectra Pro2300i). The photocurrent detected at the PMT accumulated for 150 ms for each monochromator wavelength step (usually 1 nm, 600 nm/min). The entrance and exit slits were fixed at maximum values of 3 mm. The 455 nm cutoff high band pass filter was placed in front of the PMT aperture and kept fixed in its position with elastic bands. The filter was 3 mm thick.

Laser desorption ionisation time of flight mass spectroscopy

Laser Desorption-Ionisation Time of Flight Mass Spectra (LDI-TOF) were obtained in collaboration with Prof. Stefano Bettati and Prof. Samanta Raboni of the Università di Parma, using an Applied Biosystems/MDS SCIEX 4800 MALDI TOF/TOF™ Analyser equipped with a Nd:YAG laser at 355 nm wavelength.

Electron spray ionisation mass spectroscopy

Mass spectrometer Waters Xevo G2-XS QTof with ESI-APCI, eluent H_2O/ACN in different ratios, from 95/5 to 20/80, with a pre-column C-18 liquid chromatography before injection for the separation from the electrolyte.

Silica flash chromatography

Silica flash chromatography was performed with a 30 cm glass chromatography column using silica for chromatography ∅ 0.05 ÷ 0.20 μm AnalytiCals (Carlo Erba). Eluent 1:1 cyclohexane - ethyl acetate mixture.

Atomic force microscopy

AFM images were taken with a Bruker Icon Dimension in Scan Assyst mode and a Si3N4 probe (Scanasyst-air), 0.4 N/m spring constant. Feedback parameter was software adjusted (scan assist mode). The peak force amplitude was between 80-120 nm and usual scan rate was 0.3 μm/s. Images were taken with 1024 lines and usually as 5x5 μm or smaller. The film thickness determination was performed by scratching the film with a very sharp needle and through multiple AFM line scans the average thickness was calculated.

Confocal Raman spectroscopy

Raman spectroscopy was carried with a Renishaw inVia confocal microscope and a 532 nm Renishaw laser (RL532C100) with a 20x Olympus optic. The laser power was maintained at 5% to avoid substrate degradation, and the Raman signal was accumulated 20 times and integrated for 1s each. The HBC Raman spectra showed a strong fluorescence background, and the baseline was removed by fitting it to a 2nd order polynomial and subtracting the fitted baseline from the raw data.

Optical microscopy

Optical images were taken with an Olympus microscope BX51 with different optics from 5x to 100x in the bright-field mode or in fluorescence mode with a wide spectrum UV lamp.

Computational details

Quantum chemical calculations were performed by Prof. Daniele Fazzi and Prof. Fabrizia Negri at the University of Bologna with DFT calculations with wB97X-D/Def2TZVP functional. For the conformational analysis of BBPP-Mes dimer, CREST (GFN2-xTB) was used and optimised at the GFN2-xTB and wB97X-D/def2-SVP or def2-TZVP levels.

References:

1. Xu, X. *et al.* Synthesis and Characterizations of 5,5′-Bibenzo[rst]pentaphene with Axial Chirality and Symmetry-Breaking Charge Transfer. *Advanced Science* **9**, 2200004 (2022).

2. Sakurai, H., Daiko, T. & Hirao, T. A synthesis of sumanene, a fullerene fragment. *Science (1979)* **301**, 1878 (2003).

3. Chen, X. *et al.* Palladium-Catalyzed Reaction of Arylamine and Diarylacetylene: Solvent-Controlled Construction of 2,3-Diarylindoles and Pentaarylpyrroles. *European J Org Chem* **2012**, 4380–4386 (2012).

4. Ito, S., Tokimaru, Y. & Nozaki, K. Benzene-Fused Azacorannulene Bearing an Internal Nitrogen Atom. *Angewandte Chemie International Edition* **54**, 7256–7260 (2015).

5. Scott, L. T. *et al.* Corannulene. A Three-Step Synthesis [1]. *J Am Chem Soc* **119**, 10963–10968 (1997).

6. Yang, S. G., Hwang, J. P., Park, M. Y., Lee, K. & Kim, Y. H. Highly efficient epoxidation of electron-deficient olefins with tetrabutylammonium peroxydisulfate. *Tetrahedron* **63**, 5184–5188 (2007).

7. Molenda, R., Boldt, S., Villinger, A., Ehlers, P. & Langer, P. Synthesis of 2-Azapyrenes and Their Photophysical and Electrochemical Properties. *Journal of Organic Chemistry* **85**, 12823–12842 (2020).

8. Vardanyan, A., Boldt, S., Villinger, A., Ehlers, P. & Langer, P. Synthesis and Properties of 1-Azapyrenes. *Journal of Organic Chemistry* **87**, 11296–11308 (2022).

9. A. J. L. Pombeiro & J. A. McCleverty. *Molecular Electrochemistry of Inorganic, Bioinorganic and Organometallic Compounds.* (Springer Netherlands, 1993). doi:10.1007/978-94-011-1628-2.